

# Pulsed Electroluminescent Devices for Emission Across Energy and Length Scales

*Vivian Wang*



Electrical Engineering and Computer Sciences  
University of California, Berkeley

Technical Report No. UCB/EECS-2023-158

<http://www2.eecs.berkeley.edu/Pubs/TechRpts/2023/EECS-2023-158.html>

May 12, 2023

Copyright © 2023, by the author(s).  
All rights reserved.

Permission to make digital or hard copies of all or part of this work for personal or classroom use is granted without fee provided that copies are not made or distributed for profit or commercial advantage and that copies bear this notice and the full citation on the first page. To copy otherwise, to republish, to post on servers or to redistribute to lists, requires prior specific permission.



Pulsed Electroluminescent Devices for Emission Across Energy and Length Scales

by

Vivian Wang

A dissertation submitted in partial satisfaction of the

requirements for the degree of

Doctor of Philosophy

in

Electrical Engineering and Computer Sciences

in the

Graduate Division

of the

University of California, Berkeley

Committee in charge:

Professor Ali Javey, Chair

Professor Ming Wu

Professor Daryl Chrzan

Spring 2023

Pulsed Electroluminescent Devices for Emission Across Energy and Length Scales

Copyright 2023  
by  
Vivian Wang

## Abstract

Pulsed Electroluminescent Devices for Emission Across Energy and Length Scales

by

Vivian Wang

Doctor of Philosophy in Electrical Engineering and Computer Sciences

University of California, Berkeley

Professor Ali Javey, Chair

Unusual device architectures may open up unexpected opportunities for optoelectronic devices. For example, the range of luminescent materials that can be easily integrated in light-emitting devices is often limited by material processing and band alignment issues. This hinders the development of electroluminescent devices at extreme wavelengths and the use of electroluminescence spectroscopy as an analytical technique. In this thesis, I explore an unconventional scheme of electrically-driven light emission based on pulsed metal-oxide-semiconductor capacitor devices. This concept can be used to produce electroluminescence from a wide range of materials including bulk semiconductors, two-dimensional semiconductors, colloidal quantum dots, organic molecules, and more. The performance of this light-emitting device is studied through simulation and experiment, and practical characterization is undertaken with different alternating-current driving schemes. By scaling the device, low voltage operation of these devices is further demonstrated. The device not only achieves emission spanning the near-ultraviolet to near-infrared energy spectrum, but also offers a straightforward avenue towards achieving electroluminescence from materials with different physical compositions and length scales spanning single particles to thick films. As a result of the scalable fabrication approach, miniaturized arrays of many different color light-emitting devices can be easily created on a monolithic substrate. The potential of this device platform for spectroscopic applications is illustrated by spectral imaging demonstrations which combine compressive sensing-based algorithms with highly multicolored and multiplexed light-emitting arrays.

# Contents

<b>Contents</b>	<b>i</b>
<b>1 Introduction</b>	<b>1</b>
1.1 Electroluminescence . . . . .	1
1.2 Light-emitting device structures . . . . .	2
1.3 Dissertation overview . . . . .	3
<b>2 A “generic” electroluminescent device</b>	<b>4</b>
2.1 Introduction . . . . .	4
2.2 Device structure . . . . .	6
2.3 Device mechanism . . . . .	12
2.4 Device characterization . . . . .	12
2.5 Spectroscopic opportunities . . . . .	26
2.6 Conclusion . . . . .	28
2.7 Methods . . . . .	28
2.8 Tables . . . . .	33
<b>3 Performance limits of a pulsed-driven electroluminescent capacitor</b>	<b>37</b>
3.1 Introduction . . . . .	38
3.2 Device operation and simulation . . . . .	39
3.3 Low-voltage operation . . . . .	40
3.4 Compatibility with low mobility materials . . . . .	46
3.5 Efficiency characterization . . . . .	56
3.6 Modulation speed . . . . .	58
3.7 Conclusion . . . . .	63
3.8 Methods . . . . .	64
<b>4 Resonant characterization of an AC-driven electroluminescent capacitor</b>	<b>67</b>
4.1 Introduction . . . . .	67
4.2 Operating scheme . . . . .	69
4.3 Equivalent circuit model . . . . .	79
4.4 Performance characterization . . . . .	81

4.5	Conclusion . . . . .	88
4.6	Methods . . . . .	89
<b>5</b>	<b>Compressive spectroscopy with multicolored electroluminescent arrays</b>	<b>91</b>
5.1	Introduction . . . . .	91
5.2	Arbitrary spectrum generation . . . . .	93
5.3	Compressive spectral measurement . . . . .	103
5.4	Compressive spectral imaging . . . . .	113
5.5	Conclusion . . . . .	116
5.6	Methods . . . . .	118
5.7	Tables . . . . .	120
<b>6</b>	<b>An electroluminescent device for single quantum dot emission</b>	<b>127</b>
6.1	Introduction . . . . .	127
6.2	Results and Discussion . . . . .	128
6.3	Conclusion . . . . .	135
6.4	Methods . . . . .	137
<b>7</b>	<b>Conclusion</b>	<b>140</b>
	<b>Bibliography</b>	<b>142</b>

## Acknowledgments

I would first like to acknowledge my advisor Ali Javey for the opportunity to conduct research in his group and develop ownership of a research direction. The expansive lab space housed an enjoyable experimental playground, and his guidance of the group allowed me to see how original research can be performed with simple experiments – a refreshing perspective in a world of increasingly complex science and engineering.

The work in this thesis would not have been possible without the support of various group members: Yingbo, who introduced me to research in the lab in the early years; Shiekh, who worked with me on the PL setups; Jongchan, who helped out with many miscellaneous tasks and shared valuable knowledge; and many others over the years including Niharika, Aiden, Wenbo, Danny, Junho, Jonghwa, Naoki, Shu, Reaz, and others. Joel Ager supported our laboratories at Lawrence Berkeley National Laboratory and always reminded me of the importance of safety and communication.

I would also like to acknowledge my qualifying exam committee members (Ming Wu, Boubacar Kante, Daryl Chrzan) and the professors whose classes taught me an entertaining array of knowledge spanning solid-state electronics, mechanical engineering, biophysics, deep learning, and more. I hope I can continue to keep learning after I graduate from school as I will certainly miss it.

I am grateful for my parents' support, which has allowed me to pursue academic studies over the years without any practical worries, and my sister Felicia, who has always been there in times of need. Finally, I cannot imagine this journey without the companionship of Min Cheol. His unceasing optimism and abundance of scientific stories always leave me hopeful for an adventurous future, wherever our paths may take us.

# Chapter 1

## Introduction

### 1.1 Electroluminescence

It is difficult to envision a modern world without manmade lighting. From the street lights illuminating our nighttime walks to the handheld displays tucked away in our pockets, the ability to generate light by artificially engineered means has changed the way we live, enabling us to be productive for longer hours of the day beyond those naturally defined by the rise and fall of the sun [1]. At the same time, the ubiquitous presence of artificial lighting has contributed to potentially detrimental rising energy consumption. Light-emitting diodes (LEDs), the contemporary solid-state form of lighting, rely on the phenomenon of electroluminescence, a process by which electrical charges are injected and recombine in a semiconductor to produce light. Although discovered in the early 1900s, it took many decades of development to turn the physical discovery into a technology practical enough to occupy our everyday lives. Along this technological journey, many key developments transformed the applications of LEDs as compact light sources (e.g. research on efficient blue LEDs which allowed us to complete the colors of the visible spectrum [2]) and we now possess exceptional control over their emission characteristics.

The concept of electroluminescence is far from new: electroluminescence in inorganic materials was reported in 1907 and 1927 by Henry Round and Oleg Losev, respectively, who found that SiC crystals exhibited light emission upon application of electric current [3, 4]. Subsequent work on light emission from semiconductor p-n junctions led to the creation of the first inorganic red LED in 1962 by Nick Holonyak [5], soon followed by LEDs of other colors from green to orange. In recent years, a variety of emerging materials for solid-state lighting have been explored, from organic semiconductors and colloidal quantum dots to nascent materials like two-dimensional semiconductors and perovskites. While these materials offer advantages such as ease of growth and large-area processing, there is still much room for improvement in the performance and lifetime of devices made from these materials. If achievable, lighting could achieve new form factors and purer colors among other characteristics.

## 1.2 Light-emitting device structures

The generation of light by electricity is a simultaneously simple but complex operation, and there are many ways to achieve it via a solid-state device. Perhaps the first structure that comes to mind is that of a light-emitting diode, of which there exists many variants tailored to a wide array of inorganic and organic materials. In these devices, a junction is formed between a p-type (possessing an excess of holes) and n-type (possessing an excess of electrons) doped semiconducting material. Upon application of forward bias, the number of p-side electrons and n-side holes increase, thereby increasing the chance of radiative recombination of electron-hole pairs leading to light emission.

The organic analog, or organic LED (OLED), operates based on a similar principle. Organic materials are a uniquely tunable material system due to the nearly infinite synthetic space accessible to molecular materials. An early bilayer prototype developed by Tang and Van Slyke in 1987 comprised a heterojunction between an electron transport and hole transport layer, which was sandwiched between low and high work function electrodes used to inject electrons and holes, respectively [6]. Notably, the organic layers were only tens of nanometers thick, enabling efficient light emission in contrast to earlier attempts which required hundreds of volts or more due to the use of millimeter-scale organic crystals [7]. In these so-called excitonic materials, injected charges localize on emissive molecules and form a bound electron-hole pair or exciton, which radiatively recombines to produce light emission. OLED architectures have been thoroughly developed over the years, oftentimes with numerous additional layers to optimize the transport and recombination of charges. An important development was the use of doped emissive layers in which a small percent of luminescent molecules are introduced into a conducting host material with larger band gap [8]. Electrical injection leads to exciton formation in the host material with subsequent transfer to the luminescent molecule, thus avoiding concentration quenching which otherwise reduces the luminescence efficiency. This class of devices has been pursued for their potential for low-cost, low-temperature integration on large-area or flexible substrates. In a similar spirit, electrically-driven colloidal quantum dot light-emitting diodes have seen substantial recent development but have yet to be effectively commercialized. These solution-processed materials are naturally monochromatic, with a band gap energy determined by the size and composition of the nanocrystal, and present an avenue towards highly saturated colors.

In light of the work in the forthcoming chapters, it would be remiss not to mention a lesser known but equally historical device: the light-emitting capacitor [9]. Experiments on electroluminescence were performed as early as 1936 by applying extremely high alternating electric fields to zinc sulfide phosphor powder [10]. These devices, referred to as alternating current thin-film electroluminescent (AC-TFEL) devices when applied to thin film phosphors, were later commercialized into strikingly simple, robust and long-lasting display panels with acceptable power efficiency due to their inherently capacitive, energy recovering nature. In these devices, a light-emitting phosphor is sandwiched between two dielectric layers with a conducting electrode on each side (where is one transparent in order for light to escape), and electroluminescence occurs by hot-electron impact ionization of luminescent centers [11].



### 1.3 Dissertation overview

This dissertation explores a surprisingly easy means of generating light by electrical excitation which combines many elements of the aforementioned light-emitting device structures. The approach is based on a light-emitting capacitor device whose structure resembles that of a metal-oxide-semiconductor (MOS) capacitor. Unlike most other conventional light-emitting devices, the device operates only by pulsed or alternating current bias and relies on only a single charge injecting contact. The initial concept originates from photophysical studies on monolayer semiconductors and the unforeseen finding of electroluminescence from transition-metal dichalcogenide monolayers incorporated in a capacitor structure [12]. With a few slight geometric modifications, the structure can be easily adapted to new material situations, which is the subject of this dissertation.

This thesis starts with an introduction to the device concept, followed by a traversal through more detailed device analysis and optimization, before ending with an assortment of brief experimental applications. In Chapter 2, we establish the basic behavior of this device when operated with a variety of nanomaterials and look at possibilities in spectroscopic chemical analysis. In Chapter 3, we delve into the performance of the device in more detail through a combination of simulation and experiment. By scaling the device in a manner familiar to MOS transistors, we demonstrate operation of the device at low voltages approaching the band gap of the emissive material. In Chapter 4, we characterize the efficiency of these devices with high photoluminescence quantum yield emitters from the perspective of a resonant driving scheme. In Chapter 5, we demonstrate scalability of the device by creating large, multiplexed arrays of light-emitting capacitors in which a diverse palette of emitters are painted on a substrate of pre-patterned electrodes in a pointillist style. Several proof-of-concept examples of spectral measurement and imaging are demonstrated using these miniaturized, highly multicolored light-emitting arrays. In Chapter 6, we show that the device can be used to generate and probe emission from individual luminescent entities. As an example, we present electrically driven light emission from single quantum dots with narrow linewidth at low temperature. Through these vignettes, we hope to explore opportunities – whether passing or not – that might arise from an unconventional form of light emission and establish the state of its performance relative to peer light-emitting devices along the way.

## Chapter 2

# A “generic” electroluminescent device

This chapter is adapted from:

Y. Zhao\*, V. Wang\*, D.-H. Lien\*, A. Javey, “A generic electroluminescent device for emission from infrared to ultraviolet wavelengths”, *Nature Electronics*, 3, 612–621, 2020. (\*equal contribution)

---

The range of luminescent materials that can be used in electroluminescent devices is limited due to material processing challenges and band alignment issues. This impedes the development of electroluminescent devices at extreme wavelengths and hinders the use of electroluminescence spectroscopy as an analytical technique. In this chapter, we show that a two-terminal device that uses an array of carbon nanotubes as the source contact can excite electroluminescence from various materials independent of their chemical composition. Transient band bending, created by applying an alternating current gate voltage, is used to achieve charge injection across different band alignments. As a result, the device can produce electroluminescence from infrared (0.9 eV) to ultraviolet (3.3 eV) wavelengths depending on the emitting material drop cast on top of the nanotube array, and with onset voltages approaching the optical energy gap of the emitting material. Such a device can be used to probe a chemical reaction in a liquid droplet via electroluminescence spectroscopy or be used as an electroluminescence sensor for detecting organic vapors.

### 2.1 Introduction

Electroluminescence (EL) is fundamental to the operation of light-emitting devices and encodes compositional information of the emitting material that can be analysed by EL spectroscopy. To achieve EL emission, devices adopt different structures, operate with different mechanisms and have emitters of different compositions [13–18]. However, they typically require particular features to accommodate different emitting materials, as the generation

of EL requires the injection and radiative recombination of oppositely charged carriers into the emitting layer.

Common direct-current (DC) driven inorganic and organic light-emitting diodes (OLEDs) rely on either p- and n-doped regions or multiple charge transport layers designed to have proper band alignment with the emitter layer [14, 16]. Light-emitting electrochemical and electrochemiluminescence cells depend on electrochemical processes to generate EL, which require the presence of an ionic component or electrolyte in the emitting layer [19, 20]. Alternating-current (AC) driven EL devices do not necessarily require emitter-specific charge injection layers [21–23]. However, early examples (such as sulfide-based light-emitting capacitors) require high operation voltages of over 100 V to achieve impact excitation or bipolar field emission [23, 24]. Organic AC-driven light-emitting devices have recently been shown to operate at lower voltages while maintaining high brightness, but still apply voltages well beyond the optical bandgap of the emitting material [18, 21, 25, 26].

A device that can excite EL directly from a wide variety of emitters of different morphologies, compositions and emission wavelengths has not yet been achieved. However, such a device could enable the broader use of EL spectroscopy as a material analysis technique and accelerate the development of light-emitting devices at extreme wavelengths. To fabricate a generic EL device, two key challenges need to be addressed. First, deposition of the emissive material should be the last step of the fabrication process. For many molecular systems, an emitter layer would be damaged by additional processing, or the emitter layer cannot be deposited as a uniform thin film for the deposition of subsequent layers (for example, a droplet of solution). There is also a minimum thickness of the emitter layer required in conventional OLEDs, with nanometer thick films being incompatible due to pinhole formation. Secondly, the device structure must allow for carrier injection into a broad range of materials, including those with large energy barrier heights or mobilities approaching zero. Current OLEDs require optimization of multiple injection layers for each corresponding emitter material, which limits the range of wavelengths that can be excited by any single device.

This chapter describes an AC-driven metal–oxide–semiconductor (MOS) capacitor structure with a carbon nanotube (CNT) network source contact that allows carrier injection in arbitrary emissive materials deposited on top of the device (Figure 2.1). Instead of relying on specific charge injection layers, band bending induced at the interface between the CNTs and emitting layer by the AC voltage allows efficient bipolar charge injection to be attained regardless of the barrier heights between the contact and emissive material [12]. Critically, the dense CNT network allows charge injection into emissive materials with low carrier mobility. The bottom gate contact, gate oxide layer, and source contact of this structure can be fabricated prior to the deposition of the emitter layer. The emissive material can be deposited on top of the prepared substrate without any subsequent processing (Figure 2.2). By removing limits on the emitter material’s processability and band alignment between layers, our generic device can generate EL from a wide range of materials with peak emission from ultraviolet (UV; 3.3 eV) to infrared (IR; 0.9 eV) wavelengths. The potential of the approach for EL spectroscopy is illustrated by probing the dynamics of an imine condensation reaction occurring in a droplet of liquid on the device and demonstrating use of the device as a

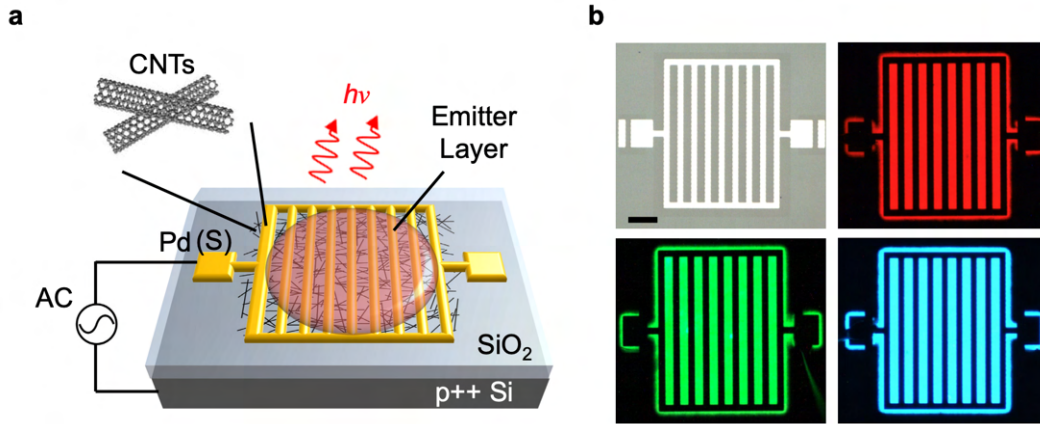


Figure 2.1: **Device structure and EL image.** The device structure with an assembled CNT network on SiO<sub>2</sub>/Si and patterned source contact. The device operates by applying AC voltage between the metal grid on the CNT network (S) and Si backgate (G) (a). Uniform EL can be excited with all type of emitters (b), where Ru(bpy)<sub>3</sub>(PF<sub>6</sub>)<sub>2</sub>, CdSSe/ZnS alloyed quantum dots (520 nm) and poly(9,9-dioctyl-9H-fluorene-2,7-diyl) (PFO) are used as red, green and blue emitters in the EL image. Devices are measured with a 15 V, 100 kHz square wave. Scale bar is 0.1 mm.

chemical sensing platform for organic vapors.

## 2.2 Device structure

To fabricate the EL device, semiconducting CNTs are assembled on a 50 nm SiO<sub>2</sub>/p<sup>++</sup> Si substrate through a solution-processing method [27]. The CNTs deposited in this way form a continuous network that is conductive (sheet resistance  $\sim 80$  k $\Omega$ /sq) but also highly porous. Varying the CNT assembly time gives different CNT densities (Figure 2.3). Although the CNT network is the source contact, a metal grid electrode is patterned by photolithography for wire-bonding and to reduce the parasitic resistance (Figure 2.2a). The CNT network outside the metal grid area is etched with O<sub>2</sub> plasma (Figure 2.2b). A field-effect transistor is fabricated next to each EL device to check the electrical properties of the CNT network (Figure 2.4). We chose semiconducting CNTs instead of metallic CNTs because the former can be uniformly assembled over large areas with poly-L-lysine, but metallic CNTs can also be used as contacts to produce EL (Figure 2.5). It is worth noting that CNTs have previously been used as additives in light emitting layers of AC organic light-emitting devices to enhance device brightness [21, 28, 29], and CNT networks have also been used as source contacts in a light emitting transistor to allow for gate control in a vertically-structured, multi-layer device [30].

The light-emitting materials are deposited on the CNT network contact by drop-casting,

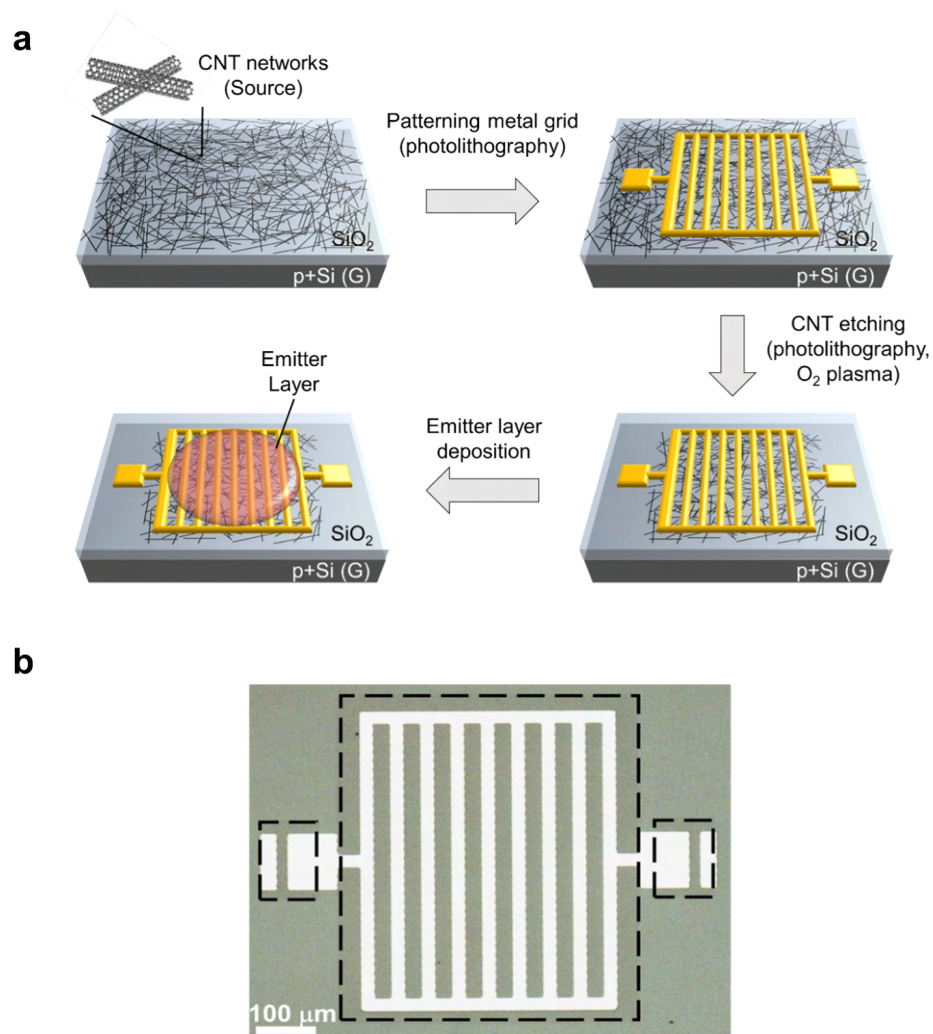


Figure 2.2: (a) Device fabrication involves CNT assembly, metal grid patterning, CNT etching, and emitter layer deposition. The unetched area of CNTs is the slightly darker region in the image and is highlighted by the dashed line (b). CNTs outside the dashed lines are removed in the O<sub>2</sub> plasma etching. Two FETs are fabricated for each EL device to check the electrical properties of CNT contacts (two smaller areas enclosed by the dashed lines).

spin-coating or evaporation, and AC voltage is applied to the gate while grounding the metal contact grid which contacts the CNT network. Uniform EL can be obtained with different types of materials at different wavelengths, as shown by the EL images of poly(9,9-dioctyl-9H-fluorene-2,7-diyl) (PFO, conjugated polymer), CdSSe/ZnS alloy quantum dots (520 nm; inorganic semiconductor), and Ru(bpy)<sub>3</sub>(PF<sub>6</sub>)<sub>2</sub> (fluorescent molecule) in Figure 2.1b. As the device does not impose any requirements on the processability of the emitters, a wide variety of materials can be used, from small molecules that form scattered crystals to polymers that

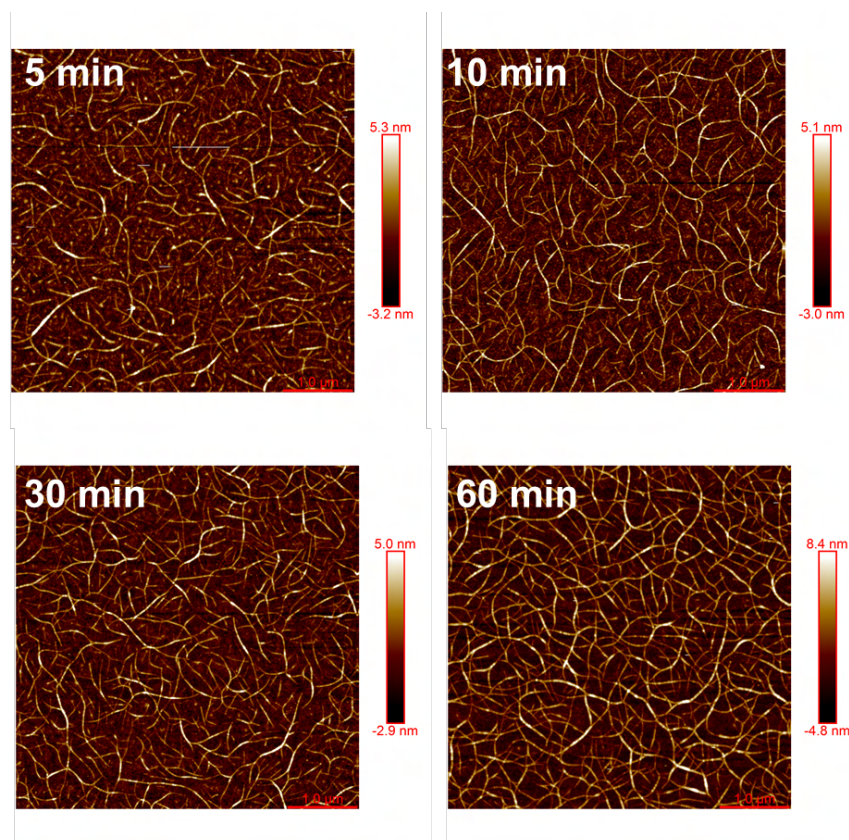


Figure 2.3: AFM of semiconducting CNT networks assembled on Si/SiO<sub>2</sub> substrate for different durations. The resulting planar CNT density is estimated by counting from the AFM image (9, 11, 14, 17 CNTS/ $\mu\text{m}^2$  for 5, 10, 30, 60 min samples, respectively). For the 60 min sample, CNTs appeared thicker due to bundling. This effect is also reflected in the FET measurement, where the device with CNT network assembled for 60 min give a much higher current at positive gate voltage (i.e. low on-off ratio).

form glassy films. Moreover, the device does not rely on emitter specific charge injection layers and therefore does not limit the choice of emitters with regard to the achievable band alignment between layers. These advantages allow for the production of EL from the IR to UV range (Figure 2.8a). Specifically, 2,7-di-tert-butylpyrene (BPYE) gives EL up to the UV region; PFO and CdSSe/ZnS alloy quantum dots (520 nm) give blue and green emission; and Ru(bpy)<sub>3</sub>(PF<sub>6</sub>)<sub>2</sub>, and PbS quantum dots give red and short-wave IR emission, respectively. Notably, small aromatic molecules such as pyrene and anthracene, which possess HOMO-LUMO gaps corresponding to the UV region, have not been reported in organic light emitting diodes due to difficulties in band alignment with selective charge injection layers and their strong tendency to crystallize into nonuniform films. EL can in other cases be absorbed by intermediate organic layers and only be observed when the emitting layer is the top layer of



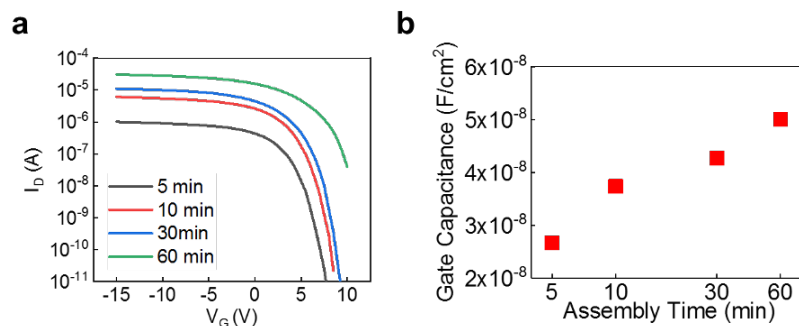


Figure 2.4: Electrical properties of CNT networks assembled for different amounts of time measured with a FET device where the channel length and width are  $20 \mu m$  and  $100 \mu m$ , respectively (a). Gate capacitance of the CNT network also shows increased CNT density with longer assembly time (b).

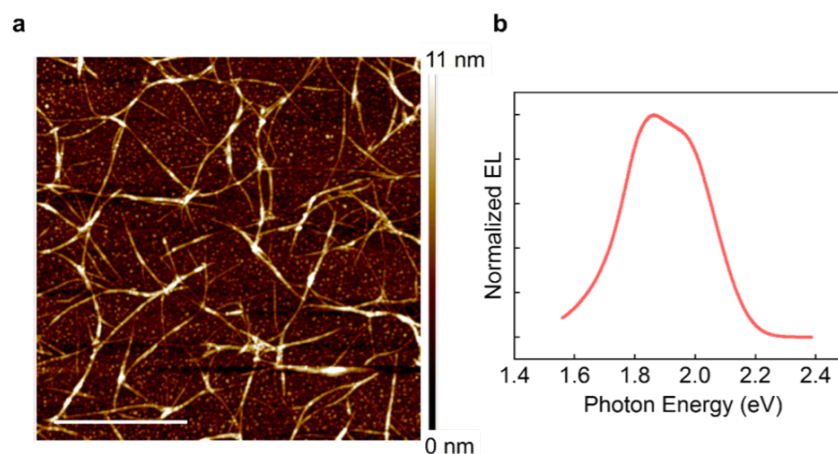


Figure 2.5: AFM of a metallic CNT network deposited on Si/SiO<sub>2</sub> substrate (a). The substrate is treated with poly-L-lysine in the same way and the solution of 99.9% purity metallic CNT was dropcasted on to the substrate kept at  $100^\circ C$ . The solution was left on the hotplate until water is evaporated, and the substrate was subsequently washed with DI water. Scale bar is  $1 \mu m$ . The EL device with metallic CNT gives same EL as semiconducting CNTs and the EL of Ru(bpy)<sub>3</sub>(PF<sub>6</sub>)<sub>2</sub> is shown in (b).

the device, likewise preventing incorporation of certain materials in conventional OLEDs.

With the device reported herein, we produce EL from materials of all types, from colloidal nanomaterials such as quantum dots (Figure 2.8b), to aromatic molecules (Figure 2.8c), conjugated polymers (Figure 2.8d) and metal complexes (Figure 2.8e). For simplicity, we only

show three to four emitters per material type and more examples can be found in the comprehensive table of emitters used on the device (Tables 2.1-2.4). With such a generic EL device, multiplexed EL from different materials can be achieved with an array of the EL devices where each emitting material is deposited on one pixel of the array. We demonstrate this multiplexed EL with four different emitters (BPYE (3), poly[(9,9-di-(2-ethylhexyl)-9H-fluorene-2,7-vinylene)-co-(1-methoxy-4-(2-ethylhexyloxy)-2,5-phenylenevinylene)] (PFV),  $\text{Ru}(\text{bpy})_3(\text{PF}_6)_2$  (2) and CdSeTe/ZnS quantum dots (850 nm; IRQD)) with each emitter belonging to a different class of materials (aromatic molecules, conjugated polymers, molecular metal complexes and inorganic semiconductors) and emitting at a different wavelength in the UV to IR region (Figures 2.8f and 2.6). EL of the four different emitters can be simultaneously measured (Figure 2.8g) within a  $2.25 \text{ mm}^2$  area, demonstrating the potential to use this EL device for multiplexed EL generation. The device area can be scaled up without fundamental limitations as demonstrated by a  $25 \text{ mm}^2$  device (Figure 2.7).

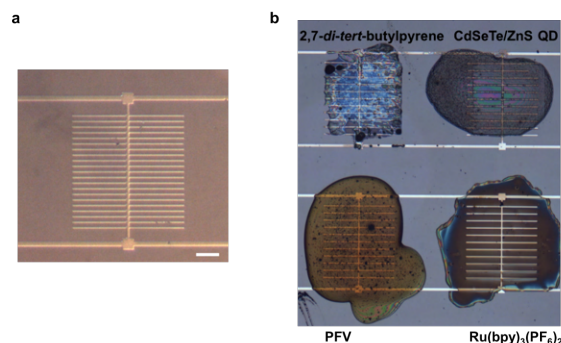


Figure 2.6: Optical image of a typical four-pixel device. (a) The pixel before emitter drop casting. Scale bar: 0.1 mm. (b) Typical four-pixel device after drop casting. The EL measurement for this device was carried out at 20 V, 100 kHz.

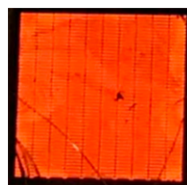


Figure 2.7: Image of EL from a large area ( $25 \text{ mm}^2$ ) device with  $\text{Ru}(\text{bpy})_3(\text{PF}_6)_2$  biased at 12.5 V, 100 kHz. The CNT network covers the entire metal electrode area.



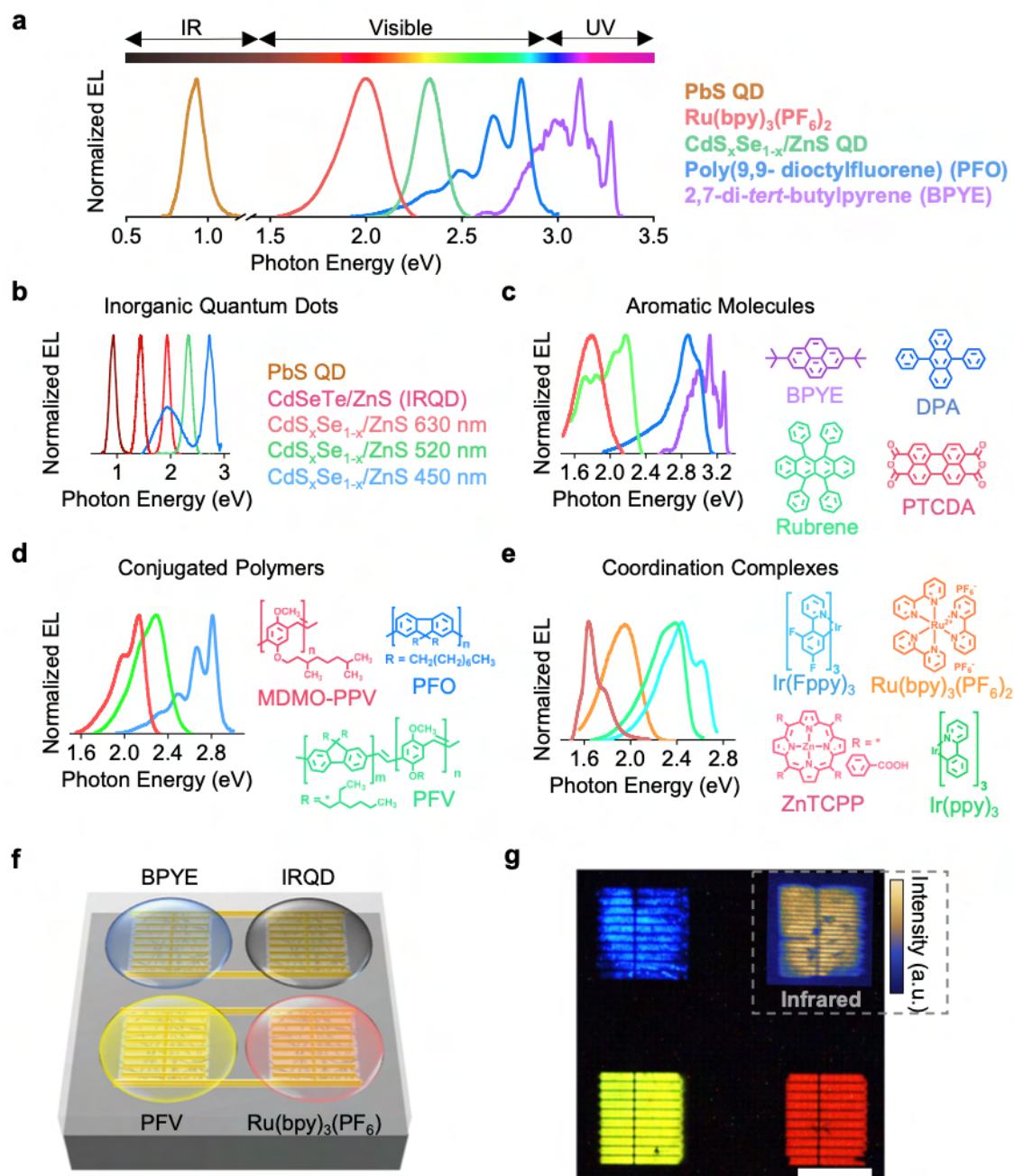


Figure 2.8: **EL from IR to UV wavelengths with different types of materials.** EL spectra of the device with different emitting materials (a). The device can excite EL from a wide variety of materials, including inorganic quantum dots (b), aromatic molecules (c), conjugated polymers (d) and coordination complexes (e). Different emitting materials can be drop casted on an array of EL devices (f), which produces EL from the IR to UV range within a  $2.25 \text{ mm}^2$  device area (g). The emitting materials are BPYE (UV to blue), PFV (yellow),  $\text{Ru}(\text{bpy})_3(\text{PF}_6)_2$  (red), and IRQD (IR), respectively. The IR EL image is shown with false color. Scale bar is 0.5 mm.

## 2.3 Device mechanism

To better understand the role of the CNT network in enabling light emission from a variety of materials, we performed device simulations based on the structure shown in Figure 2.9a, which consists of two parallel grounded CNT source contacts spanned by a light-emitting semiconducting material. The simulated emissive material was placed on top of a 50 nm SiO<sub>2</sub> layer with a gate contact on the bottom to which a  $\pm 15$  V pulsed gate voltage ( $V_g$ ) with finite slew rate was applied (Figure 2.9b). As shown in Figure 2.9a, this structure represents the region of emissive material between two individual CNTs separated by a distance  $L$  on the same plane. Energy band diagrams calculated at steady-state and transition points of the pulsed waveform demonstrate the ability to inject electrons and holes into the emissive material from the CNT contacts at upward and downward transitions, respectively (Figure 2.9c). At a gate voltage of  $-15$  V, the electron and hole quasi-Fermi levels ( $E_{Fn}$  and  $E_{Fp}$ ) are situated near the valence band ( $E_V$ ), indicating that a high density of holes is present in the semiconductor at steady-state. As the gate voltage sharply increases to 15 V, the hole density rapidly diminishes while the electron density increases, resulting in transient electroluminescence as entering electrons recombine radiatively with exiting holes (Figures 2.9d-f). Electroluminescence at the downward transition can be explained similarly and is consistent with previous explanations of AC electroluminescence [12].

Tunneling of carriers into the emissive material at voltage transitions is achieved by steep band bending at the resistive Schottky contacts as the electric field across the capacitive structure attempts to switch. Notably, the steep band bending at voltage transitions obviates the need for work function alignment of the contacts and enables carrier injection and EL even in materials with large injection barriers, as long as a pulse with sufficiently high voltage and slew rate is applied. At the gate voltages considered in this study, carriers can also occupy higher sub-band states of the low-dimensional carbon nanotubes, which may promote carrier injection into materials with large band (HOMO-LUMO) gaps.

## 2.4 Device characterization

We first characterized device performance using Ru(bpy)<sub>3</sub>(PF<sub>6</sub>)<sub>2</sub> as an example emitting material. The EL intensity increases with both voltage and frequency (Figures 2.10a and b), which is consistent with the AC charge injection mechanism. When applying a square wave gate voltage with sufficiently low frequency, charge carrier populations in the emitting material reach steady state before each gate voltage transition and the average EL intensity increases linearly with frequency, or the number of gate voltage transitions per unit time (Figure 2.10b). The linear relationship between EL intensity and frequency is found to be general to different emitters. EL continues to increase with frequency until the time interval between gate voltage transitions is not long enough for the device to reach steady state. The pulsed nature of EL is further confirmed by time-resolved electroluminescence measurement (Figure 2.10c), where EL is only observed at gate voltage transients. The difference in EL

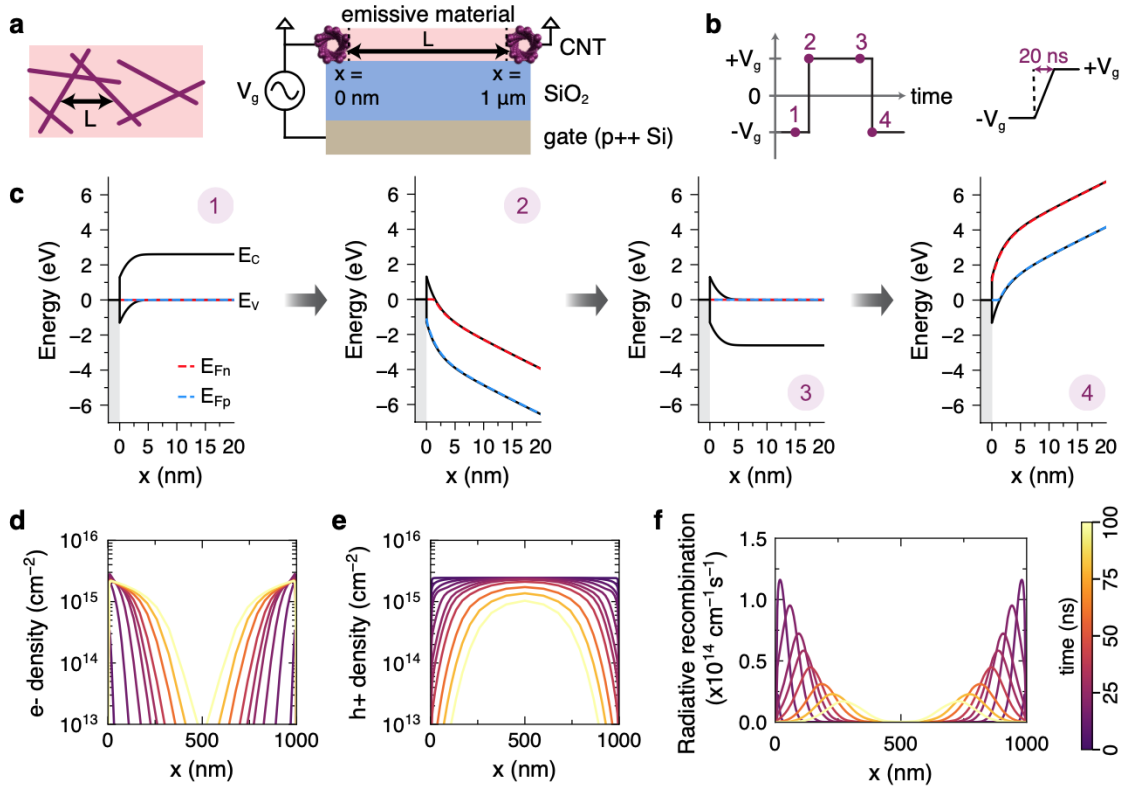


Figure 2.9: **Device simulation.** A schematic of the simulated device structure is shown in (a). The top surface area view (left) shows a random CNT network amongst a layer of emissive material. The cross-sectional view (right) shows the region of emission between two grounded CNT contacts. A square wave pulsed voltage is applied to the bottom gate contact with  $V_g = 15$  V and a slew rate of  $0.75$  V ns $^{-1}$  (b). Energy band diagrams at one of the source contacts are shown in (c) for the time points indicated in (b) using a simulated device with  $50$  nm SiO $_2$ ,  $\mu = 0.001$  cm $^2$  V $^{-1}$  s $^{-1}$ , and  $L = 1$   $\mu$ m.  $E_C$  and  $E_V$  are the conduction and valence bands.  $E_{Fn}$  and  $E_{Fp}$  are the electron and hole quasi-Fermi levels. The contact is located at  $x < 0$  and the emissive material is located at  $x > 0$  nm. Electron density (d), hole density (e), and radiative recombination (f) as a function of distance in the channel after an upward transition (i.e. from time point 1 to 2), with color indicating the time elapsed since the start of the transition.

intensity between the upward and downward transitions reflects the different barrier heights for injection of electrons and holes. The device performance characteristics agree well with our understanding of its operation mechanism and is different from that of light-emitting electrochemical cells or electrochemiluminescence cells. Light-emitting electrochemical cells rely on electrochemical processes at the electrode interface to inject carriers into the emitter, can operate in both AC and DC mode, and have a much longer (milliseconds to hours)

turn-on time [19]. Electrochemiluminescent cells operate through electrochemiluminescence, which is a charge transfer reaction between reduced and oxidized forms of luminophores that produces excited states of the molecule and leads to light emission. The EL of electrochemiluminescent cells displays a unique frequency dependence that typically peaks at 1 kHz, which corresponds to the time required to establish electrochemical double layers at the electrode (Figure 2.11) [31]. Although electrochemiluminescence could take place in the device on the molecular level, as reduced and oxidized species can co-exist during the gate voltage transients, the device characteristic is different from that of electrochemiluminescent cells since the EL linearly increases with frequency to at least 100 kHz.

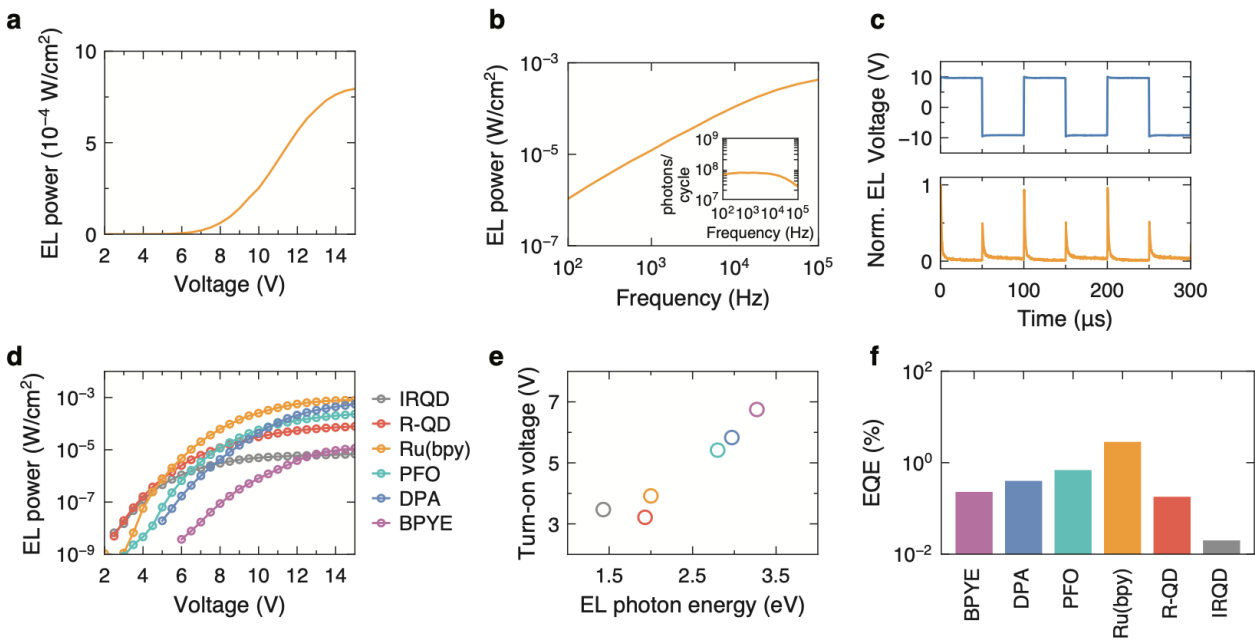


Figure 2.10: **Device characterization.** The voltage (a) and frequency (b) dependence of device electrochromiluminescence show characteristics consistent with simulation. The device produces an approximately constant EL per cycle until the frequency is too high for the device to reach steady-state (b, inset). The operating mechanism is further confirmed by time-resolved EL measurement showing the pulsed nature of EL (c). The EL intensity, turn-on voltage and external quantum efficiency of different emitters are compared in (d), (e) and (f), respectively. The turn-on voltage is defined as the voltage where the EL power density reaches  $5 \times 10^{-8} \text{ W cm}^{-2}$  (where EL can be accurately measured by the power meter). The names of different emitters are abbreviated in the legend: BPYE for 2,7-di-tert-butylpyrene, DPA for 9,10-diphenylanthracene, PFO for poly(9,9-dioctylfluorene), Ru(bpy) for  $\text{Ru}(\text{bpy})_3(\text{PF}_6)_2$ , R-QD for CdSSe/ZnS alloy quantum dots (630 nm), and IRQD for CdSeTe/ZnS quantum dots (850 nm). Devices measured at 12.5 V for (b) and 100 kHz for (a), (d), and (e).

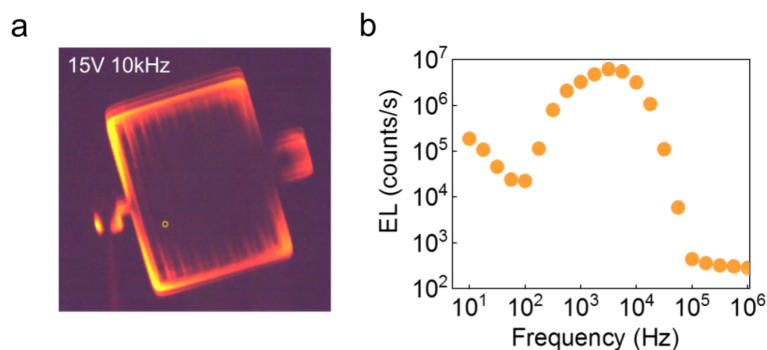


Figure 2.11: The CNT device operated based on an electrochemiluminescence (ECL) mechanism. To make ECL the dominant mechanism, a solution of an ionic emitter is used [Ru(bpy)<sub>3</sub>(PF<sub>6</sub>)<sub>2</sub>, 50 mg mL<sup>-1</sup> in dimethylacetamide]. When a negative gate voltage is applied, Ru(bpy)<sub>3</sub><sup>2+</sup> on the electrode interface is oxidized to form Ru(bpy)<sub>3</sub><sup>3+</sup> through an electrochemical process (equivalent of hole injection in solid state), which then diffuses into the solution. In the solution, the gate electric field is screened by excess Ru(bpy)<sub>3</sub><sup>2+</sup> ions and does not hinder such diffusion. When the gate voltage is reversed, the opposite electrochemical process takes place to produce a reduced molecular species Ru(bpy)<sub>3</sub><sup>+</sup> (equivalent to electron injection) that also diffuses from the electrode. Thus, the reduced and oxidized species are both present in the solution at the proximity of the electrode and can react to form excited state emitter molecule Ru(bpy)<sub>2</sub><sup>+</sup>\* that would then decay to ground state and emit light. The frequency dependence of EL shows the typical behavior of ECL which gives a peak around 1 to 10 kHz, and above this frequency the electrochemical process cannot proceed efficiently as the electrochemical double layer cannot be established at such frequencies.

To better characterize the device performance across a wide variety of emitters, we measured the voltage dependence of EL for six different emitters (BPYE, 9,10-diphenylanthracene (DPA), PFO, Ru(bpy)<sub>3</sub>(PF<sub>6</sub>)<sub>2</sub> (Rubpy), CdSSe/ZnS alloyed quantum dots (630 nm; R-QD), and IRQDs) from different material categories (inorganic semiconductors, aromatic molecules, conjugated polymers and metal complexes) and with EL wavelengths ranging from UV to IR (Figure 2.10d). The EL spectrum of each emitter is presented in Figure 2.8 and their names are abbreviated in the legend for clarity. It is clear that device operation is not limited to any specific material category. The device turn-on voltage increases with the peak EL photon energy (Figure 2.10e). It is worth noting that this trend does not take into account differences in photoluminescence quantum efficiency for different emitters. The external quantum efficiency (EQE) can be estimated by operating the device with a sine wave AC voltage and measuring the EL intensity and current. The estimated lower limit of device EQE for various emitter materials is summarized in Figure 2.10f, and the EQE for Ru(bpy)<sub>3</sub>(PF<sub>6</sub>)<sub>2</sub>, DPA, and PFO is on the same order as their DC OLED counterparts [32–34].

We further studied the effect of emitter layer thickness to investigate how much emissive

material is required for reasonably bright EL. For this purpose, we used PFO as the model emitter as it can be readily spincoated into uniform films. With PFO thickness increasing from 1.5 to 8 nm, the device EL increases linearly with thickness and does not further increase with higher PFO thickness (Figures 2.12 and 2.13). Remarkably, the device can function with an emitter layer only 1.5 nm thick. This result indicates that the device can be used to obtain EL spectra from small amounts of analyte.

CNT network contacts provide the unique ability to tune the density of contacts to the emissive material. By controlling the assembly time, the average distance  $L$  between individual nanotubes can be optimized to maximize the time-averaged electroluminescence from the emissive material. As  $L$  increases, the resistance between source contacts increases and the delay in switching the voltage across the capacitive structure becomes longer, lengthening the time during which emission is observed after the transition. At the same time, more area is available for carriers to travel and radiative recombination to occur, increasing the total amount of radiative recombination. When the CNT-CNT distance is too short, gate control of the emissive material channel is weakened and the degree of band bending in the channel is limited, akin to the short-channel effect in transistors. As shown in Figure 2.14a, the peak amount of radiative recombination increases with increasing  $L$  up to a certain length, after which the benefit of increasing  $L$  becomes less significant.

Although simulations indicate that large  $L$  (or sparse CNT networks) are beneficial for improving emission between two single nanotube contacts, the amount of radiative recombination per unit area of the device surface is proportional to both the amount of radiative recombination between two individual contacts and the density of contacts. By approximating the contact density  $\rho$  as  $1/L^2$  CNTs  $\text{cm}^{-2}$  where  $L$  is the average distance between nanotubes [35], we find that there is an optimal distance between CNT contacts that maximizes the amount of radiative recombination, or electroluminescence. Note that the average distance between nanotubes must still be lower than the percolation threshold in order for an electrically conducting network to form across large areas. Experimental measurements show that devices with very low or very high density CNT networks tend to exhibit degraded emission intensity (Figure 2.14c), thus corroborating our simulation results and demonstrating that device performance can be enhanced by controlling contact density. Importantly, the optimal distance between source contacts depends on the mobility of the semiconducting material (Figures 2.15b and 2.14b); in materials with low mobility, carriers are less able to travel far into the emissive material bulk, meaning that it is desirable to increase the contact density, i.e. reduce the distance between nanotubes, to improve the brightness of emission.

We experimentally studied the dependence of EL on CNT density for six different emitters encompassing inorganic semiconductors, aromatic molecules, conjugated polymers and metal complexes with emission wavelengths from IR to UV (Figures 2.15a and 2.14c), where different CNT assembly times were used to fabricate devices with different CNT densities. CNT assembly times of 5, 10, 30 and 60 min gave average CNT densities around 9, 11, 14, and 17 CNTs  $\mu\text{m}^{-2}$  respectively, as characterized by atomic force microscopy (AFM) (Figure 2.3). The increase in CNT density also results in increased gate capacitance and on-current of CNT FET devices consistent with literature values (Figure 2.4). For  $\text{Ru}(\text{bpy})_3(\text{PF}_6)_2$ ,

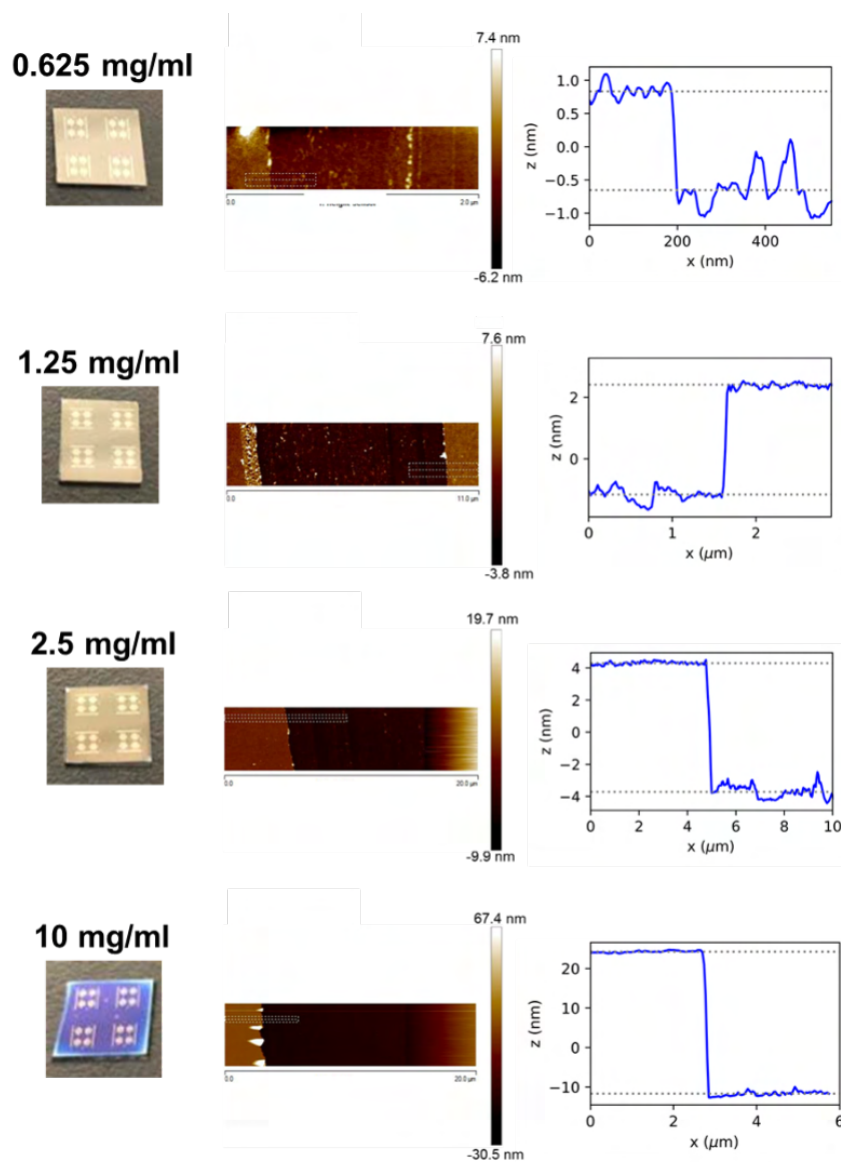


Figure 2.12: Thickness control of spincoated PFO thin films. The optical image, AFM image and cross-section of PFO films are shown in each column. PFO/toluene solutions of different concentrations ( $10, 2.5, 1.25, 0.625 \text{ mg mL}^{-1}$ ) were spin-coated at 6000 rpm for 30 sec to give PFO films with thicknesses of 35, 8, 3.5, and 1.5 nm, respectively.



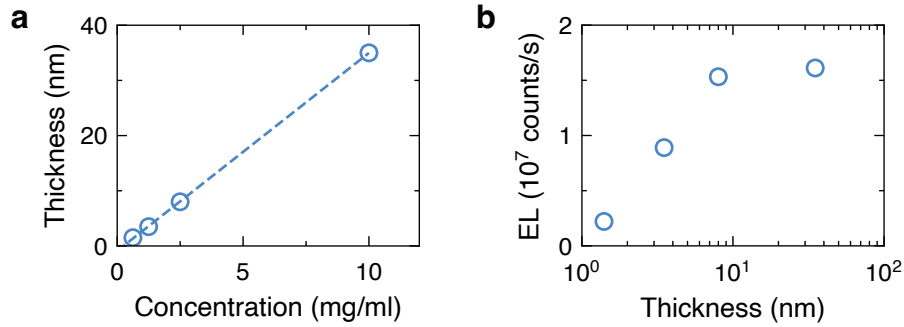


Figure 2.13: Effect of PFO thickness on device EL. The thickness of PFO films spincoated from PFO solutions of different concentration. The integrated EL of devices with different PFO emitting layer thicknesses measured at 15 V, 100 kHz.

BPYE, PFO, and DPA, the optimal CNT density was found to be 11 or 14 CNT  $\mu\text{m}^{-2}$ , which can be achieved with assembly times of 10 or 30 min. For the IRQDs, higher CNT density tends to give higher EL. The general trend of CNT density dependence is consistent with device simulation results, further supporting our picture of the operating mechanism. Simulated calculations of radiative recombination as a function of CNT density show that EL in lower mobility materials can be enhanced by using higher density CNT contacts (Figure 2.15b). In the lowest mobility case ( $\mu = 0.0005 \text{ cm V}^{-2} \text{ s}^{-1}$ ), EL appears to increase monotonically with CNT density because the optimum in CNT density lies outside the shown range of CNT densities. Thus, it is possible for the EL of certain emitters to appear to strictly increase or remain nearly constant with CNT density depending on properties of the deposited emissive material and the range of CNT densities tested. From a practical perspective, all emitter materials exhibit reasonable EL (within two times of the highest EL value measured) with a 30 min assembled CNT network contact, so it would be possible to obtain EL from different types of materials without changing the CNT density on the device.

Finally, we investigated the impact of gate dielectric scaling on EL generation in AC-driven devices (Figure 2.15c-g), which are conventionally known to suffer from high operating voltages. From both simulation and experimental results (Figure 2.16), we find that the onset voltage for EL decreases as the  $\text{SiO}_2$  dielectric thickness decreases for the device depicted in Figure 2.1. Above the turn-on voltage, devices with different oxide thicknesses exhibit similar EL as a function of the effective injected charge (Figure 2.16c). Simulated energy band diagrams elucidate the benefit of reducing the gate oxide thickness at low operating voltages (Figure 2.15e). When the gate oxide is thick, the gate capacitance is small and the AC voltage swing can only induce gradual band bending at the contacts at low voltage. The reduced quasi-Fermi level splitting and carrier concentrations in the emitter layer lead to low radiative recombination, and the energy bands and carrier concentrations do not reach the expected steady state condition either. Based on these results, we fabricated devices in



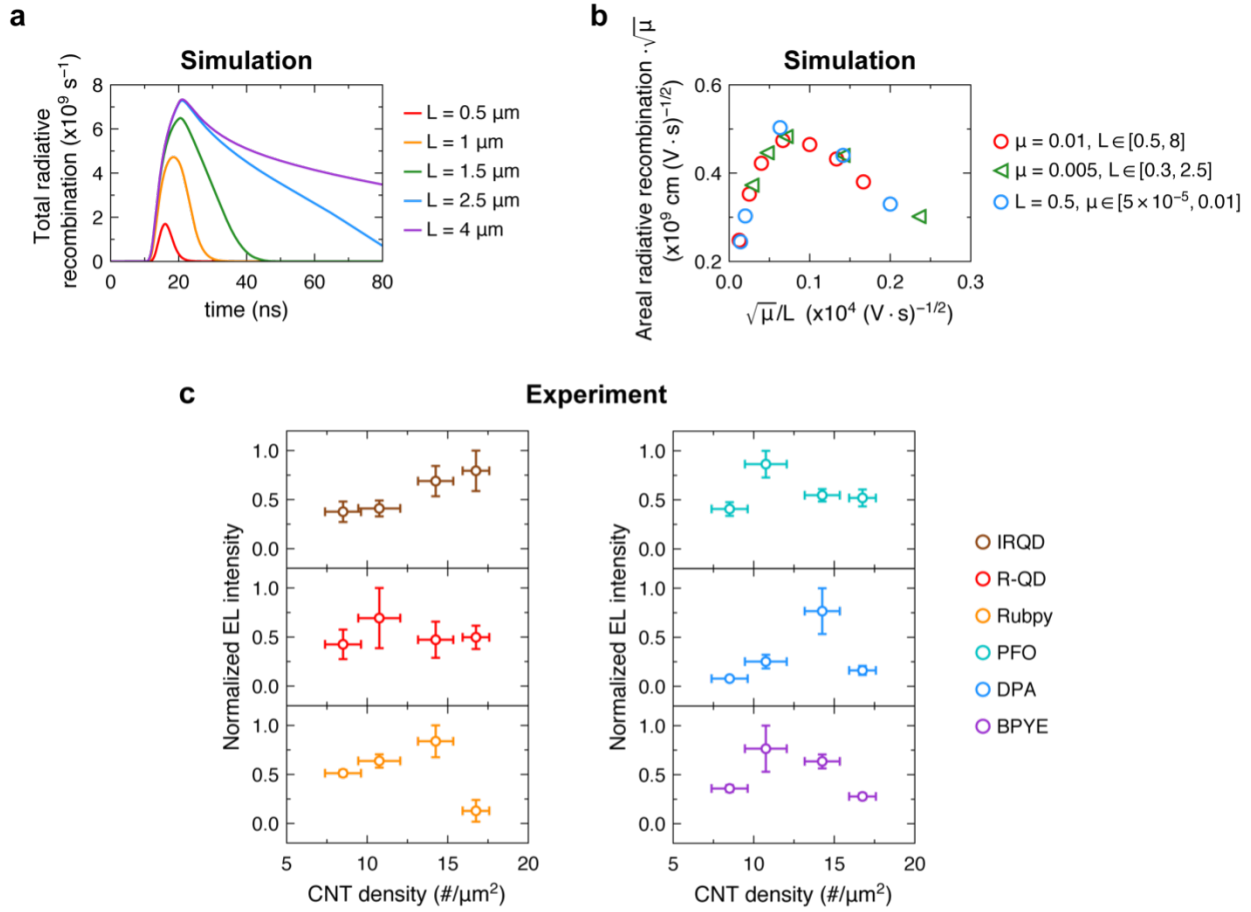


Figure 2.14: Dependence of EL on CNT density and emitter material mobility. (a) Simulated radiative recombination integrated over the emissive material volume between two CNT-CNT contacts with distance  $L$  as a function of time since the start of the upward transition. Emitter material mobility is  $\mu = 0.01 \text{ cm}^2 \text{ V}^{-1} \text{ s}^{-1}$ . (b) Simulated areal radiative recombination (radiative recombination per unit surface area for a network of CNTs with average CNT-CNT distance  $L$ ). When scaled by  $\sqrt{\mu}$ , the areal radiative recombination follows a universal trend as a function of  $\sqrt{\mu}/L$ . The simulated emission is higher in lower mobility materials as carriers are retained in the area near the contact for a longer period of time during the fast voltage transition, allowing for more radiative recombination. The optimal ratio of  $\sqrt{\mu}/L$  is around 0.07; thus, the optimal CNT-CNT distance depends on the mobility of the emissive material. For lower mobility materials, it is desirable to decrease the CNT-CNT distance, since the peak emission area is situated closer to the contact and total areal emission can be improved by increasing the number of individual CNT contacts. The unit of mobility is  $\text{cm}^2 \text{ V}^{-1} \text{ s}^{-1}$  and the unit of length is  $\mu\text{m}$ . Simulations were performed for a 50 nm SiO<sub>2</sub> gate oxide device with a  $V_g = 20 \text{ V}$  square wave gate voltage with slew rate  $1 \text{ V ns}^{-1}$ . (c) Experimental measurement of the dependence of EL intensity on CNT network density for different emitters. EL intensity was measured at 15 V for PFO, DPA, BPYE, Ru(bpy)<sub>3</sub>(PF<sub>6</sub>)<sub>2</sub> and 10 V for IRQD, R-QD. Horizontal error bars represent the standard deviation of CNT densities estimated from different  $1 \mu\text{m}^2$  areas from AFM.

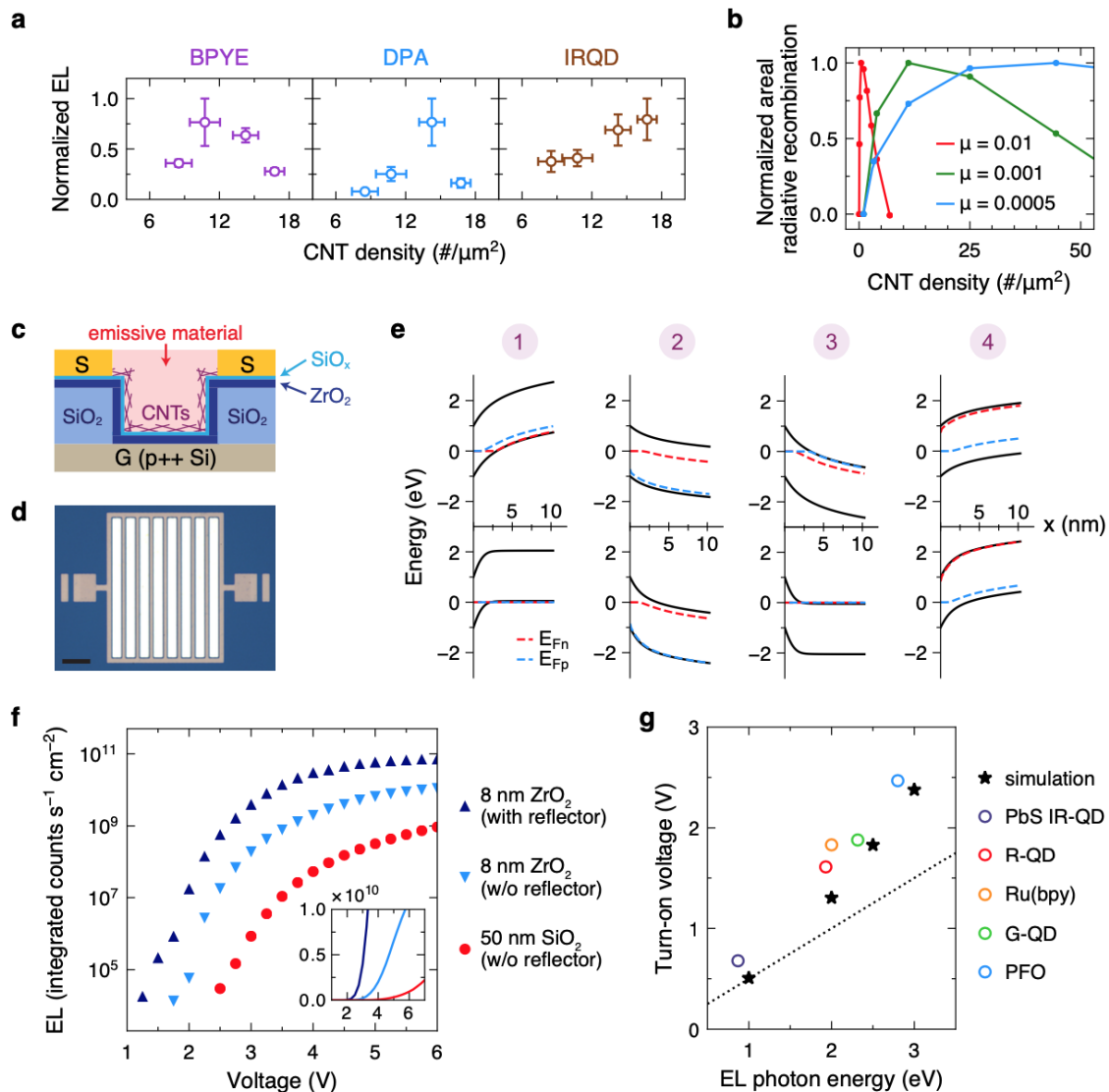


Figure 2.15: **Device optimization.** (a) Experimentally measured dependence of EL on semiconducting CNT network density for different emitters. Error bars represent standard deviation. (b) Simulated radiative recombination per unit surface area as a function of CNT density for 50 nm SiO<sub>2</sub> gate oxide devices with emitter materials of different mobility (units: cm<sup>2</sup> V<sup>-1</sup> s<sup>-1</sup>). (c) Cross-sectional schematic and (d) optical image of a device with thin gate dielectric. Scale bar: 100 μm. (e) Simulated band diagrams at the contact-emitter interface at the same timepoints in Figure 2.9 with  $V_g = 3$  V (e). The top plot represents a device with 50 nm SiO<sub>2</sub> gate dielectric; the bottom plot represents a device with 8 nm high- $\kappa$  ( $\epsilon = 22$ ) gate dielectric. (f) EL from Ru(bpy)<sub>3</sub>(PF<sub>6</sub>)<sub>2</sub> using metallic CNT devices with a gate oxide of 50 nm SiO<sub>2</sub>, 8 nm ZrO<sub>2</sub>, or 8 nm ZrO<sub>2</sub> on top of a back reflector. Inset: data with linear scaling. (g) Experimentally measured (circles) and simulated (stars) turn-on voltages for different emitters. The dotted line marks the gate voltage corresponding to half the photon energy ( $V_g = E_{ph}/2$ ), which represents a total voltage swing of  $2V_g = E_{ph}$ . Measurements were performed using 8 nm ZrO<sub>2</sub> gate oxide devices without a back reflector.

which AC voltage between the CNT network and bottom gate contact is applied across a thin high- $\kappa$  gate dielectric (Figure 2.15c-d). To reduce parasitics and improve device robustness, we maintained top contact pads on relatively thick SiO<sub>2</sub> (Figure 2.17). We also found that the use of metallic CNT networks reduces lateral resistive losses at low voltage (Figure 2.18). The combination of these improvements leads to a reduction in the EL turn-on voltage ( $V_T$ ) across emitters from IR to blue wavelengths (Figures 2.15g and Figure 2.19) compared to the earlier result (Figure 2.10e). The trend in  $V_T$  as a function of EL photon energy closely follows the values calculated from simulation of materials with different band gap energies, with vertical offset in the data partly attributable to differences in the threshold of photon counts required to determine the onset of EL experimentally. In addition, the EL photon energy is assumed to be the band gap energy in simulation whereas the measured photon energy is smaller than the band gap depending exciton binding energy of the material. As the photon energy of the emitting material decreases, the total applied voltage swing ( $2V_g$ ) at the onset of EL approaches the photon energy. To further improve device performance, a metal back reflector layer can be incorporated below the emission area to improve light outcoupling, which is degraded as the oxide thickness is reduced. The enhanced EL allows detection of EL at even lower threshold voltages as well as a steeper turn-on characteristic (Figure 2.15f). At the voltage at which the 50 nm SiO<sub>2</sub> device starts to turn on ( $\sim 2.5$  V), the 8 nm ZrO<sub>2</sub> device with a back reflector achieves the level of EL that the 50 nm SiO<sub>2</sub> device does not reach until over 5 V. Overall, our results suggest that EL can be produced with AC voltages as low as the optical energy gap of the emitting material and on par with the voltages in DC electroluminescent devices.

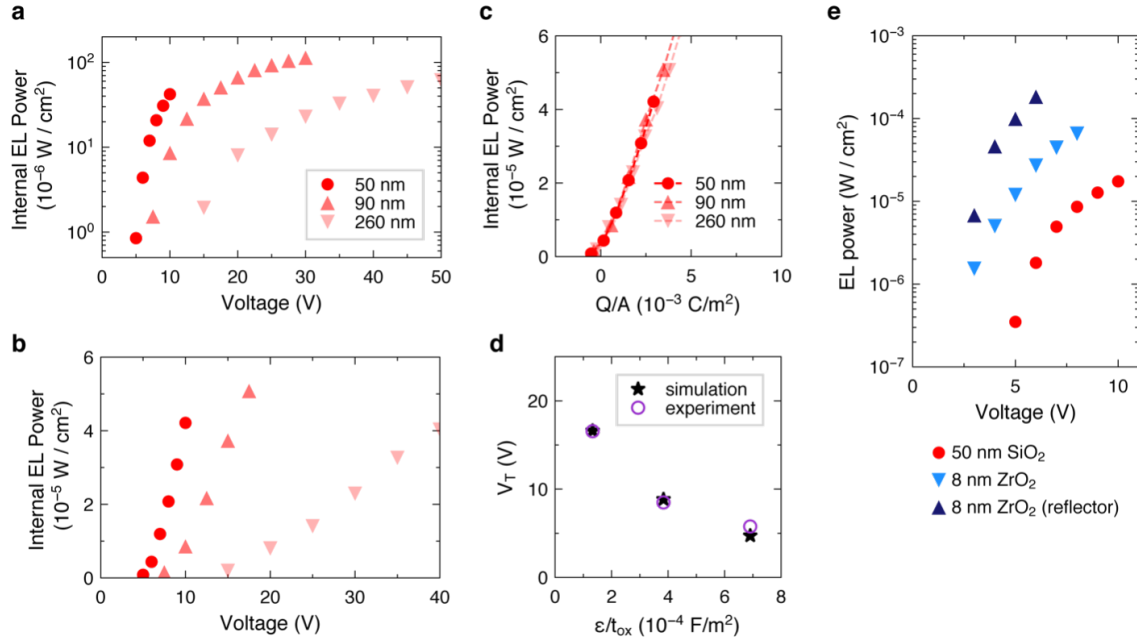


Figure 2.16: Measured internal EL power from 10 kHz sine wave excitation in (a) log and (b) linear scaling for devices with different SiO<sub>2</sub> thicknesses and metallic CNT networks. To aid quantitative comparison, the externally measured power is normalized by the light outcoupling factor as calculated using the transfer matrix approach assuming isotropic media and an emitter plane at the oxide-emitter layer interface. (c) Internal EL power as a function of the effective injected charge density ( $Q/A$  for device area  $A$ ) above the turn-on voltage, which is related to  $C(V - V_T)$  where  $V$  is the applied gate voltage,  $V_T$  is the turn-on voltage, and  $C$  is the gate oxide capacitance. (d) Experimentally measured and simulated turn-on voltages ( $V_T$ ) as a function of gate oxide capacitance, showing agreement in trend (experimental  $V_T$  is determined from the voltage where the internal EL power crosses  $3 \times 10^{-6} \text{ W cm}^{-2}$  and simulated  $V_T$  is determined from the voltage where there are more than eight radiative recombinations per transition). Simulations were performed with a 10 kHz sine wave excitation and material mobility of  $0.0001 \text{ cm}^2 \text{ V}^{-1} \text{ s}^{-1}$  and a CNT-CNT distance of 300 nm. (e) Comparison of measured external EL power of devices with 50 nm SiO<sub>2</sub> gate oxide versus 8 nm ZrO<sub>2</sub> gate oxide without (downward triangles) or with (upward triangles) a metal back reflector using the same excitation conditions, showing similar enhancement as with a 100 kHz square wave gate voltage in Figure 2.15. Experimental measurements were performed using Ru(bpy)<sub>3</sub>(PF<sub>6</sub>)<sub>2</sub> and simulations were performed using an emitter bandgap of 2 eV.

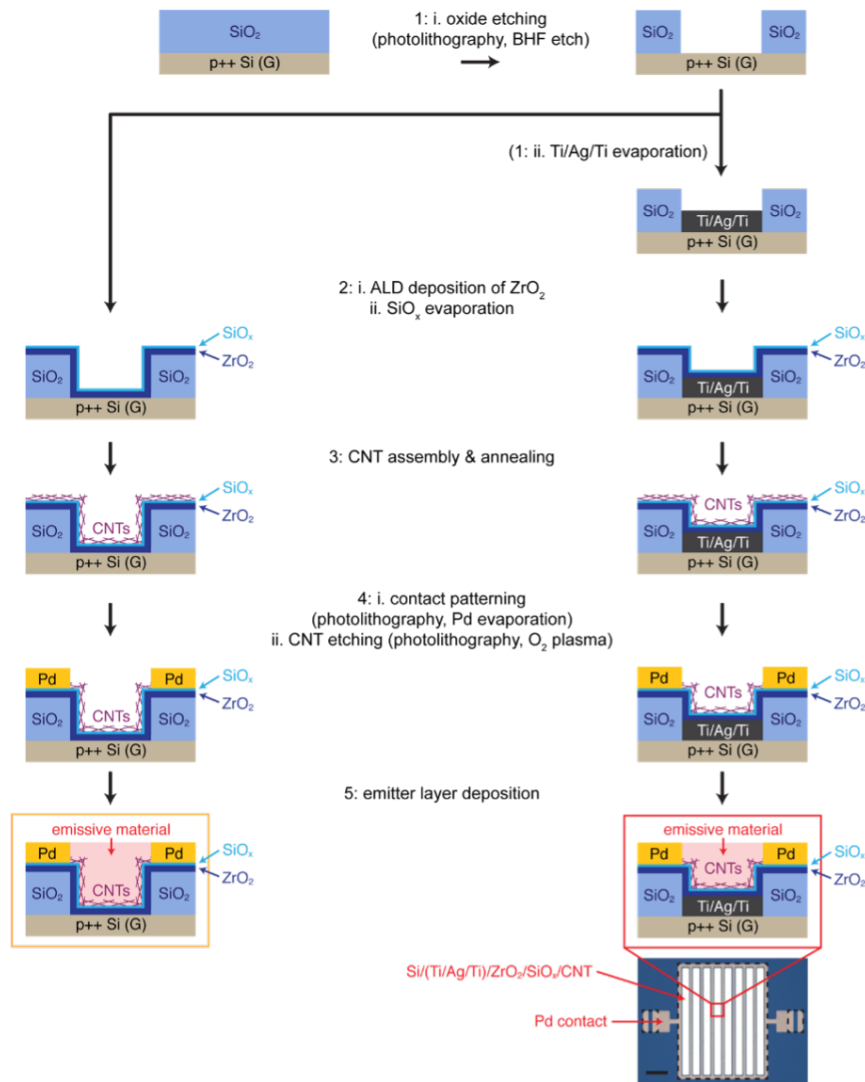


Figure 2.17: Cross-sectional schematic of the fabrication process for the EL device with a thin high- $\kappa$  gate dielectric.  $p^{++}$  Si/SiO<sub>2</sub> substrates first undergo a patterned etch using 6:1 BOE, where the exposed Si is the eventual region of emission in the final device. For devices with a back reflector, a Ti/Ag/Ti stack with thick Ag (150 nm) is optionally evaporated in the  $p^{++}$  Si region. The gate dielectric ( $ZrO_2$ ) is then deposited by ALD followed by evaporation of  $SiO_x$  to promote CNT assembly (no oxygen plasma treatment is applied). The rest of the fabrication procedure is identical to Figure 2.2. Fabrication of the high- $\kappa$  dielectric device without a back reflector is shown in the left column (final device in yellow box; starting substrate was 90 nm SiO<sub>2</sub>/Si) and fabrication of the high- $\kappa$  dielectric device with a back reflector is shown in the right column (final device in red box; starting substrate was 260 nm SiO<sub>2</sub>/Si). The cross-sectional schematic corresponds to one of the emission “stripes” between the metal grid lines. CNTs outside the regions enclosed by dashed lines are removed by  $O_2$  plasma etching.

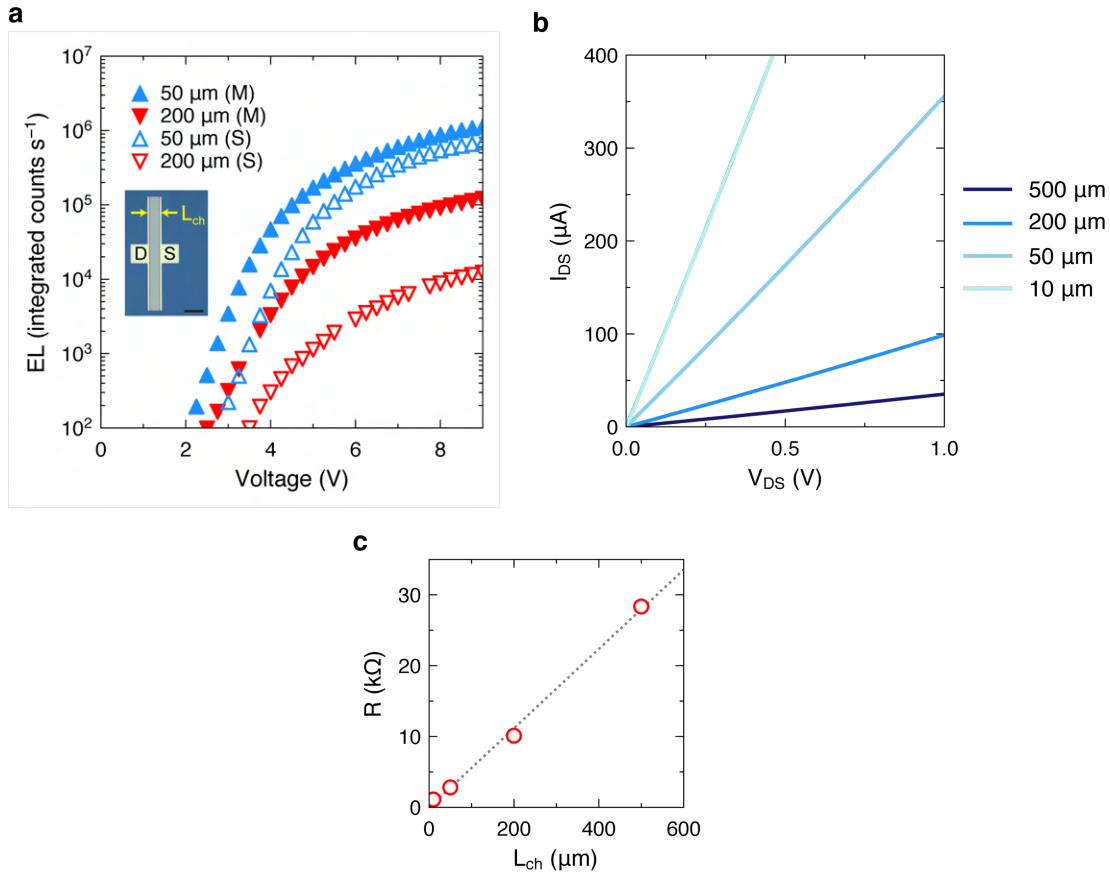


Figure 2.18: (a) EL from  $\text{Ru}(\text{bpy})_3(\text{PF}_6)_2$  using single strip devices with an emission area length ( $L_{ch}$ ) of 50 (blue) or 200  $\mu\text{m}$  (red). Solid markers represent devices with metallic CNT networks and open markers represent devices with semiconducting CNT networks. The turn-on voltage can be reduced by reducing the emission area length and using metallic networks with lower resistance. The inset shows an optical image of the two-terminal devices used to performed measurements in this figure (scale bar: 100  $\mu\text{m}$ ). EL was obtained by applying a 100 kHz square wave voltage across the backgate and source (S) terminal. (b) Drain-source current-voltage ( $I_{DS} - V_{DS}$ ) curves of devices with metallic CNT networks with different channel lengths indicated in the legend, with zero gate voltage ( $V_{GS}$ ). Electrical measurements were obtained by applying voltage across the drain (D) and source (S) terminal. (c) Resistance of metallic CNT devices determined from the drain current at 1 V drain voltage. There is a linear trend with channel length due to the resistive nature of the CNT network in the channel. All devices were fabricated with a 8 nm  $\text{ZrO}_2$  gate oxide in the channel.

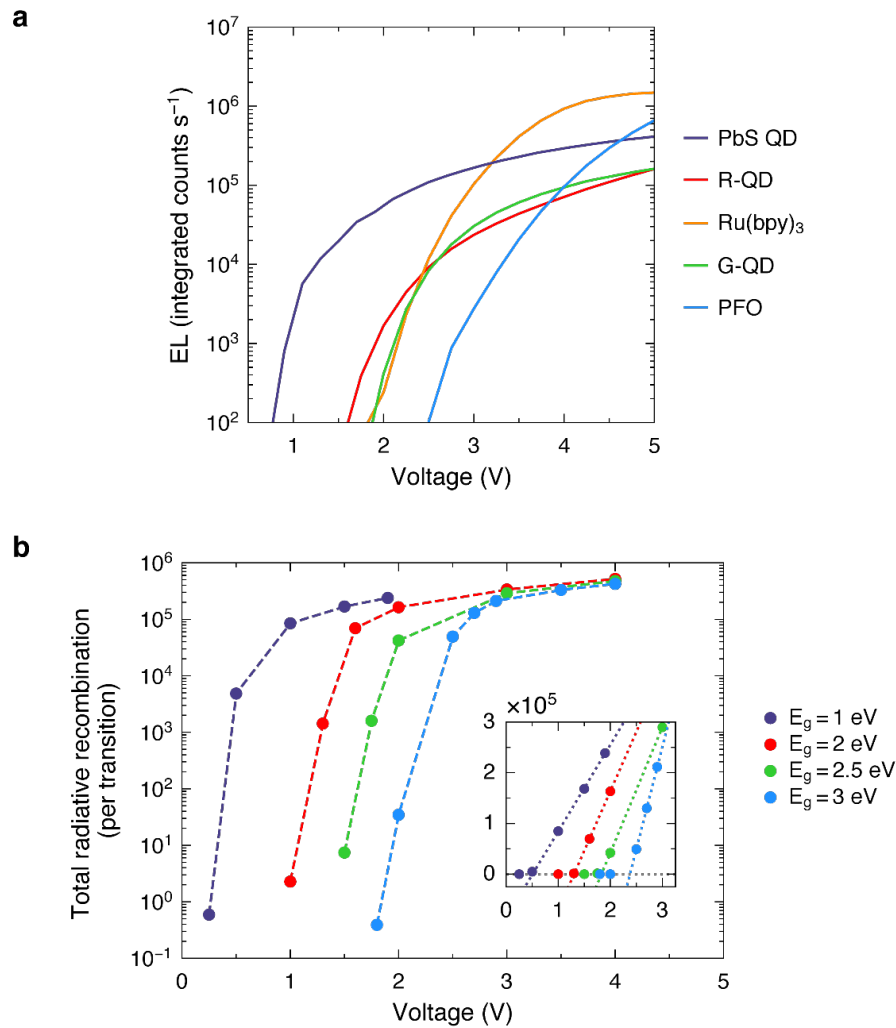


Figure 2.19: (a) Experimentally measured EL intensity as a function of gate voltage for high- $\kappa$  dielectric (8 nm  $ZrO_2$ ) devices with various emitters. Measurements were performed with a 100 kHz square wave gate voltage. Turn-on voltage was determined from the intercept with  $10^2$  integrated counts/s of a linear fit performed to the log-scale EL counts near the onset voltage. (b) Simulated radiative recombination for devices with a 8 nm high- $\kappa$  ( $\epsilon = 22$ ) gate dielectric and emitter materials of varying band gap energies indicated in the legend. Simulations were performed with a square wave gate voltage, emitter mobility of  $0.01 \text{ cm}^2 \text{ V}^{-1} \text{ s}^{-1}$ , CNT-CNT distance of  $1.5 \mu\text{m}$ , and emitter band gap energy specified in the legend. Inset: data in linear scaling. The turn-on voltage was calculated by performing a linear fit (colored dotted lines in the inset) to the data at low voltage and calculating the voltage at which the radiative recombination extrapolates to 0.

## 2.5 Spectroscopic opportunities

The presented device also enables EL spectroscopy, which can provide material compositional information similar to photoluminescence spectroscopy but without the need for an external light source. This could be especially beneficial for multiplexed material analysis since photoluminescence spectroscopy requires different excitation wavelengths for different analytes, which involves not only multiple lasers or an intense white light source but also optical path design and filtering to properly extract photoluminescence. We demonstrate the concept and potential of EL spectroscopy by probing a dynamic chemical reaction in solution. The reaction presented in Figure 2.20a-b is an imine condensation reaction, which is a type of reaction essential to dynamic covalent chemistry and the synthesis of secondary amines [36]. This reaction can proceed at room temperature with relatively high yield and no byproducts. The reaction between 9-(2-ethylhexyl)carbazole-3,6-dicarboxaldehyde (CDA) and benzylamine (BA) to form 9-(2-ethylhexyl)-9H-carbazole-3,6-diylbis(N-benzylmethanimine) (CDI) is carried out in a droplet of bis(2-ethylhexyl)benzene covering the EL device (Figure 2.20a), which remains in liquid state throughout the measurement. At the beginning of the reaction, CDA gives blue EL (peak at 2.8 eV). With the addition of BA, EL of the droplet progressively red-shifts and approaches that of CDI (Figure 2.20b). The EL spectra of the final reaction mixture indicates that the reaction reaches an equilibrium where the reagent and products coexist, which is consistent with the reversible nature of the imine condensation reaction. We believe the technique of EL spectroscopy can be generalized to study other chemical reactions and analyze mixtures with complex compositions.

With the emitter layer as the top layer, the EL device can also be used as a platform for sensing and studying structural dynamics of the emitter material. PFO is a blue-emitting conjugated polymer commonly used in organic optoelectronics and typically shows additional green EL after some period of device operation. The origin of the green emission is subjected to debate and has been correlated with the formation of fluorenone defects or excimers in the polymer chains [37]. Using our EL device, we found that the green emission from a thin PFO layer (8 nm, spincoated from 2.5 mg/ml PFO in toluene) can be reduced after exposing the device to organic vapors (Figure 2.20c-e). This effect can be quantified by the ratio of blue (2.79 eV) and green (2.27 eV) emission and is more pronounced for good solvents of PFO (e.g. toluene and chloroform) compared to poor solvents (e.g. isopropanol and water, Figure 2.20e). These results indicate that configurational changes in the polymer chains play an important role in the appearance of green emission in PFO, as the vapor of good solvents could facilitate structural rearrangement of the polymer chains but cannot remove fluorenone defects, which involves breaking covalent bonds. Furthermore, the ratio of blue to green emission can be used as a metric for organic vapor sensing. We demonstrate the feasibility of organic vapor sensing using chloroform as an analyte, where the blue-to-green ratio of EL increases after 10 sec of vapor exposure and decreases to baseline after operating the device for 5 sec (Figure 2.20f).



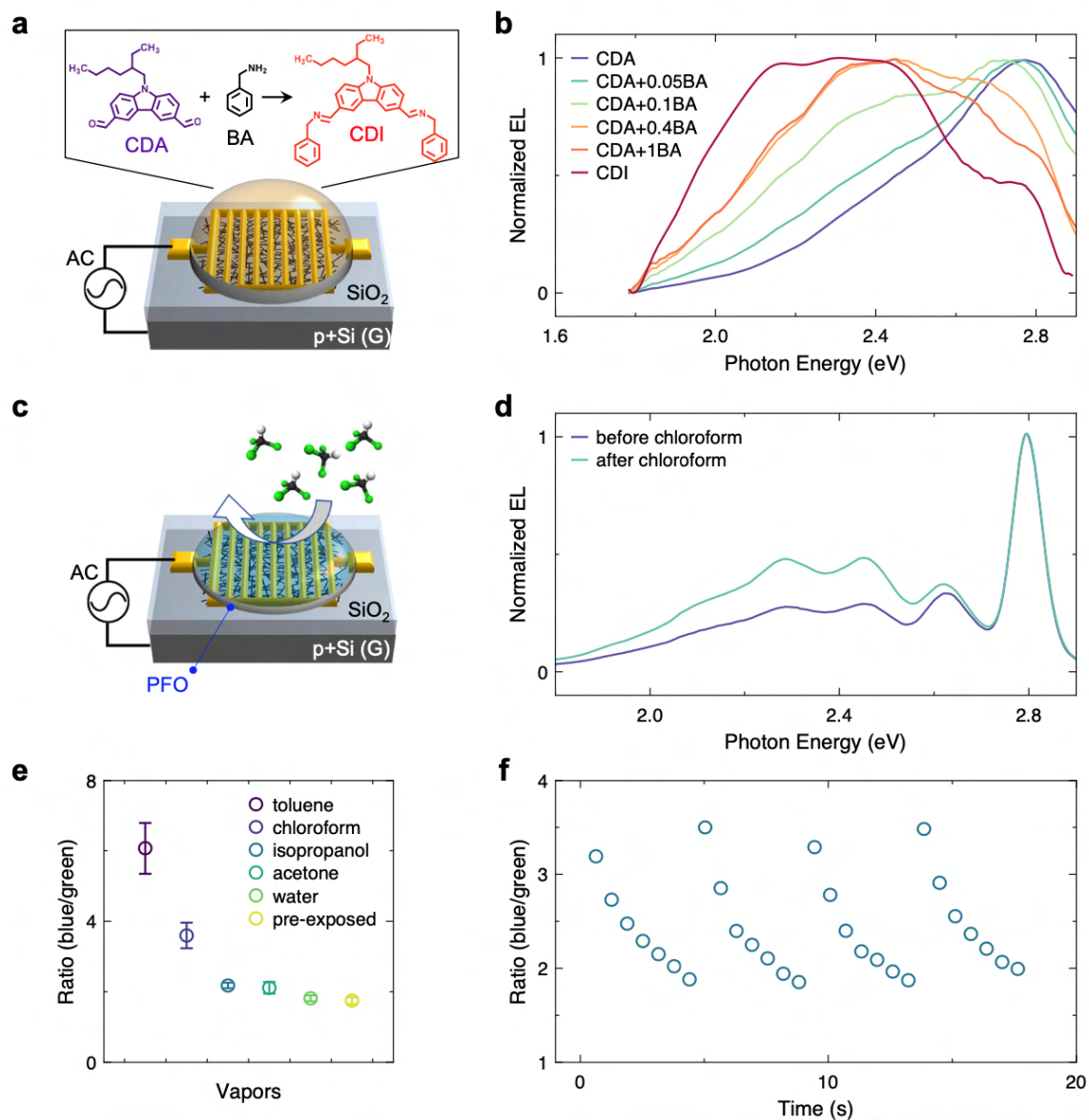


Figure 2.20: **EL spectroscopy and sensing.** The reaction of CBA and BA to form CDI is carried out in a droplet on the EL device (a) and the change in EL spectra reflects progress of the chemical reaction (b). The EL of an 8nm PFO layer changes after the device is exposed to chloroform vapor for 10sec (c), where the green emission band is substantially reduced (d). The ratio of blue (2.79 eV) to green (2.27 eV) EL after exposure of different solvent vapors is shown in (e), where better solvents of PFO give higher blue-to-green ratios. Blue-to-green ratio of the PFO device over 5sec after the device is exposed to chloroform vapor for 10sec is shown in (f), with vapor exposure repeated four times. The error bars in (e) correspond to the standard deviation of the blue/green ratio of three different devices after exposure to the vapors.

## 2.6 Conclusion

We have reported a light-emitting device that can excite EL from a wide variety of materials that emit in the IR to UV wavelength range. By using a porous CNT network as the source contact and applying an AC gate voltage, we generate band bending that can overcome carrier injection barriers in transient mode operation and eliminate the need for emitter specific charge injection layers. The design allows the emitter layers to be deposited directly on top of the source contact, which lifts limitations on the processability of the light-emitting material. We show that an array of devices can be used to generate multiplexed EL emission, where each emitting material is deposited on one pixel of the array. We also show that the device can be used as a platform for EL spectroscopy and sensing. Our approach creates opportunities for the development of light emitting devices at extreme wavelengths, as well as the use of EL spectroscopy as a metrology and sensing technique for materials previously inaccessible to this type of analysis.

## 2.7 Methods

### Fabrication of devices on Si/SiO<sub>2</sub> wafer

The assembly of semiconducting carbon nanotubes (CNTs) follows procedures reported in the literature [27]. In brief, 50 nm SiO<sub>2</sub>/p<sup>++</sup> Si substrates are washed with DI water, acetone and IPA, and then treated with O<sub>2</sub> plasma for 1.5 min. The substrate is covered by poly-L-lysine solution for 5 min and then washed with water. Semiconducting CNT solution (99.9% from Nanointegris) is then drop-casted on the substrate for 30 min and the substrate is washed with DI water and dried. The density of the CNT network can be tuned by changing the dropcasting time for CNT assembly. The substrate is then annealed under forming gas (5% H<sub>2</sub> in Ar) or nitrogen at 250 °C for 1 h. Source contacts are patterned by photolithography with metal electrodes deposited by e-beam evaporation. The CNT area is then defined by photolithography and the CNT outside the device area is etched by oxygen plasma.

### Fabrication of devices with thin gate dielectric

To improve device robustness and reduce parasitics, we designed the devices such that the top contact/bond pad are situated on top of a thick oxide layer, while the emitting region is situated on a thin oxide layer. The flexible CNT mesh contact allows for continuous electrical connection between the top contact and bottom emitting regions. The fabrication process for the thin gate dielectric devices is schematically illustrated in Figure 2.17. The device with a metal back reflector was used to improve light outcoupling and demonstrate the limits of EL performance at low voltage.

90 nm SiO<sub>2</sub>/p<sup>++</sup> Si substrates are first patterned by photolithography (Heidelberg  $\mu$ PG 101) and the exposed SiO<sub>2</sub> is etched completely away with 6:1 BOE (buffered oxide etch)

until the underlying Si is exposed. (For devices with a metal back reflector, 260 nm  $\text{SiO}_2/\text{p}^{++}$  Si substrates are used instead to accommodate a thick metal back layer; in these devices, a Ti/Ag/Ti (2 nm/150 nm/1 nm) stack is immediately evaporated via e-beam (Ti) and thermal (Ag) evaporation, followed by liftoff.) Around 8 nm  $\text{ZrO}_2$  of gate oxide is deposited by atomic layer deposition (Cambridge Nanotech) at 180 °C. Because neither semiconducting nor metallic CNTs assemble in significant quantity on the  $\text{ZrO}_2$  surface (as determined from AFM imaging and electrical measurement), 2 nm  $\text{SiO}_x$  is evaporated on top of the  $\text{ZrO}_2$  to promote assembly of CNT networks. To reduce the parasitic resistance at low voltage, metallic (as opposed to semiconducting) CNTs are used in these devices. The substrate is treated with poly-L-lysine in the same manner and 99.9% metallic CNT solution (Nanointegris) is drop-casted on the substrate at 100 °C. After evaporation, the substrate is washed with DI water. The remainder of the fabrication process (annealing, contact patterning, CNT area patterning) is identical to the general device fabrication procedure described above, where here we used 25 nm Pd contacts. For all devices, AC voltage was applied between the top contact and  $\text{p}^{++}$  Si substrate which served as a backgate. It is important to note that EL performance depends on the distance between the contact and etched trenches, and this distance should be minimized as much as possible to reduce loss.

## Materials and deposition method

Toluene and ethanol were purchased from Sigma Aldrich. Emitters that are soluble or dispersible in solvents were drop-casted or spin-coated, and the ones that are not soluble were thermally evaporated under high vacuum. The deposition method for each material is listed below.

CdSSe/ZnS alloy quantum dots were purchased from Sigma Aldrich as 1mg/ml toluene solution. For a 0.25 cm<sup>2</sup> chip, 5  $\mu\text{L}$  of solution is drop-casted and dried at room temperature. The substrate is then put in acetone for 1 min, then 1 wt% acetic acid in acetone for 5 min, and finally 1 min in acetone to remove extra ligands from the quantum dots. Only washing with the first step (acetone 1 min) is enough to get EL, however this leads to lower device stability and larger device-to-device variation.

CdSeTe/ZnS quantum dots were purchased from NanoOptical Materials Inc. as 5 mg mL<sup>-1</sup> toluene solution with excess surfactant. The quantum dots were first washed before deposition: 0.1 mL of the toluene solution was added to 1.5 mL ethanol and the quantum dot precipitates to give a suspension, which is centrifuged at 8800 rpm for 5 min and the clear supernatant was decanted. The quantum dots are then re-dispersed in 0.2 mL toluene. For a 0.25 cm<sup>2</sup> chip, 5  $\mu\text{L}$  of this solution is drop-casted and dried at room temperature. The substrate is then put in 1 wt% acetic acid in acetone for 5 min, and then 1 min in acetone to remove extra ligands from the quantum dots. Without the initial washing step, drop-casting directly from the initial solution would give a film that cannot be completely dried and appeared oily due to excess oleic acid surfactant.

PbS quantum dots were purchased from NNCrystals Inc. as 5 mg mL<sup>-1</sup> solution in toluene with excess surfactant. The quantum dots were first washed before deposition: 0.1 mL of

the toluene solution was added to 1.5 mL ethanol and the quantum dot precipitates to give a suspension, which is centrifuged at 8800 rpm for 5 min and the clear supernatant was decanted. The quantum dots are then re-dispersed in 0.2 mL toluene. For a 0.25 cm<sup>2</sup> chip, 5  $\mu$ L of this solution is drop-casted and dried at room temperature. No subsequent wash was carried out as the quantum dot film would easily delaminate from the substrate while submerged in solution, probably due to the comparably small size of the quantum dot.

Perovskite nanowire was prepared according to literature method, washed extensively by centrifugation with the supernatant decanted, and re-dispersed in hexane. The suspension was drop-casted to give a similar coverage compared to other inorganic quantum dots however the emission from this material is unstable compared to other emitters, only allowing the measurement of its EL spectrum.

All aromatic molecules and conjugated polymers were purchased from Sigma Aldrich. For soluble emitters (all except PTCDA), the emitters were dissolved in toluene with 10 mg mL<sup>-1</sup> concentration. 2  $\mu$ L of this solution is drop-casted on a 0.25 cm<sup>2</sup> sized chip and dried at room temperature. Drop-casting solution with too high volume leads to long evaporation times and crystallization of the molecules, which could lead to non-uniform EL. PTCDA, due to its very low solubility, was deposited by evaporation under high vacuum and the thickness is 20 nm.

All metal coordination complexes were purchased from Sigma Aldrich except for tris[2-(2,4-difluorophenyl)pyridine]iridium(III), which is purchased from Strem Chem. Ru(bpy)<sub>3</sub>(PF<sub>6</sub>)<sub>2</sub> was drop-casted from 20 mg mL<sup>-1</sup> acetonitrile solution with 2  $\mu$ L solution dispensed on 0.25 cm<sup>2</sup> chip. Alq<sub>3</sub>, and the two iridium complexes were evaporated to give 20 nm film due to low solubility. The coordination polymer ZnTCPP was prepared similar to a literature method [38], where TCPP was heated in dimethylformamide with excess amount of zinc acetate for 5 h to give the product as solid precipitate.

All conjugated polymers were purchased from Sigma Aldrich. These polymers were typically spin-coated at 6000 rpm at 5 mg mL<sup>-1</sup> concentration (toluene solution) or drop-casted from 2.5 mg mL<sup>-1</sup> toluene solution with 2  $\mu$ L solution dispensed on a 0.25 cm<sup>2</sup> chip. The film thickness can be varied by changing the spin speed or concentration (Figure 2.12) and the thickness dependence of EL for PFO is presented in Figure 2.13.

## Electrical and optical characterization

Electroluminescent devices were operated under vacuum at 10 mTorr and EL was collected through a quartz window. The devices were pumped using a bipolar square wave from an Agilent 33522A arbitrary waveform generator applied to the gate electrode, while the source contact was grounded. For voltage above 10 V, a voltage amplifier was used with the waveform generator. The EL data presented in this work was measured using a custom-built quantitative micro-PL instrument described in detail in Ref. [39] (Methods). EL was collected using a 10 $\times$  objective lens. EL was dispersed by a spectrometer with a 340 mm focal length and 150 groove per mm grating, and detected using a Si charge-coupled device (CCD) (Andor iDus BEX2-DD). Prior to each measurement, the CCD background was obtained and

subsequently subtracted from the EL acquisition. Time resolved EL measurements were collected using a photomultiplier tube connected to an oscilloscope. EL imaging was performed with either a fluorescence microscopy setup with a CCD detector (Andor Luca) to acquire images or a Olympus optical microscope with CMOS camera. The emission power was measured by Thorlabs PM100D power meter with S120C sensor and cross calibrated with CCD counts. Transistor  $I_d - V_g$  characteristics were taken using an Agilent B1500A semiconductor parameter analyzer. For external quantum yield measurement (details in following section), sine wave gate voltage was used and current was measured by a current amplifier (Model SR570, Stanford Research Systems, gain  $1 \text{ mA V}^{-1}$ ) connected to an oscilloscope.

## Device simulation

2D simulations of the electroluminescent device cross-section were performed using Sentaurus TCAD in order to understand trends in device behavior. The simulated device structure consisted of a layer of emissive semiconducting material between two grounded edge contacts 1.4 nm in height, representing two carbon nanotubes, situated on top of a 50 nm  $\text{SiO}_2$  layer with a gate contact on the bottom. The device width in the third dimension, which corresponds to the length of the CNTs, was  $1 \mu\text{m}$ . The emissive material parameters, intended to roughly represent those similar to organic emissive materials, were  $\chi_0$  (electron affinity) = 3.3 eV,  $E_g$  (band gap) = 2.6 eV,  $\epsilon$  (relative dielectric constant) = 3.5,  $\mu_n$  (electron mobility) =  $\mu_p$  (hole mobility) =  $0.001 \text{ cm}^2 \text{ V}^{-1} \text{ s}^{-1}$ ,  $m_e^*$  (electron effective mass) =  $m_h^*$  (hole effective mass) =  $m_0$ . The frequency of the square wave pulse was 50 kHz. For simplicity, the grounded contacts were set to be ambipolar (work function = 4.6 eV) such that emission is equal for upward and downward transitions. The simulation methodology is otherwise similar to that in Ref. [12].

## Measurement of external quantum efficiency (EQE)

The measurement of external quantum efficiency involves measuring the number of carriers electrically injected into the emitter layer as well as the number of photons emitted. The number of photons emitted is determined from the light output as measured by a power meter. For measurement of carrier injection, a sine wave gate voltage is applied to the device, and the time-dependent current is measured by a current amplifier connected in series with the device that converts the current into a voltage measured by an oscilloscope. The time-averaged charge in each half-cycle is obtained by integrating the current and the total number of injected carriers is determined from the sum of the magnitudes of the charge from each half-cycle (Figure 10). For an AC-driven device with an emitter layer on top, the overall charge is composed of three components: (1) the charge involved in switching the polarity of the capacitor between the metal pad and CNT network contact; (2) the charge entering the emitter layer; and (3) the charge exiting the emitter layer. For example, when the gate voltage changes from negative to positive, electrons enter while holes exit the emitter layer. The first component can be determined by measuring the device current without any emitter

layer. To estimate the quantum efficiency associated with injection from the CNT contact to the emitter layer, the first charge component is subtracted from the overall measured charge, which yields the sum of electrons injected into the emitter layer and holes exiting the emitter layer. These two components (components 2 and 3) cannot be distinguished, even though the number of carriers injected into the emitter only corresponds to component 2. In our quantum efficiency estimate, we assume holes do not exit the emitting layer when electrons are injected, and vice versa for electrons during the other half cycle, thus providing a lower limit for the external quantum efficiency.

### EL spectroscopy of reaction mixtures in liquid state

9-(2-ethylhexyl)carbazole-3,6-dicarboxaldehyde (CDA), bis(2-ethylhexyl)benzene and benzylamine (BA) were purchased from Sigma Aldrich. 9-(2-ethylhexyl)-9H-carbazole-3,6-diylbis(N-benzylmethanimine) (CDI) was prepared by refluxing CDA with excess BA in ethanol/toluene mixture with catalytic amount of acetic acid for 5 h. The solvent, catalyst and excess BA were removed under vacuum to give the product CDI as an oily liquid.

For EL spectroscopy of the reaction mixture, 5  $\mu\text{L}$  of bis(2-ethylhexyl)benzene and 5  $\mu\text{L}$  of toluene solution of CDA ( $60 \text{ mg mL}^{-1}$ ) were deposited on the chip of the EL device (same device as Figure 2.1, overall chip size  $25 \text{ mm}^2$ ). bis(2-ethylhexyl)benzene is a high boiling point solvent chemically similar to toluene and does not give EL in the range we measure and the EL of the droplet corresponds to the EL of CDA. All measurements were carried out under vacuum at 20 V and 200 kHz. Under vacuum toluene evaporates, leaving only bis(2-ethylhexyl)benzene, thus the volume of the droplet is unchanged throughout the measurement. Then 5  $\mu\text{L}$  of toluene solution of BA ( $1.9 \text{ mg mL}^{-1}$ ) was added to the droplet, and the droplet gave EL of CDA+0.05BA. With another 5  $\mu\text{L}$  of toluene solution of BA ( $1.9 \text{ mg mL}^{-1}$ ) added, the droplet gave EL of CDA+0.1BA, and EL of reaction mixtures with other compositions can be obtained in a similar manner by adding BA solution of desired concentration to this droplet.

### EL sensing with PFO

8 nm PFO was spin-coated from  $2.5 \text{ mg mL}^{-1}$  PFO in toluene and the EL device was operated at 12.5 V, 500 kHz for 5 sec before exposing to various solvent vapors for 10 sec. The EL of the device can then be measured to give the EL spectra after exposure.

## 2.8 Tables

## EL spectra of aromatic molecules

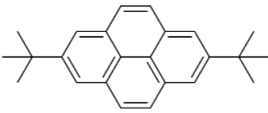
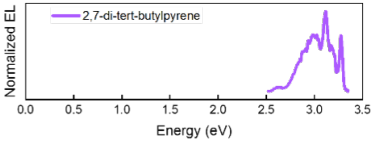
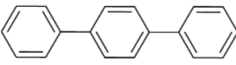
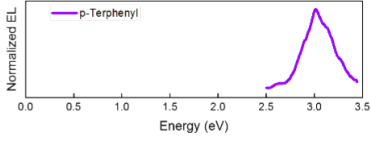
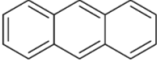
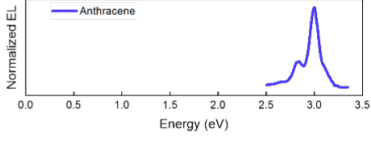
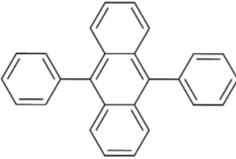
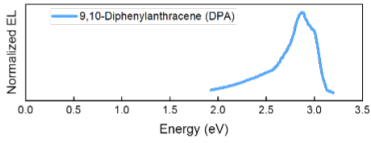
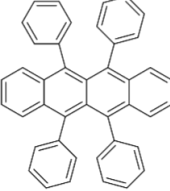
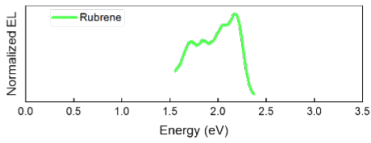
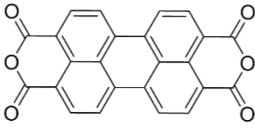
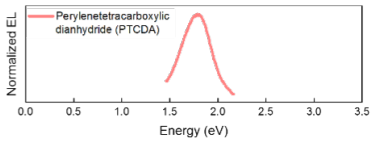
2,7-di-tert-butylpyrene		
p-Terphenyl		
Anthracene		
9,10-diphenylanthracene		
Rubrene		
Perylenetetracarboxylic dianhydride		

Table 2.1

## EL spectra of coordination complexes

Tris[2-(4,6 difluorophenyl)pyridinato-C2,N]iridium(III)		
Tris-(8 hydroxyquinoline) aluminum		
Tris[2-phenylpyridinato-C2,N]iridium(III)		
Tris(2,2'-bipyridine)ruthenium(II) hexafluorophosphate		
Tetrakis(4-carboxyphenyl) Porphyrin Zinc (II)		

Table 2.2



## EL spectra of conjugated polymers

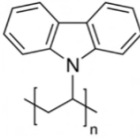
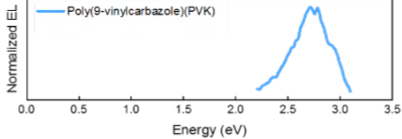
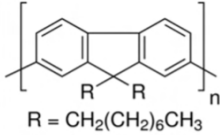
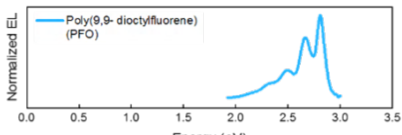
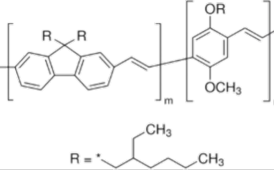
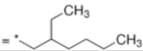
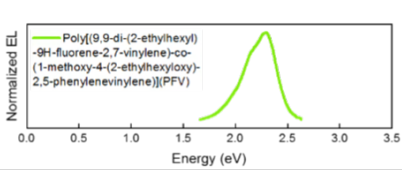
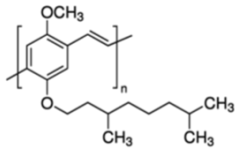
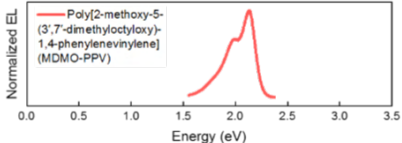
Poly(9-vinylcarbazole)		
Poly(9,9-dioctyl-9H-fluorene-2,7-diyl)	 <p>R = CH<sub>2</sub>(CH<sub>2</sub>)<sub>6</sub>CH<sub>3</sub></p>	
Poly[(9,9-di-(2-ethylhexyl)-9H-fluorene-2,7-vinylene)-co-(1-methoxy-4-(2-ethylhexyloxy)-2,5-phenylenevinylene)]	 <p>R = </p>	
Poly[2-methoxy-5-(3',7'-dimethyloctyloxy)-1,4-phenylenevinylene]		

Table 2.3

## EL spectra of inorganic quantum dots and nanomaterials

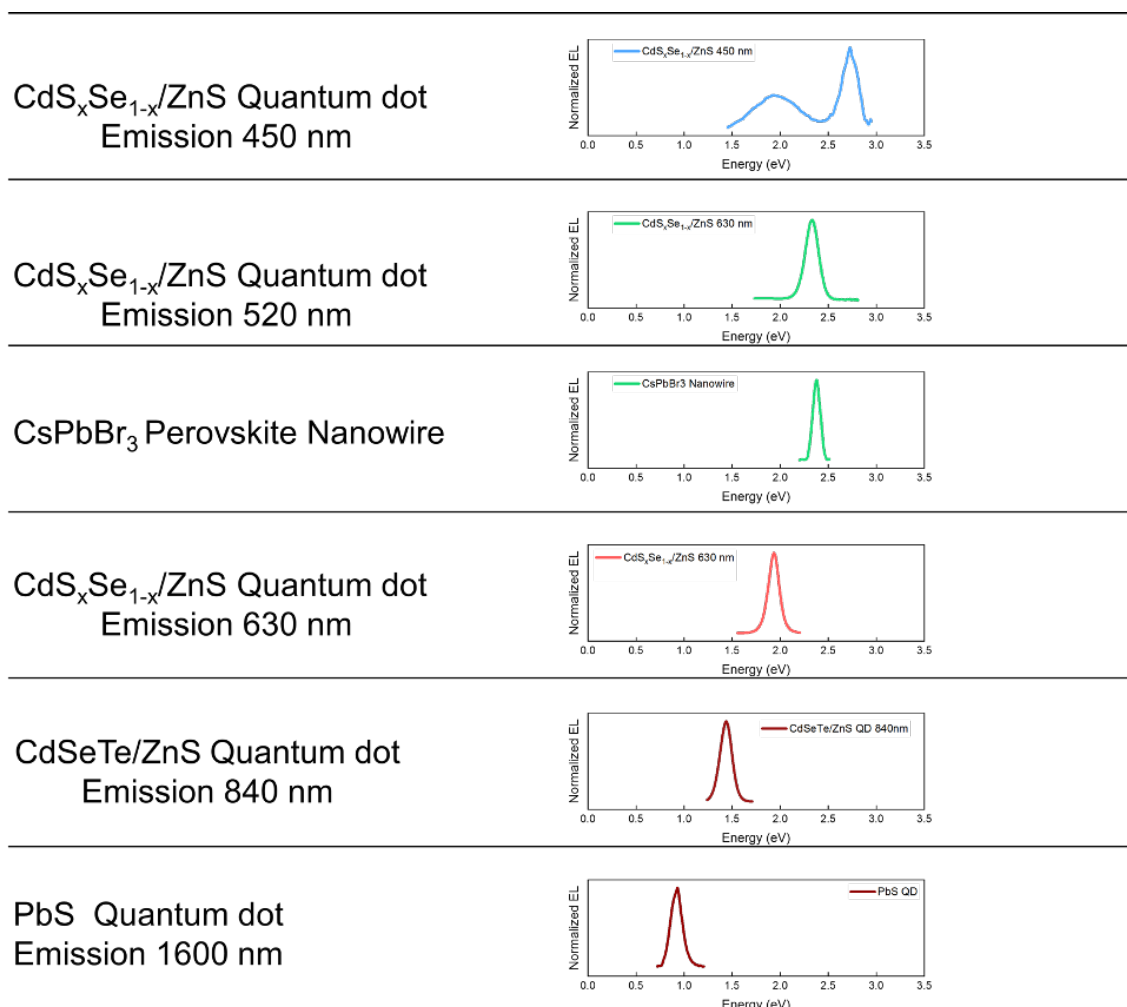


Table 2.4

## Chapter 3

# Performance limits of a pulsed-driven electroluminescent capacitor

This chapter (a tribute to the pandemic times) is adapted from:

V. Wang, Y. Zhao, A. Javey, “Performance Limits of an Alternating Current Electroluminescent Device”, *Advanced Materials*, 33 (2), 2005635, 2021.

---

The use of alternating-current (AC) voltage is a simple, versatile method of producing electroluminescence from generic emissive materials without the need for contact engineering. It has been shown that AC-driven, capacitive electroluminescent devices with carbon nanotube network contacts can be used to generate and study electroluminescence from a variety of molecular materials emitting in the infrared to ultraviolet range. Through comprehensive device simulations and illustrative experiments, we study performance trade-offs in these devices, enhancing understanding of the mechanism and capability of electroluminescent devices based on alternating as opposed to direct current (DC) schemes. AC-driven electroluminescent devices can overcome several limitations of conventional DC-driven electroluminescent devices, including the requirement for proper alignment of material energy levels and processing of emitting materials into uniform thin films. By simultaneously choosing proper device geometry, driving parameters, and material characteristics, the performance of these devices can be optimally tuned. Importantly, the turn-on voltage of AC-driven electroluminescent devices approaches the band gap of the emitting material as the gate oxide thickness is scaled, and internally efficient electroluminescence can be achieved using low mobility single-layer emitter films with varying thickness and different energy barrier heights relative to the contact.

## 3.1 Introduction

Common light-emitting devices rely on the phenomenon of electroluminescence (EL), the emission in light in response to electrical excitation. These devices include the light-emitting diode (LED), a two-terminal device driven by a DC voltage source. Bright and efficient LEDs have already been successfully developed to generate light emission from a wide variety of materials, from inorganic III-V semiconductors [40, 41] to colloidal quantum dots [42, 43] to organic molecules [16]. Generally, electrons and holes are simultaneously injected into an emissive material from n- and p-type contacts, migrate across the emitting layer, and recombine to produce light. This process can occur with nearly perfect internal quantum efficiency [44]. It is also possible to generate electroluminescence by employing an AC driving scheme [18]. Early examples includes ZnS phosphor-based devices [24], which rely on extremely high operating voltages to achieve impact excitation to excite luminescent centers. Other examples include double-insulator devices where both electrodes are covered by a dielectric layer and carriers are solely generated from internal charge generation layers [45].

Conversely, both charge carriers can be injected directly from contacts. In vertically-structured field-induced polymer electroluminescent devices, charge carriers are injected from an electrode and/or generated in charge generation layers [26, 28, 46]. EL has also been demonstrated with a laterally-structured capacitive device structure in which materials are deposited on top of a gate oxide layer across which AC voltage is applied [12, 47, 48]. A more complex transistor-based structure which applies an additional drain-source bias can also be adopted to generate light from various materials [49, 50]. These examples, which use microscale metal contacts to inject carriers, may be sufficient to produce AC EL from materials with relatively high mobility; however, denser electrical contacts are preferable for generating bright AC EL from other kinds of materials, including molecular emitters with poor mobility [51, 52]. To this end, self-assembled carbon nanotube (CNT) networks [35] can be used as a porous top contact to increase contact density and emission intensity [53]. Due to the lateral nature of charge injection, the emitting material does not need to be suited for further processing and optical properties can be easily probed without requiring transparent contacts, unlike vertical multilayered devices in which the emitting layer is sandwiched between multiple films.

In this chapter, we study the performance limits of a generic AC electroluminescent device in which direct bipolar charge injection is achieved with a single CNT network electrode, using numerical device simulations to corroborate and understand experimental measurements. We previously demonstrated such a device for applications in electroluminescence spectroscopy and sensing [53], but more elaborate knowledge is required to understand the scope of compatible materials as well as the operating parameters that are optimal for different material samples. Through studies of device scaling, we show that turn-on characteristics of the AC electroluminescent device are controlled by vertical scaling of the device's dimensions. We further elucidate the interplay between charge transport, brightness, and efficiency by analyzing spatial and temporal variations of charge density and carrier recombination. Finally, we investigate how device design affects fundamental efficiency losses and transient

responses, informing directions of future improvement for AC electroluminescent devices and demonstrating that efficient light emission can be achieved with AC voltages depending on the material and device parameters.

The structure and operating scheme of the AC light-emitting device under study is schematically illustrated in Figure 3.1a. The device consists of a layer of emissive semi-conducting material deposited on top of an oxide layer. AC voltage is applied across a bottom gate contact and top CNT network source contact. Experimentally, we fabricated this device structure on a 50 nm  $\text{SiO}_2/\text{p}^{++}$  Si substrate in which the  $\text{p}^{++}$  Si substrate serves as the bottom gate contact and a metal grid is used to contact the CNT network for probing. When a pulsed gate voltage with finite slew rate is applied across the gate and source contacts, light emission is observed after voltage transitions as confirmed by earlier time-resolved EL measurements [12]. The proposed mechanism behind such a driving scheme has been discussed previously [53]. To briefly recapitulate, electrons accumulate in the emitter layer when the gate voltage is positive, causing there to be a large electron concentration but low hole concentration. When the gate voltage switches from positive to negative, the field across the device cannot change immediately, so the applied gate voltage instead drops across resistive components such as the emitter material. The large potential drop at the source contact-emitter interface results in steep band bending that enables carrier tunneling (Figure 3.1b). Holes are injected into the emitter layer as electrons either exit the semiconductor through the contact or recombine with holes. Eventually, the transient carrier action subsides and the band diagram resembles that of a metal-oxide-semiconductor capacitor at steady state until the subsequent negative to positive voltage transition where a similar tunneling process occurs.

## 3.2 Device operation and simulation

To further understand the operating characteristics and performance limits of such a device, we performed numerical simulations of the device using Sentaurus TCAD, which simultaneously solves the Poisson and carrier continuity equations with a drift-diffusion model involving Fermi statistics and radiative carrier recombination [54, 55]. We assume equal and constant electron and hole mobilities as well as ambipolar contacts for symmetry. In both simulation and experiment, a certain turn-on voltage is required to observe EL, after which point the EL intensity increases approximately linearly with the amplitude of the square wave gate voltage (Figure 3.1b). EL occurs immediately following each voltage transition and lies dominantly near the source contacts in most cases, so the EL intensity should scale linearly with the number of voltage transitions or square wave frequency. Experimentally, the EL intensity does scale linearly with square wave frequency up to a certain cut-off frequency, after which the EL intensity rolls off due to inability of the device to reach steady-state conditions during square wave pulses (Figure 3.1c). Based on this model, we studied trends between material properties (e.g. carrier mobility, band gap), device structure (e.g. CNT network density, oxide and emitter layer thickness), and performance characteristics (e.g.

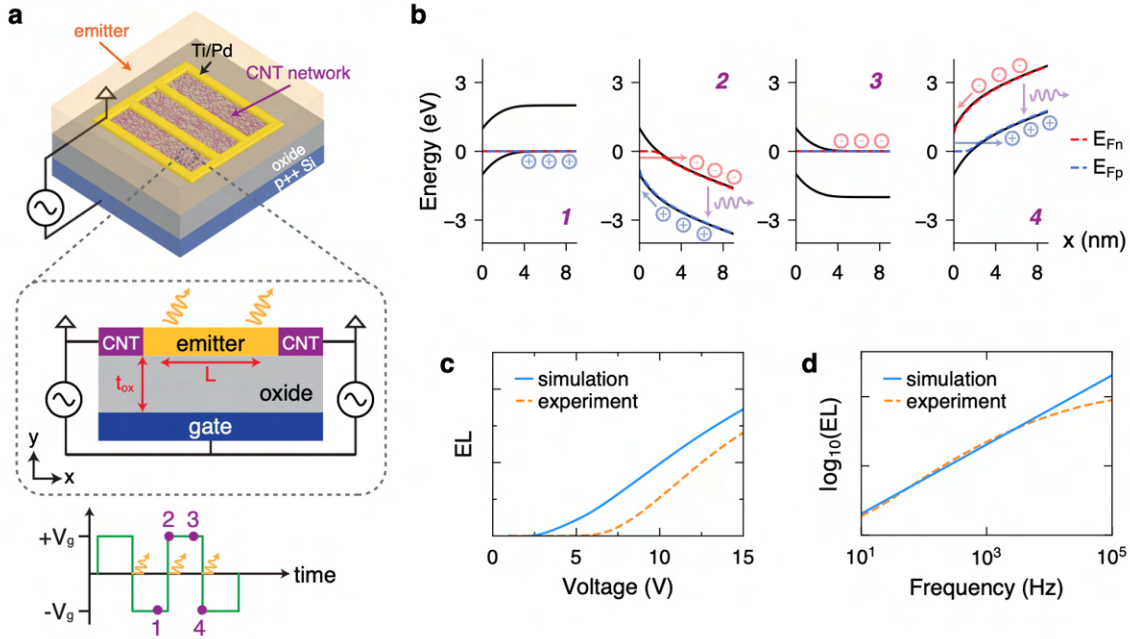


Figure 3.1: (a) Schematic of an AC electroluminescent device with a metal grid electrode (yellow) contacting a CNT network (purple lines) on an oxide substrate (grey). Square wave AC voltage is applied between the  $p^{++}$  Si gate (blue) and the grounded metal electrode. To capture device behavior, we simulate the region between two individual CNT contacts. (b) Energy band diagrams at the CNT-emitter interface at the square wave timepoints indicated in (a). Quasi-Fermi levels for electrons and holes are shown in red and blue, respectively. (c) EL intensity as a function of gate voltage from simulation (blue) and experiment (orange). (d) EL intensity as a function of square wave frequency from simulation and experiment. Experimental data were measured from devices with red CdSSe/ZnS quantum dots on 50 nm SiO<sub>2</sub> gate oxide using a 100 kHz, 10 V square wave.

turn-on voltage, brightness, quantum and power efficiency).

### 3.3 Low-voltage operation

While various AC electroluminescent devices have been proposed and demonstrated in the past, these devices largely rely on high operating voltages (in the tens to hundreds of volts) to achieve reasonable electroluminescence, rendering them less practically appealing than their DC counterparts [46, 56, 57]. In our device, the turn-on voltage reflects the presence of a charge injection barrier at the source-semiconductor contact as well as any external parasitic components in the experimental measurement. We performed EL simulations at different peak-to-peak gate voltages for devices with varying oxide thickness (Figure 3.2) in

order to understand global trends in turn-on voltage scaling. As the band gap of the emissive material increases, the threshold increases superlinearly compared to the theoretical limit ( $V_T \approx \pm E_g/2$ ), meaning that it is harder to achieve low turn-on voltage for materials with large band gaps due to the increased injection barrier.

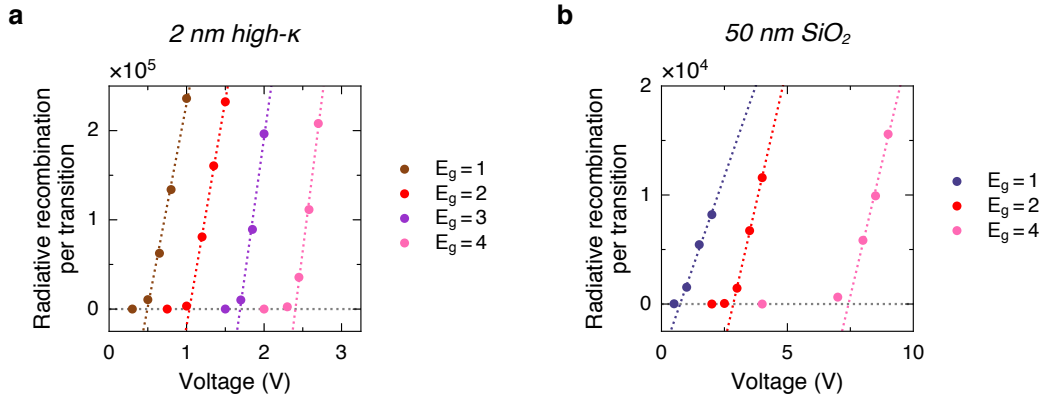


Figure 3.2: Total amount of radiative recombination integrated over the volume of the emitter layer from a single square wave gate voltage transition. The data show devices with different band gap emissive layers on a (a) 2 nm high- $\kappa$  ( $\epsilon_r = 22$ ) or (b) 50 nm  $\text{SiO}_2$  ( $\epsilon_r = 3.9$ ) gate oxide layer. Dotted lines represent the linear fit used to extract the turn-on voltage, defined as the voltage intercept where the radiative recombination extrapolates to zero.

Due to the unique ability of our device to generate EL from emissive materials with nearly any band gap in the infrared to ultraviolet range, we can study fundamental scaling relationships of turn-on voltage versus emitter band gap using a single device, without needing to design different electron and hole contacts for different materials. Experimental EL data from devices with different gate oxide thicknesses agree well with the simulated model (Figure 3.3a). In particular, scaling down the oxide thickness reduces the turn-on voltage. As in conventional field-effect transistors, gate control of the emissive semiconducting material depends on the equivalent oxide thickness (EOT) of the gate oxide, which is defined as  $t_{ox} (\epsilon_{\text{SiO}_2} / \epsilon_{ox})$  for a gate oxide of thickness  $t_{ox}$  and relative dielectric constant  $\epsilon_{ox}$  [58]. The EOT can be reduced by decreasing the oxide thickness or increasing the dielectric constant of the oxide layer. The charge on a capacitor at steady state depends on the gate capacitance and voltage ( $Q \propto C_{ox}(V_g - V_T)$ ); increasing the capacitance decreases the operating voltage required for equivalent charge input. It is worth noting that high- $\kappa$  dielectrics have been previously applied to reduce the turn-on voltage in AC electroluminescent devices with double dielectric layers, albeit based on a different mechanism which relies on field-dependent charge regeneration due to the absence of direct carrier injection [25]. For materials with very low band gap, the EOT has little effect on the turn-on voltage, which remains near the band gap for all oxide thicknesses shown. The turn-on voltage approaches the theoretical

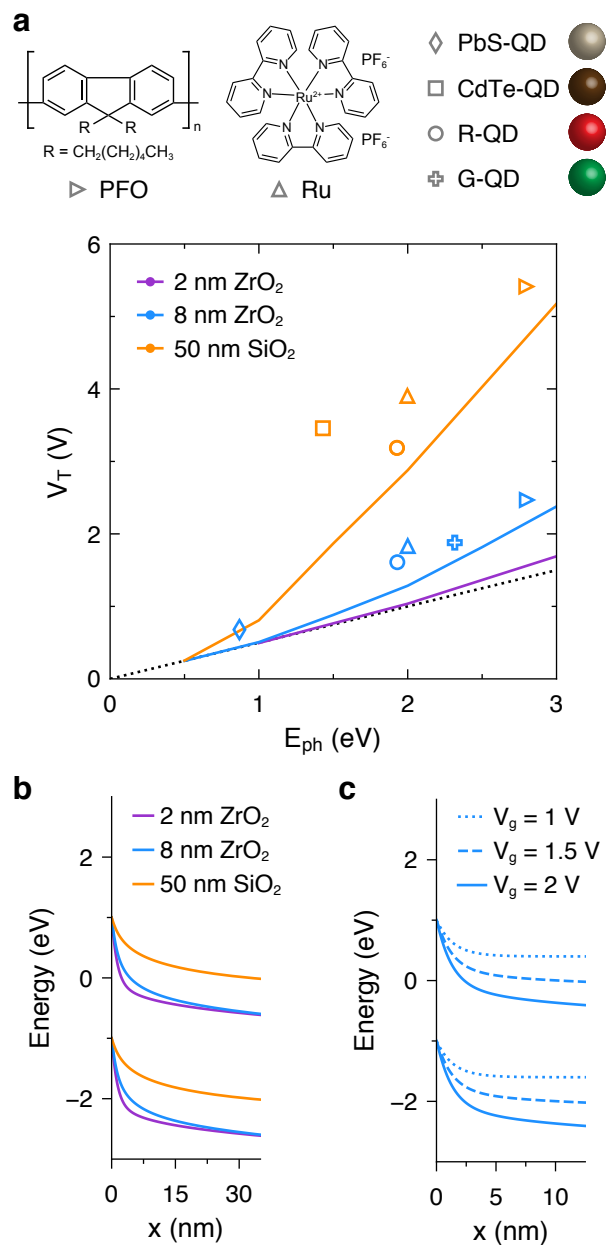


Figure 3.3: (a) Turn-on voltage as a function of photon energy from simulation (lines) and experiment (markers). Simulations were performed in 0.5 eV band gap energy increments for devices with gate oxide thicknesses corresponding to the fabricated devices indicated in the legend (2 nm  $ZrO_2 \approx 0.4$  nm EOT, 8 nm  $ZrO_2 \approx 1.4$  nm EOT, 50 nm  $SiO_2 = 50$  nm EOT). The black dotted line represents the curve  $V_T = E_{ph}/2$ . Experimental data were measured using a 100 kHz square wave. Abbreviations: PbS-QD (PbS quantum dot), CdTe-QD (CdSeTe/ZnS quantum dot), R-QD (630 nm red CdSSe/ZnS quantum dot), Ru ( $Ru(bpy)_3(PF_6)_2$ ), G-QD (520 nm green CdSSe/ZnS quantum dot), PFO (poly-(9,9-dioctylfluorene)). (b) Energy band diagrams at a source contact for devices with different gate dielectrics at  $V_g = 2$  V. (c) Energy band diagrams at a source contact for a device with 2 nm  $ZrO_2$  and different gate voltages. The simulated emissive layer band gap is  $E_g = 2$  eV.



limit across a larger range of emitter band gaps as the EOT is decreased, as exemplified by simulations of a device with a 2 nm high- $\kappa$  ( $\epsilon_{ox} \approx 22$ ) oxide layer with EOT  $\approx 0.4$  nm.

Energy band diagrams at the source-semiconductor interface shed light on the physical mechanism underlying the reduction in turn-on voltage. As the EOT decreases, the electric field or steepness of band bending at the source contact during voltage transitions increases due to higher gate capacitance, thereby thinning the tunneling barrier for carrier injection at a fixed gate voltage (Figure 3.3b). Increasing the applied gate voltage has a similar effect (Figure 3.3c). Since the breakdown voltage of the gate oxide scales with oxide thickness, practical choices for the oxide thickness should consider both the viable operating voltage regime as well as the achievable turn-on voltage. Altogether, our results show that the turn-on voltage corresponds to the transition from injection- to transport-limited behavior and depends on both emitter band gap and gate oxide thickness. Other parameters, such as carrier mobility in the emitter layer, have less effect on the turn-on voltage (Figure 3.4).

2D plots of the electrostatic potential show the evolution of voltage drops present in the device. During the gate voltage transient, the charge on the capacitor cannot switch polarity immediately, thus causing the electric potential to drop at the contact-emitter interface first. This regime, in which the potential changes mostly along the lateral ( $x$ ) direction, is depicted in Figure 3.5a(i). As time elapses, the potential drops increasingly across the oxide as opposed to across the emitter layer, yielding greater changes in electrostatic potential in the vertical ( $y$ ) direction across the oxide (Figure 3.5a(ii)). When the oxide is thick and of low dielectric constant, less voltage is dropped near the CNT contact, which reflects the more gradual band bending and decreased level of carrier injection (Figure 3.5b). In this case, the gate capacitance is smaller and less charge is accumulated in the emitter layer during the steady-state periods of the square wave pulse.

In general, the turn-on voltage of AC electroluminescent devices with ambipolar contacts should approach the optical energy gap of the emitting material as the EOT is decreased. The simulated turn-on voltages for charge injection and EL consistently underestimate the experimentally measured threshold voltages, in part due to exclusion of excitonic effects in the simulation model. In excitonic materials, electrons and holes undergo recombination by first forming bound pairs (excitons) with energies slightly smaller than the band gap for free carriers. The difference between the measured photon energy and the band gap for transport depends on the exciton binding energy. Furthermore, it is unlikely that the CNT contacts are perfectly ambipolar with respect to the experimentally measured materials. When the source contacts have p- or n-type work functions, the turn-on voltage increases by an amount similar to the increase in Schottky barrier height for the harder-to-inject carrier (Figure 3.6). In this case, DC offsets can be applied to the AC gate voltage to offset detrimental work function differences and restore low voltage device behavior equivalent to the case of mid-gap contacts. For example, it is more difficult to inject holes into the emitter material using n-type contacts due to the increased Schottky barrier height. Applying a negative DC offset pulls the emitter bands upwards, yielding sharper band bending that thins the barrier and enables carrier tunneling (Figure 3.6). Importantly, the EL at moderate to high voltage does not depend greatly on the Schottky barrier height or work function difference between

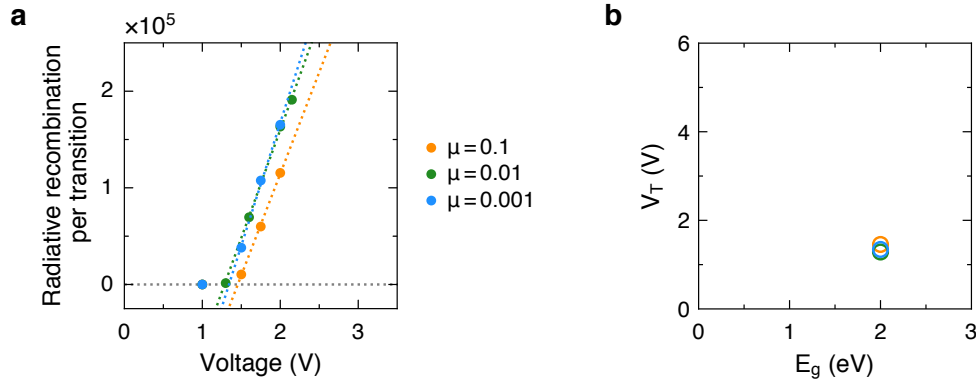


Figure 3.4: (a) Total amount of radiative recombination integrated over the volume of the emitter layer from a single square wave gate voltage transition. The device has an 8 nm-thick high- $\kappa$  ( $\epsilon_r = 22$ ) gate oxide. Different colors represent devices with emitter layers of different carrier mobilities. Electron and hole mobilities are equal in all cases. (b) Turn-on voltages corresponding to the curves in (a) where the emitter has a band gap of 2 eV.

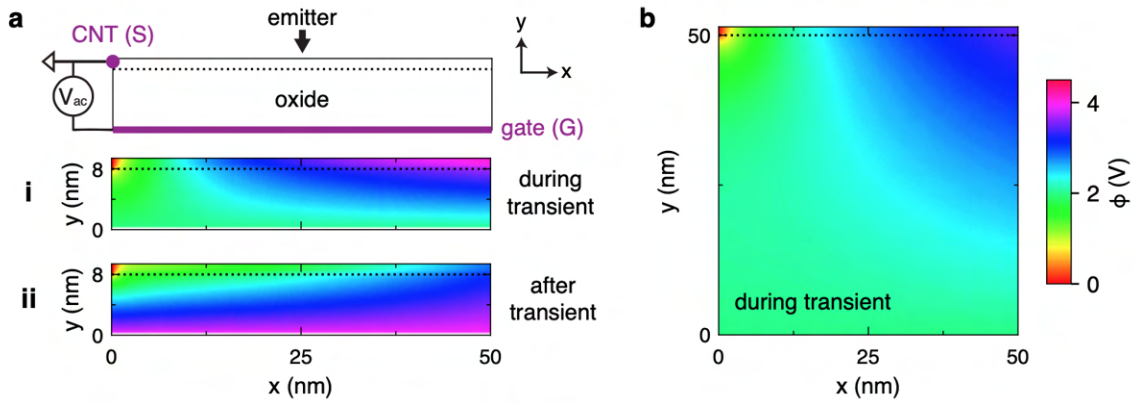


Figure 3.5: (a) Schematic of the simulated device with a grounded CNT source contact on the top left at  $x = 0$  and a gate electrode on the bottom at  $y = 0$ . The 2D electric potential distributions near the source contact during and after a square wave voltage transition are shown in panels (i) and (ii), respectively. The simulated device has an 8 nm-thick high- $\kappa$  gate dielectric (EOT  $\approx 1.4$  nm). (b) 2D electric potential distribution during a square wave voltage transition for a device with a 50 nm-thick  $\text{SiO}_2$  gate dielectric. The applied gate voltage is  $\pm 4$  V and the emitter layer mobility is  $\mu = 1 \times 10^{-3} \text{ cm}^2 \text{ V}^{-1} \text{ s}^{-1}$ .

the source contact and energy levels of the emissive material. As a result, the conventional requirement for ohmic contacts [59] or low injection barriers can be overcome.

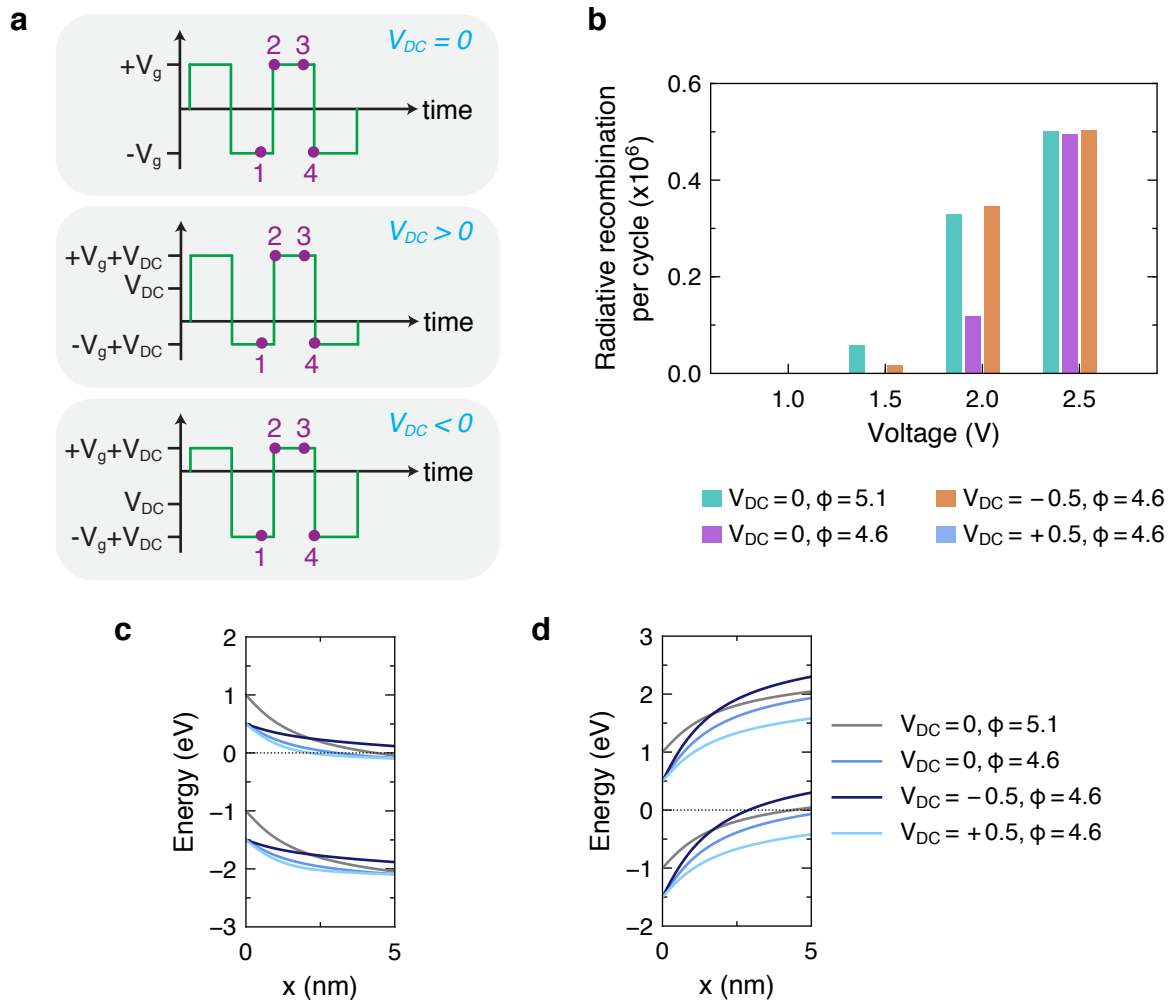


Figure 3.6: (a) Schematic of a square wave gate voltage waveform with no DC offset (default), positive DC offset, and negative DC offset. Adding DC gate voltage bias does not increase steady-state current loss through the structure due to the capacitive nature of the device. (b) Total radiative recombination per square wave cycle for a device with mid-gap source contacts (teal), n-type contacts (purple), n-type contacts with a negative DC bias (purple), and n-type contacts with a positive DC bias (blue). The emitter layer electron affinity is 4.1 eV and the band gap is 6.1 eV. Contact work function only makes a difference when the voltage is low, near the turn-on regime. Energy band diagrams displaying the conduction (upper set of lines) and valence (lower set of lines) bands relative to the contact energy level (here at 0 eV) are shown for timepoints **3** in (c) and **4** in (d). Refer to Fig. 1 in the main text for the timepoint labels.

### 3.4 Compatibility with low mobility materials

Once charge injection into the emissive material has been achieved, charge carriers move through the emitter layer and a fraction eventually undergo radiative recombination to emit photons. Although large strides have been made towards improving the mobilities of molecular emissive materials such as those used in organic LEDs (OLEDs), these materials largely possess limited carrier mobilities ( $< 1 \text{ cm}^2 \text{ V}^{-1} \text{ s}^{-1}$ ) that are orders below those of common inorganic semiconductors [52, 60, 61]. It is even more difficult to design molecular systems with both high carrier mobility and efficient solid state emission for optoelectronic applications, particularly in the case of solution-processable emitters [62–64]. In light of these constraints, it is useful to study the necessity of maintaining high carrier mobility in electroluminescent devices. Unlike traditional vertically-stacked LED architectures, our AC electroluminescent device relies on lateral transport from single carrier injection contacts which inject both electrons and holes. As carrier mobility in the emissive layer decreases, the total amount of radiative recombination between an individual pair of CNT contacts increases (Figure 3.7c). For very low carrier mobilities, the amount of EL saturates or slightly diminishes depending on the spacing between the contacts. The recombination efficiency increases concomitantly with decreasing carrier mobility until a saturation value of around 90% (Figure 3.7d). The recombination efficiency is calculated as the ratio of radiative recombination events to the number of injected electron-hole pairs; 100% recombination efficiency occurs when all electron-hole pairs produce a photon. Although we assume that emissive material has unity quantum yield in the simulation (i.e. there are no nonradiative recombination pathways), the time-alternating injection of electrons and holes and finite slew rate do not guarantee that all injected charge carriers undergo recombination with opposite charge carriers, and some of the carriers will instead return to the electrode during voltage transients.

The influence of charge transport can be explained by examining the calculated band diagrams. When carrier mobility is low, charge carriers are unable to transport far into the emissive material and accumulate near the source contact, causing the electric potential to vary dramatically near the contact (Figure 3.7a). Quasi-Fermi level splitting only occurs near the contact, in accordance with the lack of injected charge carriers far from the contact. When the mobility is high, quasi-Fermi level splitting extends along the entire lateral length of the emitter layer as carriers populate the entire volume of the emissive material. At the gate voltage transition, the potential gradient is distributed gradually along the entire length of the emitter (Figures 3.8a-b). Radiative recombination, which requires the simultaneous presence of both electrons and holes, is localized entirely near the source contact when the mobility is low (Figure 3.7b), as confirmed by the fact that changes in steady-state carrier concentrations are only observed near the contact (Figures 3.8c-d). The length of the emission region scales roughly with  $\sqrt{\mu}$ , in that 10-fold increases in carrier mobility lead to approximately 3-fold increases in emission length, consistent with the scaling of diffusion length in semiconductors. In low mobility materials, emission is limited to near the source contact in both the lateral and vertical directions, as shown by simulated 2D emission profiles

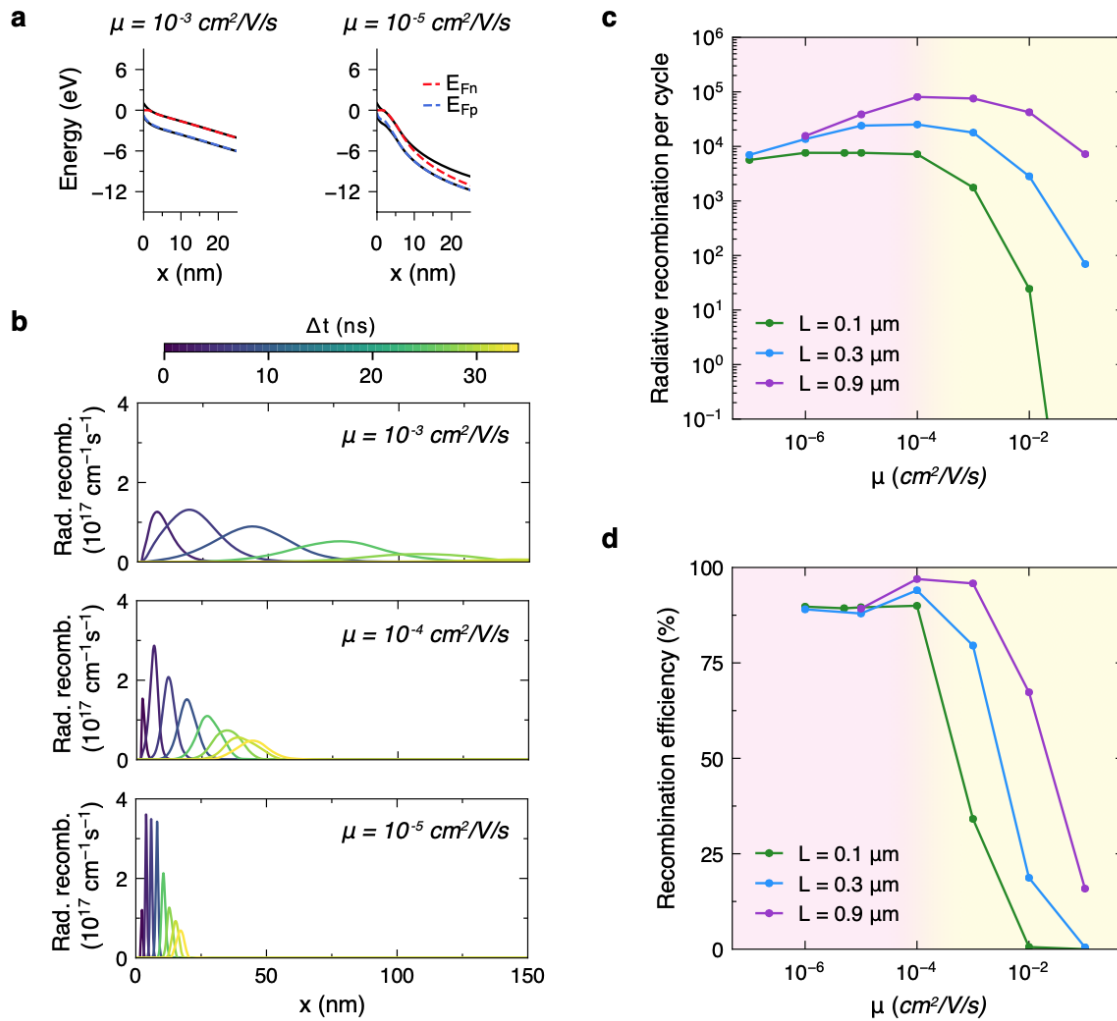


Figure 3.7: (a) Energy band diagrams at a source contact for devices with an emitter layer carrier mobility of  $1 \times 10^{-3} \text{ cm}^2 \text{ V}^{-1} \text{ s}^{-1}$  (left) or  $1 \times 10^{-5} \text{ cm}^2 \text{ V}^{-1} \text{ s}^{-1}$  (right). (b) Radiative recombination profiles over space (in the lateral direction along the length of the emitter layer) at different timepoints  $\Delta t$  after the start of a voltage transition. (c) Total radiative recombination and (d) recombination efficiency per cycle as a function of carrier mobility in the emitter layer for devices with different average CNT-CNT spacings  $L$ . Shorter  $L$  corresponds to denser CNT networks. Simulations were performed for devices with a 50 nm  $\text{SiO}_2$  gate dielectric and  $\pm 12 \text{ V}$  square wave gate voltage.

for devices with thick emitter layers (Figure 3.9). These results resemble those of OLEDs, in which the recombination zone is closer to the contact injecting the lower mobility carrier [59, 65]. As the distance between CNT contacts increases, the EL intensity and recombination efficiency increase because longer emission lengths can be accommodated. Therefore, carrier mobility and CNT network density should be simultaneously optimized to yield transport lengths similar to the spacing of the CNT network. EL tends to increase then saturate as the thickness of the emitter layer increases, suggesting that precise control of the emitter layer thickness is not essential for bright EL. At the same time, EL can be obtained from arbitrarily thin materials contacting the CNT network, including those with nonuniform morphologies. This behavior contrasts that of conventional OLEDs, which show increased turn-on voltages and decreased luminance as the thickness of the emissive layer increases due to poor charge transport properties of molecular emitting materials [66]. Furthermore, the emissive materials in OLEDs must be able to form smooth and pinhole-free thin films on the order of up to tens of nanometers [52].

The effect of emitter material mobility is illustrated in Figure 3.10 for thin gate oxide devices where  $\pm 4$  V square wave gate voltages are applied with a transient slew time of 20 ns. For  $\mu = 1 \times 10^{-1} \text{ cm}^2 \text{ V}^{-1} \text{ s}^{-1}$ , the switch in applied gate voltage from  $-4$  V (at  $\Delta t = 0$  ns, where  $\Delta t$  denotes the time since the start of the voltage transition) to  $4$  V (at  $\Delta t = 20$  ns) occurs nearly instantaneously across the oxide, with the electrostatic potential at the end of the voltage transition ( $\Delta t = 20$  ns) varying linearly across the bulk of the oxide as expected for a capacitor under steady-state DC voltage. At  $\Delta t = 12$  ns (the moment at which 60% of the voltage transition has elapsed), the gate contact voltage is  $0.8$  V and the potential near the contact is nearly uniformly equilibrated at this value. When the carrier mobility is reduced to  $1 \times 10^{-3} \text{ cm}^2 \text{ V}^{-1} \text{ s}^{-1}$ , the steady-state electrostatic potential profile is observed somewhat later at  $\Delta t = 100$  ns after the start of the voltage transition. As the carrier mobility is reduced even further to  $1 \times 10^{-5} \text{ cm}^2 \text{ V}^{-1} \text{ s}^{-1}$ , the potential distribution has not reached the steady-state condition by  $\Delta t = 100$  ns as large lateral potential drops have not yet subsided. Immediately after the voltage transition, dramatic lateral voltage drops are observed in the vicinity of the contact due to the low conductivity or large resistance of the emissive material in series with the oxide. Similar results are obtained for devices with thicker gate oxide (Figure 3.11). To summarize, the temporal dynamics show that higher peak EL is in fact obtained in materials with lower carrier mobility due to spatial localization of the charge carriers and inability of the electric potential to drop across the oxide rapidly.

Surprisingly, a square wave gate voltage waveform with fast slew rate is not necessary for bright EL when the charge carrier mobility is low. Experimentally, applying a sine wave gate voltage waveform yields similar EL levels as applying a square wave gate voltage waveform (Figure 3.12), with EL only reduced by around 50% or less. The EL per cycle typically increases with sine wave frequency, as confirmed in simulation. Through numerical simulation, we find that the difference in EL when using a sine versus square wave gate voltage is smaller when the mobility is lower. Calculated energy band diagrams indicate that sufficiently steep band bending occurs at the contact following a switch in voltage polarity for either a sine wave or square wave, with quasi-Fermi level splitting about equal

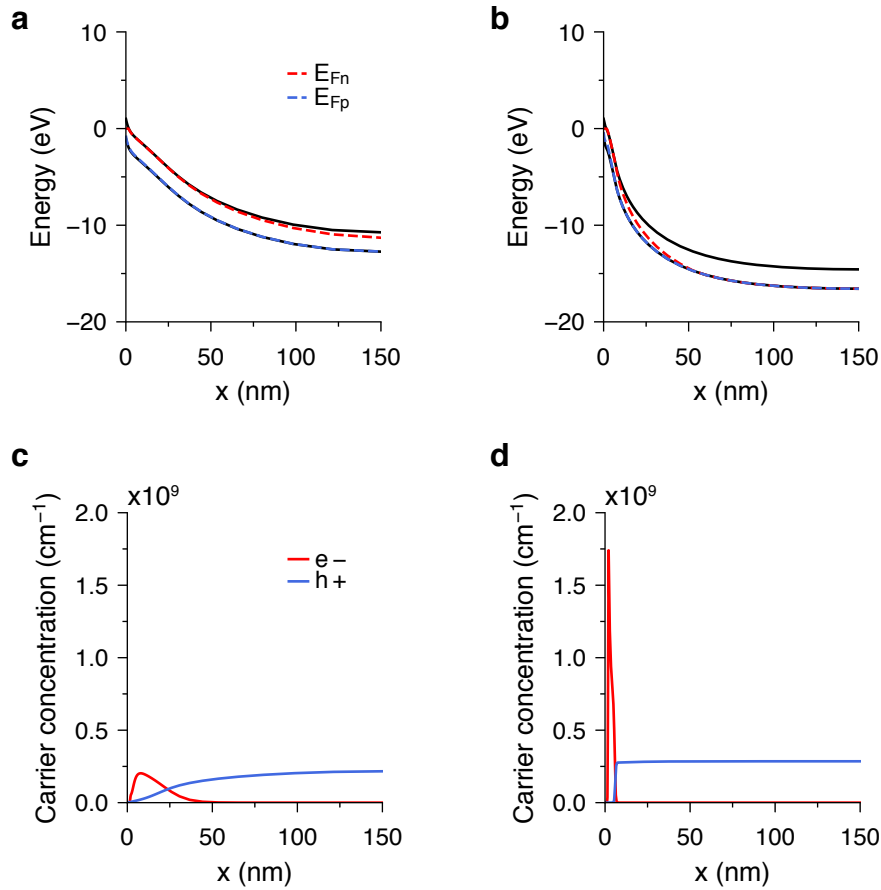


Figure 3.8: Energy band diagrams from the edge of a source contact (at  $x = 0$ ) for a device with an emitter layer possessing a carrier mobility of (a)  $1 \times 10^{-3} \text{ cm}^2 \text{ V}^{-1} \text{ s}^{-1}$  or (b)  $1 \times 10^{-5} \text{ cm}^2 \text{ V}^{-1} \text{ s}^{-1}$ , corresponding to the data in Fig. 4a in the main text. The dashed red and blue lines denote the quasi-Fermi level for electrons and holes, respectively. Carrier concentration per unit length along the lateral direction of the emitter layer for a device with an emitter layer possessing a carrier mobility of (c)  $1 \times 10^{-3} \text{ cm}^2 \text{ V}^{-1} \text{ s}^{-1}$  or (d)  $1 \times 10^{-5} \text{ cm}^2 \text{ V}^{-1} \text{ s}^{-1}$ . Carrier action only occurs very close to the contact in the latter case. The red and blue lines denote the concentration of electrons and holes, respectively. The total emitter layer length in the lateral direction is 300 nm; by symmetry, the plots at the opposite source contact are identical. The gate oxide is 50 nm  $\text{SiO}_2$  and the applied gate voltage is  $\pm 12 \text{ V}$ .

to the band gap in both cases. The overall lateral voltage drop across the emitter is greater when a square wave is applied, but carrier injection is located near the contact in either case as indicated by the lack of quasi-Fermi level splitting in the middle of the domain. The exact

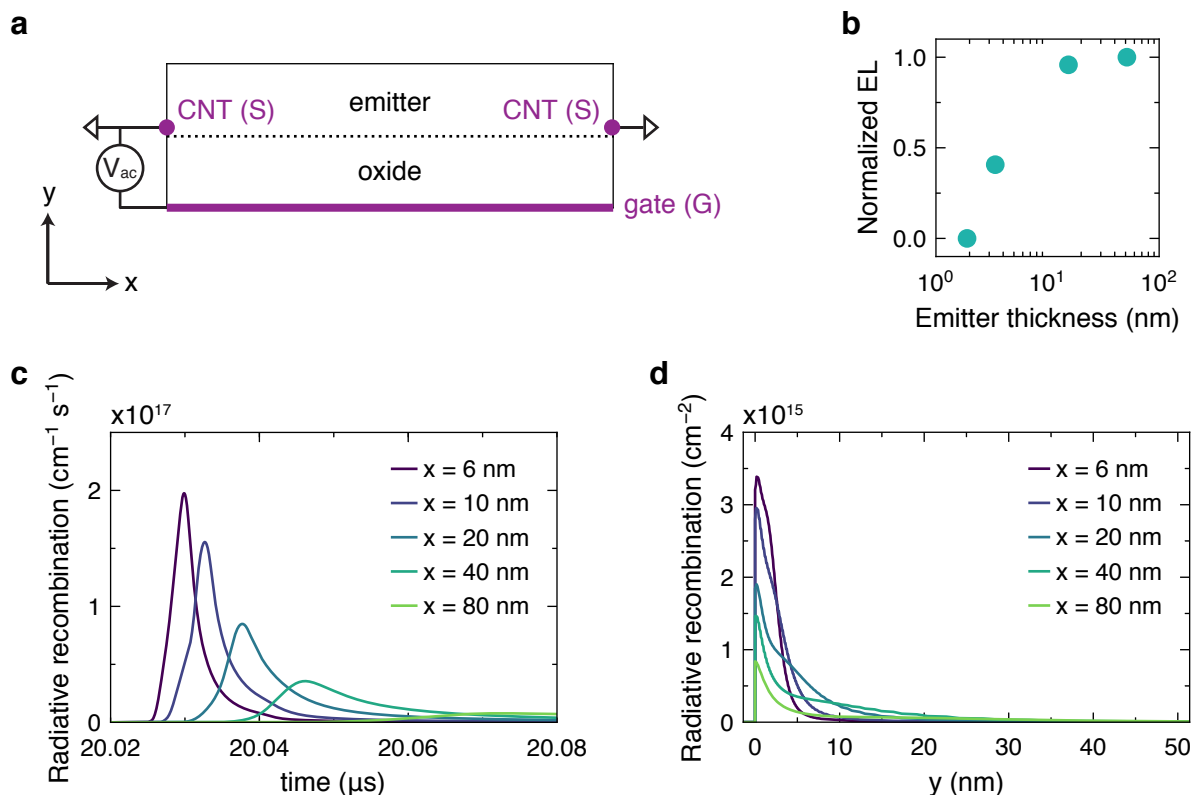


Figure 3.9: (a) Schematic of an AC electroluminescent device with a thick emitter layer. (b) Total radiative recombination (normalized) as a function of emitter thickness for a device with 50 nm  $\text{SiO}_2$  gate oxide. (c) Radiative recombination as a function of time integrated at different  $x$ -positions (i.e. integrated over different vertical slices ranging from near the contact (purple) to near the center of the emitter layer (green)). As time progresses, emission propagates along the length of the emitter (in the  $x$ -direction) and becomes weaker. (d) Radiative recombination profiles as a function of height in the vertical direction at different distances along the emitter layer. The emission is weaker moving from near the source contact (purple) to farther from the contact (green). In all cases, emission is largely localized within 10 nm of the surface (i.e. the emitter/oxide interface). The CNT-CNT spacing in the  $x$ -direction is 300 nm, the applied gate voltage is  $\pm 12$  V, and the emitter layer has carrier mobility  $1 \times 10^{-4} \text{ cm}^2 \text{ V}^{-1} \text{ s}^{-1}$ .

relationship between frequency (for a sine wave) or slew rate (for a square wave) scaling and emission intensity would depend on the radiative recombination rate in practice.

Until now, the presented results have assumed equal mobilities for electrons and holes. It has been shown that balance of charge carrier mobilities improves OLED brightness and efficiency by reducing the fraction of one carrier type that travels across the device without



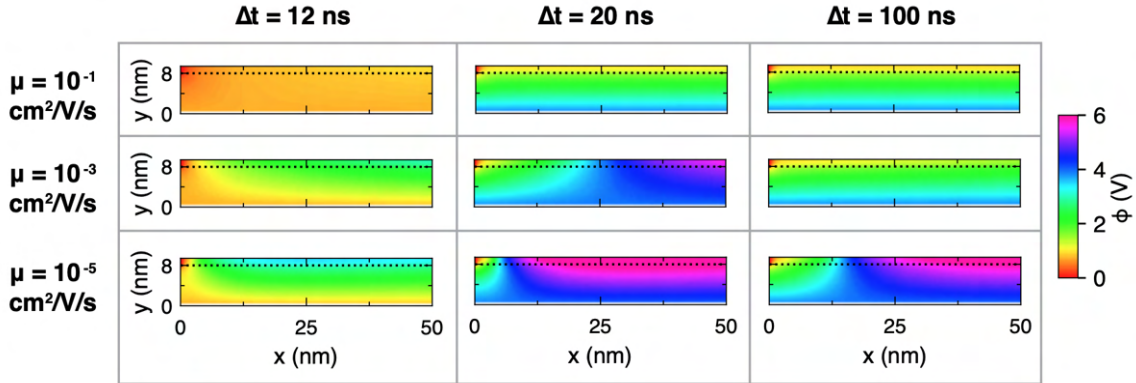


Figure 3.10: 2D maps of the electrostatic potential for devices with an 8 nm-thick high- $\kappa$  gate dielectric (EOT  $\approx$  1.4 nm). Simulations were performed with a  $\pm 4$  V square wave gate voltage and the plots represent behavior from the upward voltage transition ( $-4$  V to  $4$  V). For each emitter layer mobility case (shown in separate rows), the potential map is plotted for different times  $\Delta t$  (shown in separate columns) after the start of the voltage transition at  $t = 0$ . The rise time of the voltage transition is 20 ns. From left to right, the columns correspond to the potential during the gate voltage transition, at the end of the gate voltage transition, and 80 ns after the end of the gate voltage transition. The black dotted line represents the interface between the gate oxide and the emitter layer as shown in Figure 3.5.

recombining [65]. Due to the alternating injection of carriers in the AC EL scheme, recombination efficiency is dominated by the lower mobility carrier, in that high efficiency can be achieved as long as one of the carriers has sufficiently low mobility (Figure 3.13). If the hole mobility is greater than the electron mobility, then holes exit the emitter layer much faster than electrons are able to enter the emitter layer at the downward voltage transition, leading to negligible EL. However, at the upward transition, holes are able to populate the bulk of the emitter layer much faster while electrons exit slowly, giving rise to substantial EL comparable to the case of equal and low carrier mobility (Figure 3.14). Asymmetric EL at voltage transitions therefore results not only from non-ambipolar contacts [12] but also from asymmetric charge transport. Even when the charge carrier mobilities are imbalanced, EL can still be obtained due to the use of a single contact to inject both carriers near the contact.

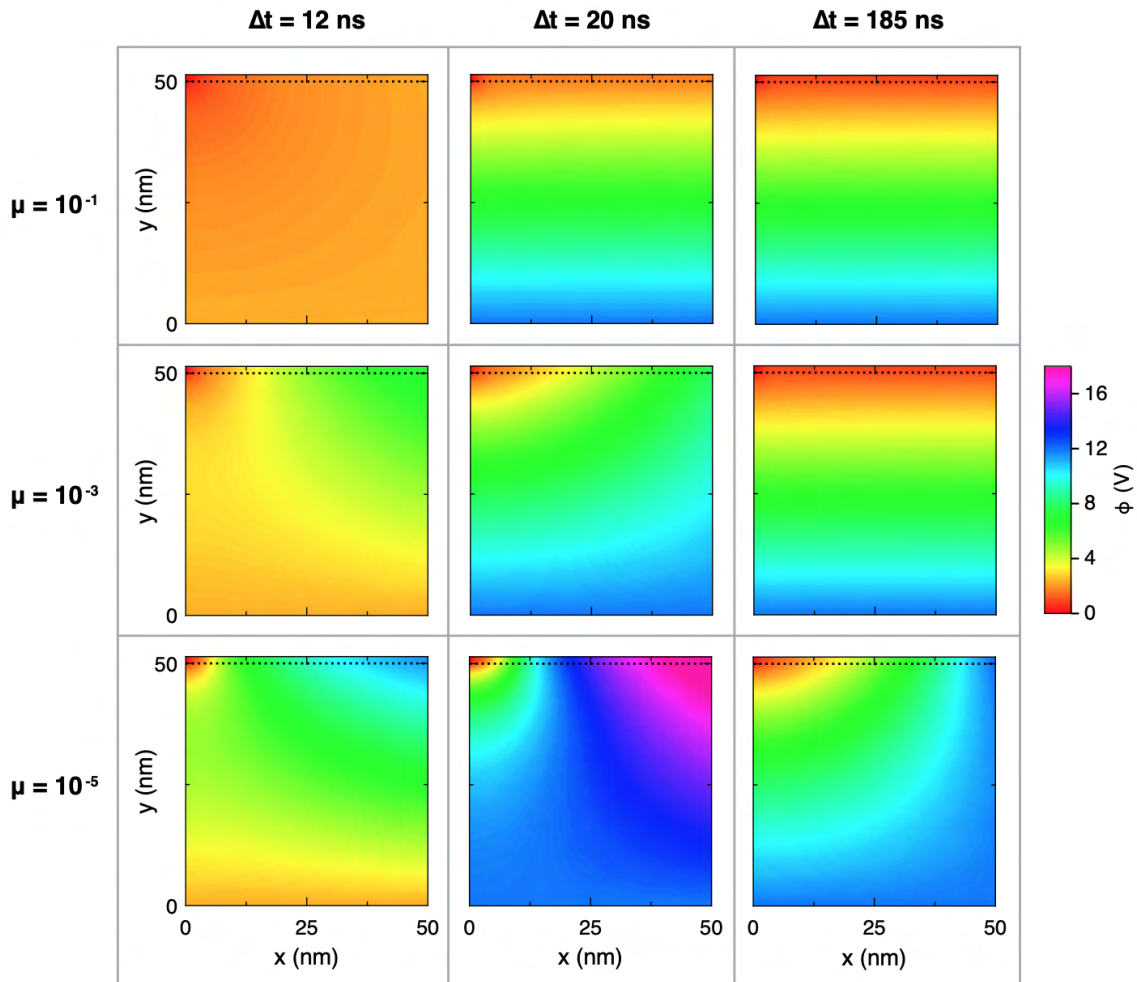


Figure 3.11: 2D maps of the electrostatic potential corresponding to Fig. 5 in the main text for devices with 50 nm SiO<sub>2</sub> as the gate oxide and a  $\pm 12 \text{ V}$  applied square wave gate voltage. For each carrier mobility case (shown in separate rows), the potential map is shown for different times  $\Delta t$  (in each column) after the start of the voltage transition at  $t = 0$ . The rise time of the voltage transition is 20 ns. The CNT-CNT spacing is 300 nm.

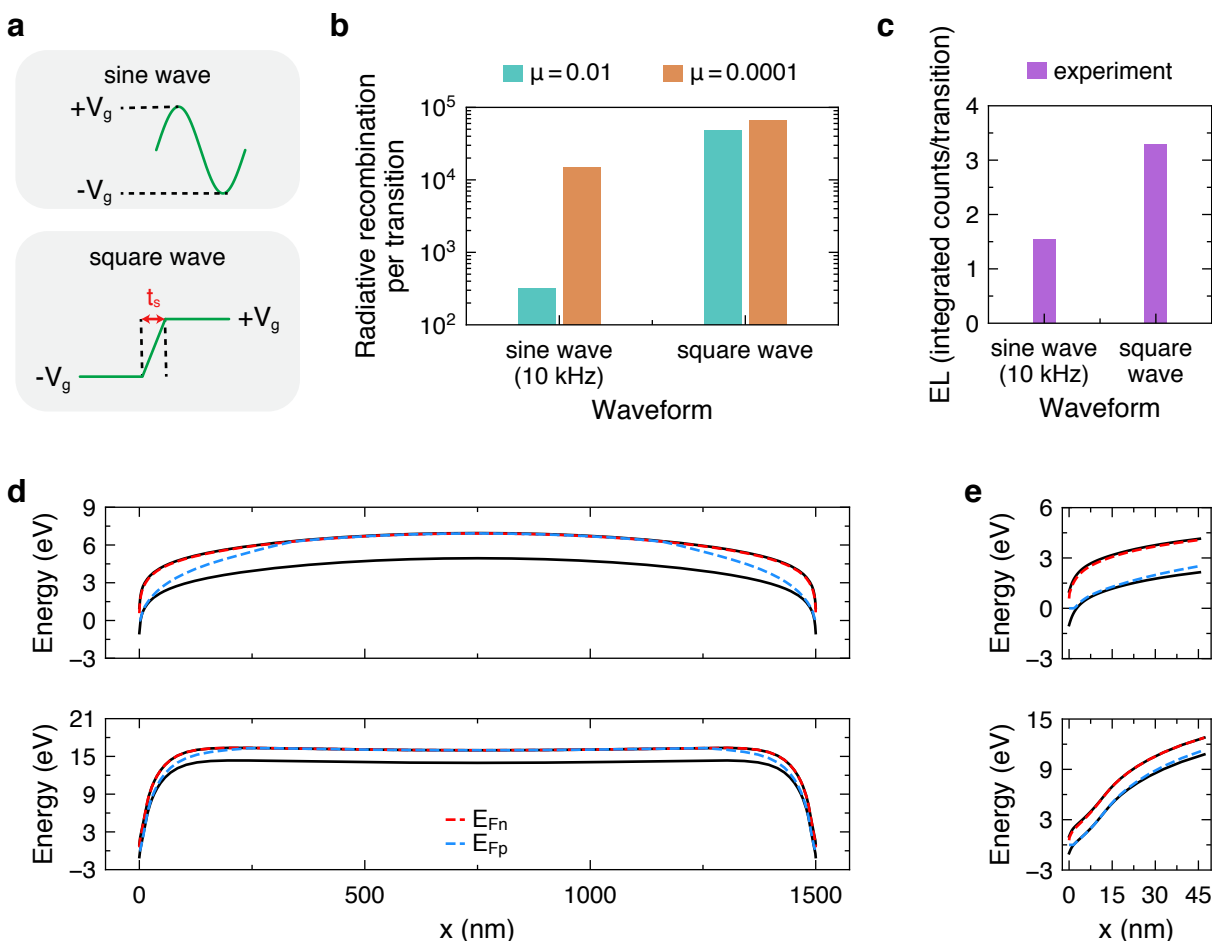


Figure 3.12: (a) Schematic of sine wave (top) and square wave (bottom) gate voltage waveforms where  $t_s$  is the slew time (here, the rise time) for a voltage transition from  $-V_g$  to  $+V_g$ . (b) Total radiative recombination per sine or square wave transition (half of a period) for devices with 50 nm  $\text{SiO}_2$  gate oxide and emitter layers with different carrier mobilities. The gate voltage magnitude is  $\pm 12$  V. Low emitter layer mobility is more important for maintaining bright EL when the gate voltage waveform has low frequency. (c) Experimental measurement of EL intensity when applying a 10 kHz sine versus square wave. Data were measured using a device with 50 nm  $\text{SiO}_2$  gate oxide and 9,10-diphenylanthracene (DPA) emitter layer. (d) Energy band diagrams between the two source contacts for the device simulations in (b) where a sine wave (top diagram) or square wave (bottom diagram) was applied. The emitter layer carrier mobility is  $\mu = 1 \times 10^{-4} \text{ cm}^2 \text{ V}^{-1} \text{ s}^{-1}$ . (e) Energy band diagrams showing band bending near the source contact in (d) in the case of a sine wave (top diagram) or square wave (bottom diagram) gate voltage.

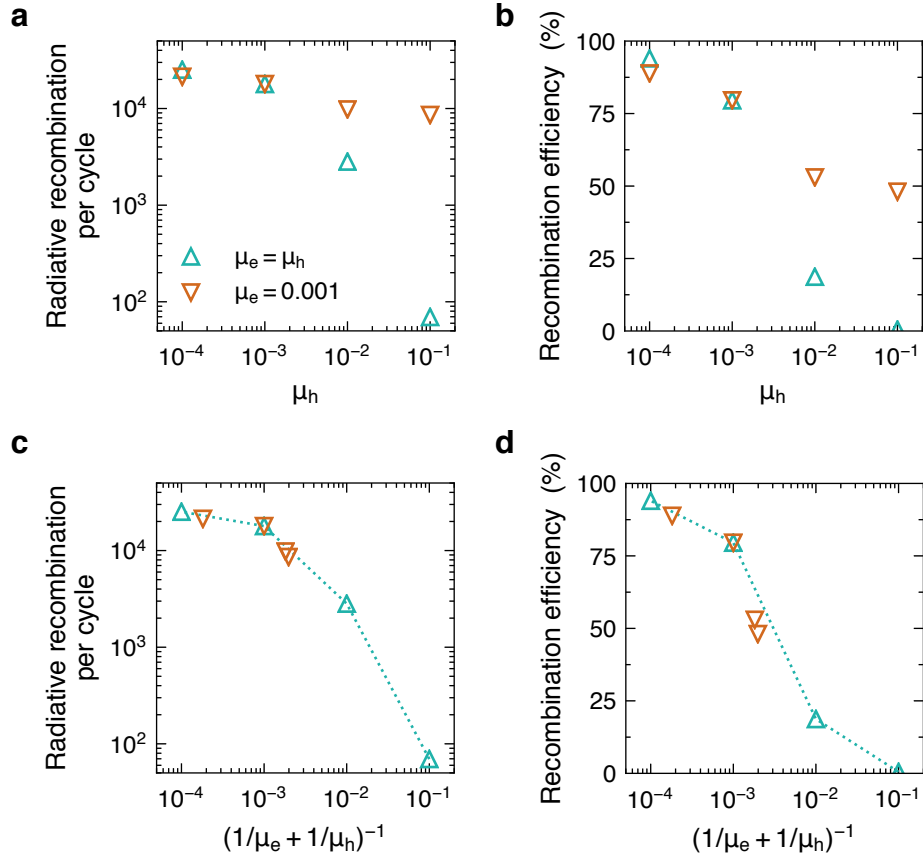


Figure 3.13: (a) Total radiative recombination per square wave cycle for devices with emitter layers of varying hole mobility. The electron mobility is either kept equal to the hole mobility (upward teal triangles) or at a constant value of  $0.001 \text{ cm}^2 \text{ V}^{-1} \text{ s}^{-1}$  (downward brown triangles). The brightness is similar when  $\mu_h$  is low ( $10^{-4}$  or  $10^{-3}$ ) but diverges when  $\mu_h$  is high ( $10^{-2}$  or  $10^{-1}$ ). When  $\mu_h$  is high, the EL has the potential to be bright if the other carrier (electrons) has lower mobility. (b) Recombination efficiency as a function of hole mobility corresponding to the data in (a), showing a similar behavior between the two cases. (c) Total radiative recombination per square wave cycle as a function of an “effective” mobility  $1/\mu_{eff} = 1/\mu_e + 1/\mu_h$ , showing correspondence between the two curves in (a). (d) Recombination efficiency corresponding to the data in (c). The CNT-CNT spacing is 300 nm, the gate oxide is 50 nm SiO<sub>2</sub>, and the applied gate voltage is  $\pm 12$  V.

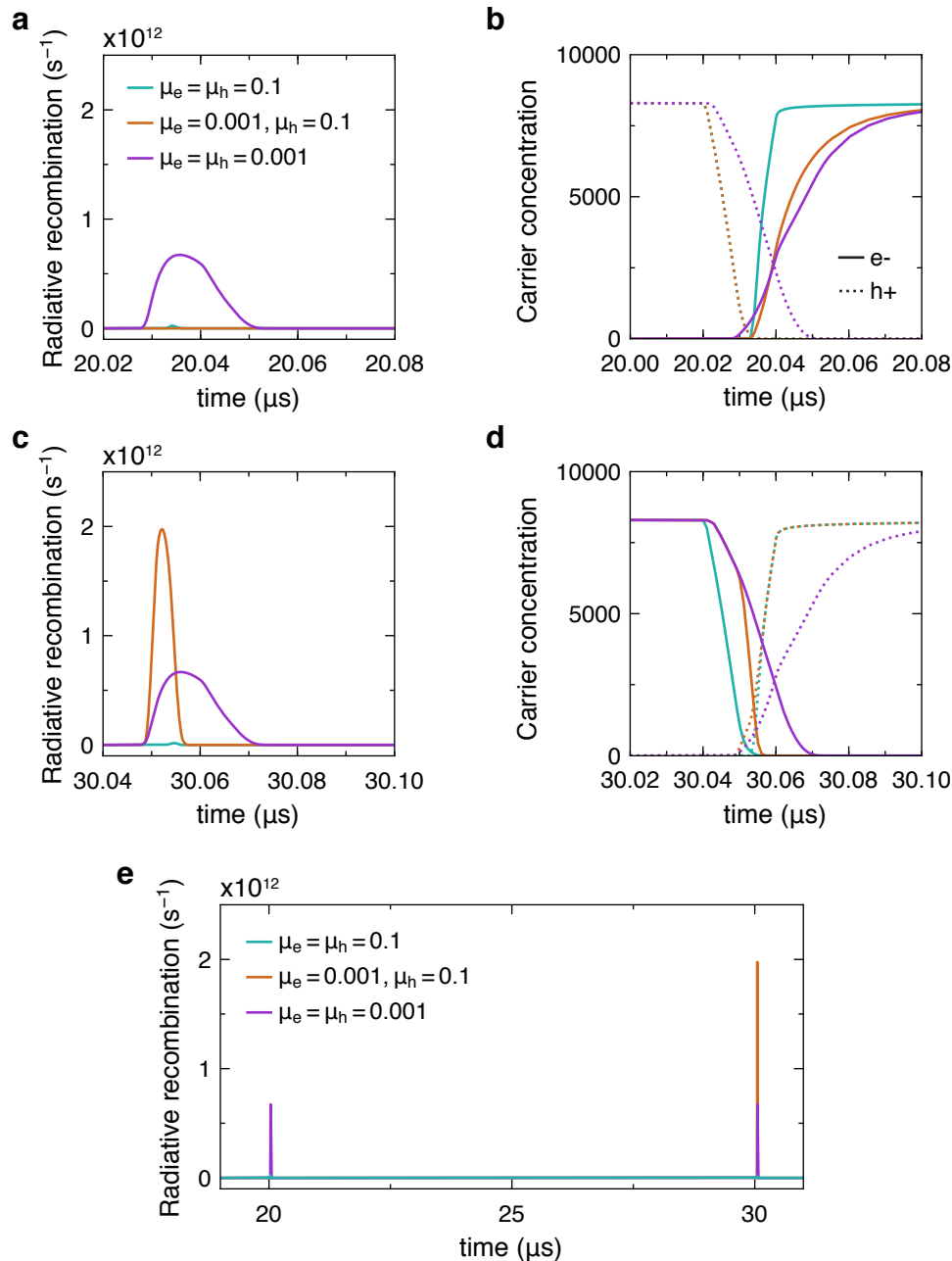


Figure 3.14: Detailed data for Fig. 3.13. Total (a) radiative recombination and (b) number of carriers versus time when the emitter layer has (a) equal electron and hole mobilities of  $0.1 \text{ cm}^2 \text{ V}^{-1} \text{ s}^{-1}$ , (b) lower electron than hole mobility, or (c) equal electron and hole mobilities of  $0.001 \text{ cm}^2 \text{ V}^{-1} \text{ s}^{-1}$ . The gate voltage undergoes a 20 ns-long upward transition from  $-12 \text{ V}$  to  $12 \text{ V}$  beginning at  $20.02 \mu\text{s}$ . Solid and dotted lines in (b) represent electron and hole numbers. The equivalent data are shown in (c), (d) for a downward gate voltage transition from  $12 \text{ V}$  to  $-12 \text{ V}$  which begins at  $30.04 \mu\text{s}$ . (e) Radiative recombination over a longer time period where the upward transition occurs around  $20 \mu\text{s}$  (as shown in a,b) and the downward transition occurs around  $30 \mu\text{s}$  (as shown in c,d). EL intensity is similar at both transitions when carrier mobilities are equal, but stronger at the downward voltage transition when the hole mobility is higher.

### 3.5 Efficiency characterization

Aside from turn-on voltage and brightness, other important figures of merit for light-emitting devices include quantum and power efficiency. The internal quantum efficiency (IQE) of a light-emitting device is given by  $\eta_{int}=\phi\gamma$  and the external quantum efficiency (EQE) is given by  $\eta_{ext}=\eta_{int} \eta_{coupling}$ , where  $\phi$  relates to the intrinsic photoluminescence efficiency of the emissive material,  $\gamma$  is the recombination efficiency (fraction of injected charge carriers that recombine in the emissive layer; Figure 3.16), and  $\eta_{coupling}$  is the outcoupling efficiency (fraction of photons that are able to escape the device) [67]. For organic excitonic materials with singlet emission, the intrinsic efficiency of the emissive material also takes into consideration  $r_{st}$ , the ratio of singlet to triplet excitons. To evaluate the fundamental efficiency of an alternating current-based carrier injection scheme, we focus on the efficiency of carrier injection leading to radiative recombination ( $\gamma$ ), which is the term that depends on the mechanism of device operation. According to simulation, the recombination efficiency tends to increase with gate voltage near the turn-on voltage of the device, but slowly decreases thereafter (Figure 3.15a). The recombination efficiencies for devices with different oxide thicknesses are similar, with the thicker oxide device only being slightly less efficient. Peak recombination efficiency is achieved when the band bending is just steep enough to allow for efficient carrier tunneling and subsequent injection. Beyond this point, higher gate voltages increase the rate at which the steady-state carriers are swept out of the emissive material, decreasing the fraction of injected carriers that are able to recombine with opposite charge carriers exiting the emissive material.

Experimentally, we observe a similar trend for a high- $\kappa$  gate oxide device with  $\text{Ru}(\text{bpy})_3(\text{PF}_6)_2$  in which the IQE increases with voltage up to a certain point before decreasing (Figure 3.15a, inset). For simplicity, we performed the simulations assuming 100% quantum yield in the emitter layer; however, the experimentally measured materials have non-unity quantum yield [68, 69]. Hence, the experimentally extracted internal quantum efficiencies, which are a product of  $\phi$  and  $\gamma$ , do not reach the same levels as the calculated efficiencies and in this case are around one-fifth lower than the simulated performance limit. This value is consistent with analogous photoluminescence quantum yield measurements of the emitter layer on the device substrate. In addition, the peak experimental quantum efficiencies are achieved at almost double the gate voltage calculated from simulation, which may be due to parasitic device resistances which reduce the voltage applied to the emitter as well as nonradiative recombination mechanisms which dampen the EL intensity at low carrier concentrations. Strikingly, the total amount of radiative recombination and net recombination efficiency does not depend on the contact work function or Schottky barrier height after the turn-on regime has been surpassed (Figure 3.17), although unbalanced charge injection has been found detrimental to the performance of quantum dot LEDs [43] and OLEDs [70]. While devices simulated with p- and n-type contacts (0.1 eV Schottky barrier height in each case) show similar overall results as a device simulated with ambipolar contacts, EL at the upward voltage transition is higher with an n-type contact than with a p-type contact due to more facile electron injection, and vice versa at the downward transition.

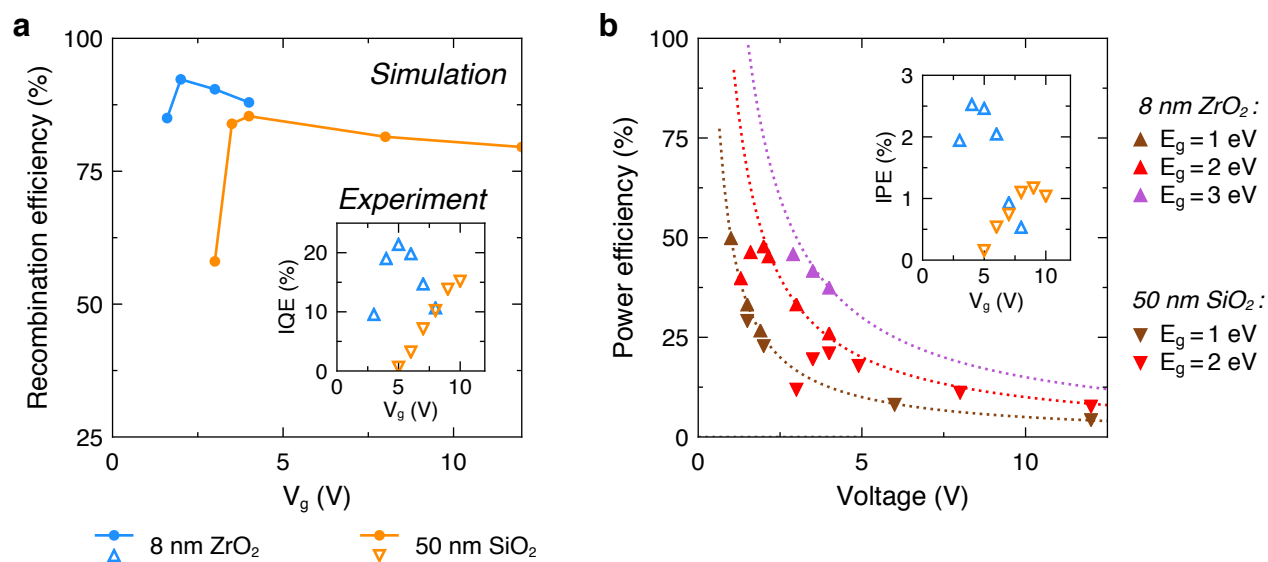


Figure 3.15: (a) Gate voltage dependence of recombination efficiency from simulation (solid lines). Blue and orange data represent devices with 8 nm high- $\kappa$  gate dielectric or 50 nm  $SiO_2$  gate dielectric, respectively. Experimentally measured internal quantum efficiencies (IQE), which normalize for differences in light outcoupling, are shown in the inset (open markers). (b) Gate voltage dependence of power efficiency from simulation for devices with different gate dielectric (upward triangles: 8 nm  $ZrO_2$ , downward triangles: 50 nm  $SiO_2$ ) and emitter layer band gap  $E_g$ . Dotted lines are guides to the eye and represent an inverse voltage relationship of the form  $E_g/V_g$  with a constant scaling factor. Experimentally measured internal power efficiencies (IPE) are displayed in the inset (colors same as in (a)). Data were measured from devices with a drop-casted  $Ru(bpy)_3(PF_6)_2$  emitter layer ( $E_g = 2$  eV).

Similar to our findings on recombination efficiency, larger CNT-CNT distances (corresponding to sparser CNT networks) are preferable for achieving higher power efficiency, particularly in materials with higher mobility (Figure 3.18). Here power efficiency is defined as the time-averaged output light power (assuming photons are emitted with an energy equal to the band gap) divided by the input electrical power, which is calculated by integrating the product of the time-dependent current and voltage over a full AC cycle. Power efficiency approximately depends on the quantum efficiency and the factor  $(h\nu)/(qV)$  where  $h\nu$  is the photon energy and  $qV$  is the energy of the injected carriers based on the effective applied voltage. Assuming the CNT-CNT spacing is long enough for the quantum efficiency to saturate, the power efficiency tends to increase with the band gap of the emissive material due to the higher energy of photons produced (Figure 3.15b). However, the turn-on voltage is also higher for larger band gap materials, resulting in similar power efficiencies at the voltages required for similar emission intensities. Beyond the turn-on voltage, the maximum power efficiency decreases approximately inversely with applied gate voltage. The peak power efficiency for a thicker oxide device is lower than that of a thinner oxide device and occurs at a larger gate voltage due to the higher turn-on and operating voltages. Although the internal recombination efficiency can approach unity, the power efficiency lags the quantum efficiency in both simulation and experiment because each carrier type contributes to the electrical current when it enters and exits the material. Resistive losses in the large-area CNT network, which are neglected in the model, impose further reductions in power efficiency in the fabricated device.

## 3.6 Modulation speed

Lastly, we investigated the temporal response of the device, which determines the maximum frequency or speed at which the gate voltage can be modulated while retaining linear frequency response. Even when external parasitic capacitances in the measured device are minimized, the lifetime of electroluminescence can still be limited by device characteristics such as carrier mobility. From the transient carrier density and EL profiles in Figures 3.19a-b simulated using a square wave gate voltage, we observe that the number of holes in the emitter layer decreases and the number of electrons increases as the gate voltage switches from  $-12\text{ V}$  to  $12\text{ V}$ . This behavior is consistent with the mechanism in which downward band bending enables tunneling of electrons into the emitter layer as holes are extracted out, leading EL to occur for a finite period of time following the voltage transition. EL requires electron and hole populations to overlap in both space and time; as the mobility decreases, the time required for the slow holes to exit the semiconductor increases and EL is longer-lived. The EL lifetime, calculated as the length of time in which the radiative recombination is at least 1% of its peak value, increases with decreasing carrier mobility but saturates at  $10\text{ }\mu\text{s}$  (the length of a half-period of the  $50\text{ kHz}$  applied square wave) for very low carrier mobility. Consequently, the emitter mobility should be increased if higher AC operating frequencies are desired, so that the device can reach steady-state conditions after



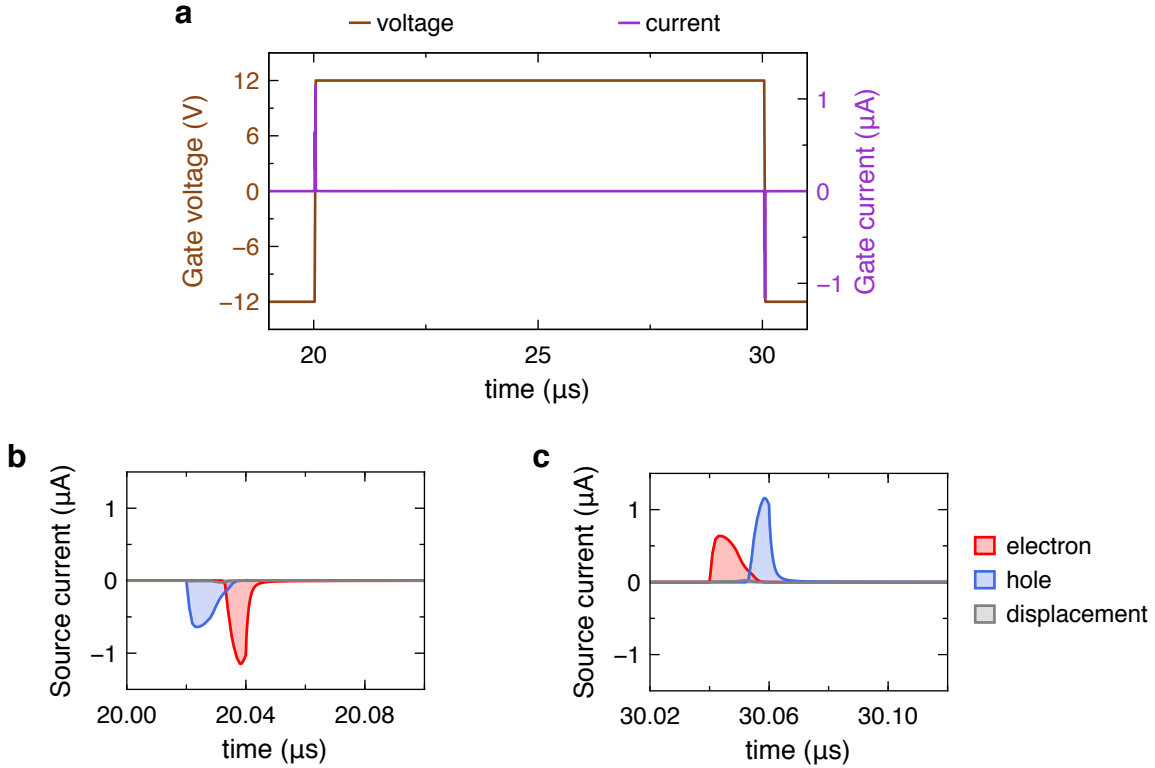


Figure 3.16: Example of gate (a) voltage  $v_g(t)$  (brown) and current  $i_g(t)$  (purple) versus time. Source current from the two CNT contacts at the (b) upward and (c) downward gate voltage transition are shown separately. Red and blue curves are the electron and hole current components. Shaded areas represent the total charge injected into or leaving from the emissive layer at the source contact. Electrons are injected at the upward transition while holes are injected at the downward transition. The displacement current (grey) is negligible. Current at the gate (which only contacts the oxide) does not involve direct carrier injection, although it has the same magnitude (opposite sign) as the total source current. (1) To calculate simulated recombination efficiency, we only consider injected carriers and assume radiative recombination events generate photons emitting at the band gap energy. The recombination efficiency is the ratio between the number of emitted photons and the number of injected electron-hole pairs. The number of emitted photons from the 2D cross-section is  $n_{ph} = \int_0^T \int_0^L \int_0^{t_{emitter}} R(x, y, t) dy dx dt$  for a square wave with period  $T$  and  $R$  being the time- and space-varying radiative recombination density. The emitted power is  $\hbar\omega n_{ph}$ . The input electrical power is  $\int_0^T v_g(t) \cdot i_g(t) dt$ . (2) To calculate experimental IQE, we estimate the number of carriers injected into the emissive layer by measuring AC current through the device with and without the emissive layer, integrating the difference over time, and dividing by  $q$ . As we cannot distinguish separate electron and hole currents, this estimate merely provides a lower bound on the efficiency (some of the estimated charge includes carriers exiting the emitter layer). We performed measurements with a 10 kHz sine wave to avoid excessive influence of external parasitics and equipment bandwidth limitations. The external quantum efficiency is converted to an internal efficiency by dividing by the light output by the light extraction efficiency: the percentage of light able to escape ( $\approx 1/4n^2$  [71]) and couple out of the structure due to optical interference from the substrate (estimated via the transfer matrix method [72, 73]), assuming an emissive layer refractive index  $n \approx 1.6$ .

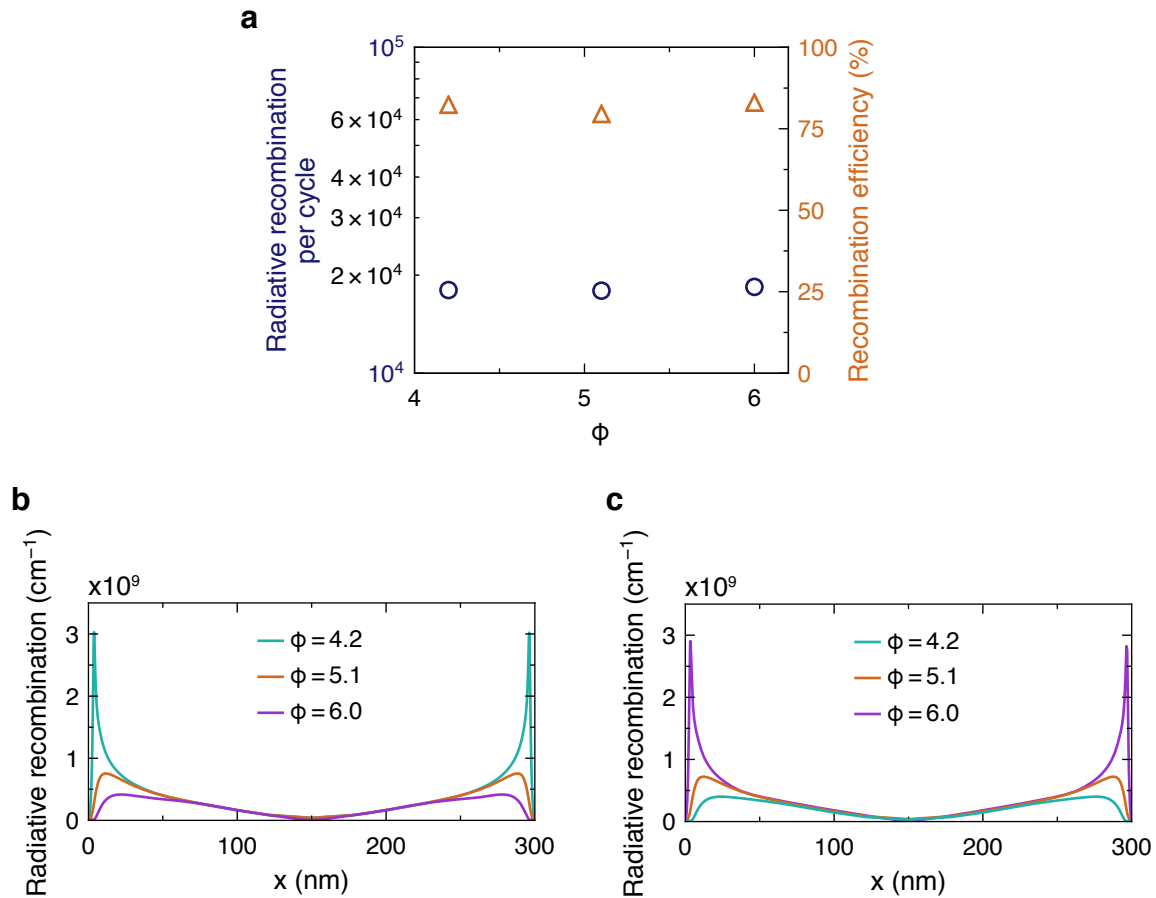


Figure 3.17: (a) Total radiative recombination per square wave gate voltage cycle (blue) and recombination efficiency (brown) as a function of source contact work function. The emitter has an electron affinity of 4.1 eV and band gap of 2 eV; changing the source contact work function is equivalent to changing the relative Schottky barrier heights for electrons and holes. From left to right, the work function values  $\phi$  correspond to n-type ( $\phi = 4.2$  eV), ambipolar ( $\phi = 5.1$  eV), and p-type ( $\phi = 6.0$  eV) contacts respectively. Radiative recombination per unit length in the lateral direction is integrated over time over the half-cycle following the (b) upward and (c) downward gate voltage transitions. When the source contact is n-type relative to the emitter (green), it is more difficult to inject holes at the downward transition, leading to lower peak EL in (c) (and vice versa for p-type contacts at the upward transition in (b)). The gate oxide is 50 nm  $\text{SiO}_2$  and the gate voltage is  $\pm 12$  V.

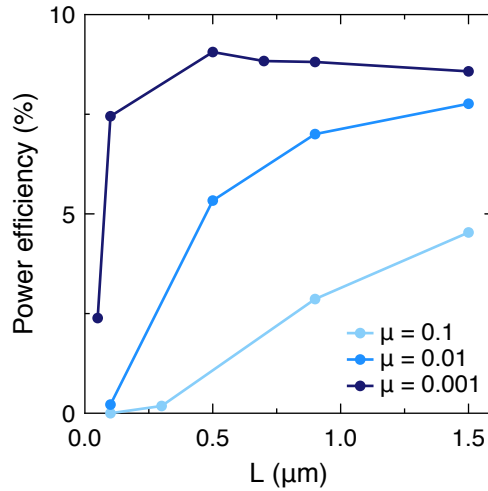


Figure 3.18: Power efficiency versus CNT-CNT spacing  $L$  for 50 nm  $\text{SiO}_2$  gate oxide devices with emitter layers of different carrier mobility. The applied gate voltage is  $\pm 12$  V.

each voltage transition. We performed device simulations using a higher frequency square wave gate voltage to confirm these trends (Figure 3.20). With a 5 MHz square wave, the radiative recombination begins to fall off at a higher carrier mobility than for a 50 kHz square wave, as indicated by the similar levels of EL at  $\mu \geq 1 \times 10^{-3} \text{ cm}^2 \text{ V}^{-1} \text{ s}^{-1}$  but lower EL at  $\mu = 1 \times 10^{-4} \text{ cm}^2 \text{ V}^{-1} \text{ s}^{-1}$ . Band diagrams of the device operated at 50 kHz show a constant concentration of electrons accumulated in the emitter layer before a downward voltage transition, with almost no holes present. Flat energy bands along the lateral direction indicate that the applied gate voltage is dropped in the vertical direction across the oxide. On the other hand, the device operated at 5 MHz continues to show large quasi-Fermi level splitting in the emitter layer, meaning that a substantial population of holes is still present. At this frequency, the 0.1  $\mu\text{s}$ -long period of constant positive gate voltage is insufficient to allow the carrier populations and electrostatics to reach equilibrium.

A simple method to probe the temporal behavior is to measure the frequency-dependent EL intensity. The increase in EL lifetime with decreasing carrier mobility relates to the higher resistance imposed by the emissive material. Hence, increasing the CNT network density, or reducing the CNT-CNT distance, should decrease the EL lifetime and increase the maximum frequency for which the EL intensity per voltage transition does not decrease. This behavior is confirmed in both simulation and experiment as shown in Figure 3.19c-d. The cut-off frequency in the experimentally measured data is around 100 kHz. This frequency corresponds to an EL lifetime of around 5  $\mu\text{s}$ , which is higher than the simulated values. This suggests that parasitic  $RC$  delays in the fabricated microscale device structure, CNT network, and measurement setup may additionally contribute to prolonged EL responses,

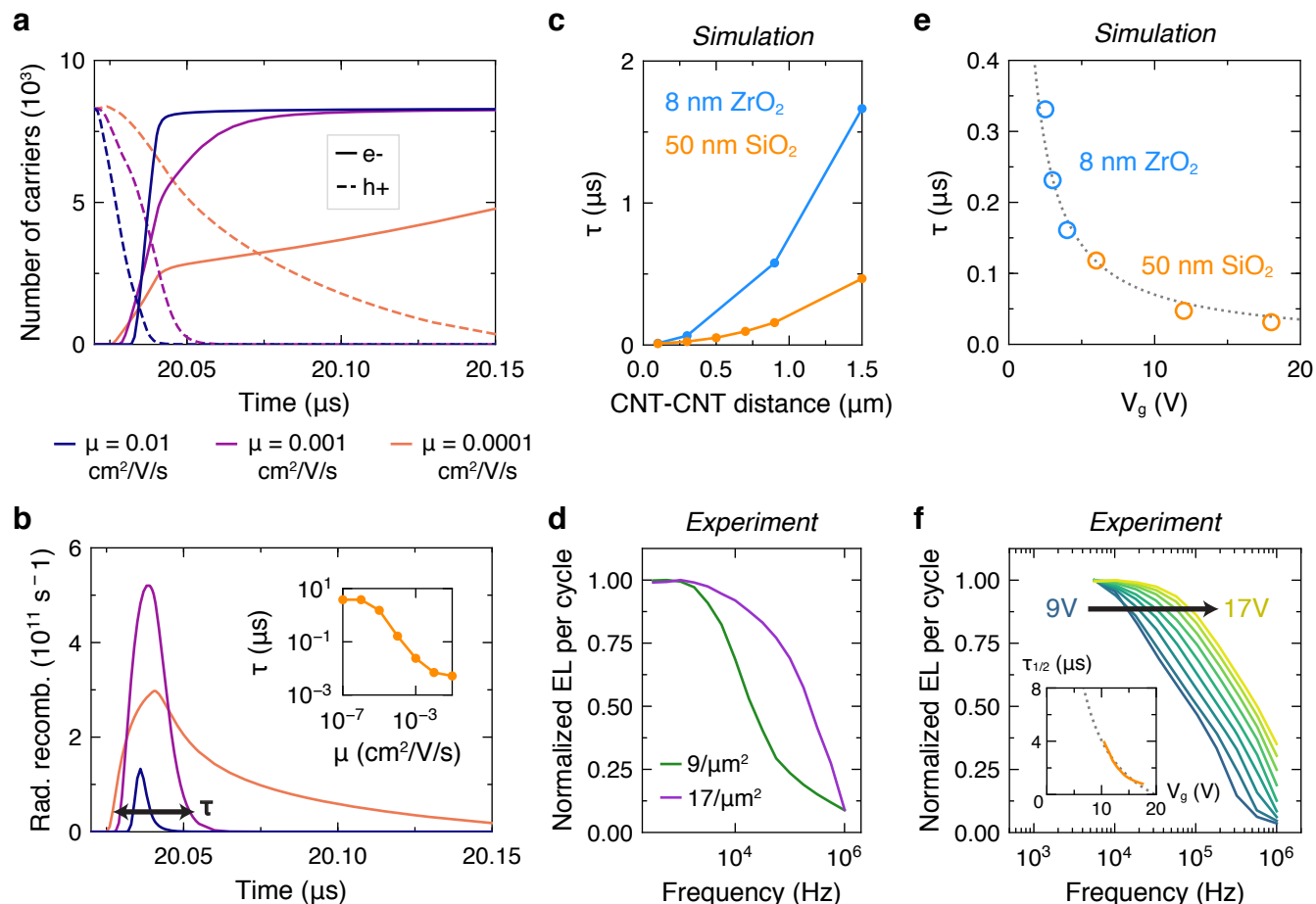


Figure 3.19: Simulated total (a) number of carriers and (b) radiative recombination versus time where an upward square wave transition from  $-12\text{ V}$  to  $12\text{ V}$  is initiated at  $20.02\ \mu\text{s}$ . Solid and dashed lines in (a) represent electrons and holes. Simulations were performed for a  $50\text{ nm SiO}_2$  gate oxide device. The effective EL lifetime  $\tau$  is calculated as the difference between the times when the EL rises and falls to 1% of its peak low-frequency value. Inset in (b) shows  $\tau$  as a function of carrier mobility in the emitter layer. (c) Simulated EL lifetime as a function of CNT-CNT spacing. (d) Experimentally measured EL intensity per square wave cycle as a function of square wave frequency for devices with CNT networks assembled for 5 min ( $\approx 9\text{ CNT}/\mu\text{m}^2$ ) or 60 min ( $\approx 17\text{ CNT}/\mu\text{m}^2$ ), where longer assembly times yield more dense CNT networks (shorter CNT-CNT distances). (e) Simulated EL lifetime versus gate voltage for devices with different EOT. (f) Experimentally measured EL intensity per square wave cycle as a function of square wave frequency for devices with gate voltages between  $5\text{ V}$  (blue) and  $17.5\text{ V}$  (yellow). Inset shows the time constant corresponding to the inverse of the frequency at which the normalized EL drops by half. Dotted lines in (e) and (f) represent inverse gate voltage scaling of the form  $1/V_g$ . Data were measured from  $50\text{ nm SiO}_2$  gate oxide devices with 9,10-diphenylanthracene (DPA) as the emitter.

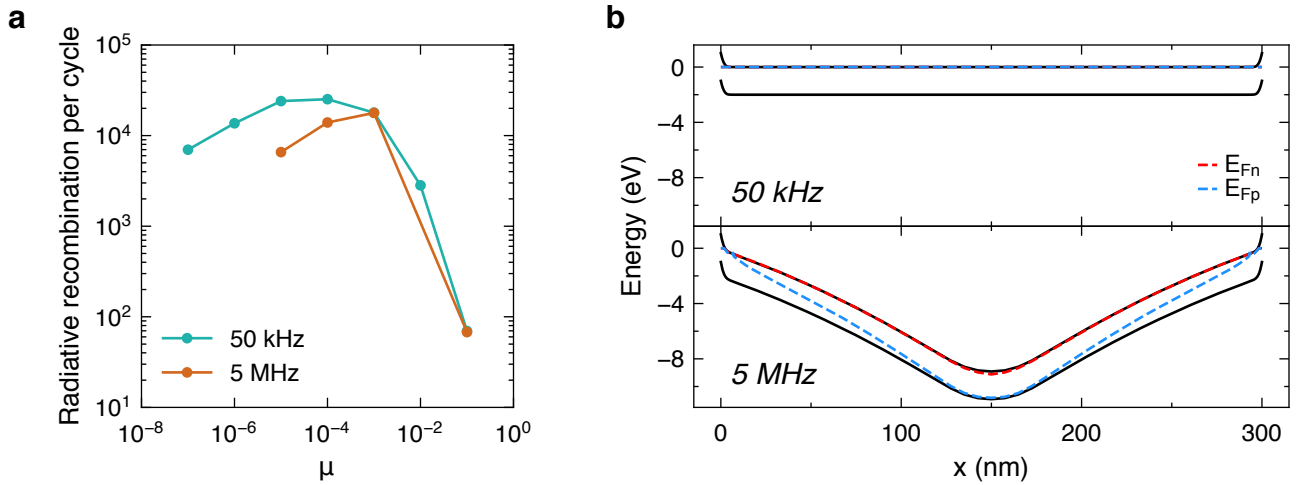


Figure 3.20: (a) Total radiative recombination per square wave gate voltage cycle as a function of emitter layer mobility  $\mu$  ( $\text{cm}^2 \text{V}^{-1} \text{s}^{-1}$ ). The frequency of the square wave gate voltage is either 50 kHz (teal) or 5 MHz (brown). The gate oxide is 50 nm  $\text{SiO}_2$  and the gate voltage is  $\pm 12$  V. (b) Energy band diagrams between opposing source contacts at timepoint **3** for a square wave frequency of either 50 kHz (top plot) or 5 MHz (bottom plot). The emitter layer mobility is  $1 \times 10^{-4} \text{cm}^2 \text{V}^{-1} \text{s}^{-1}$ . The device reaches steady-state in the former but not the latter case (within the timespan of a half-cycle of the square wave period).

as well as differences in luminescent lifetimes of the experimentally measured and simulated emissive materials. The EL lifetime decreases with increasing gate voltage, at the expense of efficiency, as carriers in the emissive material are swept out more quickly under influence of steeper potential profiles near the contact (Figure 3.19e). Experimental measurements show a similar trend in which the EL intensity per transition remains constant over a larger frequency range when the applied gate voltage is higher (Figure 3.19f). In the future, parasitic device resistances, which are currently largely dominated by the resistive CNT network used as the porous source contact, should be minimized to improve the operating frequency of the device and increase the time-averaged EL intensity.

### 3.7 Conclusion

In conclusion, we studied the performance of an AC electroluminescent device through numerical simulations and experiments, thereby guiding the rational design of high-performance AC electroluminescent devices for different applications. The model captures the essential physics of an AC electroluminescent device based on direct bipolar carrier injection and demonstrates that performance metrics are dictated by a combination of material properties, device structure, and operating parameters. In the ultimate limit of gate oxide scaling,

EL can be generated at peak-to-peak gate voltages equal to the band gap of the emitting material. Moreover, there are negligible differences in EL intensity and efficiency for materials with different energy level alignments with the source contact once the turn-on regime has been surpassed. The device thus renders electroluminescence spectroscopy a practical tool for studying and characterizing emissive materials with varying morphological, optical, and electronic properties in different environments. Since EL can be obtained from any material deposited on top of a pre-prepared device and does not require any specific material properties to occur, AC electroluminescent devices may serve as a promising solution for in-situ metrology of unmodified materials and could have potential applications in a broad range of scientific fields in the future. Finally, the photon energy-band gap scaling trends established from our model show that there are no fundamental limitations associated with generating EL from wide band gap materials, suggesting that AC injection may be a viable approach for developing LEDs in the deep-UV regime and beyond.

## 3.8 Methods

### Device fabrication

50 nm  $\text{SiO}_2/\text{p}^{++}$  Si substrates were subjected to  $\text{O}_2$  plasma treatment for 1.5 min, immersed in poly-L-lysine solution for 5 min then rinsed with DI water. The substrate was subsequently immersed in 90% semiconducting CNT solution (NanoIntegris) for 30 min unless otherwise specified, then rinsed with DI water. Increasing the assembly time increases the density of the CNT network as reported previously [74]. Afterwards, the substrate was annealed for 1 h in forming gas at  $250^\circ\text{C}$ . Metal grid electrodes contacting the CNT network were patterned by photolithography and deposited by e-beam evaporation (0.5 nm Ti/25 nm Pd). CNTs outside the device area were patterned by photolithography and etched with  $\text{O}_2$  plasma to prevent leakage. For devices with thin gate dielectric, 90 nm  $\text{SiO}_2/\text{p}^{++}$  Si substrates were patterned by photolithography and the exposed  $\text{SiO}_2$  was etched completely away with 6:1 buffered oxide etch. Around 8 nm  $\text{ZrO}_2$  was deposited at  $180^\circ\text{C}$  by atomic layer deposition, followed by e-beam deposition of 2-3 nm  $\text{SiO}_x$  for adherence of CNT networks [27]. The remainder of device fabrication follows the process described earlier, except here we used metallic CNT networks as the source electrode to reduce the turn-on voltage. Metallic CNT networks were deposited by drop-casting 99% metallic CNT solution (NanoIntegris) on the substrate at  $100^\circ\text{C}$  followed by a DI water rinse.

All emissive materials were purchased commercially from Sigma Aldrich (unless otherwise noted) and prepared at room temperature under ambient conditions. Visible wavelength quantum dot (QD) emitter layers were prepared by drop-casting a  $1\text{ mg mL}^{-1}$  solution of CdSSe/ZnS alloyed quantum dots in toluene on the device and letting the solution dry at room temperature. In this work, red and green QDs correspond to 630 nm and 520 nm wavelength quantum dots, respectively. CdSeTe/ZnS quantum dots (NanoOptical Materials) were first washed (by adding 0.1 mL of the  $5\text{ mg mL}^{-1}$  QD solution to 1.5 mL ethanol,

centrifuging at 8800 rpm for 5 min, then decanting the clear supernatant) before redispersing in 0.2 mL toluene. The resulting solution was drop-casted on the device and left to dry at room temperature. To remove extra ligands, devices with CdSSe/ZnS or CdSeTe/ZnS QDs were immersed in acetone for 1 minute, 1 wt% acetic acid in acetone for 5 min, and then acetone again for 1 min to remove extra ligands. PbS quantum dots (NNCrystal) were washed and redispersed in the same manner as the CdSeTe/ZnS QDs, then drop-casted on the device and left to dry at room temperature. The film was not washed afterwards due to its tendency to delaminate when immersed in solution. Ru(bpy)<sub>3</sub>(PF<sub>6</sub>)<sub>2</sub> was deposited by drop-casting a 20 mg mL<sup>-1</sup> solution of Ru(bpy)<sub>3</sub>(PF<sub>6</sub>)<sub>2</sub> in acetonitrile on the device and letting it dry on a hotplate at 70 °C in air. 9,10-diphenylanthracene (DPA) was deposited by drop-casting a 10 mg mL<sup>-1</sup> solution of DPA in toluene on the device and letting it dry at room temperature. For all drop-casted emitter materials, around 5 μL of solution was dispensed on chips around 0.25 cm<sup>2</sup> in size. Poly-(9,9-dioctylfluorene) (PFO) was measured by spin-coating a 5 mg mL<sup>-1</sup> solution of PFO in toluene on the device at 6000 rpm.

## Device characterization

AC voltage was applied using an arbitrary waveform generator (Agilent 33522A) and a voltage amplifier for voltages beyond 10 V. Optical measurements were performed using a custom-built micro-PL instrument in which EL is dispersed by a spectrometer and detected with a charge-coupled device (CCD) (Andor iDus BEX2-DD). Emission power was measured with a power meter (Thorlabs PM100D with S120C sensor) and cross-calibrated with CCD counts. Electrical measurements were performed with a current amplifier (Stanford Research Systems SR570) and oscilloscope. Devices were measured in vacuum (around 10 mTorr). The experimental IQE was determined by dividing the number of emitted photons (estimated from the EL power and emission spectrum) by the time-averaged number of injected electron-hole pairs (estimated by integrating the electrical current, refer to Figure 3.16).

## Device simulation

In order to capture the basic physics of the device, 2D simulations of the device cross-section were performed using Sentaurus TCAD (Synopsys) following a previously described approach [53]. The modeled device consisted of a layer of semiconducting material between two 1.4 nm tall edge contacts representing CNT source contacts. The underlying gate oxide layer (50 nm SiO<sub>2</sub> with  $\epsilon = 3.9$  unless otherwise stated) was contacted by a bottom gate electrode. For devices with a high- $\kappa$  gate dielectric, the oxide dielectric constant was  $\epsilon = 22$ . Unless otherwise specified, material parameters used for the semiconducting layer were  $E_g$  (band gap) = 2 eV,  $\epsilon$  (relative permittivity) = 3.5,  $\mu_n$  (electron mobility) =  $\mu_p$  (hole mobility) = 0.001 cm<sup>2</sup> V<sup>-1</sup> s<sup>-1</sup>,  $m_e^*$  (electron effective mass) =  $m_h^*$  (hole effective mass) =  $m_0$  with CNT-CNT spacing  $L = 300$  nm. These parameters are similar to those used in numerical simulations of optoelectronic devices with similar material systems [75–77]. Contact work functions were set to be mid-gap relative to the emitter band gap in order

to produce ambipolar behavior (i.e. symmetric results for upward and downward voltage transitions). For simplicity, we assumed a free carrier model in which carrier recombination occurs only radiatively. A nonlocal tunneling model for electrons and holes at the source contact-semiconductor interface was applied. The total amount of radiative recombination was calculated by integrating the volume density of the radiative recombination rate over the volume of the emitter layer over one period of a 50 kHz square wave voltage applied between the gate and source contacts. The slew time (rise and fall time) of the square wave gate voltage was 20 ns.



## Chapter 4

# Resonant characterization of an AC-driven electroluminescent capacitor

This chapter is adapted from:

V. Wang, A. Javey, “A Resonantly Driven, Electroluminescent Metal Oxide Semiconductor Capacitor with High Power Efficiency”, *ACS Nano*, 15, 9, 15210–15217, 2021.

---

Electroluminescence can be generated from a wide variety of emissive materials using a simple, generic device structure. In such a device, emissive materials are deposited by various means on a metal-oxide-semiconductor capacitor structure across which alternating current voltage is applied. However, these devices suffer from low external efficiencies and require the application of high voltages, thus hindering their practical usage and raising questions about the possible efficiencies that can be achieved using alternating current driving schemes in which injection of bipolar charges does not occur simultaneously. We show that appropriately chosen reactive electrical components can be leveraged to generate passive voltage gain across the device, allowing operation at input voltages below 1 V for devices across a range of gate oxide thicknesses. Furthermore, high power efficiencies are observed when using thermally activated delayed fluorescence emitters deposited by a single thermal evaporation step, suggesting that the efficiency of a light-emitting device with simplified structure can be high.

### 4.1 Introduction

Electroluminescent devices, which generate light emission in response to electrical excitation, have been extensively studied and developed since the early 1900s [78]. The phenomenon of

electroluminescence (EL) was discovered in silicon carbide in 1907 and was later observed to occur in insulating materials containing zinc sulfide (ZnS) phosphor powder as well. The ZnS powder-based electroluminescent devices developed by Destriau in 1936 were operated by applying alternating current (AC) voltages [10]. Although this class of devices requires large voltages in the range of 100 V or more, they have found modern use in applications requiring simple and robust fabrication procedures, such as decorative electroluminescent wire [79], large-area textile displays [80], and sprayable interfaces [81]. EL in organic materials was demonstrated in 1953 by Bernanose, who applied kilovolts of alternating voltage to fluorescent dyes like acridine orange [82]. Since the initial demonstration of EL, a variety of light-emitting diodes (LEDs) based on inorganic and organic materials have been developed with ongoing improvements in brightness and efficiency over the past few decades [83–85]. In these devices, electrons and holes are injected into an emissive layer by applying direct current (DC) voltage, often with the aid of multiple charge injection and transport layers surrounding the emissive layer [86].

We have shown that EL can also be achieved from a variety of emissive materials at relatively low AC voltages ( $< 100$  V) using a metal-oxide-semiconductor (MOS) capacitor structure with a porous carbon nanotube (CNT) network as the top contact (Figure 4.1a) [53]. These devices are compatible with emissive layers spanning a wide range of material classes (from colloidal quantum dots to small organic molecules to conjugated polymers and more), physical forms (from thin evaporated films to thick drop-casted films), and colors (across the entire visible range and beyond). The generic, open-top device structure enables facile integration of arbitrary emitters with applications in EL spectroscopy, light-emitting devices, and sensing. For inorganic semiconducting materials with sufficiently high carrier mobility such as transition metal dichalcogenide (TMDC) monolayers, applying AC voltage to MOS capacitors with top metal contacts alone is enough to generate EL [12]. However, visible EL cannot be obtained from molecular materials using the same structure due to poor lateral carrier transport. By using a CNT network as the top source contact, large-area emission can be obtained from materials with low or imbalanced charge carrier mobility, such as organic thin films. Previous work elucidates the critical role of the CNT network in such a device: the density of the CNT network must be high enough for electrical percolation across a large area, but not so high that it hinders gate control of the semiconducting layer [53]. These devices, while versatile, suffer from low efficiencies in the range of less than 1% which hinders their practical utility, and it remains unknown whether reasonable operating efficiency can be attained using such a scheme. Furthermore, bright electroluminescence typically requires either thin gate oxide layers or high drive voltages. Reducing the gate oxide thickness to the several nanometer range requires tight fabrication tolerances and limits the operating voltage range, while high drive voltages require high voltage electronics that impose bandwidth constraints and increase the system size.

Similar top-emitting AC electroluminescent devices based on MOS transistors (e.g. light-emitting field-effect transistors) have been previously developed, but the power efficiencies are unreported or low (on the order of  $< 10^{-5}$  lm/W [49, 50, 87, 88]). Here, we show that high power efficiencies can be achieved with AC-driven MOS capacitor devices by using a bright,

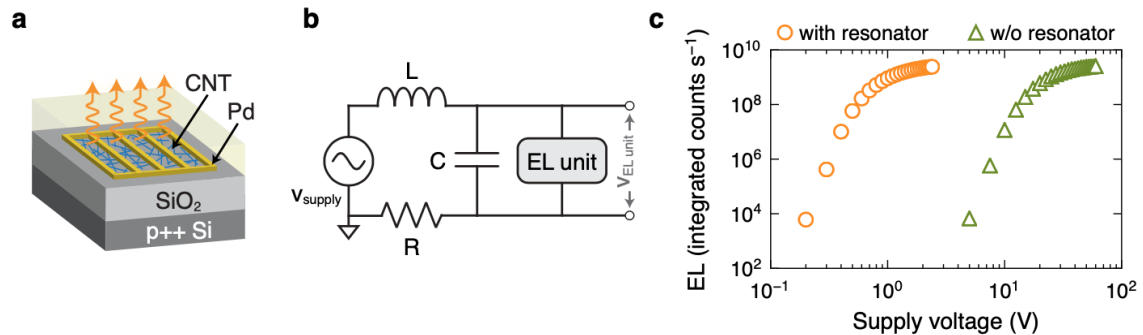


Figure 4.1: (a) Schematic of the device structure which consists of an emissive film deposited on top of a capacitor on a silicon substrate. The device is operated by applying an alternating current sinusoidal voltage across the two terminals of the capacitor. (b) Simplified diagram of the device operating scheme, where external reactive elements ( $L$ ,  $C$ ) are used to tune the operating frequency. (c) EL intensity as a function of voltage when the device is driven directly by an approximately 15 kHz sinusoidal voltage source (without a resonator, green triangles) or via the scheme depicted in (a) with  $L = 100$  mH,  $C = 1$  nF (with a resonator, orange circles).

vacuum deposited, organic emissive layer. We further analyze AC electrical characteristics of the device through impedance spectroscopy and demonstrate how devices with different gate oxide thicknesses can be driven with low supply voltages, simply by operating the device in a resonant  $LC$  tank circuit with reactive components that match the impedance of the device (Figures 4.1b-c). By combining these strategies, we demonstrate an AC-driven electroluminescent device with a power efficiency  $> 20$  lm/W at a luminance of  $> 1000$  cd/m<sup>2</sup> when driven by a 0.7 V input RMS voltage.

## 4.2 Operating scheme

The structure of the AC electroluminescent device is shown in Figure 4.1a and the fabrication procedure is depicted in Figure 4.2. A solution-processed CNT network (Figure 4.3) serves as the top electrode and a p<sup>++</sup> Si/SiO<sub>2</sub> substrate serves as the bottom electrode and dielectric layer. An emissive layer is deposited directly on top of this capacitive structure and EL is generated upon application of a sinusoidal AC voltage between the top and bottom electrodes. The CNT network serves as a dense but porous source contact [89] and enables greater emission intensity from low mobility molecular materials while still allowing the transverse gate field to modulate the contact-semiconductor interface. We used metallic as opposed to semiconducting CNT networks [90] in order to reduce resistive losses in the source contacts and produce devices with relatively linear electrical response in above-threshold AC operation (Figure 4.4).

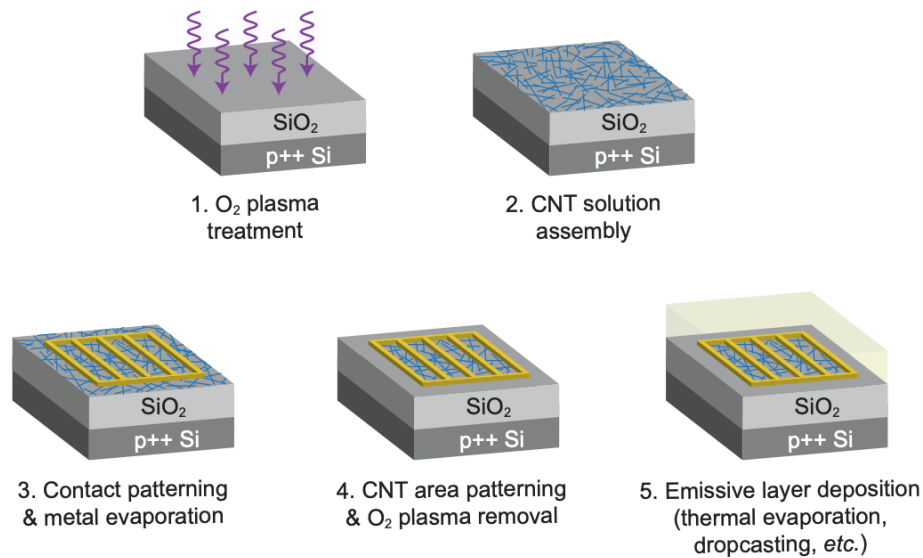


Figure 4.2: Fabrication process flow for AC-driven metal-oxide-semiconductor capacitor devices with details described in the Methods section. Starting from a SiO<sub>2</sub>/Si substrate, O<sub>2</sub> plasma treatment is applied followed by CNT network assembly from CNT solution. A metal contact is patterned on top of the CNT network and the CNT network area is patterned. An emissive layer is deposited as the last step; the patterned CNT network area defines the emission area.

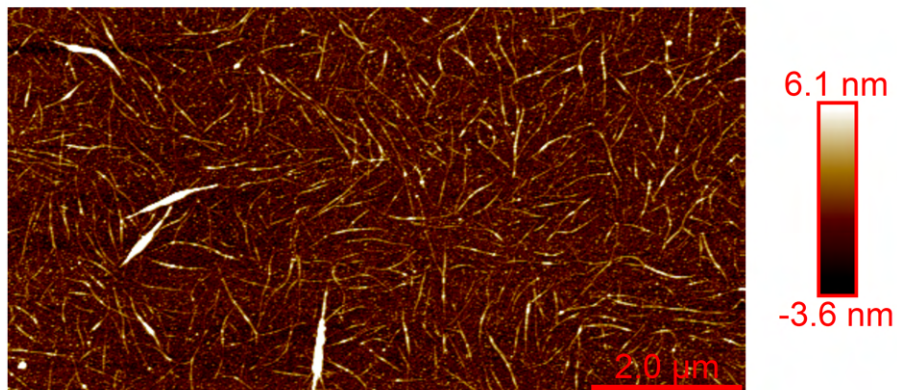


Figure 4.3: Atomic force microscopy image of a sparse CNT network on top of a silicon substrate, deposited by drop-casting a mixed 90% metallic/10% semiconducting CNT solution on top of the substrate heated at 110 °C.

The operating mechanism of the device has been discussed previously and is supported

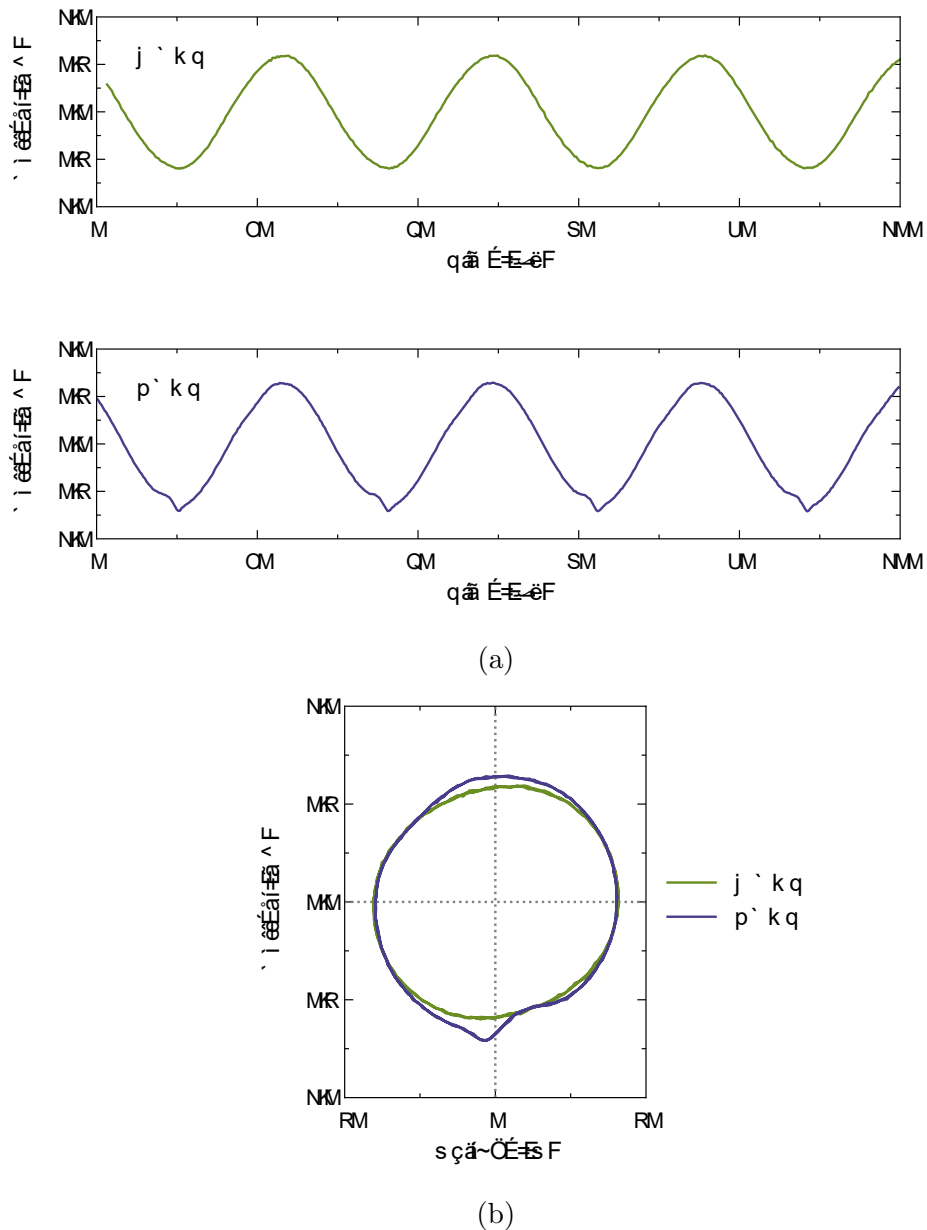


Figure 4.4: (a) Current across an AC-driven electroluminescent device with a top CNT network contact fabricated from 90% metallic/10% semiconducting (top) or 90% semiconducting/10% metallic (bottom) CNT solutions. The applied voltage waveform is a  $\sim 40 V_{pp}$ , 38 kHz sine wave. (b) Current *versus* voltage data corresponding to waveforms in (a).

by simulations which show how both electrons and holes can be injected into the emissive layer [12] (Figure 4.5a). At the positive peak of the applied sine wave voltage, electrons

are accumulated in the emissive semiconducting material. As the gate voltage changes from positive to negative, the bands of the semiconducting material near the CNT source contact bend upward, causing holes to tunnel into the emissive semiconducting material while electrons exit. The temporary presence of both charge carriers permits subsequent exciton formation and radiative recombination leading to light emission (Figure 4.6). As the gate voltage reaches its peak negative value, the semiconducting material now largely contains only holes, and a similar carrier injection process occurs at the negative-to-positive voltage transition.

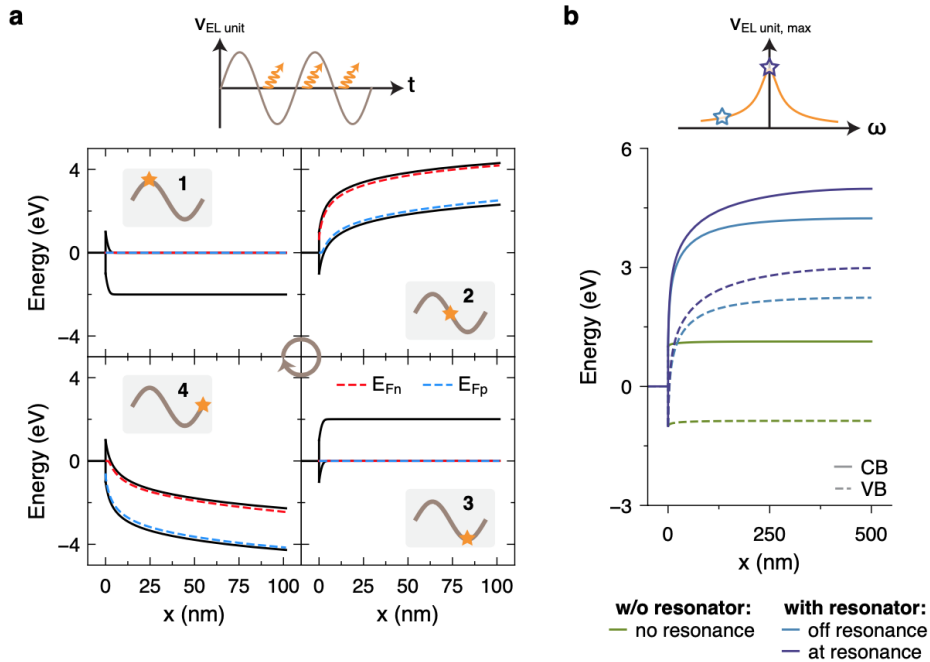


Figure 4.5: (a) Simulated energy band diagrams at the interface between a metallic CNT contact and a semiconducting emissive material at different timepoints of a sine wave excitation. Dashed red and blue lines present the quasi-Fermi levels for electrons and holes, respectively. (b) Conduction (solid lines) and valence (dashed lines) bands corresponding to timepoint 2, for a device operated in a resonant driving scheme at the resonance frequency (purple lines, corresponding to Figure 4.5a) and 1 kHz away from the resonance frequency (blue lines) with a supply voltage of 1 V. Band bending is nearly absent when driven non-resonantly (green lines), leading to substantially less quasi-Fermi level splitting (not shown). The driving is scheme illustrated in Figures 4.1b-c; the assembled CNT network is assumed to be lossless.

In this operating scheme, high input voltages are required to generate band bending steep enough to enable sufficient carrier tunneling. However, due to the AC mode of device operation, the capacitive electroluminescent device can be operated resonantly such that

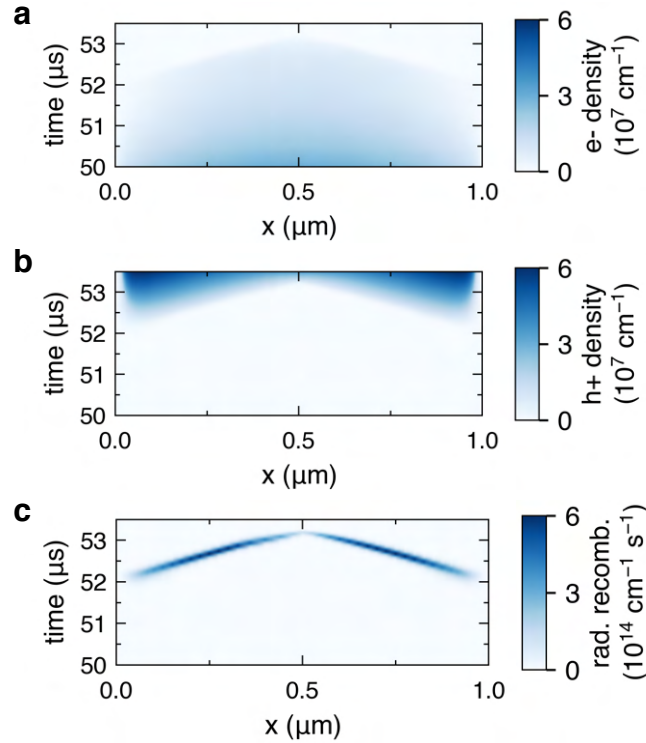


Figure 4.6: Simulated (a) electron density, (b) hole density, and (c) amount of radiative recombination as a function of time and space after the onset of a negative voltage transition. Simulations correspond to those in Figure 4.5a.

bright emission is achieved at low supply voltages. By adding reactive electronic components to the driving scheme that cancel the capacitive reactance of the device, the supply voltage can be entirely dropped across the lossy resistive components of the circuit at resonance, which include the source contact (paths along the CNT network) and process of carrier injection from the contact to the emissive layer (Figure 4.5b). During this process, voltage is dropped at the contact-semiconductor interface and within the semiconductor, but the former dominates. At the same time, the peak voltage across the gate oxide is magnified, further enhancing the band bending at the metal-semiconductor interface as energy sloshes between the capacitive and inductive elements. For instance, when an inductor is added in series with the capacitive device, electrical resonance is achieved at the frequency where the impedance of the inductor ( $Z_L = j\omega L$ ) matches the impedance of the capacitive component of the device ( $Z_C = 1/(j\omega C_{device})$ ). At the resonance point of this tuned resistor-inductor-capacitor (RLC) resonator (i.e. at  $\omega_0 = 1/\sqrt{LC_{device}}$ ), the reactive impedances of the inductor and capacitor cancel out and the total impedance only reflects resistive components of the impedance of the components [91]. The resonance frequency can be additionally tuned by adding more

reactive elements to the driving scheme such as a capacitor  $C_p$  in parallel with the device.

Impedance data show that the device largely behaves as a capacitor with a capacitance around 55 pF, which is consistent with the geometry of the device; the metal grid has a  $\sim 30$  pF capacitance on  $\text{SiO}_2$  with  $\epsilon = 3.9\epsilon_0$ , in addition to extra capacitance arising from the metallic CNT network covering a fraction of the emission area. When the device is connected in parallel with a 1 nF capacitor and in series with a 100 mH inductor, electrical resonance is achieved at the frequency where the impedance dips to a minimum and the phase shifts from  $-90^\circ$  (mostly capacitive) to  $+90^\circ$  (mostly inductive), as shown in Figure 4.7a. In this case, the resonance frequency is mostly determined by  $L$  and  $C_p$  since  $C_p \gg C_{device}$ . Due to the decrease in total impedance, the maximum source current is magnified as well, yielding higher carrier injection at a lower supply voltage (Figure 4.7b). The reduction in supply voltage depends on the Q-factor of the circuit, which is given by  $Q = (\omega_0 L)/R = (1/R)\sqrt{L/C}$  and is around 25 in this case. The Q-factor can be increased by decreasing parasitic resistance in the device and setup, as well as by maximizing the  $L/C$  ratio. Figure 4.7c shows a more complete equivalent circuit model of the resonant circuit which characterizes frequency-dependent impedance data of the device operated at different resonance frequencies using different component choices; detailed discussion of the resonant circuit model and Q-factor optimization can be found in the following subsections.

A simple analysis of RLC circuits shows how electrical resonance can be leveraged to achieve passive voltage gain across reactive elements and enable the supply voltage to be dropped entirely across the resistive elements. The voltage across reactive elements in a basic series resistor-inductor-capacitor (RLC) circuit can be determined in the frequency domain using complex impedances, where  $Z_R = R$ ,  $Z_C = 1/(j\omega C)$ ,  $Z_L = j\omega L$ :

$$V_C = V_{in} \cdot \frac{Z_C}{Z_L + Z_C + Z_R}$$

The voltage gain across the capacitor is simply

$$\frac{|V_C|}{|V_{in}|} = \frac{1}{\sqrt{(1 - \omega^2 LC)^2 + (\omega RC)^2}}$$

which at resonance ( $\omega_0^2 = \frac{1}{LC}$ ) attains a peak value of

$$\frac{|V_{C,0}|}{|V_{in}|} = \frac{1}{\omega_0 RC} = \frac{1}{R} \sqrt{\frac{L}{C}} = Q$$

where  $Q$  is defined as the quality factor of the circuit and denoting quantities at resonance with subscript 0. Similarly,

$$\frac{|V_{L,0}|}{|V_{in}|} = \frac{\omega^2 LC}{\sqrt{(1 - \omega^2 LC)^2 + (\omega RC)^2}}$$

which at resonance gives the same amplification factor as  $|V_{C,0}|/|V_{in}|$ . Note all the voltages,  $V_{in} = v_i e^{j\omega t}$  and  $V_{C,L} = v_{c,\ell} e^{j(\omega t + \phi_{c,\ell})}$ , are sinusoidal. In the simplified schematic presented



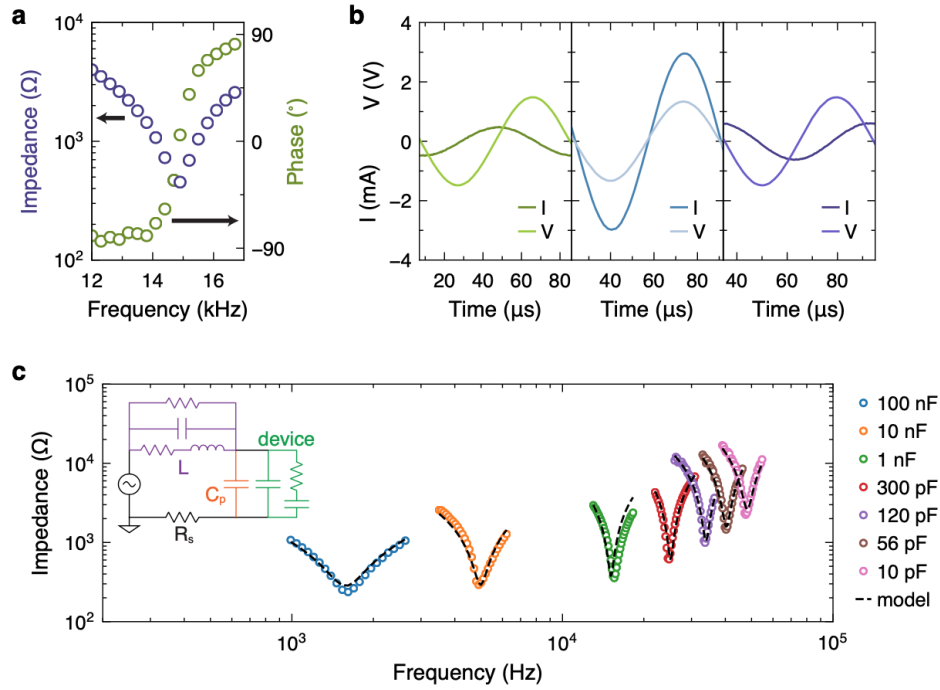


Figure 4.7: (a) Impedance and phase between the current-voltage waveforms near the resonance frequency measured using the scheme depicted in Figure 4.1b. (b) From left to right: current and voltage seen at the source below, at, and above the resonance frequency. The amplitude of the voltage source is 1.5 V. (c) Impedance of  $LC$  tank circuits with a 100 mH inductor and the base device structure in parallel with different capacitors (inset: model of the resonant circuit).

in Figure 4.1,  $L$  is the inductance of the external inductor,  $C = C_p + C_{device}$  is the sum of the capacitance of the external capacitor and the device capacitance, and  $R = R_s$  is the resistance of the sense resistor used for measurement. The total current is

$$I = \frac{V_{in}}{Z_L + Z_C + Z_R} = \frac{V_{in}}{j\omega L + \frac{1}{j\omega C} + R}$$

which at resonance is simply  $|I_0| = \frac{|V_{in}|}{R}$  (in phase with the input voltage waveform) due to cancellation of the reactive impedances, meaning the impedance seen by the source reaches a minimum and the voltage across the resistive element has amplitude  $|V_{in}|$ . In the schematic shown in Figure 4.1, the current through the device is a fraction of the total current:

$$I_{device} = I \cdot \frac{C_{device}}{C_{device} + C_p} \implies |I_{device,0}| = \frac{|V_{in}|}{R(1 + C_p/C_{device})} = Q(|V_{in}| \cdot \omega_0 C_{device})$$

so the current is also magnified by a peak value of  $Q$ , at resonance.

Using the full model in Fig. 4.15 and parameters extracted earlier, we can optimize over possible values for  $L$  and  $C$  to maximize the gain factor. For a given specific inductor, there are two resonance frequencies: one related to the resonance with the parallel external capacitance and device capacitance, and one related to the resonance with the parasitic capacitance of the inductor (Fig. 4.8). Only the first resonance pertains to the voltage gain of interest. A global sweep of different  $L$  and  $C$  (Fig. 4.9) shows that  $L \approx 100$  mH and  $C \approx 1$  nF gives roughly optimal peak  $|V_{C,0}|/|V_{in}|$  (from the first resonance of interest), which are the primary component values chosen in this work.

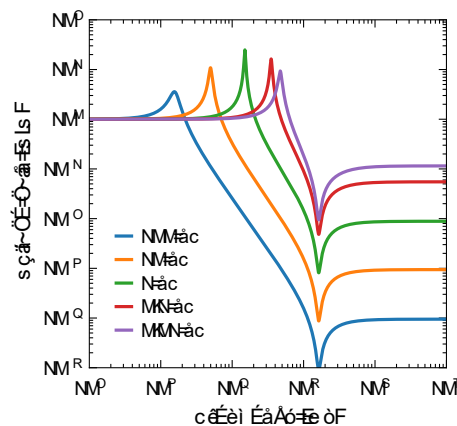


Figure 4.8: Simulated voltage gain across the device for the  $L = 100$  mH used in this work and varying  $C$  (indicated in the legend).

The resonance frequency can be tuned by choosing suitable values of externally added reactive components in conjunction with the device impedance. To demonstrate the electrical tunability of the operating scheme, we used devices with a drop-casted emissive layer of  $\text{Ir}(\text{dtb-bpy})(\text{ppy})_2\text{PF}_6$  due to its ease of fabrication, low volumes of material required, and relatively bright single-layer emission even when processed under ambient conditions [92]. Figures 4.10a-b show how the resonance frequency changes when the parallel capacitance and series inductance are varied, respectively. As the parallel capacitance or series inductance increases, the resonance frequency decreases. The resonance frequency ranges from 1-2 kHz at the largest  $LC$  value used to 8-9 MHz at the smallest  $LC$  value used, which represents a span of 4 orders of magnitude. Broad frequency-dependent measurements also enable quantification of the resonance frequency, which should scale linearly with  $\sqrt{LC}$  as Figure 4.7d shows for varying inductance values. The equivalent circuit capacitance can be alternately extracted by finding the value of  $C_{eq}$  that yields the closest straight-line relationship between the resonance frequency and  $\sqrt{C} = \sqrt{C_p + C_{eq}}$  (for known  $C_p$ ) as shown in Figure 4.10c. In both cases, the measured device has an equivalent capacitance around 0.1 nF. It should be noted that the behavior of resonant circuits depends on stray parasitics and nonideali-

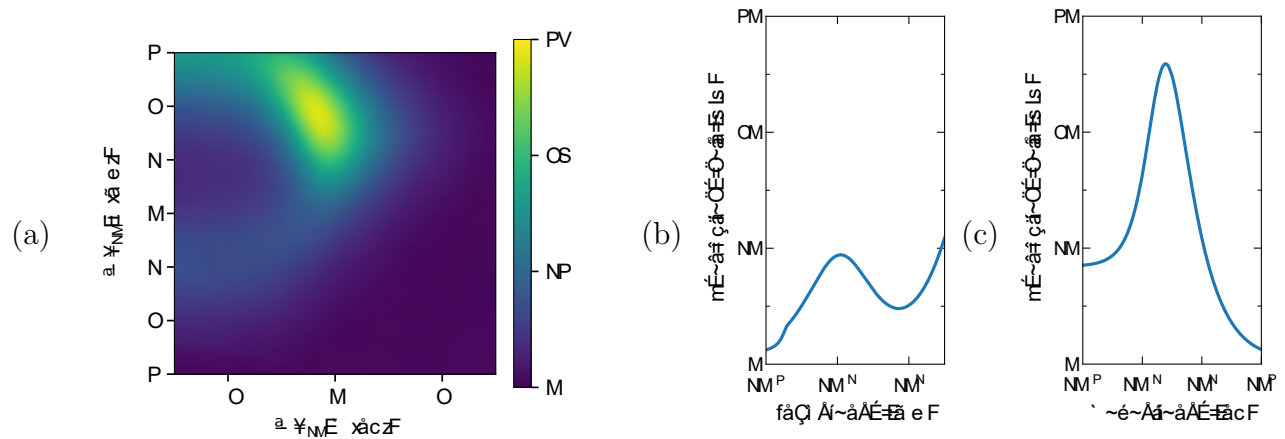


Figure 4.9: (a) Simulated peak voltage gain across the device (in V/V, indicated by color bar scale) ( $|V_{C,0}|/|V_{in}|$ ) for varying series  $L$  and parallel  $C$ . (b) Simulated peak voltage gain for varying  $L$  assuming no parallel  $C$ . (c) Simulated peak voltage gain for varying parallel  $C$  assuming series  $L = 100$  mH. In this simulation we neglect  $R_p$  and  $C_L$  but include estimated  $R_L$  based on measurements of different discrete inductors available; this value increases linearly with  $L$  generally.

ties in the discrete components, which have been disregarded so far for simplicity. These complexities, such as self-resonance in the inductor, are elaborated in the following section.

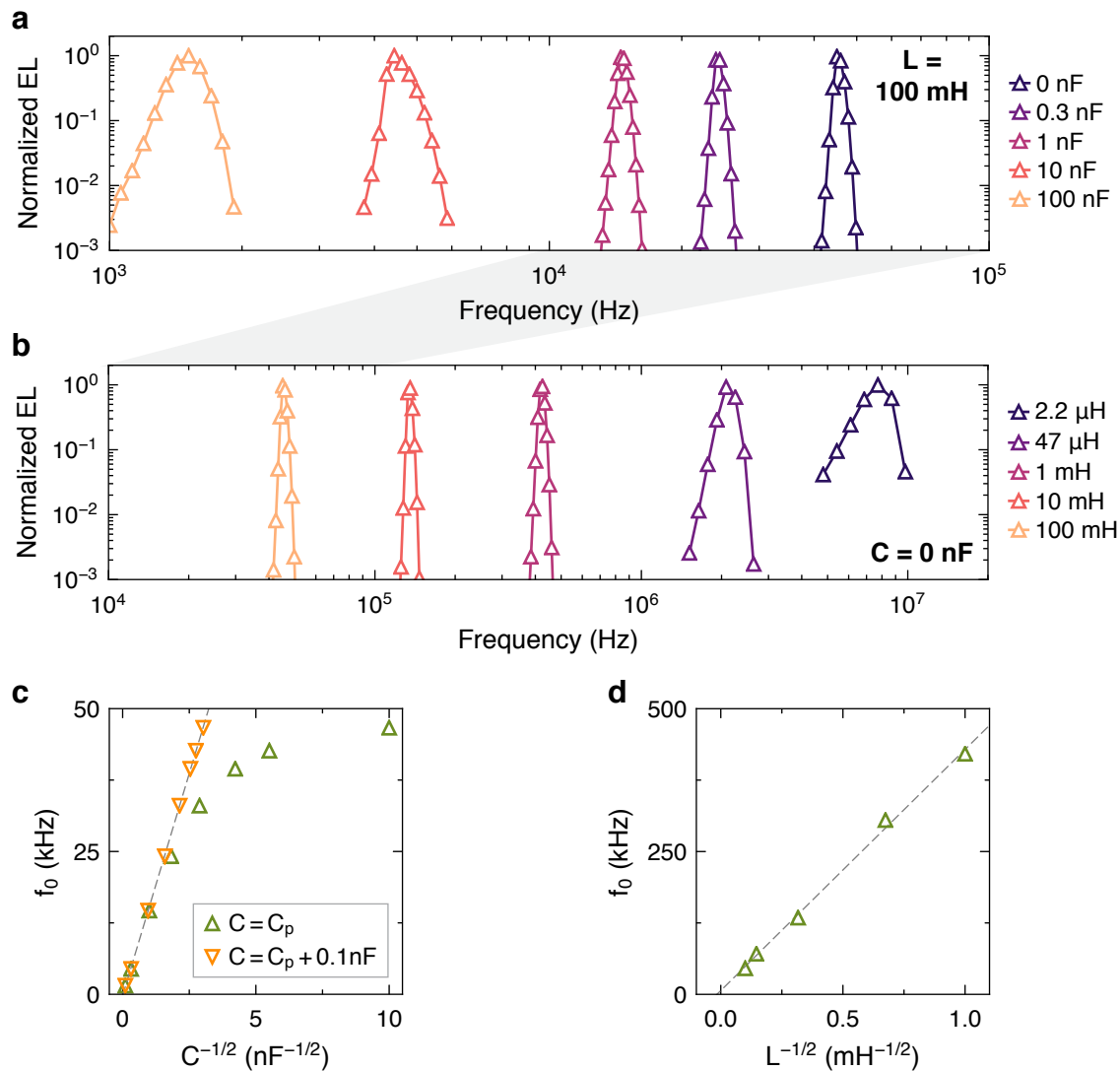


Figure 4.10: (a) Normalized EL intensity as a function of frequency for resonantly operated AC electroluminescent devices using (a) a 100 mH inductor and varying parallel capacitances  $C_p$  indicated in the legend, or (b) no parallel capacitance and varying series inductances  $L$  indicated in the legend. (c) Resonance frequency as a function of  $\sqrt{C}$  for the data in (a) where  $C$  represents the external capacitance alone (upward triangles) or in sum with a fitted value (downward triangles). (d) Resonance frequency as a function of  $L$  for the data in (b). Dashed lines represent least-squares linear fits.

### 4.3 Equivalent circuit model

The experimental setup contains nonidealities and parasitics omitted in the simplified diagram presented above. A more accurate model can be constructed from impedance spectroscopy measurements as detailed below. For example, inductors have parasitic resistance and capacitance, as illustrated in Fig. 4.11. Here we only consider frequency-independent component values for simplicity. For the inductor used in this work (which has a nominal value of 100 mH), the model yields  $L \approx 101$  mH,  $C_L \approx 9.5$  pF,  $R_p \approx 1.1$  M $\Omega$ , and  $R_L \approx 208$   $\Omega$  (the latter of which matches DC measurement) when fitted to experimental AC measurements. The secondary self-resonant frequency is around 175 kHz, which is higher than the operating frequencies applied using this inductor. Here the inductor quality factor,  $Q_L = \omega L/R_L$ , is around 30 at 10 kHz. These parameters, along with  $\approx 10$  pF stray capacitance in the setup, fit impedance data from different resonant circuits relatively well. Figure 4.12 shows the impedance seen at the source for different component values.

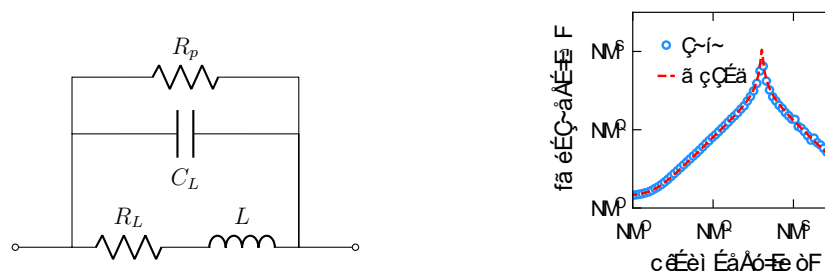


Figure 4.11: Left: an equivalent circuit model of an inductor. Right: model fit to experimental data for a 100 mH inductor.

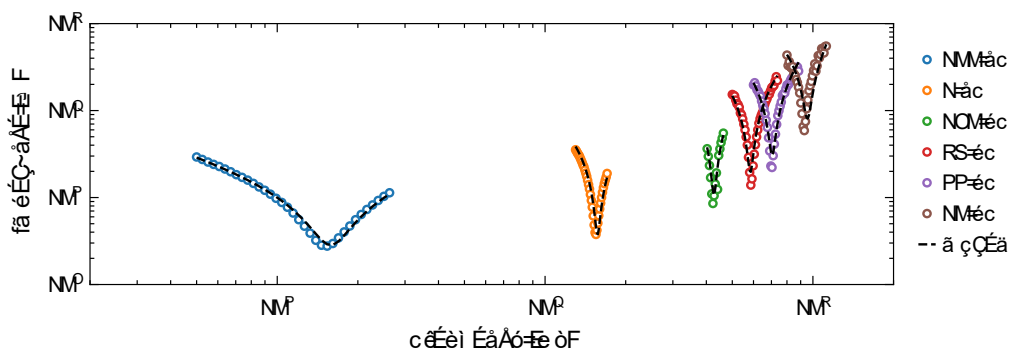


Figure 4.12: Impedance of  $LC$  tank circuits with a 100 mH inductor in series with different capacitors.

The base device structure can be modeled as the metal pad capacitance in parallel with a RC branch representing the lumped contribution of the injecting CNT network on the gate oxide (Fig. 4.13), where the series  $R_{CNT}$  and  $C_{CNT}$  can be converted to the parallel equivalent by the transformations  $C_{CNT,\parallel} = \frac{C_{CNT}K^2}{1+K^2}$  and  $R_{CNT,\parallel} = R_{CNT}(1+K^2)$  in which  $K = \frac{1}{\omega R_{CNT}C_{CNT}}$  at a given frequency  $\omega$ . Note  $K \gg 1$  when  $\omega \ll 1/\tau_{CNT}$  where  $\tau_{CNT}$  is the RC delay constant of the CNT branch. In this case,  $C_{CNT,\parallel} \approx C_{CNT}$  and  $R_{CNT,\parallel} \approx \frac{1}{\omega^2 C_{CNT}^2 R_{CNT}}$ , *i.e.* the equivalent parallel dissipation is smaller when  $R_{CNT}$  is smaller. The devices in this study are largely dominated by the capacitive component and thus show mostly reactive impedance (Fig. 4.14). The device quality factor is  $\approx R_{device}/X_{device}$  (ratio of effective parallel reactance to resistance), which here is  $\omega_0 R_{CNT}(C_{pad}(1+K_0^2)+C_{CNT}K_0^2) \approx (C_{pad} + C_{CNT})/(\omega_0 R_{CNT}C_{CNT}^2)$ .

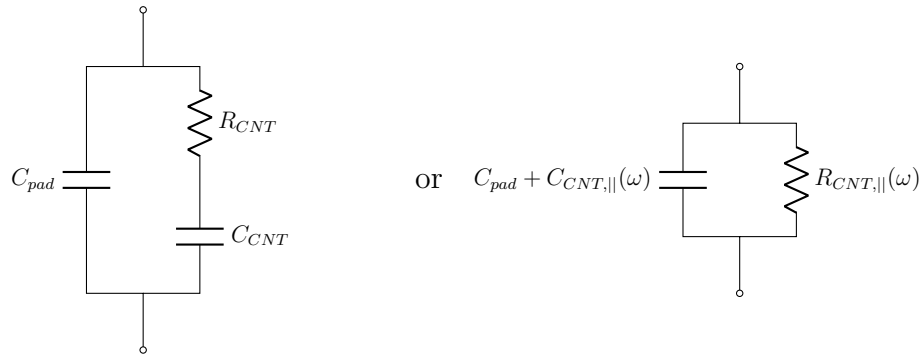


Figure 4.13: Left: an equivalent circuit model of the EL device. Right: a simplified representation of the left circuit.

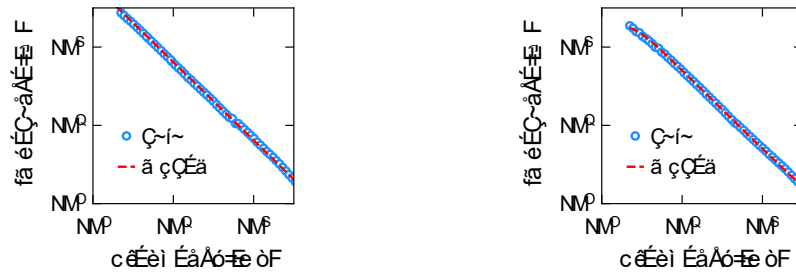


Figure 4.14: Left: single capacitor model fit to impedance of the metal grid and bond pad ( $C_{pad} \approx 38$  pF). Right: device model fit to impedance of device without emissive layer ( $C_{CNT} \approx 25$  pF). For the electroluminescent device with a deposited emissive layer, the impedance is similar, with a marginal increase in effective capacitance ( $\Delta C \approx 5$  pF).

Similarly, we can use these parameters to fit impedance data with the base structure of the device now added to the resonant circuit (Fig. 4.15).

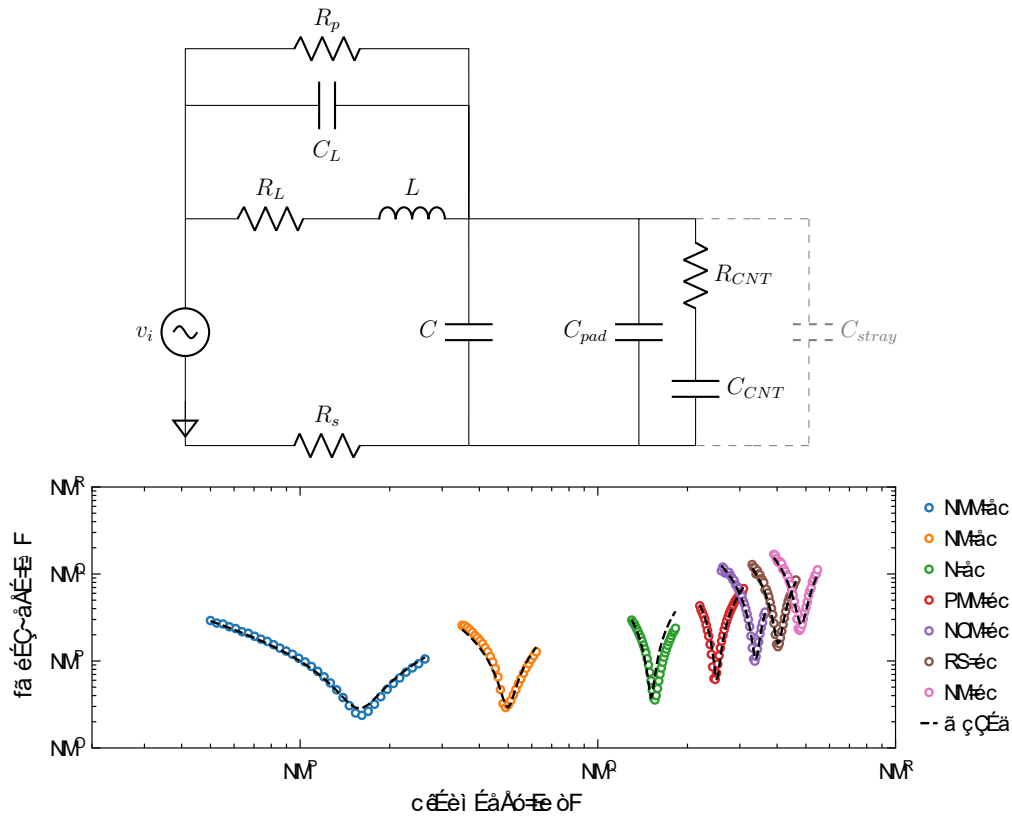


Figure 4.15: Top: Model of the resonant circuit used in this work, including major parasitic components. Bottom: Impedance of  $LC$  tank circuits with a 100 mH inductor and the base device structure (capacitor with CNT network top electrode) in parallel with different capacitors.

## 4.4 Performance characterization

Previous work on MOS capacitor-based AC electroluminescent devices showed dim brightness levels on the order of  $1 \times 10^2$  cd/m<sup>2</sup> and low external quantum efficiencies in the range of a few percent or less, with power efficiencies lagging even further behind [53]. The external efficiency of a light emitting device depends fundamentally on the internal efficiency of the emissive material. Conventional fluorescent materials are limited by spin statistics and can only achieve 25% internal efficiency at best due to nonradiative triplet transitions. To address this problem, highly efficient next generation phosphorescent and thermally-activated delayed fluorescence (TADF) emitters have been developed [93–95]. To demonstrate the performance limits of the presented device and operating scheme, we fabricated devices with a  $\sim 30$  nm, thermally evaporated emissive layer consisting of the TADF emitter CzDBA doped in the host material CBP [96, 97] (Figure 4.16a). The emission spectrum redshifts with in-

creasing dopant concentration and a moderate ( $\sim 16$  wt%) dopant to host concentration was found to yield brighter EL in general (Figure 4.17). The EL spectra for this emissive layer show a peak EL intensity around 550 nm with bright yellow-green emission in between the metal grid lines where the underlying CNT networks have been patterned (Figures 4.16b-c). Frequency-dependent measurements of EL generated from this material show monotonically increasing EL intensity with increasing sine wave frequency (Figure 4.18), which is expected since there are more voltage polarity transitions per second at higher frequencies. When the EL intensity is normalized by frequency, there is a frequency (on the order of 10 kHz) at which peak EL per sine wave cycle is achieved. Below this frequency, the EL intensity per cycle decreases with decreasing frequency due to the increasingly sluggish voltage transitions which produce less sharp band bending. Above this frequency, the EL intensity per cycle decreases due to the slow electroluminescent response of the device, which depends on both the  $RC$  time constant as well as the intrinsic photoluminescence lifetime.

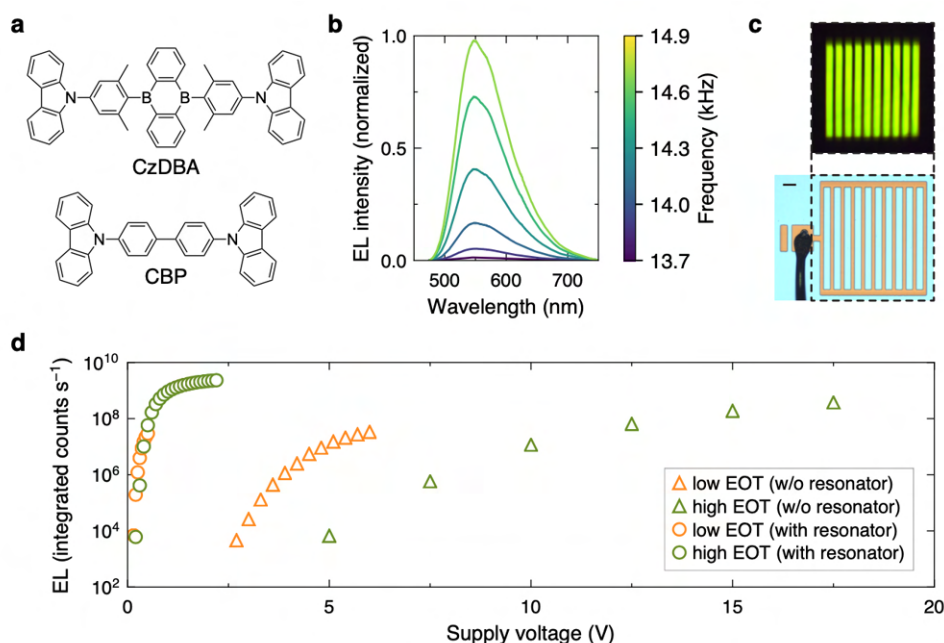


Figure 4.16: (a) Molecular structures of the dopant (CzDBA) and host (CBP) co-evaporated as the emissive layer of the device. (b) EL spectra for different frequencies near the resonance frequency, with the voltage across the device increasing towards 15 kHz. The device is driven by a  $0.7 V_{\text{rms}}$  source voltage using  $L = 100$  mH,  $C_p = 1$  nF. (c) Optical image of the device and visible green emission from the emission area between the metal grid lines. Scale bar is  $50 \mu\text{m}$ . (d) EL intensity as a function of supply voltage for devices with low ( $\approx 4$  nm) and high ( $\approx 90$  nm) equivalent oxide thickness driven without and with the resonator at the resonance frequency.



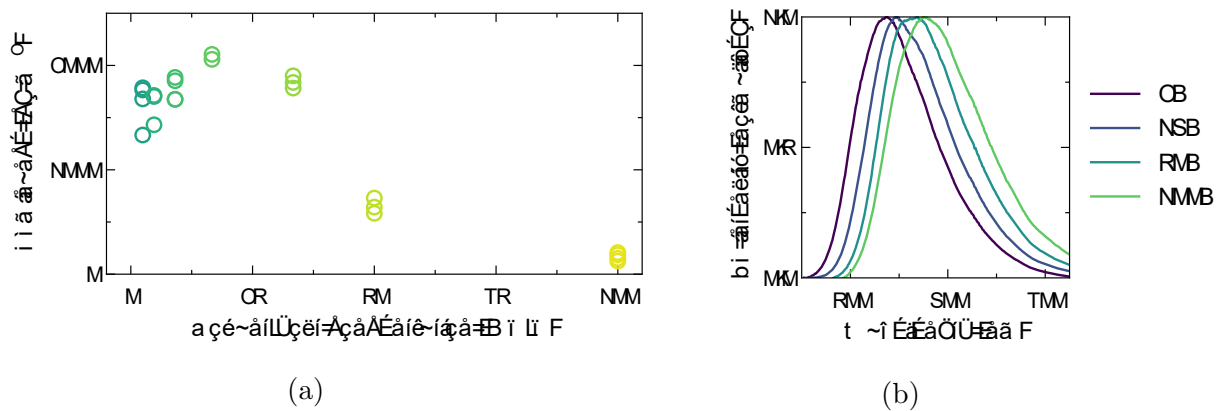


Figure 4.17: (a) Luminance of devices with emissive layers comprising of different concentrations of a dopant (CzDBA) in a host material (CBP). (b) EL spectra of CzDBA at different doping concentrations (w/w%) in CBP.

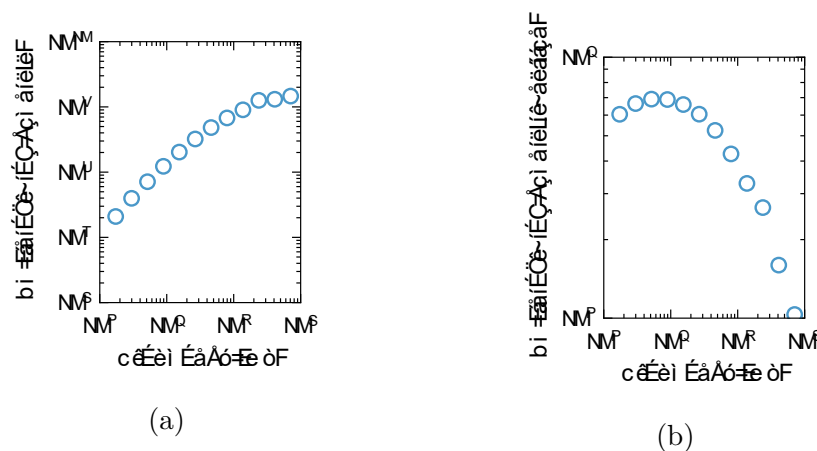


Figure 4.18: (a) EL intensity (integrated counts per second) for a device with a CzDBA emissive layer driven by a 25 V sine wave. (b) Data in (a) normalized by the frequency, yielding the average EL counts per sine wave voltage transition (either negative to positive or positive to negative) as a function of frequency. The EL intensity is relatively linear with frequency given the similar number of counts per transition across the kHz frequency range, with more significant decrease occurring towards the MHz range.

Based on the frequency-dependent EL and earlier Q-factor analysis, we characterized the device at an operating frequency around 15 kHz. The resonant driving scheme can be applied at this frequency by choosing a series inductance of 100 mH and a parallel capacitance of 1 nF, which yields a Q-factor around 25. Voltage-dependent measurements of the device operated at this frequency show that EL is generated at much lower supply voltages when

driven resonantly as opposed to non-resonantly (Figure 4.16d). As established in previously [98], the turn-on voltage for electroluminescence can be fundamentally reduced by decreasing the equivalent gate oxide thickness to the several nanometer range; however, this imposes constraints on the precision of the fabrication process. Absent the resonant driving scheme, the turn-on voltage is reduced by half by using a device with a thinner, high- $\kappa$  gate dielectric layer. However, by driving the device resonantly, the turn-on voltage of the device (as defined at the source) is reduced to the millivolt range for devices with different equivalent gate oxide thicknesses. EL can be observed at around 0.25 V for a device with either a thin high- $\kappa$  gate dielectric or a thicker low- $\kappa$  gate dielectric, meaning that the resonant driving scheme enables EL at low turn-on voltages for a wide range of gate oxide thicknesses. Reducing the sensitivity of the turn-on voltage to gate oxide thickness is attractive from a design and fabrication perspective, as it eases the requirement for thin, precisely fabricated gate oxide layers.

Finally, we characterized the brightness and power efficiency of the resonantly driven electroluminescent device. Under an AC driving scheme, the average real power consumed by the device can be calculated as  $(1/T) \int_0^T I(t)V(t)dt$  where  $I(t)$  and  $V(t)$  are the current and voltage across the device, respectively [99]. For sinusoidal modulation, the real dissipated power simplifies as  $I_{rms}V_{rms} \cos(\theta)$  where  $\cos(\theta)$  is the phase shift or power factor that determines the loss. Alternatively, the power consumption at resonance can be interpreted from the Q-factor, which relates to the ratio of energy stored to energy lost per cycle.

Conceptually, the Q-factor represents  $\left(2\pi \cdot \frac{\text{maximum energy stored}}{\text{energy lost per cycle at resonance}}\right)$  in a circuit, and as such reflects total real power loss. As defined earlier,  $Q = \frac{\omega_0 L}{R} = \frac{1}{\omega_0 RC}$  when considering a series resistive-reactive component circuit. The total energy stored at a time is  $\frac{1}{2}C|V_{C,0}|^2$  or  $\frac{1}{2}L|I_0|^2$ . The real power dissipation at resonance is  $\frac{2\pi}{Q} \cdot (\text{energy stored}) \cdot \frac{1}{T} = \frac{\omega_0}{Q} \cdot (\text{energy stored}) = \frac{1}{2}R|I_0|^2 = \langle I_0^2 \rangle R$  which is just the average power dissipation across the resistance for sinusoidal voltages and currents. The electroluminescence intensity from a fast-responding MOS capacitor device is approximately proportional to the number of voltage transitions and charge accumulated,  $\propto \omega C_{device}(|V_C| - V_T)$  for some threshold voltage level  $V_T$ . The power efficiency at resonance is then proportional to

$$\propto \frac{\omega_0 C_{device}(|V_{C,0}| - V_T)}{\frac{\omega_0}{Q} \cdot \frac{1}{2}C|V_{C,0}|^2} \propto \frac{Q|V_{in}| - V_T}{Q|V_{in}|^2} \cdot \frac{1}{1 + C_p/C_{device}}$$

which in the limit of high input voltage is  $\propto 1/|V_{in}|$ , *i.e.* inversely proportional to the input voltage. The peak efficiency occurs when  $|V_{in}| = 2V_T/Q$  and has a value  $\propto Q/V_T$ . Thus in this highly simplified analysis, the power efficiency improves when the turn-on voltage is reduced or the Q-factor is increased. The turn-on voltage depends on the band gap of the emissive material and the equivalent gate oxide thickness, which is further constrained by the desired dynamic range and light outcoupling considerations. A more accurate and quantitative discussion would incorporate the full equivalent circuit model and more precise description of the electroluminescence power, particularly near the turn-on regime.

It should be pointed out that this discussion only refers to the circuit Q-factor, which will be lower than any individual component Q-factor. The power consumption intrinsic to the device itself can be estimated from the device's Q-factor. The circuit Q-factor of a standard series RLC circuit at resonance is approximately  $Q = Q_{ideal} || Q_L || Q_C = (1/Q_{ideal} + 1/Q_L + 1/Q_C)^{-1}$  where  $Q_L$ ,  $Q_C$ , and  $Q_{ideal}$  are the Q-factors of the inductor, capacitor, and circuit with "ideal" components, respectively. Here we refer to the Q for series impedance (in general terms,  $Q = X/R$  for some total impedance  $Z = R + jX$ ); at resonance,  $Q \approx X_r / (R_{ideal} + R_L + R_C)$  where  $X_r$  is the capacitive reactance at resonance and the denominator is the total equivalent series resistance.  $R_{ideal}$  is the series resistance in the circuit assuming ideal or non-lossy  $L$  and  $C$ . In our device operating scheme,  $R_L$  and  $R_C$  are the series losses in the inductor (approximated using a simple series resistance-inductance model at frequencies well below the self-resonant frequency) and series capacitive components (which are dominated almost entirely by losses in the electroluminescent device). Based on this approximation and experimentally measured values ( $Q \approx 25$ ,  $Q_L \approx 45$ , and external resistance in the circuit), we can extract the equivalent Q-factor of the light-emitting device to be around 100. At a operating frequency of 15 kHz and input source voltage of  $f_0 = 1.5 V_{pk}$ , this corresponds to a power consumption of  $\frac{2\pi}{Q_{device}} \cdot \frac{1}{2} C V_{device}^2 f_0 \approx 7 \times 10^{-5} W$  which is on the order of the values from experimental time-dependent measurements, further corroborating our analysis. Using the estimated component values and earlier equation for device Q-factor (and ignoring possible frequency dependence of component values), we can estimate the effective series resistance in the electroluminescent device to be around 9 k $\Omega$ . Note that this resistance is small enough to not impact the bandwidth of the device response in the available measured frequency range (on the order of 10 MHz or below).

Using this operating scheme, a peak EL brightness of 1108 cd/m<sup>2</sup> is observed for a device driven by a 0.7 V<sub>rms</sub>, 14.9 kHz sinusoidal input (Figure 4.19). In this luminance range, the power efficiency generally increases in the vicinity of the resonance frequency, with a peak power efficiency of 28 lm/W. The EL intensity increases near resonance as the current through the device increases and more charge is injected. The spectral shape or color is invariant to the applied frequency and voltage (Figure 4.20). Voltage-dependent EL measurements of a device operated at the resonance frequency show that the power efficiency increases with voltage near the turn-on regime ( $\sim 1 V$ ) but steadily decreases thereafter (Figure 4.21), as the increase in luminance fails to keep pace with the increase in power consumption. The efficiency of organic electroluminescent devices typically exhibits a roll-off at high current densities or brightness levels due to a combination of exciton loss mechanisms such as triplet-triplet annihilation and field-induced quenching [100]. These effects may be exaggerated in AC electroluminescent devices where charge carriers are injected one polarity at a time in alternating pulses with high energies and concentrations near the contact depending on the degree of band bending. Although the net power consumption of AC-driven devices is lower than equivalently driven DC devices due to the largely non-dissipative charging and discharging-based operation, the peak current densities into the semiconducting layer can still be high. Furthermore, temporal simulations of the device's operating mechanism suggest that pulsed carrier injection is less efficient above a certain threshold voltage, since

returning carriers are swept out through the source contact more rapidly and are less likely to recombine with incoming injected carriers of the opposite polarity [98]. Finally, heating effects may play a role in degraded device behavior.

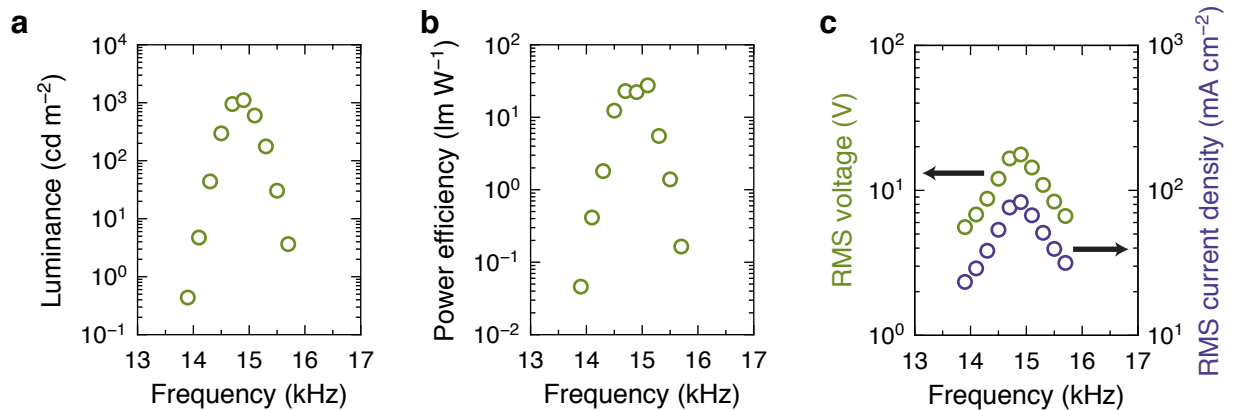


Figure 4.19: (a) Luminance, (b) power efficiency, and (c) RMS voltage and current density as a function of frequency for a device driven by a  $0.7 V_{\text{rms}}$  source voltage using  $L = 100 \text{ mH}$ ,  $C_p = 1 \text{ nF}$  with a CzDBA/CBP emissive layer.

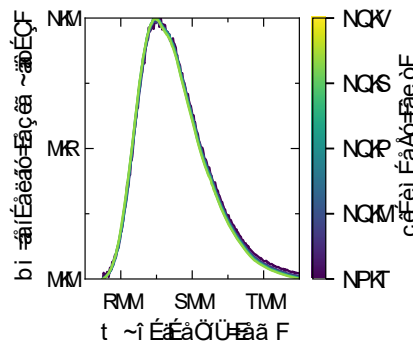


Figure 4.20: EL intensity (normalized counts per second) as a function of wavelength for varying operating frequencies during resonant operation of a CzDBA-based device, corresponding to data in Figure 4.16b with the effective voltages across the device shown in Figure 4.19c.

The maximal performance values are overall considerably higher than those for the same device structure previously reported (around  $\sim 0.1 \text{ lm/W}$  power efficiency at  $10 \text{ cd/m}^2$  for a similar driving waveform and frequency [53]) and rival the highest values reported for AC electroluminescent devices, which typically show relatively poor power efficiencies [53, 101].

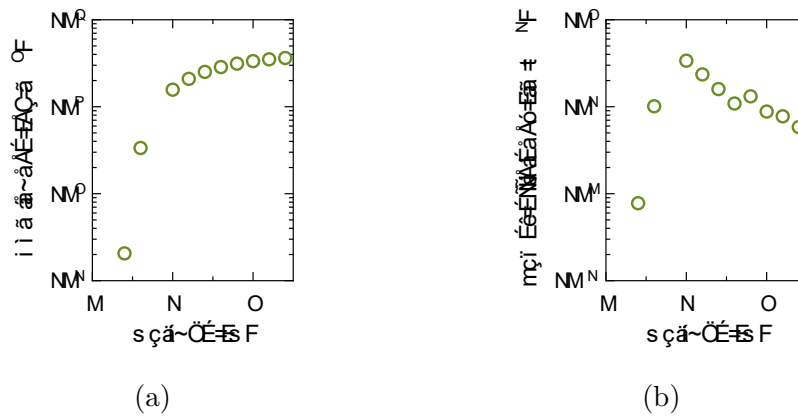


Figure 4.21: (a) Luminance of emission for a device with a CzDBA emissive layer driven by a  $\sim 15$  kHz sine wave in parallel with a 1 nF capacitor, together in series with a 100 mH inductor. (b) Power efficiency corresponding to data in (a) obtained by simultaneously measuring the electrical power consumption and the optical emission power. The horizontal axis represents the peak magnitude of the applied voltage. Here, a peak power efficiency of 33 lm/W is observed at a luminance of 1570 cd/m<sup>2</sup>.

A variety of other capacitive AC electroluminescent devices based on insulating and organic emissive layers have been developed, but these devices either have low power efficiencies (below 1 lm/W [21, 25]) or require complex multilayered structures to reach comparable power efficiency [102]. Table 4.1 presents a comparison of the power efficiency of the device in this paper with related technologies.

While the performance of the presented device still lags that of DC-driven LEDs based on the same emissive materials, the results show that relatively bright and efficient light-emitting devices can still be achieved with a concise device structure that requires only one active semiconducting layer and no additional layers specifically engineered for the emissive material. The simplified device architecture allows for pinhole-tolerant fabrication of the active organic layer since thickness variations and particles on the substrate do not create detrimental electrical shunt paths [66]. From an electrical standpoint, the limit of device efficiency in this scheme ultimately depends on dissipative processes intrinsic to the device; such losses can be revealed by resonant measurements as described in this work. To improve efficiency of the methodology, external resistance in the source contact (i.e. the loss measured before the electroluminescent layer is deposited) and external circuitry should be minimized such that losses at or in the semiconductor dominate. Based on the impedance observed at resonance for the base device structure with and without the emissive layer (Figure 4.7), the effective resistance during AC operation increases by around two times when the luminescent material is deposited. Thus, the efficiency and effectiveness of the driving scheme could be up to twice as high in this case if the losses extrinsic to the EL process were to be theoretically eliminated.

Device	Material	Reference	PE (lm/W)	Brightness
DC LED	AlInGaN (green)	[103]	49	107 mW
DC LED	InGaN (green)	[104]	90	209 mW
DC OLED	CzDBA:CBP	[96]	122	1000 cd/m <sup>2</sup>
DC OLED	CzDBA	[97]	82	1000 cd/m <sup>2</sup>
DC OLED	4CzIPN:CBP	[105]	79	1000 cd/m <sup>2</sup>
DC OLED	Ir(ppy) <sub>3</sub> :CBP	[105]	63	1000 cd/m <sup>2</sup>
DC OLED	Alq <sub>3</sub> :CBP	[106]	4	100 cd/m <sup>2</sup>
AC OLED	Ir(ppy) <sub>3</sub> :PVK:OXD-7	[99]	34	~11 000 cd/m <sup>2</sup>
AC OLED	Ir(ppy) <sub>3</sub> :TCTA	[107]	3	500 cd/m <sup>2</sup>
AC OLED	fluorescent polymer	[21]	~0.15	~250 cd/m <sup>2</sup>
DC OLET	NBTA crystal	[108]	37	~0.1 nW
DC OLET	F8BT	[109]	~1	~5000 cd/m <sup>2</sup>
AC LET	MAPbI <sub>3</sub> perovskite	[49]	$8 \times 10^{-6}$	$9 \times 10^{-1}$ cd/m <sup>2</sup>
AC TFEL	ZnS:Mn	[110]	2	572 cd/m <sup>2</sup>
AC TFEL	ZnS:Mn	[111]	5	~2000 cd/m <sup>2</sup>
AC MOS capacitor	CzDBA:CBP	[this work]	~20	1000 cd/m <sup>2</sup>

Table 4.1: Comparison of representative related light-emitting technologies. “Device” indicates the type of device (direct or alternating current mode of operation and structure). “Material” indicates the material of the emissive layer. “PE” indicates the reported power efficiency. “Brightness” indicates the luminance or output power at which the power efficiency was reported. *Abbreviations:* DC (O)LED = DC-driven (organic) light-emitting diode, AC OLED = AC-driven organic light-emitting device, (O)LET = (organic) light-emitting transistor, AC TFEL = AC thin-film electroluminescent device, MOS = metal-oxide-semiconductor.

## 4.5 Conclusion

In summary, we have demonstrated how reactive components can be designed to generate passive voltage gain across capacitive AC electroluminescent devices via a resonant tank circuit with high Q-factor. This simple operating scheme enables AC electroluminescent devices to be driven at low input voltages in a variety of applications and circumvents the need for additional active electronics which have limited gain-bandwidth product at high operating frequencies, an important consideration for high-speed light-emitting devices. The insensitivity of the operating scheme to the thickness of the dielectric and emissive layers suggests that electroluminescent MOS capacitor devices, alongside properly engineered on-chip inductors, may be amenable to large-scale fabrication via solution-based printing methods, although the efficiency of this methodology depends critically on parasitic but typically unavoidable losses in the external inductive components. By selecting a bright

and high-quality emissive layer, luminance levels (on the order of  $10^3$  cd/m<sup>2</sup>) and power efficiencies (on the order of 10s of lm/W) are achieved, which are over an order of magnitude higher than the values previously measured for the same device structure and approach the values for conventional, direct current-driven organic light-emitting diodes. Thus, relatively high power efficiencies can be attained even with just a single generic contact for bipolar injection and it may be possible to construct viable light-emitting MOS capacitors at other wavelengths for practical light-emitting device applications in the future.

## 4.6 Methods

### Device Fabrication

The fabrication of solution-processed CNT networks has been previously described [112]. Devices were fabricated on 90 nm SiO<sub>2</sub> since the light outcoupling factor due to optical interference from the substrate stack is relatively higher with this gate oxide thickness at the wavelengths of interest [72]. 90 nm SiO<sub>2</sub>/p<sup>++</sup> Si substrates underwent O<sub>2</sub> plasma treatment for 1.5 min, followed by immersion in poly-L-lysine solution (0.1% w/v aqueous solution, Ted Pella) for 5 min and rinsing with deionized (DI) water. Next, 90% metallic CNT solution (1 mg M90% IsoNanotubes-M, NanoIntegris) was drop-casted on the substrate at 100 °C, then rinsed with DI water after the solution dried. The substrate was annealed in forming gas for 1 h at 250 °C. Metal bond pads were patterned by photolithography with positive resist (LOR 5A/S1818) using a laser writer (Heidelberg  $\mu$ PG 101) and deposited by e-beam evaporation of 0.5 nm Ti/25 nm Pd, followed by liftoff in PG remover at 70 °C. To reduce leakage current, the emission area for each device was defined by a second photolithography step and CNTs outside the device areas were etched by O<sub>2</sub> plasma. For the solution-processed emissive layer, a 10 mg mL<sup>-1</sup> solution of Ir(dtbbpy)(ppy)<sub>2</sub> ([4,4'-Bis(1,1-dimethylethyl)-2,2'-bipyridine-N1,N1']bis[2-(2-pyridinyl-N)phenyl-C]iridium(III) hexafluorophosphate, Sigma Aldrich) in acetonitrile was prepared under ambient conditions and drop-casted on top of the device at 60 °C to promote solvent evaporation and uniform film formation. For the thermally evaporated emissive layer, a 16 wt% dopant:host film was co-deposited on top of the device at a base pressure below  $2 \times 10^{-6}$  Torr, where the dopant is CzDBA (5,10-Bis(4-(9H-carbazol-9-yl)-2,6-dimethylphenyl)-5,10-dihydroboranthrene,  $\geq 99\%$ , Luminescence Technology) and the host is CBP (4,4'-Bis(N-carbazolyl)-1,1'-biphenyl,  $\geq 99.5\%$ , Ossila).

### Device Characterization

AC voltages were applied with a function generator (Agilent 33522A). Optical measurements were performed in vacuum ( $\sim 20$  mTorr) with a custom micro-PL instrument in which EL is dispersed by a spectrometer and detected with a charge-coupled device (CCD) (Andor iDus BEX2-DD). The emission power was measured with a power meter (Thorlabs PM100D with S120C photodiode sensor) and cross-calibrated with CCD counts. AC electrical mea-

measurements were performed simultaneously with an oscilloscope (Tektronix TDS 640A) and electrical current was measured with a shunt resistor or a current preamplifier (Stanford Research Systems SR570) where necessary. Component measurements and impedance values were cross-checked with an LCR meter (Agilent E4980AL). DC electrical measurements were performed with a semiconductor parameter analyzer (Agilent 4155C). The external power efficiency was determined by dividing the emission power by the electrical power consumption, which is calculated by integrating the current-voltage product over one period of the sinusoid.

## Device Simulation

Two-dimensional device simulations were performed using Sentaurus TCAD (Synopsys) as previously described [12]. The simulated device consisted of a layer of emissive semiconducting material situated on top of a 90 nm  $\text{SiO}_2$  gate oxide layer with relative permittivity  $\epsilon = 3.9$ . Two 1.4 nm-tall contacts representing neighboring CNTs were placed on each lateral end of the emissive semiconducting material. A sinusoidal AC voltage was applied between the CNT source contacts and a bottom gate electrode underneath the gate oxide. The CNT–CNT spacing was 1  $\mu\text{m}$  and the work function of the CNT contacts was set to be mid-gap relative to the band gap of the semiconducting material in order to generate ambipolar behavior. Material parameters were  $E_g$  (bandgap) = 2 eV,  $\epsilon$  (relative permittivity) = 3.5,  $m_e^*$  (electron effective mass) =  $m_h^*$  (hole effective mass) =  $m_0$ , and  $\mu_n$  (electron mobility) =  $\mu_p$  (hole mobility) = 0.001  $\text{cm}^2 \text{V}^{-1} \text{s}^{-1}$  for the semiconducting layer [113]. Carrier tunneling is enabled at the interface between the source contacts and semiconducting layer. The simulation, which provides a simplified view of device operation for illustrative purposes, assumes a free carrier model with entirely radiative recombination.



## Chapter 5

# Compressive spectroscopy with multicolored electroluminescent arrays

This chapter is adapted from:

V. Wang, S. Z. Uddin, J. Park, A. Javey, “Highly multicolored light emitting arrays for compressive spectroscopy”, *Science Advances*, 9, eadg1607, 2023.

---

Miniaturized, multicolored light-emitting device arrays are promising for applications in sensing, imaging, computing, and more, but the range of emission colors achievable by a single light-emitting diode architecture is limited by material or device constraints. In this work, we demonstrate a highly multicolored light-emitting array with 49 different, individually addressable colors on a single chip. The array consists of pulsed-driven metal-oxide-semiconductor capacitors which generate electroluminescence from micro-dispensed materials spanning a diverse range of colors and spectral shapes, enabling facile generation of arbitrary light spectra across a broad wavelength range (400-1400 nm). When combined with compressive reconstruction algorithms, these arrays can be used to perform spectroscopic measurements in a compact manner without diffractive optics. As an example, we demonstrate microscale spectral imaging of samples using a multiplexed electroluminescent array in conjunction with a monochrome camera.

### 5.1 Introduction

Although multicolored light-emitting arrays are valuable in many areas including low-power sensing, computing, and spectroscopy [1, 114, 115], the emission range of light-emitting devices integrated on a single chip is typically limited to no more than a few colors. Among

the most ubiquitous examples of multi-color light-emitting device arrays are displays, which integrate red, green and blue light-emitting diodes (LEDs) to produce a wide color gamut [116]. Although light-emitting device arrays with a greater number of colors and broader spectral range are useful for multispectral sensing, lattice matching requirements limit the breadth of inorganic materials and thus band gaps that can be grown on a single substrate [117]. Commercial multi-wavelength LED packages instead integrate devices fabricated on separate chips, which results in large package sizes relative to the size of individual devices. Organic materials can be integrated more readily on a single chip due to less demanding growth requirements, but such an approach is cost-prohibitive from a manufacturing standpoint due to the number of process steps and sources required to fabricate the many layers of a conventional vacuum-deposited organic LED. These methods, while sufficient for few-color arrays, are not ideal for scaling light-emitting arrays to tens or hundreds of different colors.

Here, we address this problem by using arrays of electroluminescent, alternating current-driven metal-oxide-semiconductor (MOS) capacitors in which the device electrodes are lithographically defined before deposition of the emitting materials [53]. Since deposition of the emissive layer is the final fabrication step in these devices, microprinting techniques can be used to dispense many different color emitters on a single chip with ease. The rich photo-physical diversity of solution-processable molecular and quantum dot materials allows for a large palette of spectral shapes to be achieved, with no modification to the device structure required for different luminescent materials. By using such an array to actively illuminate objects with spectrally varying light, spectral properties of samples can be interrogated at many wavelengths. The illuminating light spectra need not be narrowband, as optimization algorithms can be used to numerically reconstruct spectral properties of the unknown sample when using many random broadband illumination spectra. The use of compressive reconstructive methods simplifies the fabrication process since essentially any emitter with any arbitrary spectra can be used in the light generating array. Our approach contrasts other reconstructive spectroscopic techniques which focus on modulating passive as opposed to active elements. For example, compressive spectral imaging has been demonstrated with tunable filters and many-colored filter arrays [118, 119]. Recent work has also shown that intrinsically or extrinsically tuned photodetectors based on nanomaterials can be used as micro-spectrometers to measure incident spectra in a highly compact fashion without traditional dispersive optics (e.g. diffraction gratings), heavily engineered optical components (e.g. tunable narrowband filter arrays), or bulky mechanical systems (e.g. interferometers) [120, 121]. These systems, in which numerical methods compensate the lack of precisely engineered components, could find use in consumer or field applications where portable, low power devices with small footprints and costs are desirable [122]. In this work, we illustrate how miniature arrays of electroluminescent devices with arbitrary emission spectra can be leveraged to perform active spectral measurements in a compressive manner.

## 5.2 Arbitrary spectrum generation

Multiplexed arrays of light sources are developed based on a MOS capacitor device in which emissive materials are deposited on top of capacitors fabricated on a silicon substrate (Figures 5.1a and 5.2). Alternating current voltage is applied between the two terminals of the capacitors in order to overcome differences in band alignment at the metal-semiconductor contact and produce transient electroluminescence (EL) at each voltage transition (Figure 5.1c). The application of pulsed bias enables steep band bending and relatively efficient charge injection into different semiconducting materials from metal contacts of different work functions [12]. By using conductive carbon nanotube networks as the top source contact, a high areal density of charge carriers can be injected into materials with poor lateral charge transport [53, 98]. EL can be produced from materials spanning the visible to infrared range (Figure 5.1e), and the intensity increases with both frequency and voltage (Figure 5.1d). Figure 5.1f shows a dense library of emission spectra in the visible range from different material classes such as organic small molecules, conjugated polymers, and colloidal quantum dots [123–126].

Characterization of the brightness, efficiency, color, and spectral bandwidth of the electroluminescent devices as compared to the photoluminescence characteristics of the emitting materials is shown in Figures 5.3 and 5.4, in supplement to previous reports [53, 98, 127]. The frequency response of electroluminescence from these devices depends on the resistance and capacitance of the device structure, in addition to properties of the emitting material such as radiative lifetime, of which a few examples are depicted in Figure 5.5 for different materials [92, 128, 129]. For example, electroluminescence persists much longer after each voltage transient for a PtOEP:PFO emitter layer compared to a PFO emitter layer, in correspondence with the relatively long phosphorescence lifetime of PtOEP [130].

Due to the simplicity of device fabrication, large multicolor electroluminescent arrays can be fabricated on a single substrate. Figure 5.1b depicts an example of a  $7 \times 7$  array of 49 light-emitting devices in which a different emissive layer is deposited on each pixel of the array by micro-dispensing (Figure 5.6, Table 5.1). Nanometer film thicknesses can be obtained using this technique, corresponding to equivalent film volumes of a few picoliters (Figure 5.7). Notably, the bottom array of capacitors is entirely prefabricated by standard photolithography procedures and no processing is required after deposition of the emissive layer, which reduces the complexity of device fabrication and lifts constraints on the processability of different monolithically integrated luminescent materials. The emissive layer can comprise of mixtures of different materials and does not need to be thin, pinhole-free, or any particular shape. The device size and pitch accuracy can be improved in the future by adopting more advanced techniques to automate the deposition of small liquid volumes (e.g. microarray printing technology in which thousands of samples can be processed on one chip [131]).

To emphasize the versatility of this device platform, we first demonstrate how nearly any light spectra can be generated given a sufficiently large library of emitters. The total light spectrum from a miniature EL array is a linear combination of the spectra from the

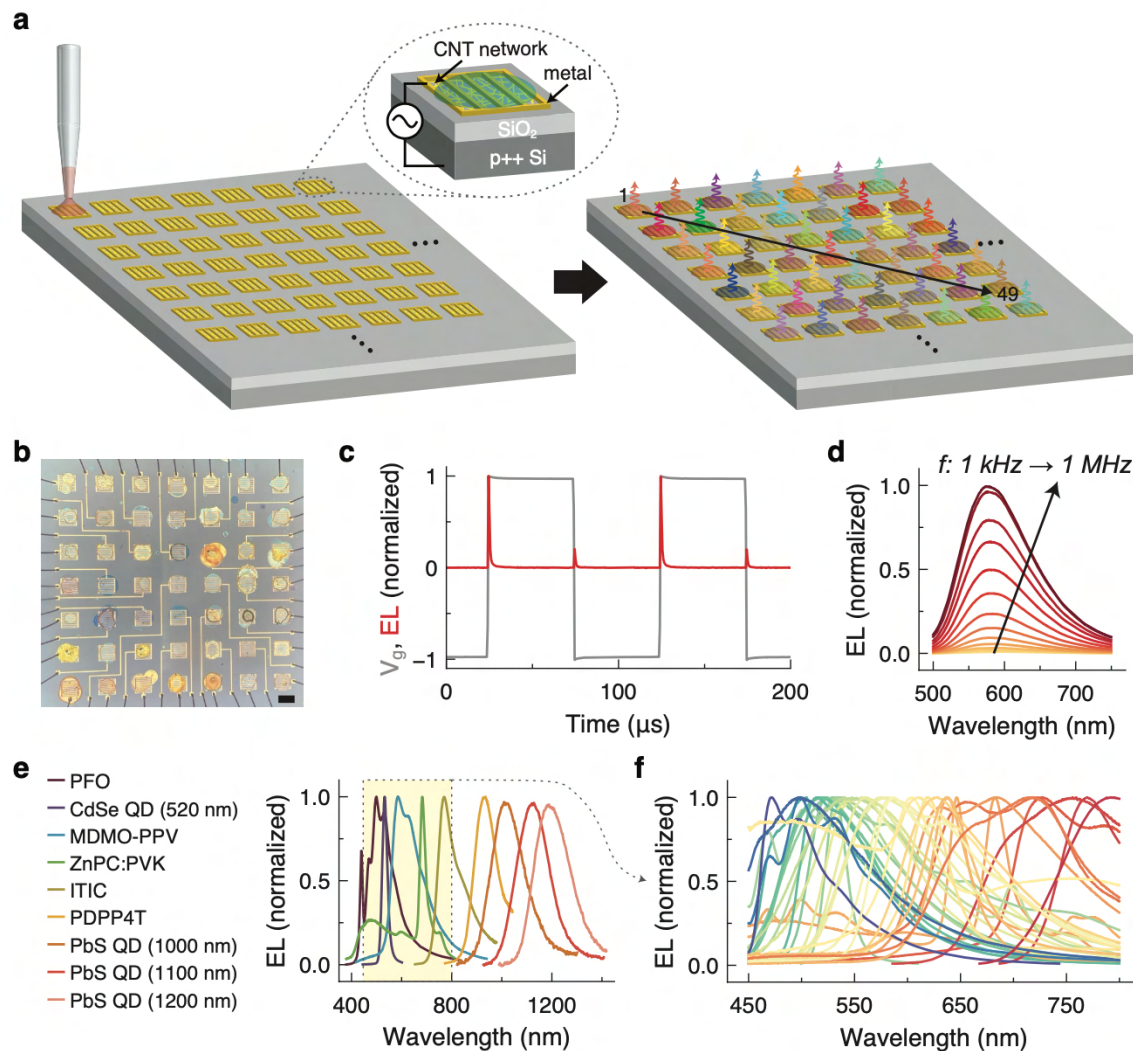


Figure 5.1: **Multiplexed array of multicolored electroluminescent devices.** (a) Schematic of an array of light-emitting MOS capacitors in which different emitting materials are micro-dispensed on each capacitor. (b) Optical image of a fabricated 7 × 7 array of devices with a different emitter dispensed on each pixel of the array. Scale bar: 400 μm. (c) Example of time-resolved electroluminescence (red) corresponding to a square wave pulsed gate voltage waveform (grey). (d) Example of increase in EL intensity with driving frequency. (e) EL spectra from several materials emitting across the blue to near-infrared range, with emission at all wavelengths in between. (f) Example of EL spectra from a wide range of materials emitting in the visible range (Table 5.2).

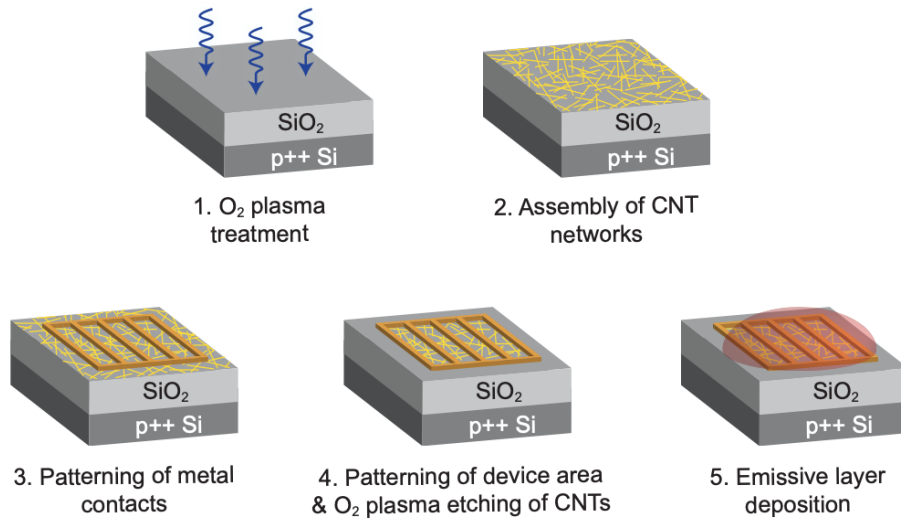


Figure 5.2: **Fabrication process of a pulsed metal-oxide-semiconductor (MOS) capacitor device.** A 1.5 min O<sub>2</sub> plasma treatment is applied to a SiO<sub>2</sub>/Si substrate. The surface is modified with poly-L-lysine, then covered with aqueous carbon nanotube (CNT) solution for 5 to 10 min to self-assemble CNT networks before being rinsed with DI water. A metal contact is patterned on top of the CNT network to reduce lateral parasitics and provide a bond pad for electrical connection. CNTs outside the device area are etched with O<sub>2</sub> plasma to prevent leakage between devices. The emissive layer is deposited as the last step (in this work, by simple drop-casting of dye solutions on top of the device using a micropipette). The devices are then wire-bonded to a chip carrier for measurement.

individual elements. Based on this framework, an array of emitters can be designed to yield a desired light spectrum  $\mathbf{y} = \mathbf{y}(\lambda)$  by solving the least-squares optimization problem  $\min_{\boldsymbol{\beta}} \|\mathbf{A}\boldsymbol{\beta} - \mathbf{y}\|_2^2$  (subject to  $\beta_j \geq 0$ ) where  $\mathbf{A}$  is the set of EL spectra and  $\boldsymbol{\beta}$  is the vector of linear weights for each spectrum. Since we wish to minimize the number of utilized spectra for practical purposes, we perform an additional initial optimization step to select a smaller subset of emitters for the array design:  $\min_{\boldsymbol{\beta}} \|\mathbf{L}\boldsymbol{\beta} - \mathbf{y}\|_2^2 + \gamma\|\boldsymbol{\beta}\|_1$  where  $\mathbf{L}$  is the entire large library of EL spectra.  $\mathbf{A}$  is then composed of the  $N$  highest-weighted spectra, where  $N$  depends on the acceptable error tolerance. The L<sub>1</sub> regularization term encourages sparsity in the solution and therefore reduction of  $N$ .

Figure 5.8 illustrates an example of spectrally matched light generation in which we targeted a spectrum that linearly varies with wavelength in the shown range. By solving the above optimization problem using a prior library of EL spectra, we found that five chosen emitters were sufficient to recreate the desired spectrum (Figures 5.8b-d; Figure 5.9). The spectral weights were implemented by tuning the driving voltage and frequency for each device such that the EL intensity matched the estimated coefficient. Unlike macroscale approaches where custom light synthesis is performed using commercial inorganic LEDs [132–

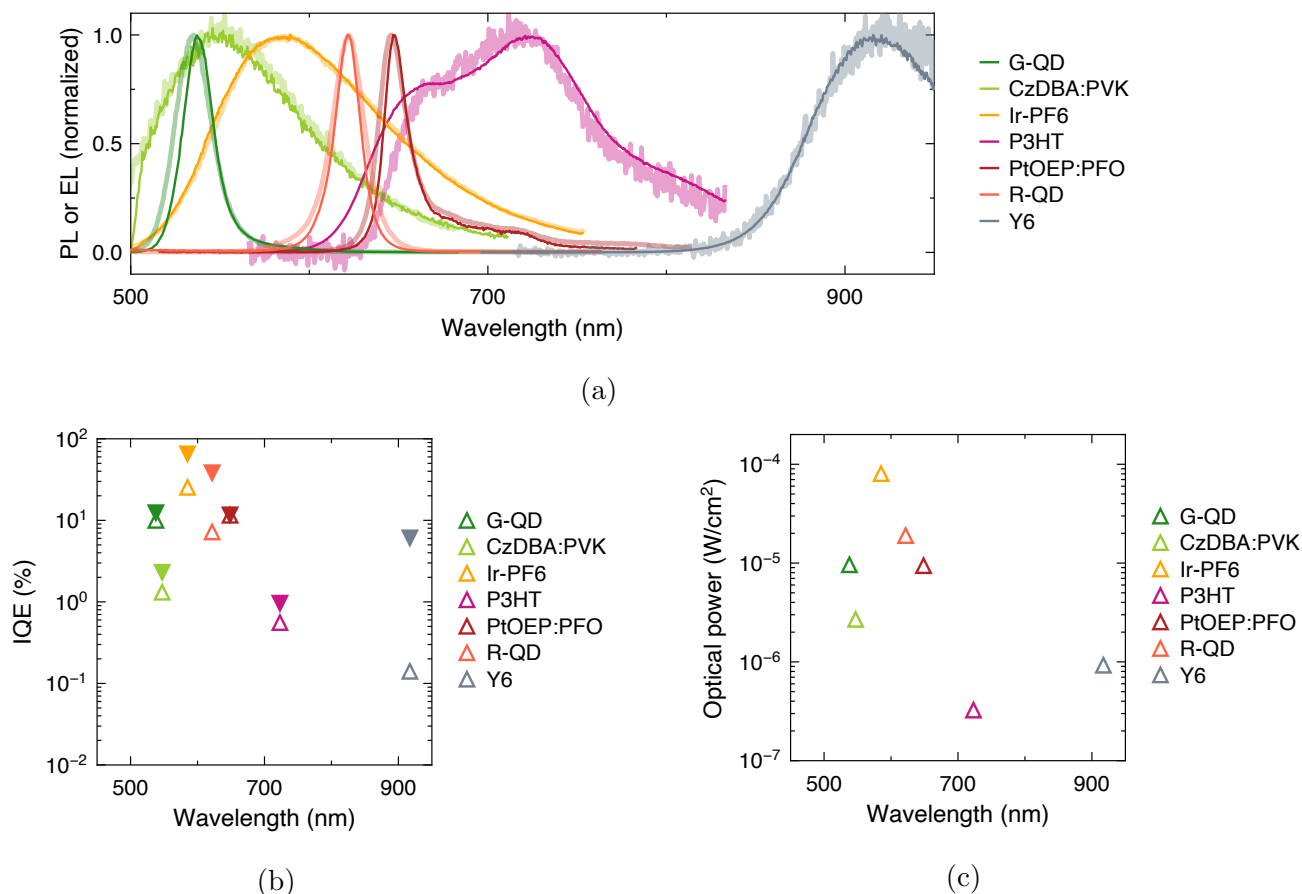
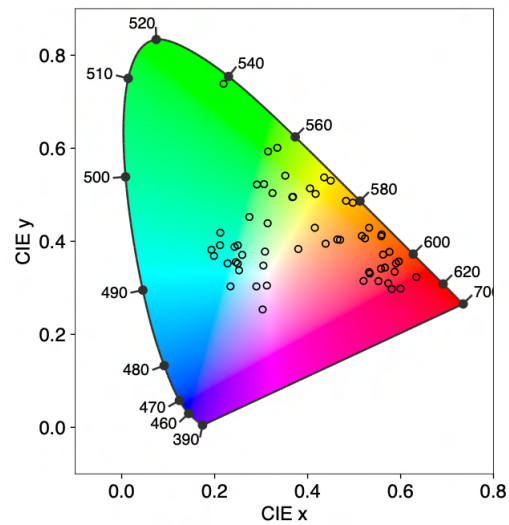
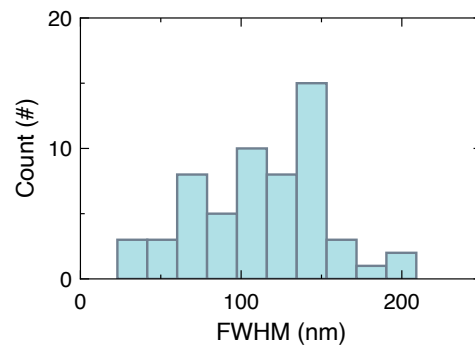


Figure 5.3: **Performance of light-emitting capacitor devices.** Performance is shown for different types/colors of drop-cast emitters on 50 nm SiO<sub>2</sub> gate oxide. (a) Photoluminescence (thin dark lines) and electroluminescence spectra (light shaded lines) of emitters indicated in the legend. (b) Internal electroluminescence quantum efficiency (open markers) and photoluminescence quantum yield (PL QY, solid markers) for different emitters. PL QY of drop-cast films was estimated from calibrated micro-photoluminescence measurements based on a previously described procedure [39]. Device quantum efficiency was estimated based on the procedure described earlier [53]. (c) Brightness of electroluminescent devices based on different emitters. G-QD and R-QD refer to CdSe-based quantum dots with peak emission around 520 nm and 620 nm, respectively.

134], our approach is miniaturized and compatible with spectrally diverse materials, from quantum dots with sharp emission peaks to organic polymers with broad spectral responses. This flexibility permits more accurate spectral targeting and overcomes technological limitations in the spectral availability of certain materials, such as the “green gap” from which III-nitride LEDs suffer [135].



(a)



(b)

Figure 5.4: **Characterization of electroluminescent colors.** (a) Chromaticity diagram showing CIE coordinates of different electroluminescent emitters in Table 5.1. (b) Distribution of full-width at half-maximum (FWHM) of electroluminescence spectra of emitters in Table 5.1.

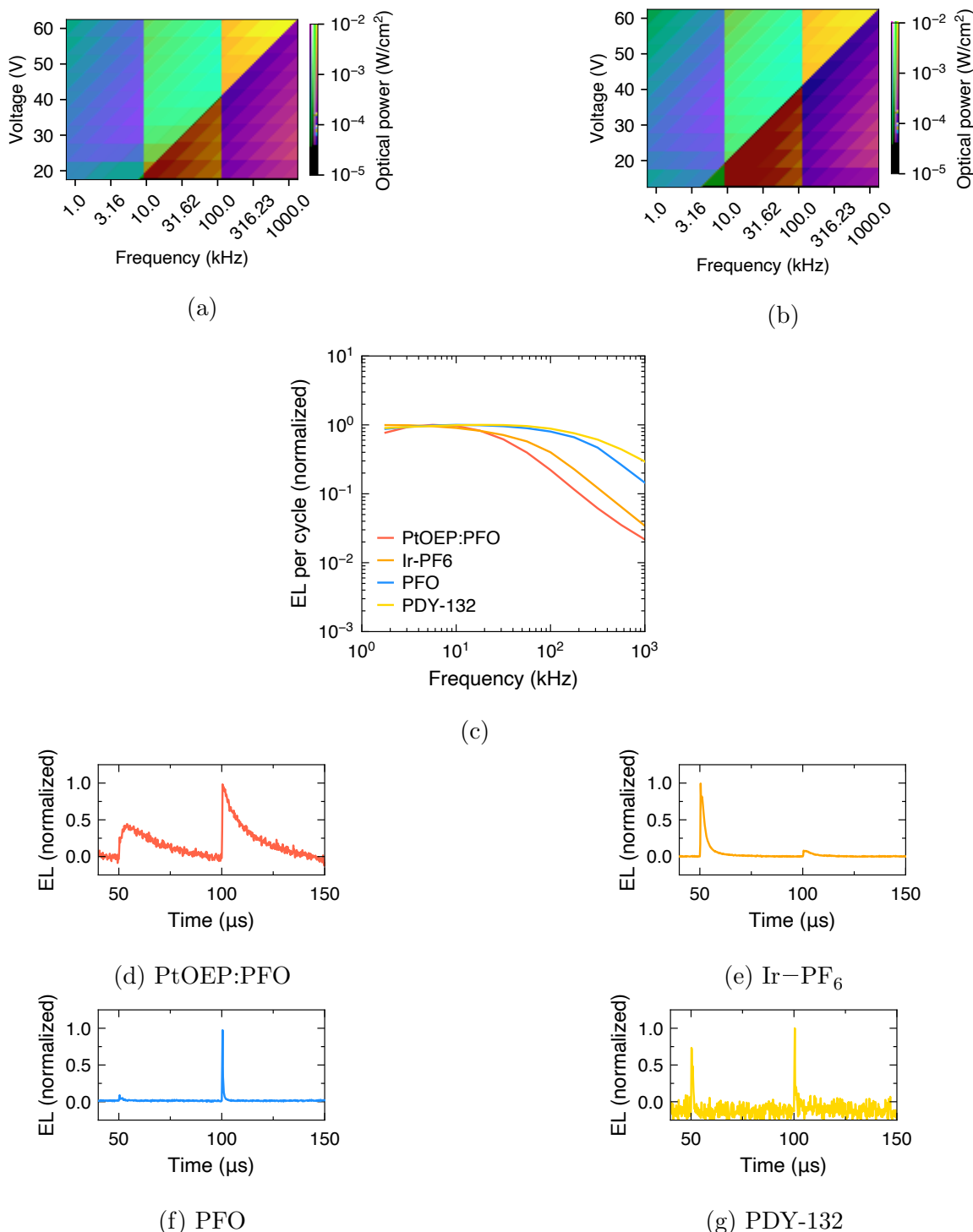


Figure 5.5: **Frequency response of electroluminescence.** Brightness of (a) Ir-PF<sub>6</sub> and (b) red CdSe quantum dot emitters as a function of square wave voltage and frequency. (c) Normalized light emission per cycle versus frequency for different emitter materials, as well as their respective time-resolved electroluminescence response (d-g). The lifetime of these materials are, in order, approximately 55  $\mu\text{s}$  (PtOEP) [130], 0.6  $\mu\text{s}$  ([Ir(ppy)<sub>2</sub>(dtb-bpy)](PF<sub>6</sub>)) [92], 5 ns (PFO) [128], and 2 ns (PDY-132) [129]. An upward  $\pm 25$  V voltage transition occurs at  $t = 100$   $\mu\text{s}$ , and a downward voltage transition occurs at  $t = 50$   $\mu\text{s}$ . Devices were fabricated on 90 nm SiO<sub>2</sub> gate oxide.



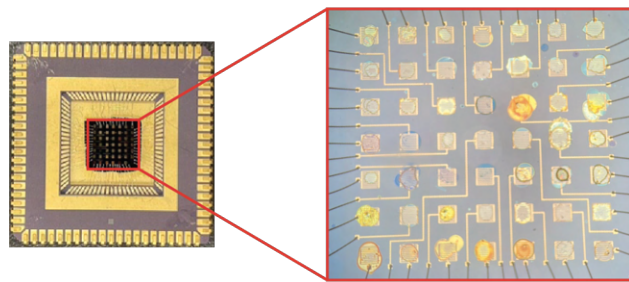


Figure 5.6: **Photograph of bonded device chip.** An example  $7 \times 7$  array of 49 electro-luminescent devices is wirebonded to a chip carrier, with a different emissive layer drop-cast on each device (refer to Table 5.2 for the full description of the emissive layer compositions).

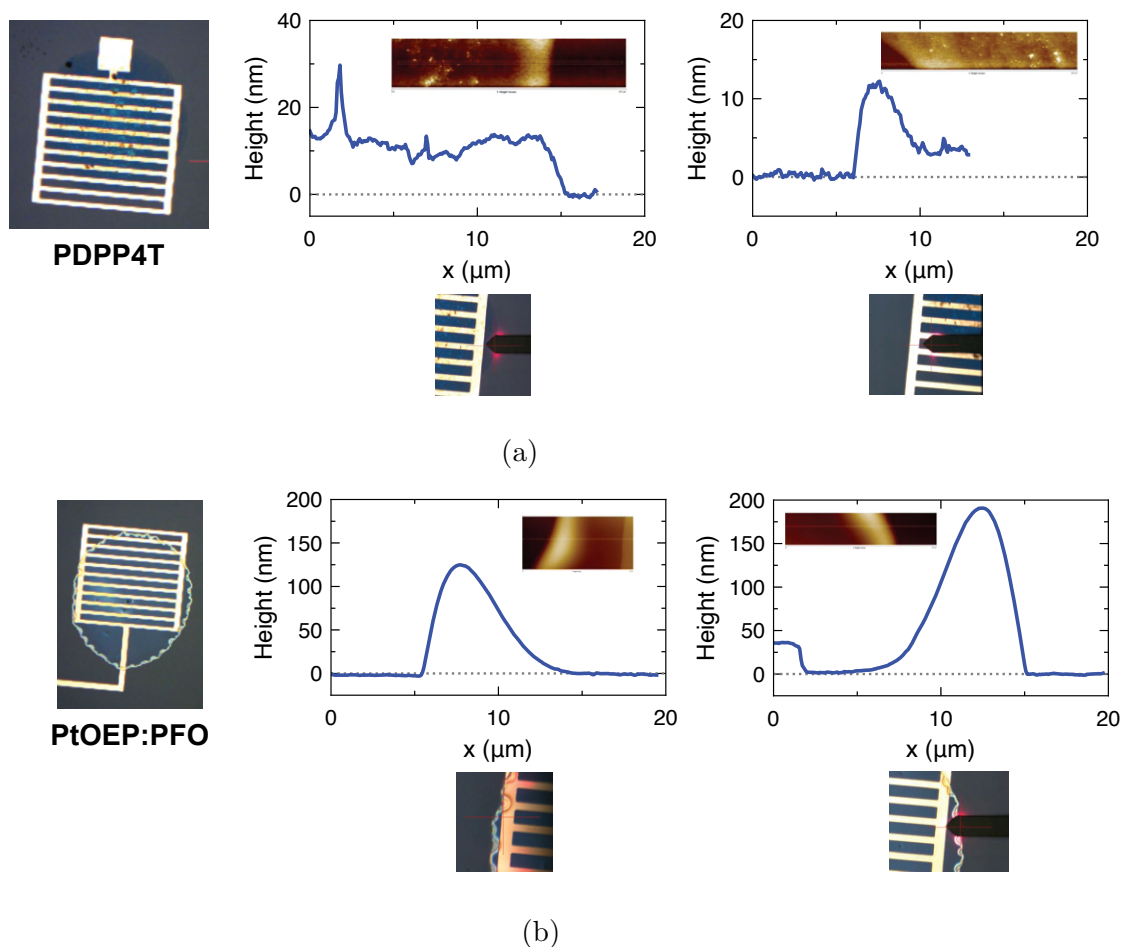


Figure 5.7: **AFM measurement of drop-cast films.** Images of (a) PDPP4T and (b) PtOEP:PFO devices are shown on the left, with the AFM image of the edge area shown in the inset of each plot and the imaged location shown below each plot. The thickness of these films are on the nanometer scale. Note the film thickness in the right plot in (b) is well below the  $\approx 30$  nm height of the metal contact. For a  $\approx 5$  nm thick film on the grid which has an area around  $500 \mu\text{m} \times 500 \mu\text{m}$ , the film volume is on the order of  $1 \times 10^{-15} \text{m}^3 \approx 1 \text{pL}$ .

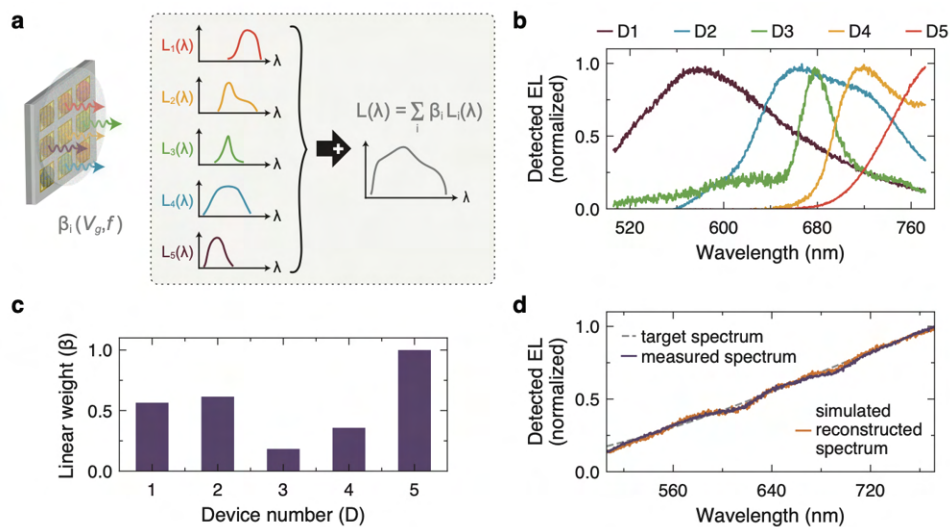


Figure 5.8: **Design of arbitrary EL spectra.** (a) Schematic depicting generation of arbitrary EL spectra using an EL array. (b) Example of EL spectra and (c) relative weights of the corresponding spectra used to reconstruct the target spectrum in (d). The dashed grey curve represents the desired target spectrum. The purple curve represents the experimentally measured spectrum from the implemented 5-device EL array. The gold curve represents the designed spectrum from calculation.

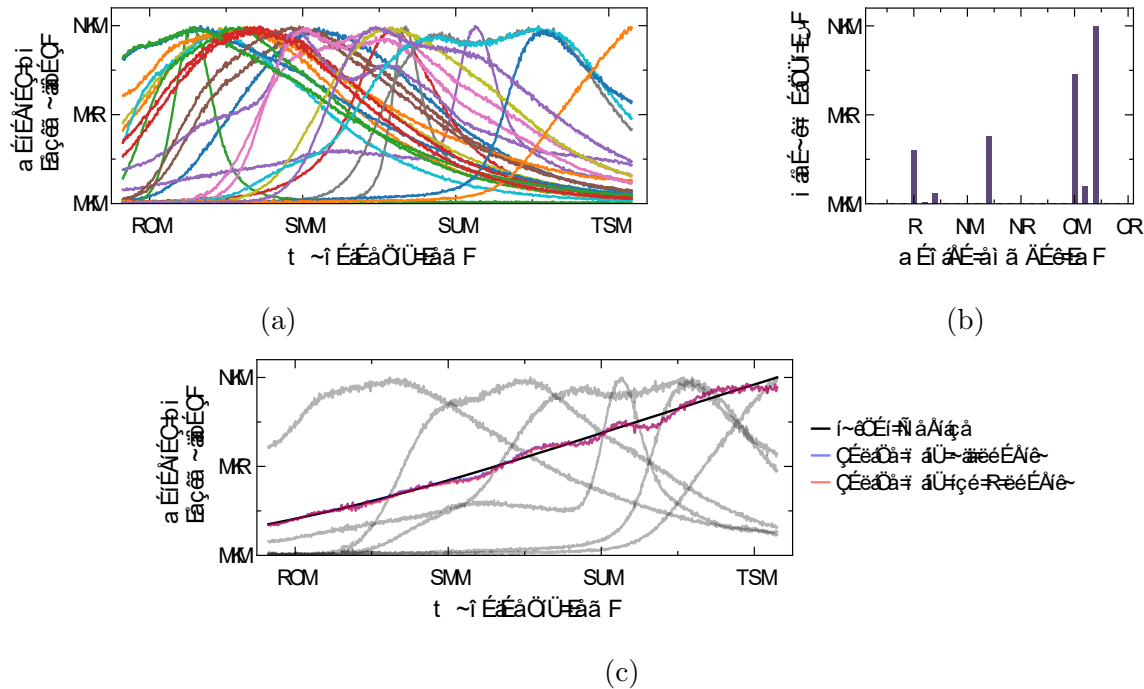


Figure 5.9: **Design of arbitrary light spectra.** Starting from a set of feasible EL spectra (in this case, 25 different EL spectra as shown in (a)), we attempt to estimate the target spectral function (shown by the solid black line in (c)) using regularized least-squares with  $L_1$  regularization. From this optimization step, we find that only a few devices are needed to reconstruct the target function relatively accurately as shown in (c). The designed spectra using all 25 emitters is very similar to the designed spectra using just 5 emitters (in which we selected the 5 emitters with the highest linear coefficients). The 5 spectra used to design the target function in this example are shown in transparent grey. This design procedure allows the experiment complexity to be greatly reduced as a fewer number of devices need to be fabricated, characterized, tuned and driven.

### 5.3 Compressive spectral measurement

Having demonstrated the scalability and versatility of the device platform, we now show how the breadth of achievable EL spectra enables active spectral measurements. As an example, we consider the problem of measuring transmittance spectra with a single-pixel detector. The transmittance spectrum of an unknown sample is traditionally measured by passing a broadband light source through the sample, separating wavelengths of the light with a dispersive element (e.g. grating), and measuring the intensity of transmitted light with an arrayed detector. The spectral range and resolution of these systems is dictated by properties such as the grating groove density and focal length, with longer focal lengths and higher groove densities preferable for higher spectral resolution. An alternative approach to measuring spectral information, which does not require bulky engineered optical components, is reconstructive spectrometry in which spectral information can be algorithmically recovered. Figure 5.10a illustrates how transmittance spectra can be determined using arbitrary variable incident light and a single photodetector. By sending sufficient different but known light spectra through the sample, the transmission function of the sample can be estimated from the photodetector readings through an inverse calculation. Specifically, we solve the following optimization problem:

$$\begin{aligned} \min_{\mathbf{c}} \quad & \|\mathbf{A}\mathbf{c} - \mathbf{I}\|_2^2 + \gamma\|\mathbf{c}\|_2^2 \\ \text{subject to} \quad & c_j \geq 0 \quad \forall j \end{aligned}$$

in which regularization is used to compute a solution to the underdetermined set of equations and the sample function is estimated using a set of Gaussian basis functions [136, 137].  $\mathbf{A}$  is the matrix of EL spectra (Figure 5.10b) transformed by the basis functions,  $\mathbf{I}$  is the measured photodetector values for each incident EL spectra (Figure 5.10c), and  $\mathbf{c}$  is the unknown weights of the basis functions. To elaborate in more detail, spectra were reconstructed using least-squares with Tikhonov regularization and a non-negativity constraint (or, non-negative least-squares). To reduce the dimension of the estimated parameter space, we approximated the sample functions using a smaller set of Gaussian basis functions  $\phi_j(\lambda)$ . Mathematically, this is represented as:

$$S(\lambda) \approx \hat{S}(\lambda) = \sum_{j=1}^m c_j \phi_j(\lambda)$$

$$\text{where } \phi_j(\lambda) = \frac{1}{\sigma\sqrt{2\pi}} \cdot e^{-\frac{1}{2}\left(\frac{\lambda-\mu_j}{\sigma}\right)^2}$$

In practice, we use Gaussians with evenly spaced means  $\mu_j$  and constant standard deviation  $\sigma$ . Since the measured value on the photodetector is an integral of the product of the illumination spectra, sample function (i.e. its spectral transmittance or reflectance), and detector spectral responsivity, we can linearize the optical system with the following matrix

equation:

$$\sum_{j=1}^m \left( \int_{\lambda_1}^{\lambda_2} L_i(\lambda) D(\lambda) \phi_j(\lambda) d\lambda \right) c_j = I_i$$

$$\mathbf{A}\mathbf{c} = \mathbf{I}$$

in which each element  $A_{ij}$  of matrix  $A$  is computed using the stated integral. Here,  $L_i(\lambda)$  is the illumination (EL) spectra of the  $i$ th device,  $D(\lambda)$  is the spectral responsivity of the detector, and  $I_i$  is the measured photodetector value corresponding to illumination from the  $i$ th device. This system of equations is underdetermined, but an estimated solution can be found using least-squares minimization with regularization:

$$\min_{\mathbf{c}} \|\mathbf{A}\mathbf{c} - \mathbf{I}\|_2^2 + \alpha \|\mathbf{c}\|_2^2$$

s.t.  $c_j \geq 0 \quad \forall j$

where the estimated solution  $\hat{S}(\lambda)$  is constructed as a linear combination of the basis functions weighted by the  $c_j$  values.

The result of employing this scheme to measure the transmission function of a test sample is shown in Figure 5.10d. The same measurement scheme can also separately distinguish two narrow bandpass filters with 10 nm spectral separation, as well as other spectral transmission functions (Figures 5.11 and 5.12). From simulated experiments of test samples with two closely spaced spectral peaks, the spectral resolution of the measurement scheme using the current set of electroluminescence spectra is estimated to be around 10 nm (Figure 5.13) and varies depending on the number of light-emitting devices used, with better spectral accuracy obtained as the number of measurements increases.

Due to the unique inherently pulsed nature of the devices, alternate spectral measurement schemes are possible. For example, a photodetector and lock-in amplifier can be used to perform lock-in detection of the transmitted light. This detection method enables high signal-to-noise measurement under ambient light conditions since the transmitted light is modulated at kHz rates and distinguishable from background lighting (Figure 5.14). As another example, near single-shot spectral measurement is possible using a high-speed photodetector. Each device in the array can be modulated with a different phase shift such that the light intensity from each device is distinguishable in the time-resolved capture of the photodetector readings (Figure 5.10e). As a proof-of-concept, we fabricated a  $2 \times 3$  array of devices and simultaneously drove each device with a square wave in which there is fixed delay between every device's applied voltage waveform (Figure 5.15). We then measured the time-resolved EL using a silicon photodiode, with and without the sample in between the EL array and detector (Figures 5.16 and 5.17). The transmittance spectrum of a simple unknown sample can be estimated from the known EL spectra and integrated values of time-resolved EL for each device (Figure 5.10f). In principle, spectral acquisition under this scheme could be executed in as little as  $N\tau$  seconds (where  $N$  is the number of devices in the array and  $\tau$  is the average EL lifetime), thereby enabling fast spectral measurement without device switching.

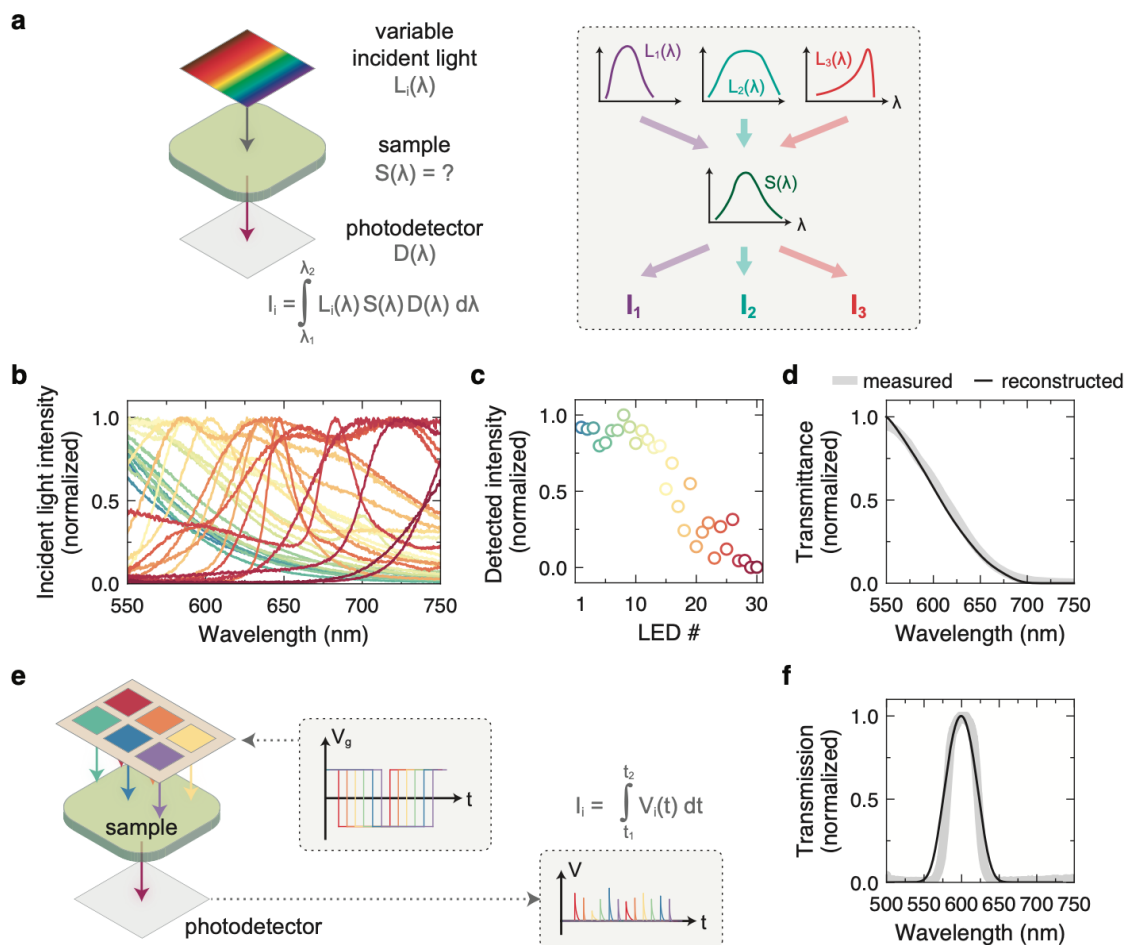


Figure 5.10: **Spectral measurement with highly multicolored arrays.** (a) Schematic depicting the concept behind transmittance measurement using variable incident illumination and a single photodetector. (b) The spectra of EL devices (Table 5.3) and (c) photodetector readings used to reconstruct the sample transmittance in (d). (e) Schematic depicting the concept behind time-multiplexed transmittance measurement using a series of phase-shifted gate voltage waveforms applied to each device in a  $2 \times 3$  EL array. (f) Reconstruction of spectral transmittance based on the concept in (e).

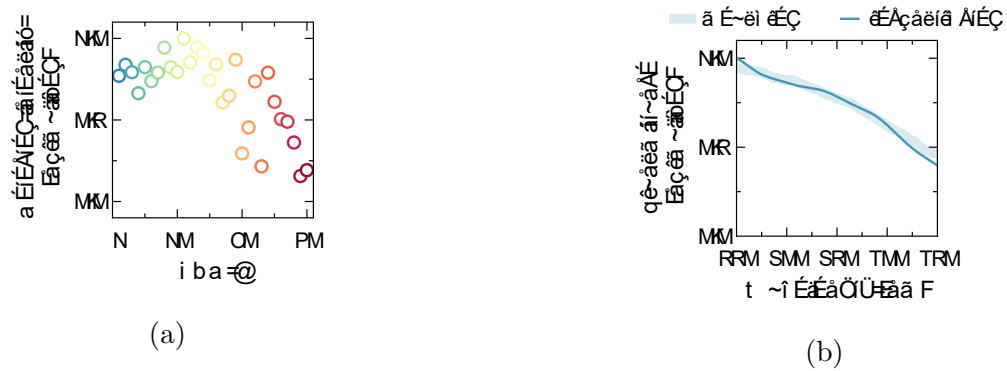


Figure 5.11: **Example of spectral reconstruction.** Reconstruction of another sample is performed using the same EL device spectra in Figures 5.10b-d. (a) Normalized photodetector values corresponding to each light-emitting device. (b) Recovered transmittance spectra and comparison to measured transmittance spectra of the sample.



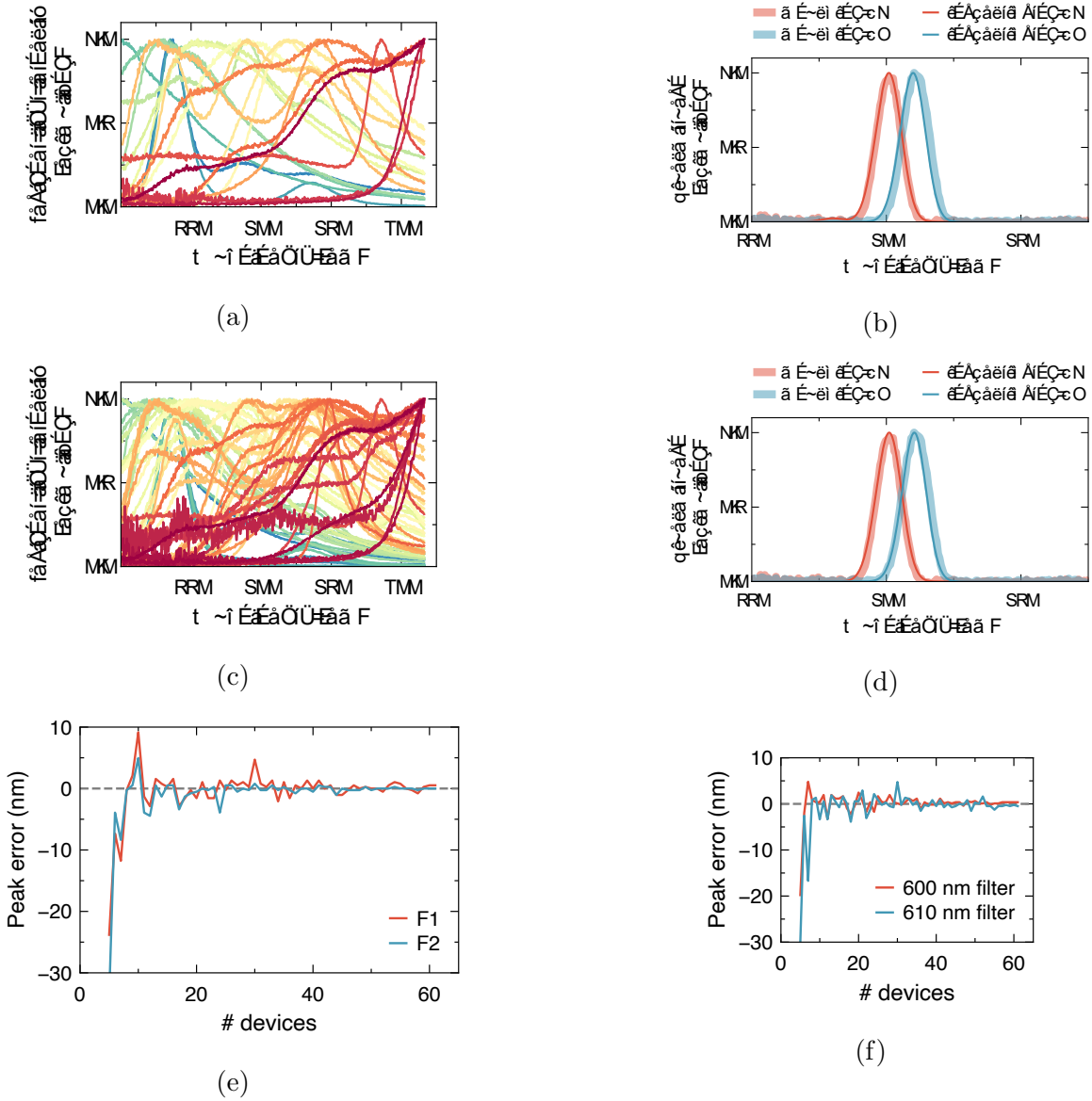


Figure 5.12: **Spectral reconstruction of band-pass filters.** Two band-pass filters with peak transmittances around  $\lambda_0 = 600$  nm (F1, red) and 610 nm (F2, blue) are characterized using a simple least-squares solution without regularization. The peak wavelengths of the reconstructed transmittance spectra match closely to that of the measured data (within 1 nm). The same sets of devices were used to perform measurements of both filters in each plot. (b) shows the result when 20 EL devices are used (with the corresponding spectra in (a)). (d) shows the result when combined data from 61 different EL devices are used (with the corresponding spectra in (c)). As indicated by the reconstructed spectra, similar results can be obtained using the fewer number of devices, as long as the basis of EL spectra provides appropriate coverage over the spectral range. (e) Error of peak wavelength ( $\Delta\lambda = \lambda_{\text{pk, reconstructed}} - \lambda_0$ ) of reconstructed result for F1 and F2 as a function of number of devices  $N$ , where the devices are randomly sampled from the set of all devices for each  $N$ . (f) Simulated result for (e) in which simulated photodetector measurements (calculated by integrating the illumination spectra and filter transmittance and adding Gaussian noise  $\sim \mathcal{N}(0, 1)$ ) are used instead of the experimentally measured photodetector measurements.

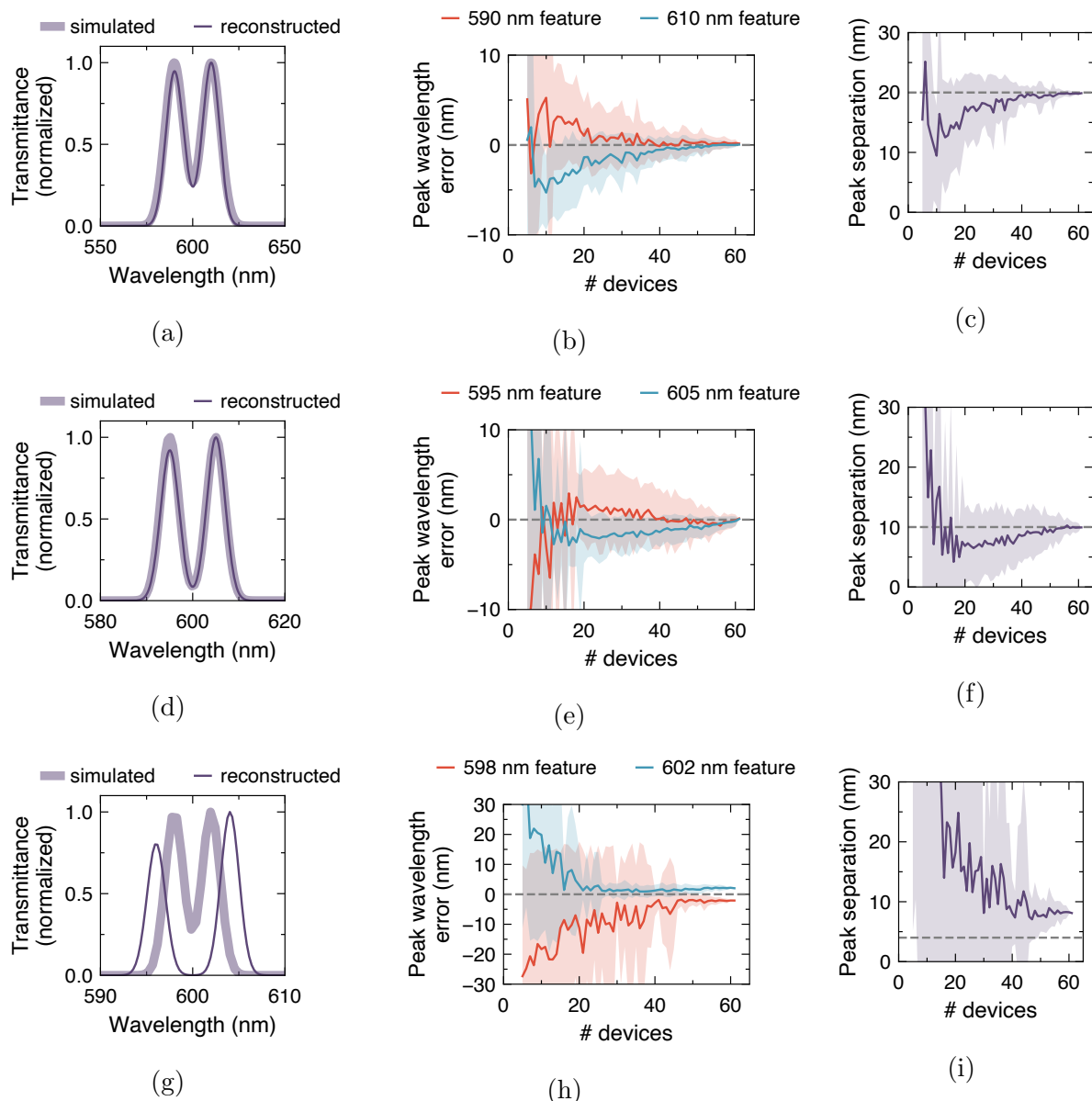


Figure 5.13: **Spectral resolution of reconstructed spectra.** Simulated experiments are performed on samples with different spectral resolution as a function of the number of light-emitting devices  $N$ . Photodetector measurements were simulated by integrating the illumination spectra and sample transmittance and adding Gaussian noise  $\sim \mathcal{N}(0, 1)$ . As shown in Figure 5.12, simulated experiments represent the experimental measurement relatively well. Simulated samples with Gaussian features separated by 20 (a,b,c), 10 (d,e,f), and 4 (g,h,i) nm are reconstructed. The standard deviation of the Gaussian peaks are also scaled ( $\sigma = 5, 2$ , and  $1$  nm for the simulated samples with 20, 10, and 4 nm peak separations respectively). In (a,d,g), the shaded curve represents the simulated sample transmittance and the solid curve represents the reconstructed result. (b,e,h) show the error of each peak's center wavelength in the reconstructed result. (c,f,i) show the distance between the two peaks in the reconstruction. The solid line represents the mean result from 50 batches of a set of  $N$  randomly sampled devices. The shaded region represents  $\pm 1$  standard deviation.

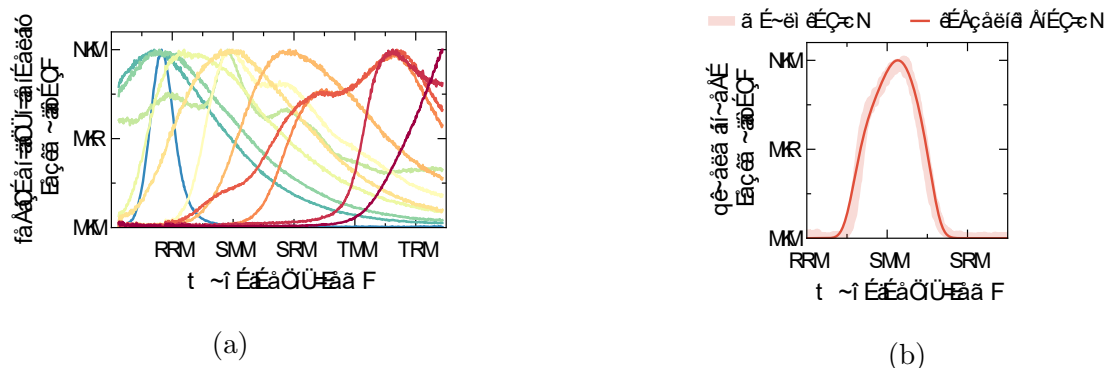


Figure 5.14: **Spectral reconstruction using lock-in detection.** Reconstruction is performed using 12 EL devices and a silicon photodiode connected to a lock-in amplifier to record the EL intensities. EL intensity is acquired for every device with and without the sample in place. From these values as well as the known EL spectra from the preceding array calibration step, the sample function can be reconstructed.

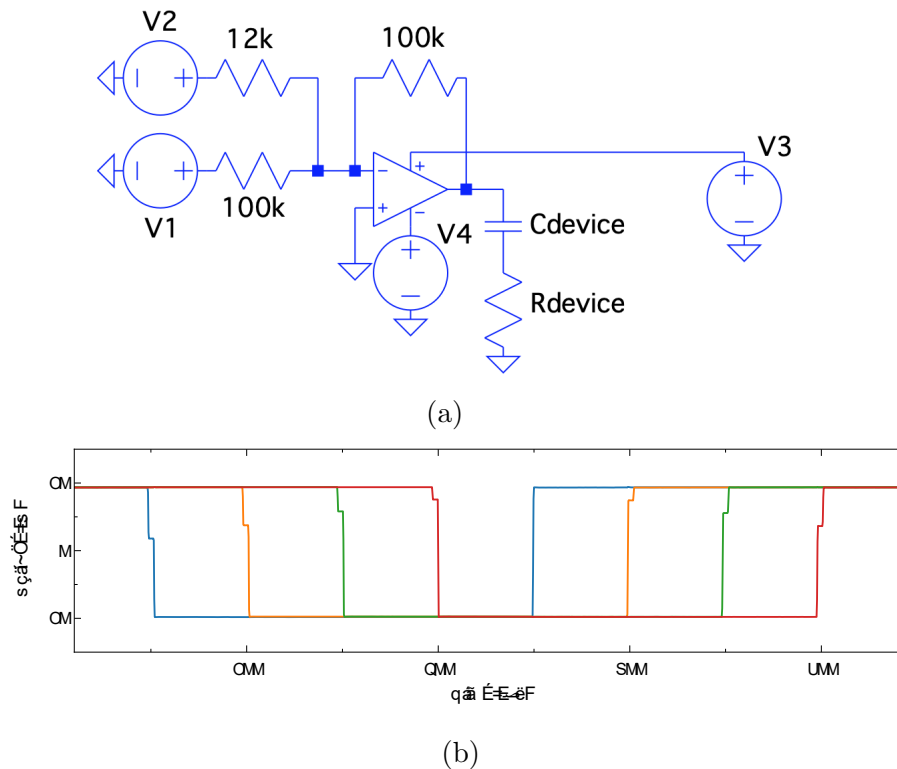


Figure 5.15: **Generation of time-shifted electrical pulses.** (a) Diagram of a square-wave generating circuit for driving a pulsed light-emitting MOS capacitor. The device is connected between the output of the operational amplifier (TLE2141, Texas Instruments) and electrical ground.  $V2$  represents a 50% duty cycle pulse between 0 V to 5 V which is generated from a digital output pin on an Arduino microcontroller. Here, we set  $V1$  and  $V4$  to  $-20$  V and  $V3$  to 20 V using a dual output DC power supply (E3620A, Hewlett-Packard), but these voltages can be adjusted depending on the magnitude of the square wave desired. To drive multiple devices with phase-shifted pulse waveforms, we replicated this circuit for every device but shifted  $V2$  by an extra  $100 \mu\text{s}$  for each consecutive device (the  $V2$  pulses are controlled directly by an Arduino program). (b) Measured voltage waveforms produced by four parallel repetitions of the circuit above. Note that there is some jitter in this simple driving setup, which manifests as double transitions or pulses in time-averaged oscilloscope traces, even though the rising/falling edges of the waveform at the output of the operational amplifier have a single transition with slew time around  $1 \mu\text{s}$ .

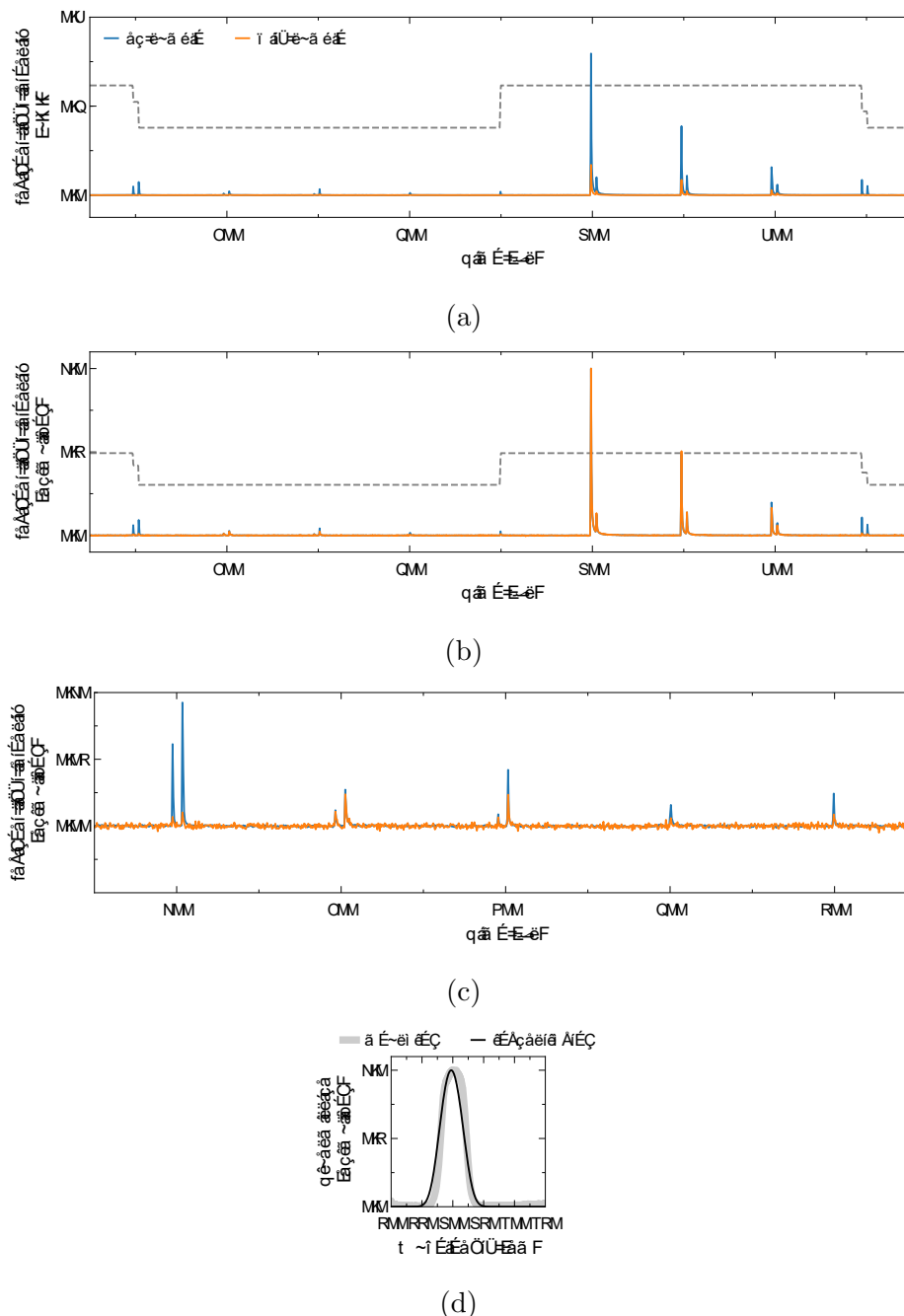


Figure 5.16: **Measurement of time-multiplexed electroluminescence from a  $2 \times 2$  device array.** The emitters are P3HT:MEH-PPV,  $[\text{Ir}(\text{dtbbpy})(\text{ppy})_2]\text{PF}_6$ , PFO, and  $\text{Ru}(\text{bpy})_3(\text{BF}_4)_2$ . The dashed grey line shows the voltage waveform applied to the first device; the voltage waveforms applied to the second through fourth devices are each delayed by  $100 \mu\text{s}$  from the previous waveform. The plots above show approximately  $900 \mu\text{s}$  of time-resolved signal from an oscilloscope, during which time we can observe the EL at both upward and downward transitions for all four devices. The blue and orange curves represent the time-resolved light intensity without and with a sample placed between the device array and photodetector. (b) and (c) show the normalized data at different timescales. (d) Reconstruction result for a measured sample using this scheme.

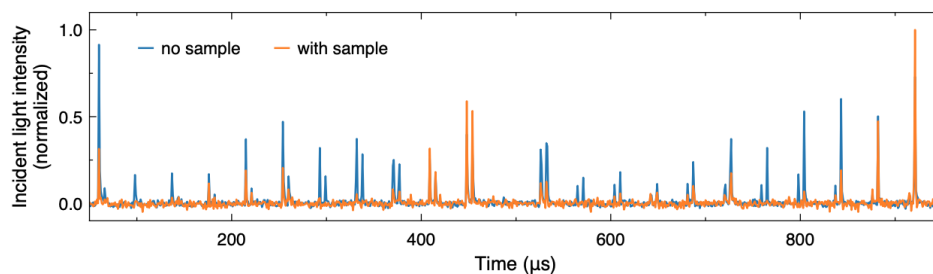


Figure 5.17: **Measurement of time-multiplexed electroluminescence from a  $3 \times 2$  device array.** The emitters are F8BT/PDY-132, F8BT,  $[\text{Ir}(\text{dtbbpy})(\text{ppy})_2]\text{PF}_6$ , PFO, P3HT,  $\text{Ru}(\text{bpy})_3(\text{BF}_4)_2/\text{P3HT}$ . The voltage waveform applied to each device is delayed by  $40 \mu\text{s}$  from the previous waveform. The blue and orange curves represent the time-resolved light intensity without and with a sample between the device array and photodetector (corresponding to Figure 5.10e). The results of sample reconstruction are shown in Figure 5.10f.

## 5.4 Compressive spectral imaging

Finally, reconstructive spectral measurements can be parallelized across space by using a detector array to perform microscopic spectral imaging. Figures 5.19a-b illustrate measurement schemes for microscale reflected- and transmitted-light spectral imaging in which the EL array serves as the light source and a monochrome silicon CCD camera captures images of the sample. With a single detector reading, we can only probe the micro-reflectance spectra of a single spot on a sample (several examples are shown in Figure 5.18), but we can reconstruct spectral reflectance at multiple spatial locations using arrayed readings from a camera. To maximize the signal and uniformly illuminate the sample, we scan each device in the EL array one at a time and capture an image of the sample under each device’s illumination. We then decode the spectral response at each pixel using the reconstruction algorithm described earlier. Figures 5.19c-d show an example of reflected-light imaging of a thin film sample where different colors correspond to different thicknesses of silicon dioxide on a silicon substrate. When the sample is illuminated by different devices, different greyscale images are captured (Figure 5.19c) and this data is used to reconstruct the reflectance spectra at different regions (Figure 5.19d). The obtained spectra closely match the simulated reflectance spectra for this thin film stack based on transfer matrix method calculations and AFM measurements of the oxide thicknesses (Figure 5.20). Spectral imaging of semi-transparent biological samples (in this case, a stained human tissue slice) can be performed in a transmitted light configuration, from which we extract the deconvolved spectral image set displayed in Figure 5.19e.

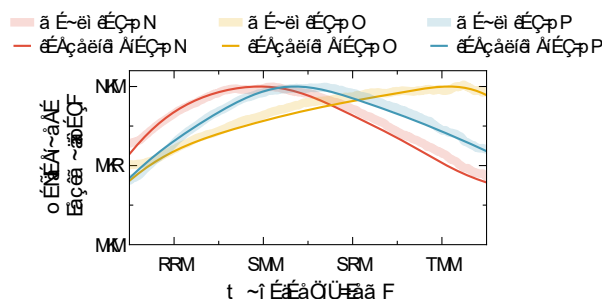


Figure 5.18: **Reconstruction of spectral reflectance.** Measurements are performed for a single spot on a sample. Different colors represent difference samples, with the recovered spectra in solid lines overlaying the measured spectra. Reflectance was collected from the spot through a 10× objective in a home-built microscope. 25 EL spectra were used in these experiments.

A summary of different reconstructive spectral imaging approaches can be found in Table 5.5. Compared to reconstructive microscale spectral imaging approaches which rely on the modulation of passive elements such as a single tuned photodetector, modulation of the

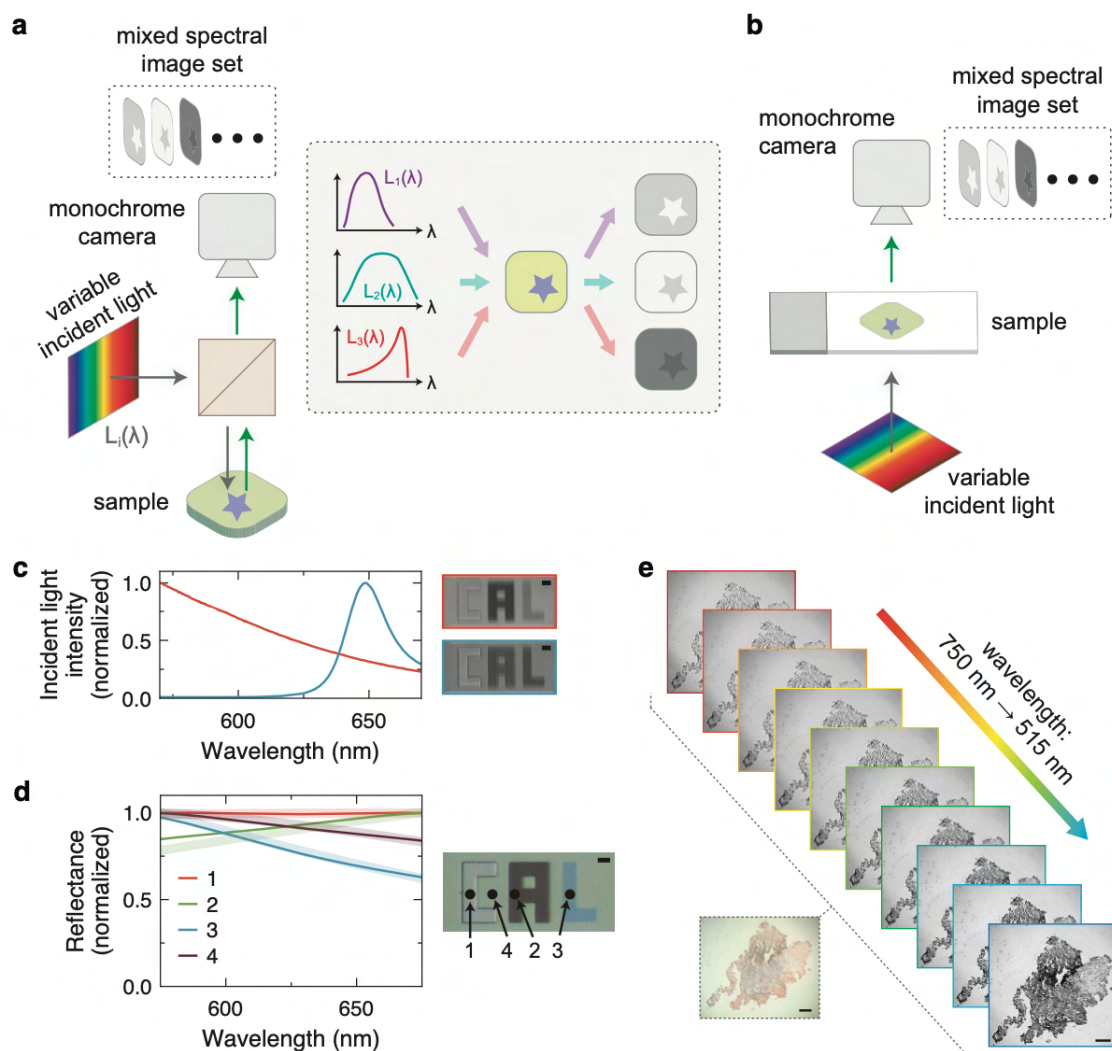


Figure 5.19: **Spectral imaging with highly multicolored arrays.** Schematic depicting the concept behind microscale (a) reflected- and (b) transmitted-light spectral imaging using variable incident illumination and a monochrome camera. (c) Example of different incident light spectra and the corresponding reflected-light microscope images. Scale bar: 40  $\mu\text{m}$ . (d) Reconstructed reflectance spectra at different spots on the sample shown in the optical micrograph, using the emitters in Table 5.4. Scale bar: 40  $\mu\text{m}$ . (E) Spectral data cube for a human tissue sample imaged using a transmitted-light imaging setup. Scale bars: 100  $\mu\text{m}$ .



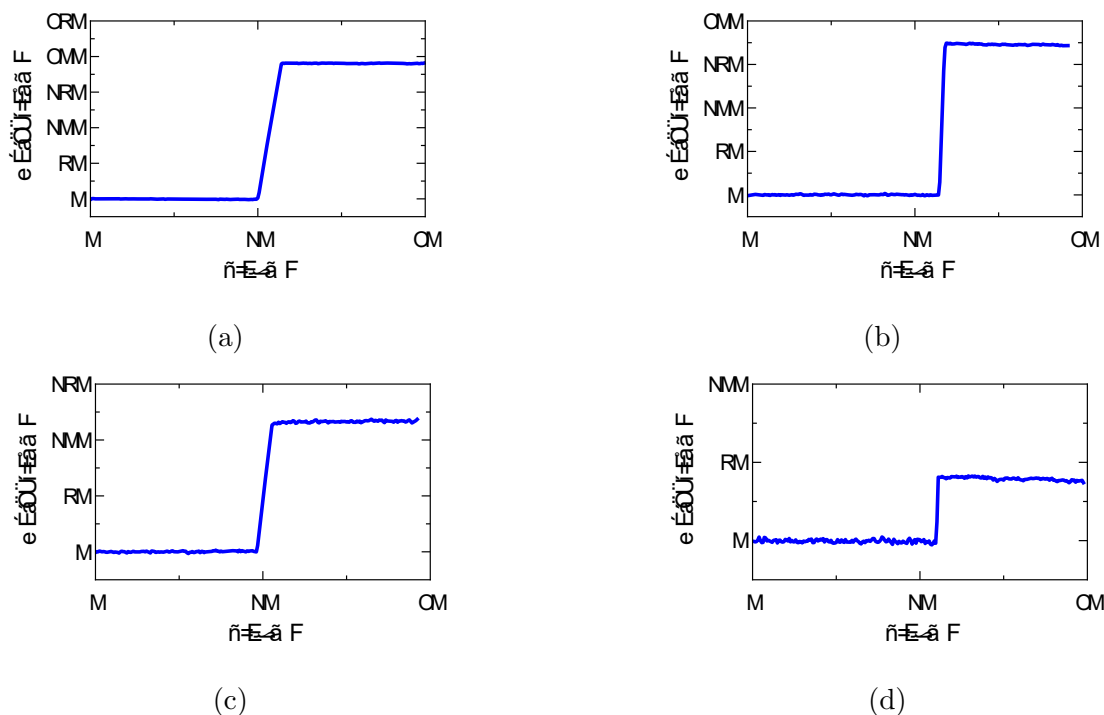


Figure 5.20: **AFM measurement of thin film thicknesses for the “CAL” sample target.** Silicon dioxide thicknesses for each pattern in the “CAL” sample (used for reflected-light spectral imaging in Figures 5.19c-d) are characterized for validation. Height profiles are shown for the (a) background substrate, (b) letter “C”, (c) letter “A”, and (d) letter “L”. The substrate oxide thickness was measured by patterning an edge via photolithography and etching down the substrate oxide with HF until the Si substrate is exposed. From the AFM measurements, we find that the background substrate is around 190 nm thick. The oxide thickness of each letter was determined by measuring the height between the letter and the background substrate, and subtracting that value from the previously determined substrate thickness. From this calculation, we find that the letters “C”, “A”, and “L” have around 175 nm, 120 nm, and 40 nm of oxide. These thickness values were used to simulate the expected reflectance of the sample via the transfer matrix method.

active illumination enables faster acquisition of spectral image stacks with larger image sizes due to its compatibility with standard microscopes which avoids the need for time-intensive spatial scanning. Similarly, our approach does not rely on modification of or adaptation of the spectral element to the camera or image sensor [138–140]. Due to the ability to generate light emission across a broad spectral range, the potentially achievable spectral range is broader and does not rely on carefully engineered material syntheses or highly material-specific physics [120, 141, 142].

Multiplexed illumination has been previously explored as an approach towards multi-

spectral imaging at the macroscale [143, 144]; however, the methodology made use of only a handful of LEDs due to limited commercial availability of different wavelength light sources. Compressive approaches towards active illumination-based spectral imaging have also been developed based on macroscale assemblies of commercial LEDs [145–147], and concepts from these works may complement the development of new spectral imaging approaches based on a highly multispectral light-emitting capacitor array for which the generic nature of the light emission mechanism enables spectral sensing across a broad photon energy range. The ability to miniaturize the light-emitting array to nano- or micro-scale dimensions on a single substrate could further enable chip-scale operation of applications necessitating many spectral bands. In the future, design procedures for the selection of optimal electroluminescent spectra for different applications could be developed based on principles from compressive sensing theory [148]. For example, using a series of linearly spaced Gaussian emission spectra may yield smaller reconstruction error for a broadband spectral reconstruction task than using the happenstance matrix of electroluminescence colors presented here (Figure 5.21). By using an illumination basis set with less correlated spectra, lower reconstruction error and higher spectral accuracy could be achieved with a fewer number of light sources. It may also be possible to design an adaptive sensing scheme in which light-emitting sources are dynamically chosen based on preceding measurements in order to optimize the number and sequence of measurements.

## 5.5 Conclusion

In summary, we have developed a simple and scalable means of creating monolithic light-emitting device arrays with highly multiplexed emission spanning the visible to infrared wavelength range. By using pulsed-driven MOS capacitors, we can achieve bipolar charge injection and bright EL without relying on emitter-specific injection or transport layers which complicate the integration of multi-color devices. Our platform can be used as a source of variable and arbitrary light emission with which to probe the spectral properties of samples, where here we show spectral reflectance and transmittance imaging as an example. Spectral accuracy and coverage could be improved by using spectrally tuned materials instead of arbitrary commercially available materials. Examples include colloidal quantum dot and perovskite nanomaterials in which narrowband emission spectra at different wavelengths can be achieved by tuning the size and alloy composition [149–151], or thin luminescent films fabricated by combinatorial deposition in which materials with tunable emission might be achieved in a single step [152]. While we focus on the visible spectrum in this work, this concept can be extended to more extreme wavelengths by exploring other materials [53]. Importantly, a virtually infinite number of different colors can be achieved on any length scale since lithographic patterning of the devices allows for the fabrication of large arrays and small light-emitting pixel sizes. Finally, more advanced machine learning algorithms may further improve the fidelity of spectral reconstruction [153, 154]. Since pixels in the light-emitting array can be addressed individually or collectively, light can be generated

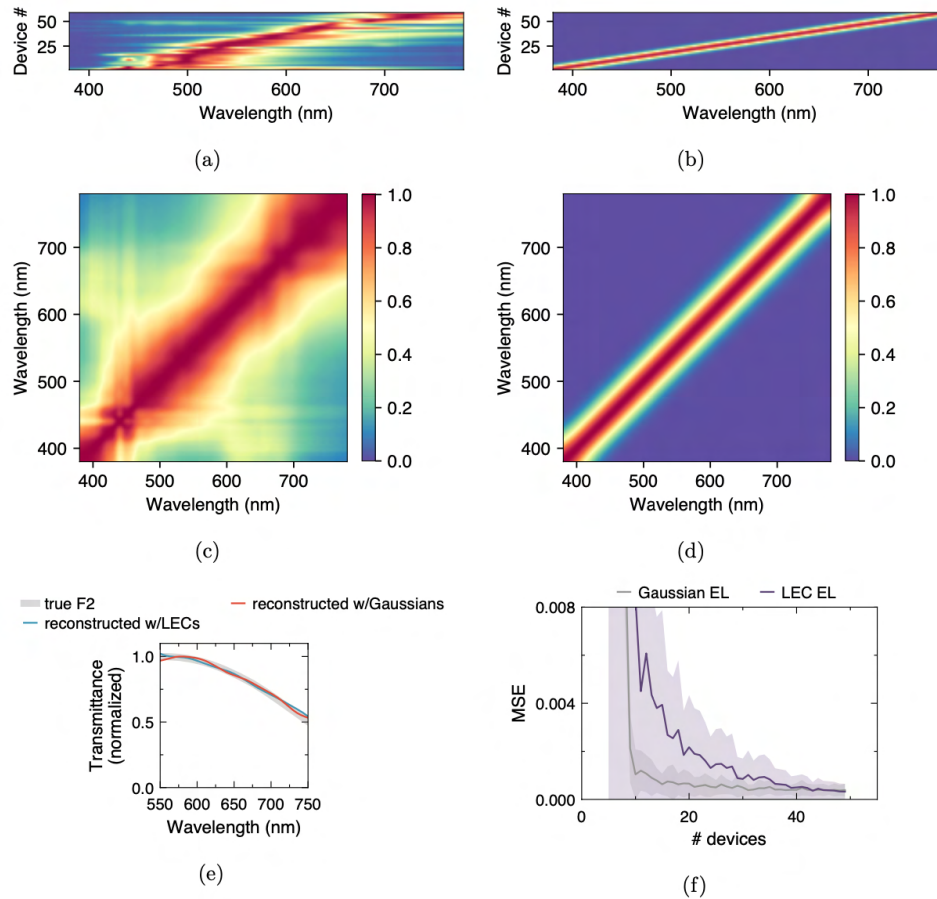


Figure 5.21: **Simulation of spectral reconstruction for different sets of electroluminescence spectra.** (a) Spectra of light-emitting capacitors (LECs) in this work. (b) Simulated hypothetical Gaussian emission spectra spanning the shown wavelength range. Each row of the matrix corresponds to the electroluminescence spectra of a separate device. (c) and (d) show  $|X_i^T X_j|$  where  $X_i, X_j$  are columns of the electroluminescence matrix from (a) and (b), respectively (normalized to have unit norm). (e) Example reconstruction results of a monotonic transmittance function using the measurement matrices in (a) (blue) and (b) (red). (f) Mean squared error of the reconstructed result as a function of number of devices  $N$  (electroluminescence spectra), where  $N$  devices are randomly sampled from the set of devices shown in (a) and (b). The solid lines represent the mean result over 50 randomly sampled batches of devices for each  $N$ .

with customizable patterns in frequency, space, and time, offering an avenue towards active spectral measurements across time and space.

## 5.6 Methods

### Device fabrication

The fabrication of carbon nanotube MOS capacitors follows a procedure previously described in the literature [112]. To summarize, clean 90 nm  $\text{SiO}_2/\text{p}^{++}$  Si substrates are treated with  $\text{O}_2$  plasma for 1.5 min. Poly-L-lysine solution (0.1% w/v aqueous solution, Ted Pella) is drop-cast on the substrate for 5 min, then rinsed off with deionized (DI) water. 90% semi-conducting single-walled carbon nanotube (SWNT) solution (IsoNanotubes-S, NanoIntegris) is drop-cast on the substrate for 10 min, then rinsed off with DI water. The substrate is subsequently annealed in forming gas for 1 h at 250 °C. Metal contacts are patterned by photolithography and deposited by e-beam evaporation of Ti (5 nm)/Au (30 nm). The active device areas are patterned by photolithography and SWNTs outside the device areas are etched by  $\text{O}_2$  plasma.

Emitters are dispensed on the devices using glass micropipettes, which are fabricated using a micropipette puller (P-30, Sutter Instrument) and thin-wall borosilicate glass capillaries with 1 mm outer diameter (B100-75-10, Sutter Instrument or TW100-4, World Precision Instruments). Emissive materials, which include organic molecules and quantum dots in this work, are dispensed from solution with a typical concentration around 5-10 mg mL<sup>-1</sup> in chlorobenzene or toluene, except for ionic transition-metal complexes which are dissolved in acetonitrile. Organic small molecule emitters and metal phthalocyanines are diluted as dopants in a poly(9-vinylcarbazole) (PVK) polymer host at a relative weight concentration of typically a few percent, except for platinum octaethylporphyrin (PtOEP) and pentacene which are dispersed in poly(9,9-dioctyl-9H-fluorene-2,7-diyl) (PFO) [130, 155]. Refer to Table 5.1 for more detail. Materials are obtained from Sigma Aldrich (520 nm and 600 nm CdSe/ZnS quantum dots in toluene; 525 nm and 630 nm CdSeS/ZnS alloyed quantum dots in toluene; 9,10-diphenylanthracene; 4CzIPN; rubrene; Ir(ppy)<sub>3</sub>; Ru(bpy)<sub>3</sub>(PF<sub>6</sub>)<sub>2</sub>; Ru(p-CF<sub>3</sub>-bpy)<sub>3</sub>(BF<sub>4</sub>)<sub>2</sub>; Ir(dtb-bpy)(ppy)<sub>2</sub>PF<sub>6</sub>; Ir(dF-ppy)<sub>2</sub>(dtb-bpy)]PF<sub>6</sub>; zinc phthalocyanine; titanyl phthalocyanine; MDMO-PPV; PFV; PDY-132; PFO; PVK; 1000 nm PbS quantum dots in toluene), Luminescence Technology Corp. (Ir(ppy)<sub>2</sub>(acac); CzDBA; PtOEP; Alq<sub>3</sub>; F8BT; MEH-PPV; FIrPic; CBP; pentacene), Quantum Solutions (1100 nm and 1200 nm PbS quantum dots, dissolved in toluene), Ossila (PDPP4T), Strem (Ir(Fppy)<sub>3</sub>), 1-Material (P3HT; Y6), Solaris Chem (PTB7), Nano-C (C<sub>60</sub>-PCBM), and Brilliant Matters (ITIC; PBDB-T).

## Sample fabrication

The “CAL” sample for reflected light imaging is fabricated from 500 nm SiO<sub>2</sub>/Si substrate. The substrate is first immersed in 6:1 buffered oxide etch (HF) until the desired oxide thickness is achieved, then rinsed with DI water and dried. Three successive rounds of photolithography are performed using a direct-write tool (Heidelberg  $\mu$ PG 101) to pattern each of the letters. After each photolithography step, the substrate is immersed in 6:1 buffered oxide etch until the desired oxide thickness is achieved, then rinsed with DI water and dried. The remaining photoresist is removed with remover PG before continuing onto the subsequent photolithography step. The etch rates and oxide thicknesses are calibrated and validated by atomic force microscopy (AFM) measurement.

## Device measurement

To drive the devices, pulsed electrical bias is applied using a function generator (33522A, Agilent) and voltage amplifier, where multiplexing is implemented with a commercial board (EL Escudo Dos, SparkFun) or solid-state relays. A custom-built square wave generating circuit controlled by an Arduino microcontroller is used for phase shift-multiplexed measurements (Figure 5.15). Optical measurements, including direct measurement of EL, reflectance, and transmittance spectra, are performed using a custom-built micro-photoluminescence setup in which EL can be collected by a photodiode, camera, or dispersed by a spectrograph (HR-640, Instruments SA) with a 150 groove per mm grating and detected by a Si charge-coupled device (CCD) (iDus BEX2-DD, Andor) [39]. For each measurement, the dark background of the CCD is measured and subtracted from the acquired signal. The instrument sensitivity as a function of wavelength is determined by measuring the response of a Lambertian light source generated by illumination from a temperature stabilized lamp (SLS201, ThorLabs) on a diffuse reflector (Spectralon). Reflected-light spectral imaging is performed using the same fluorescence microscopy setup, while transmitted-light spectral imaging is performed using a separate custom-built microscope (Cerna Microscopy Platform, ThorLabs) in which illumination from the electroluminescent array is defocused at the sample. Imaging measurements are acquired with a CCD camera (Luca-R, Andor). A silver mirror and glass microscope slide (on part of which the tissue sample in Figure 4 is mounted) are used as references for calibrating spectral reflectance and transmittance. A low-pass and high-pass filter were included in the optical path to define the spectral range in the reconstruction experiments to the wavelength limits shown. Time-resolved EL measurements are acquired using a Si photodetector (APD410A, ThorLabs) and oscilloscope (TDS-640A, Tektronix), and time-averaged measurements are acquired using the same detector with a lock-in amplifier (SRS-830, Stanford Research Systems). Devices are operated under vacuum at room temperature. A diffuser is placed above the device array when measuring composite EL spectra. Hardware control and data acquisition is performed using custom Python software based on the open-source ScopeFoundry platform. Data is analyzed in Python using the *cvxpy* package for numerical optimization.

## 5.7 Tables

### 7 × 7 emitters

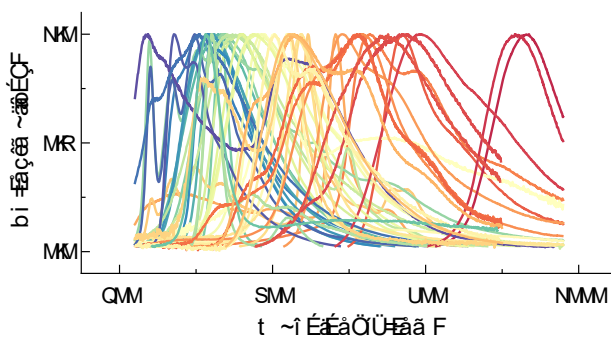
Device #	Row	Column	Emitter	Solution
1	1	1	Ir(ppy) <sub>3</sub> :PVK (2.9 wt%)	4.7 mg mL <sup>-1</sup> in CB
2	1	2	Ir(Fppy) <sub>3</sub> :PVK (2.9 wt%)	4.7 mg mL <sup>-1</sup> in CB
3	1	3	ZnPC:PVK (1.2 wt%)	9.2 mg mL <sup>-1</sup> in CB
4	1	4	MDMO-PPV	1.5 mg mL <sup>-1</sup> in toluene
5	1	5	4CzIPN:PVK (2.0 wt%)	4.6 mg mL <sup>-1</sup> in CB
6	1	6	TiOPc:PVK (9.1 wt%)	10 mg mL <sup>-1</sup> in CB
7	1	7	[Ir(dFppy) <sub>2</sub> (dtbbpy)]PF <sub>6</sub>	20 mg mL <sup>-1</sup> in acetonitrile
8	2	1	520 nm CdSe/ZnS QD	5 mg mL <sup>-1</sup> in toluene
9	2	2	9,10-diphenylanthracene	10 mg mL <sup>-1</sup> in toluene
10	2	3	630 nm CdSeS/ZnSQD	1 mg mL <sup>-1</sup> in toluene
11	2	4	PtOEP:PFO (2.4 wt%)	3 mg mL <sup>-1</sup> in toluene
12	2	5	[Ir(dtbbpy)(ppy) <sub>2</sub> ]PF <sub>6</sub>	10 mg mL <sup>-1</sup> in acetonitrile
13	2	6	600 nm CdSe/ZnS QD	5 mg mL <sup>-1</sup> in toluene
14	2	7	525 nm CdSeS/ZnS QD	1 mg mL <sup>-1</sup> in toluene
15	3	1	PFV	2.5 mg mL <sup>-1</sup> in toluene
16	3	2	Ru(bpy) <sub>3</sub> (PF <sub>6</sub> ) <sub>2</sub>	5 mg mL <sup>-1</sup> in acetonitrile
17	3	3	FIrPic:CBP (4.8 wt%)	5 mg mL <sup>-1</sup> in CB
18	3	4	Y6 (BTP-4F)	9 mg mL <sup>-1</sup> in CB
19	3	5	MEH-PPV	3.3 mg mL <sup>-1</sup> in toluene
20	3	6	Ru(p-CF <sub>3</sub> -bpy) <sub>3</sub> (BF <sub>4</sub> ) <sub>2</sub>	20 mg mL <sup>-1</sup> in acetonitrile
21	3	7	PDY-132 (SuperYellow)	2 mg mL <sup>-1</sup> in CB
22	4	1	P3HT	3.5 mg mL <sup>-1</sup> in CB
23	4	2	ITIC	3 mg mL <sup>-1</sup> in CB
24	4	3	CzDBA:PVK (3.6 wt%)	6.3 mg mL <sup>-1</sup> in CB
25	4	4	PFO	2 mg mL <sup>-1</sup> in CB
26	4	5	Ir(ppy) <sub>2</sub> (acac):PVK (2.4 wt%)	6.2 mg mL <sup>-1</sup> in CB
27	4	6	~600 nm CdSe/CdS nanorods	hexane solution from Molecular Foundry
28	4	7	~630 nm CdSe/CdS nanorods	xylene solution from Molecular Foundry
29	5	1	C60-PCBM:PVK (7.0 wt%)	6.5 mg mL <sup>-1</sup> in CB
30	5	2	PTB7	5 mg mL <sup>-1</sup> in CB

31	5	3	PBDB-T	5 mg mL <sup>-1</sup> in CB
32	5	4	PDPP4T	1 mg mL <sup>-1</sup> in CB
33	5	5	1000 nm PbS QD	10 mg mL <sup>-1</sup> in toluene
34	5	6	1100 nm PbS QD	~30 mg mL <sup>-1</sup> in toluene
35	5	7	1200 nm PbS QD	~30 mg mL <sup>-1</sup> in toluene
36	6	1	F8BT	6 mg mL <sup>-1</sup> in toluene
37	6	2	Alq <sub>3</sub> :PVK (2.9 wt%)	6.2 mg mL <sup>-1</sup> in CB
38	6	3	rubrene:F8BT (6.3 wt%)	5.8 mg mL <sup>-1</sup> in toluene
39	6	4	520 nm CdSe/ZnS QD : 630 nm CdSeS/ZnS QD (56 wt%)	1.8 mg mL <sup>-1</sup>
40	6	5	520 nm CdSe/ZnS QD : MDMO-PPV (91 wt%)	4.1 mg mL <sup>-1</sup> in toluene
41	6	6	pentacene:PFO (9.1 wt%)	2 mg mL <sup>-1</sup> in CB
42	6	7	CBP	5 mg mL <sup>-1</sup> in CB
43	7	1	P3HT : MDMO-PPV (71 wt%)	3.5 mg mL <sup>-1</sup> in 33 v/v% CB/toluene mixture
44	7	2	P3HT : PDY-132 (65 wt%)	3.8 mg mL <sup>-1</sup> in CB
45	7	3	P3HT : MEH-PPV (36 wt%)	4.2 mg mL <sup>-1</sup> in 20 v/v% CB/toluene mixture
46	7	4	P3HT : F8BT (24 wt%)	6.3 mg mL <sup>-1</sup> in 20 v/v% CB/toluene mixture
47	7	5	P3HT : PTB7 (94 wt%)	7.3 mg mL <sup>-1</sup> in CB
48	7	6	Ir(ppy) <sub>2</sub> (acac) (1 wt%):PVK (37 wt%): 630 nm CdSeS/ZnS QD (62 wt%)	1.5 mg mL <sup>-1</sup> in 9.1 v/v% CB/toluene mixture
49	7	7	P3HT : PBDB-T (56 wt%)	3.4 mg mL <sup>-1</sup> in CB

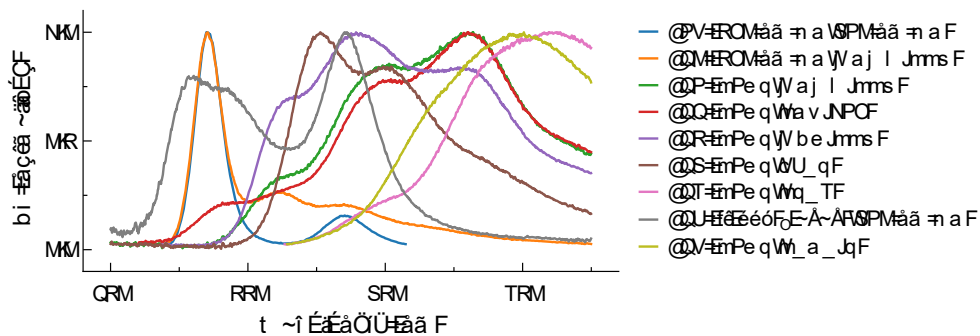
Table 5.1: Emitters drop-cast on the 7 × 7 array shown in Figure 5.1b and Figure 5.6, as well as each drop-cast solution composition (which the other tables of emitter arrays also draw from).

Weight percent in the emitter column refers to the relative percentage of the first material in the solid film formed from the binary blend solution. For small molecules diluted in polymer solutions, the dopant molecule is indicated first and the host polymer is indicated second. The solution column indicates the concentration of the liquid solution from which the emissive layer was drop-cast.

*Abbreviations:* ZnPC = zinc phthalocyanine. TiOPc = titanyl phthalocyanine. QD = quantum dot. PFO = poly(9,9-dioctyl-9H-fluorene-2,7-diyl). CB = chlorobenzene.



(a)



(b)

Electroluminescence spectra for the emitters in Table 5.1 are shown above in panel (a). Selected electroluminescence spectra highlighting blends of different materials are shown above in panel (b). ‘#’s in the legend correspond to the solution number in Table 5.1. Spectra of the mixtures resemble the spectra of the constituent emitters.



Figure 5.1 emitters

ID	Emitter
1	FIrPic:CBP
2	9,10-diphenylanthracene
3	PFO
4	Ir(Fppy) <sub>3</sub> :PVK
5	Ir(ppy) <sub>3</sub> :PVK
6	[Ir(dFppy) <sub>2</sub> (dtbbpy)]PF <sub>6</sub>
7	4CzIPN:PVK
8	Ir(ppy) <sub>2</sub> (acac):PVK
9	Alq <sub>3</sub> :PVK
10	520 nm CdSe/ZnS QD
11	pentacene:PFO
12	CzDBA:PVK
13	TiOPc:PVK
14	PFV
15	F8BT
16	rubrene:F8BT
17	[Ir(dtbbpy)(ppy) <sub>2</sub> ]PF <sub>6</sub>
18	PDY-132 (SuperYellow)
19	MDMO-PPV
20	MEH-PPV
21	~ 600 nm CdSe/CdS nanorods
22	CBP
23	600 nm CdSe/ZnS QD
24	Ru(bpy) <sub>3</sub> (PF <sub>6</sub> ) <sub>2</sub>
25	630 nm CdSe/ZnS QD
26	~ 630 nm CdSe/CdS nanorods
27	PtOEP:PFO
28	ZnPC:PVK
29	P3HT:F8BT
30	P3HT
31	P3HT:MEH-PPV
32	C60-PCBM:PVK
33	PBDB-T
34	ITIC
35	PTB7

Table 5.2: Emitters shown in Figure 5.1f, in order from shortest to longest peak wavelength.

**Figure 5.10 emitters**

Device #	Emitter
1	$[\text{Ir}(\text{dtbbpy})(\text{ppy})_2]\text{PF}_6$
2	$[\text{Ir}(\text{dFppy})_2(\text{dtbbpy})]\text{PF}_6$
3	630 nm CdSeS/ZnS QD
4	ZnPC:PVK
5	PDY-132 (SuperYellow)
6	MDMO-PPV
7	PtOEP:PFO
8	4CzIPN:PVK
9	$\text{Ir}(\text{ppy})_3$ :PVK
10	PFO
11	Alq <sub>3</sub> :PVK
12	pentacene:PFO
13	F8BT
14	MEH-PPV
15	P3HT
16	$\text{Ru}(\text{bpy})_3(\text{PF}_6)_2$
17	P3HT:MEH-PPV
18	C60-PCBM:PVK
19	$\text{Ir}(\text{Fppy})_3$ :PVK
20	P3HT:F8BT
21	PTB7
22	$[\text{Ir}(\text{dFppy})_2(\text{dtbbpy})]\text{PF}_6$
23	$\text{Ir}(\text{ppy})_3$ :PVK
24	TiOPc:PVK
25	PFO
26	rubrene:F8BT
27	ITIC
28	PBDB-T
29	$\sim 600$ nm CdSe/CdS nanorods
30	$\sim 630$ nm CdSe/CdS nanorods

Table 5.3: Emitters used for spectral reconstruction in Figure 5.10.

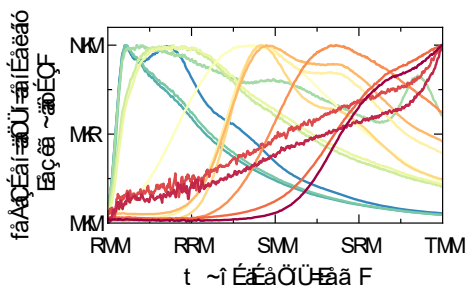
Note that some emitters are repeated; however, they still contribute beneficially to spectral reconstruction due to device-to-device variations in EL spectra (for example, variations in the thickness of the particular drop-cast film, which can affect the film properties and light outcoupling), in addition to contributing more data points.

Figure 5.19 emitters

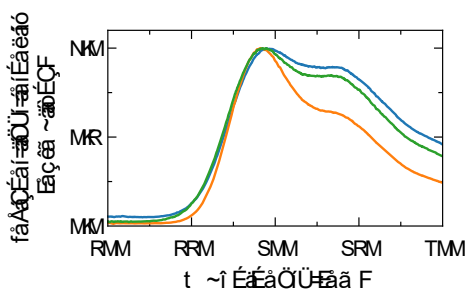
Device #	Emitter
1	Ir(Fppy) <sub>3</sub> :PVK
2	Ru(bpy) <sub>3</sub> (PF <sub>6</sub> ) <sub>2</sub>
3	MEH-PPV
4	C60-PCBM:PVK
5	Ir(ppy) <sub>2</sub> (acac):PVK
6	P3HT
7	Ir(Fppy) <sub>3</sub> :PVK
8	PFO
9	[Ir(dtbbpy)(ppy) <sub>2</sub> ]PF <sub>6</sub>
10	Ir(ppy) <sub>2</sub> (acac):PVK
11	ZnPC:PVK
12	P3HT
13	MEH-PPV
14	MEH-PPV
15	C60-PCBM:PVK

Table 5.4: Emitters used for spectral reconstruction in Figure 5.19d.

The EL spectra are plotted below:



Due to natural variations in drop-casting, different films of the same emitter (particularly in the case of polymer emitters) can exhibit different spectra, which we can leverage to generate more variations in EL spectra for the same number of materials. Thus, a large number of different emitting materials need not be obtained depending on the spectral range of interest. As an example, below are the EL spectra of drop-cast MEH-PPV films on three devices from the above list:



### Comparison of reconstructive spectral imaging approaches

Approach [Ref.]	Spectral Range	Spectral Resolution	Pixel Number	Footprint
Single nanowire [120]	500-630 nm	15 nm	20 × 10	75 μm
Photonic crystal slab [138]	550-750 nm	1 nm	10 × 10	0.21 mm
Fabry-Perot filters [139]	450-650 nm	10 nm	1920 × 1080	-
Filter array [140]	400-700 nm	5 nm	640 × 480	~1 cm
2D material junction [141]	405-845 nm	3 nm	12 × 10	22 μm
2D material junction [142]	1.15-1.47 μm	20 nm	~ 250 × 200	6 μm
Liquid crystal filters [118]	500-710 nm	10 nm	400 × 400	-
LED array [145]	450-690 nm	30 nm	256 × 256	-
This work	up to 400-1400 nm	10 nm	1000 × 1000	<1 cm

Table 5.5: Due to the different approaches to reconstructive spectral imaging referenced in the table, the metrics are not necessarily directly comparable between references. The footprint refers to the chip or device size for approaches relying on custom or newly fabricated materials or devices. The pixel number refers to the image size reported in the main work and may not be the defining limit.

## Chapter 6

# An electroluminescent device for single quantum dot emission

### 6.1 Introduction

Scaling the dimensions of light sources is important for technological applications ranging from augmented reality to quantum science, where electrically driven light emission from micro- to nano-scale devices is highly desirable [156–158]. In the extreme limit, light emission may be achieved from single semiconductor nanostructures, offering a potential avenue towards compact, electrically triggered single-photon sources for quantum technologies [159, 160]. However, conventional light-emitting diodes (LEDs) can be difficult to scale to ultra-small dimensions. Devices based on self-assembled quantum dots suffer from nonradiative losses owing to deleterious effects of fabrication processes as the active area is scaled down, and it is difficult to design device structures which can selectively inject current in sub-micron active regions [158]. LEDs based on organic materials are typically fabricated by shadow masking, which limits the size of an individual light emitting device to microscale dimensions, and in general rely on inherently macroscale device structures which preclude the exploration of light emission at the nanoscale. Here, we describe an electroluminescent device structure in which the light emitting region can be scaled from the macroscale to nanoscale with minimal modification of the fabrication process. Using this device, we demonstrate highly reproducible, electrically generated light emission from single colloidal quantum dots using single carbon nanotubes (CNTs) as nanoscale contacts to single luminescent entities.

Previous work has shown that conventional vertically layered light-emitting diodes can be used to generate light emission from a collection of single molecules or colloidal quantum dots [161, 162]. In these device structures, the emitters are typically embedded in a host matrix at extremely low concentrations, rendering it difficult to control the positions of emitters in both the vertical and lateral dimensions due to the finite thickness of the host matrix which serves as the active layer of the device. The insulating nature of the host matrix also prevents direct and uniform charge injection into the emitters, which can lead to background emission

from adjacent material layers in addition to reduced injection efficiency [163]. Furthermore, the sandwiched nature of the device structure hinders efficient optical access and coupling since the emitters are located between two electrode layers. Alternatively, it is possible to generate electroluminescence (EL) from single nanocrystals using metal electrodes with nanometer-scale gaps [164, 165], but these devices require intricate nanofabrication processes which typically suffer from poor yield and are difficult to scale reliably. Single-molecule light-emitting devices have been similarly demonstrated using nanogapped electrodes formed by graphene or carbon nanotube contacts, but the positioning of a molecule between two separate electrodes is challenging [166, 167].

Our approach offers an alternate strategy based on a light-emitting device with a single charge injecting contact. We have previously shown that a pulsed-driven, metal-oxide-semiconductor (MOS) capacitor device can be used to generate EL from material systems across the entire range of dimensions, including molecules, quantum dots, nanowires, two-dimensional semiconductors, and bulk materials [12, 53, 168, 169]. In the case of nanomaterials, bright light emission was demonstrated using capacitors in which networks of CNTs serve as spatially dense nanoscale contacts from which bipolar charge can be injected into luminescent materials with band gap energies spanning infrared to ultraviolet wavelengths. Such a device is unique in its requirement for only a single charge injection contact, in contrast to other light-emitting devices which require separate electron- and hole-injecting contacts with work functions appropriately engineered for the emitting entity. Furthermore, the emissive layer need not be uniform or possess any particular thickness, allowing freeform deposition of the desired emitters. This device concept can thus be easily leveraged to generate electroluminescence from individual particles placed on a single plane on a silicon substrate.

## 6.2 Results and Discussion

Figure 6.1a depicts the structure of the two-terminal pulsed electroluminescent device, which consists of colloidal quantum dots on carbon nanotube contacts which sit atop a silicon dioxide/silicon substrate. The mechanism of such a device has been described previously [12]. During periods of steady-state positive or negative back-gate voltage, negative or positive charge is accumulated in the active material, respectively. When the polarity of the gate voltage rapidly switches sign, the opposite charge carrier is injected before the existing charge carrier in the material can exit, allowing for exciton formation and radiative recombination. Previous demonstrations of this device structure used random networks of single-walled carbon nanotubes which were assembled from solution onto a functionalized substrate [53]. Using this method, nanotubes are randomly oriented on the substrate, with the average density of nanotubes on the surface depending on the self-assembly time. The average nanotube-nanotube spacing in electrically percolating networks is no more than several hundred nanometers as a result of the short lengths of the nanotubes, which are several micrometers long or less [170, 171]. Here, we use aligned arrays of CNTs grown by

chemical vapor deposition (CVD) instead of randomly assembled carbon nanotube networks as contacts to the luminescent emitters. By tuning the CVD growth process via control of the catalyst thickness, sparsely spaced nanotubes with relatively long lengths can be obtained. The use of these nanotube arrays enables the creation of MOS capacitor devices with single quantum dot emission resolvable by widefield imaging, while simultaneously reducing parasitic series resistances that arise from abundant nanotube-nanotube junctions in the earlier micrometer-scale, self-assembled carbon nanotube networks. Representative dimensional characteristics of an as-grown nanotube array on quartz substrate are shown in the scanning electron microscopy (SEM) image in Figure 6.1c.

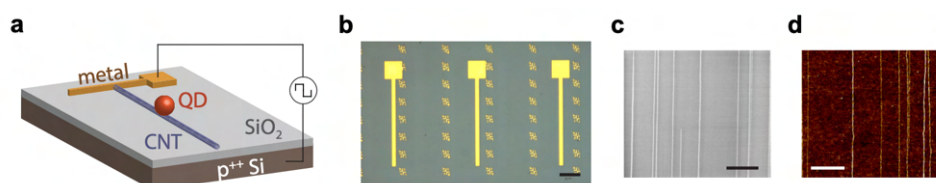


Figure 6.1: **Concept of a single quantum dot light-emitting device.** (a) Schematic of a device structure used to obtain light emission from single quantum dots by applying pulsed voltage across a capacitor with a carbon nanotube top contact, silicon dioxide dielectric, and silicon back-gate contact. (b) Optical micrograph of several devices fabricated on a substrate with markers to aid subsequent location of single quantum dots (scale bar: 100  $\mu\text{m}$ ). (c) SEM image of individual nanotubes in an aligned carbon nanotube array grown on quartz (scale bar: 5  $\mu\text{m}$ ). (d) AFM image of individual nanotubes transferred from quartz to a  $\text{SiO}_2/\text{Si}$  substrate (scale bar: 1  $\mu\text{m}$ ).

To briefly summarize the device fabrication process, aligned CNT arrays are first transferred to a silicon dioxide/ $p^{++}$  silicon substrate (Figure 6.1d) via a dry transfer process described in more detail in the Methods section [172]. Metal contacts for wire-bond connections are then patterned and deposited on the CNTs. The active area of the device is defined by a second photolithography step in which CNTs outside the active area are etched away by  $\text{O}_2$  plasma, thus allowing a device to contact only a single nanotube if so desired. Due to lithographic patterning of the metal/carbon nanotube electrodes, many devices can be fabricated in parallel (Figure 6.1b). Finally, the emitters are spin-coated on top of the substrate from a solution which is dilute enough to yield the deposition of isolated single emitters. In this work, we use colloiddally synthesized CdSe/CdZnSe/ZnSeS quantum dots with peak photoluminescence (PL) emission around 620 nm at room temperature, where the solution is diluted by several orders of magnitude before spin-coating. Device fabrication is completed after the emitter deposition step, and light emission can be observed promptly by applying pulsed voltage between the top metal contact and back gate  $p^{++}$  silicon.

As shown in Figure 6.2a, the density of light-emitting spots decreases as the density of quantum dots decreases due to fewer quantum dots contacting carbon nanotubes. By spin-coating an appropriately dilute concentration of quantum dots for the particular density

of CNT array used, we can observe electroluminescence from single isolated emitting spots (Figure 6.2a, panel iii). Many of these spots show temporal intensity fluctuations in which the emission turns off and on transiently over time (Figure 6.6f), as illustrated by successive frames of electroluminescence images captured in real time (Figure 6.2c). In this example, we observe the electroluminescence from different quantum dots contacting a single nanotube turning on and off as time elapses. The emission intermittency suggests that these spots represent emission from single quantum dots, which are known to exhibit characteristic ‘blinking’ at the single dot level due to non-radiative Auger processes [173, 174]. In general, the yield of these devices is high: single blinking electroluminescent spots were observed from every device tested so long as carbon nanotubes were successfully transferred to the region of the substrate where the devices were fabricated and measured. Due to the manual transfer process, the transfer of CNTs from the quartz growth substrate to target silicon wafer is not always successful, especially near the edges of the relatively small substrates used. As expected, the number of emitting spots increases as the concentration of the spin-coated quantum dot solution increases, and as the line density of the aligned carbon nanotube array increases (Figure 6.2).

From atomic force microscopy (AFM) measurements, the areal density of quantum dots is found to vary linearly with the concentration of the spin-coated solution, allowing control of the average number of dots deposited on the surface of the device as shown in Figure 6.3. There is a concomitant decrease in the photoluminescence signal as the quantum density decreases, with the total photoluminescence at one spot varying similarly linearly with concentration until there is on average no more than one quantum dot excited by the laser with spot size around  $5\ \mu\text{m}$ . From correlated AFM and widefield photoluminescence imaging, we can identify the location of single quantum dots (Figure 6.4a), for which a representative photoluminescence spectrum at room temperature is shown in Figure 6.4c.

The density of single quantum dot emission spots in this scheme depends on the likelihood of a quantum dot landing on a CNT. In a purely random deposition process in which there are  $N_Q$  dots (of diameter  $20\ \text{nm}$ ) per  $\mu\text{m}^2$  on a substrate with a line density of  $\rho_C$  nanotubes per  $\mu\text{m}$ , the probability that at least one quantum dot lands on a nanotube is roughly  $1 - (1-p)^{N_Q}$ , where  $p = \rho_C/50$  is the probability of a quantum dot landing on a nanotube (assuming each dot is deposited independently of one another and ignoring size exclusion effects). This event occurs with 50% probability if  $N_Q = 11\ \mu\text{m}^{-2}$  when  $\rho_C = 3\ \mu\text{m}^{-1}$  for example. In the event this case happens, we would have the opportunity to observe quantum dot EL, although not necessarily from individually resolvable quantum dots given the optical diffraction limit. The probability of having no more than one dot-on-nanotube per  $1\ \mu\text{m}$  length along the axis of the aligned CNT array is  $(1-p)^{N_Q} + N_Q p (1-p)^{N_Q-1} \approx 86\%$  for the same example parameters. If we now consider an aligned CNT array with a sparser line density of  $\rho_C = 0.1\ \mu\text{m}^{-1}$ , then the probability of the opportunity for EL is 2% and the probability of having no more than one dot-on-nanotube is 99.97%, i.e. a greater density of quantum dots should be deposited to be able to observe quantum dot EL. By scanning fifty  $1\ \mu\text{m}^2$  areas, one spot with possible EL would be expected, and the spot would be extremely likely to represent emission from a single quantum dot. In practice, the quantum dot spin-coating process may not be uniformly



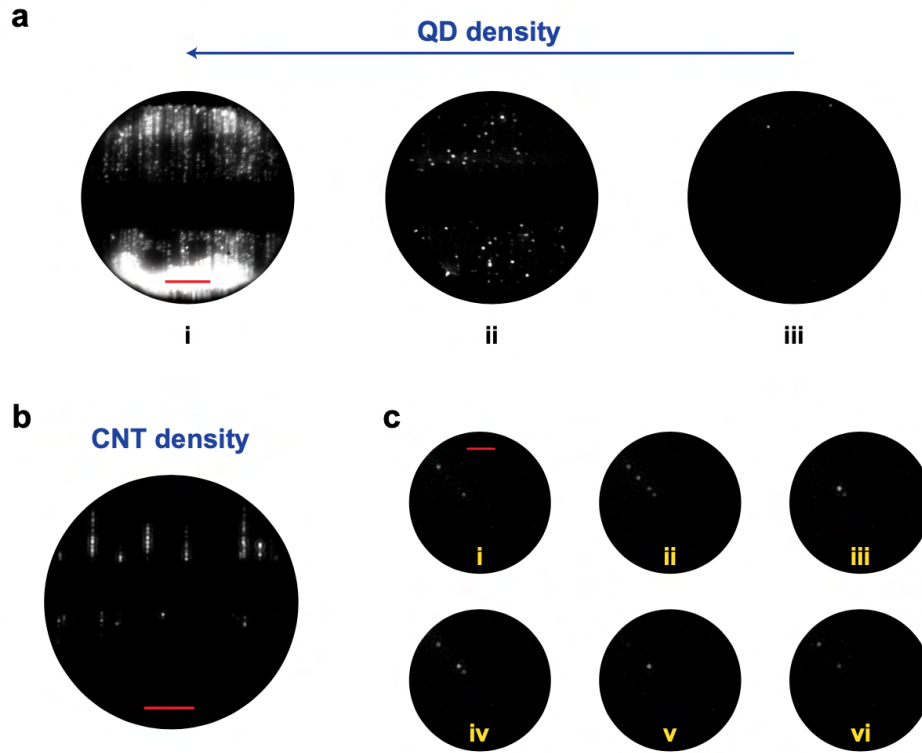


Figure 6.2: **Emission area control by emitter density and carbon nanotube density.** (a) Electroluminescence images of devices with decreasing quantum dot surface density from panel i to iii. Measurements were performed at room temperature. (b) Electroluminescence image of a device with a sparse array of carbon nanotubes. (c) Electroluminescence images captured over time (in chronological order from panel i to vi) show multiple blinking quantum dot emission spots along a single carbon nanotube. Measurements were performed at 4 K. Scale bars: 20  $\mu\text{m}$ .

random and depending on the processing conditions and surface chemistries, quantum dots may be more or less likely to deposit on or near CNTs, biasing the optimal concentration for observing likely single quantum dot emission. Examples of electroluminescence from devices with different quantum dot and carbon nanotube density are shown in Figure 6.2, in which the likelihood of single quantum dot emission is controlled by adjusting both the emitter and contact density. With direct nano-patterning techniques, deterministic placement of quantum dot emitters could be achieved in the future, thereby avoiding the current method of probabilistic fabrication.

Figure 6.5 shows operating characteristics of the device. The emission intensity from individual dots increases with the peak voltage of the pulsed square wave applied to the device (Figure 6.5b). In correspondence with previous work on pulsed electroluminescent

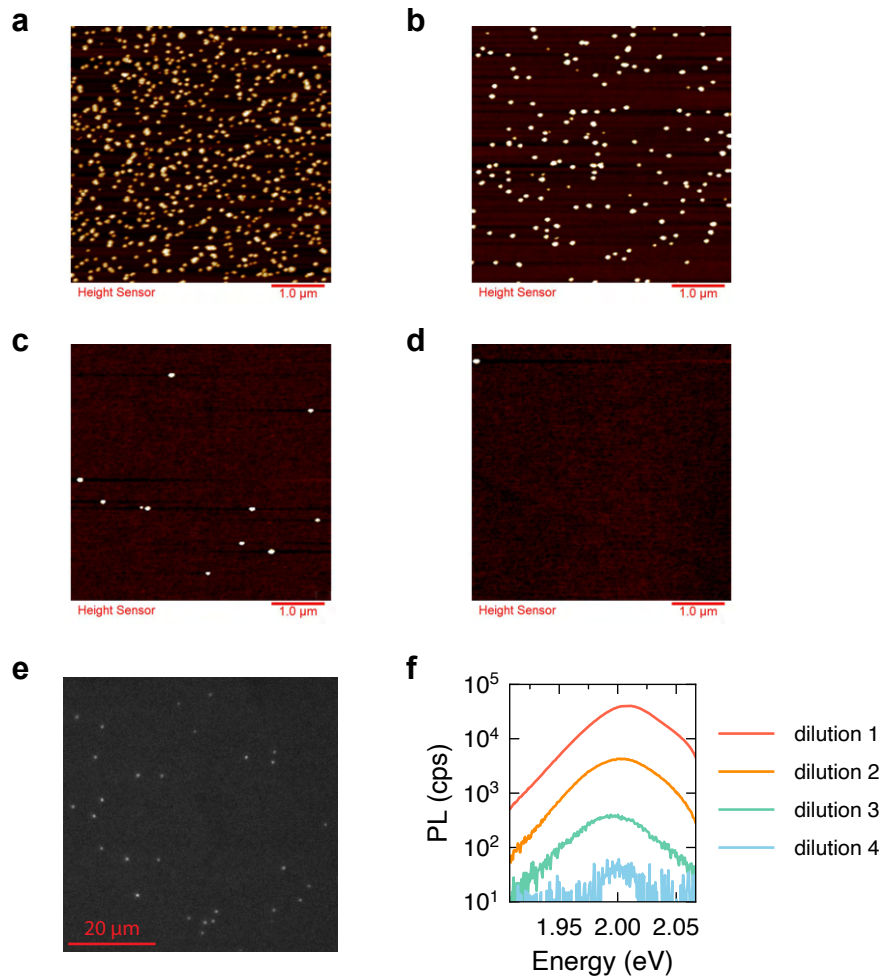


Figure 6.3: AFM images of quantum dot surface coverage from high to low density (a-d), in which samples b, c, and d were produced by spin-coating quantum dot solutions with  $10\times$  lower concentration each time. (e) Photoluminescence image of single quantum dots on a SiO<sub>2</sub>/Si substrate, obtained using a 450 nm LED and longpass filter. (f) Photoluminescence signal from samples with different surface densities of quantum dots fabricated by spin-coating different dilutions of quantum dot solutions. Dilutions 1-4 correspond to the sample preparations in panels a-d. The photoluminescence signal decreases correspondingly around  $10\times$  after each dilution step.

MOS capacitor devices [98], the emission intensity is also found to increase generally with the slew rate and frequency of the pulsed waveform (Figure 6.5a), although the exact shape of the waveform applied at the device depends on bandwidth and parasitics in the equipment and device connections, which are fed externally through a cryostat in which EL measurements

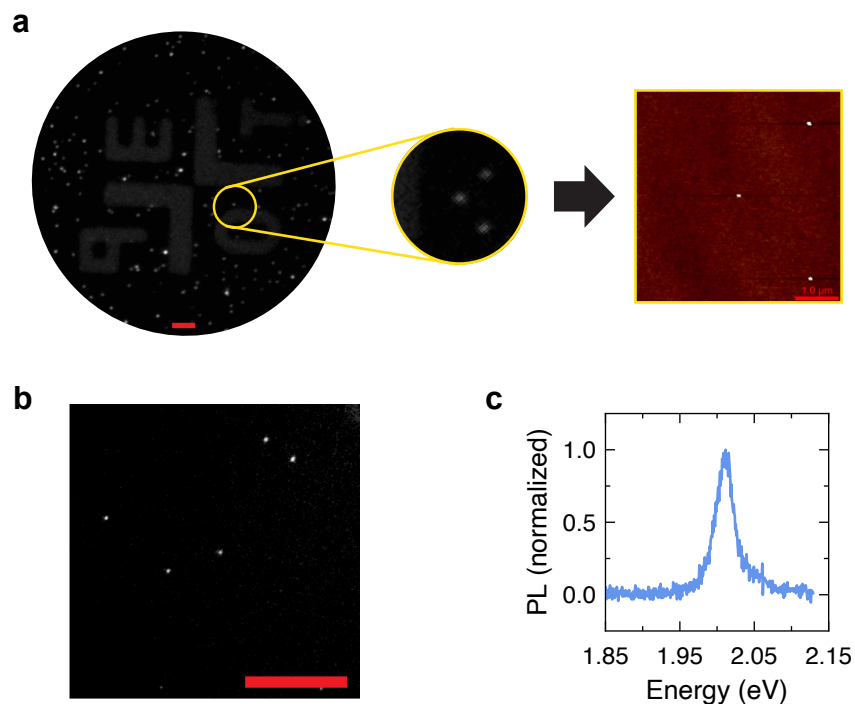


Figure 6.4: (a) Photoluminescence image of quantum dots on a SiO<sub>2</sub>/Si substrate with coordinate marker to aid identification and physical confirmation of emitting spots in subsequent AFM imaging (scale bar: 20 μm). Inset shows photoluminescence of three quantum dots of interest. The AFM image of these three quantum dots, showing the same spatial arrangement, is shown on the right. (b) Photoluminescence image of several sparsely arranged quantum dots on a SiO<sub>2</sub>/Si substrate (scale bar: 20 μm) and (c) the photoluminescence spectrum of one of the dots at room temperature.

are performed in vacuum. Based on these trends, we operated a device with a custom GaN-based circuit board in which moderately high voltage pulses can be applied with a faster slew rate than that of the combination of the function generator and voltage amplifier used earlier (Figure 6.9).

Images of electroluminescence from the device driven under these conditions show that it is possible to obtain quantum dot emission using square wave voltages with amplitudes of only a few volts. In addition to shortening the slew time of the pulse, the operating voltage of the device could be potentially reduced even further by thinning down the gate oxide thickness as shown previously [98], similar to scaling trends for MOS transistors. We note that pulsed, alternating current voltages have previously applied to obtain electroluminescence from single molecules by temporally separating electron and hole injection processes, albeit using a different device structure which is fabricated in a highly specific manner to the molecules investigated (Ag nanoclusters) and exhibits poor spectral control [175, 176].

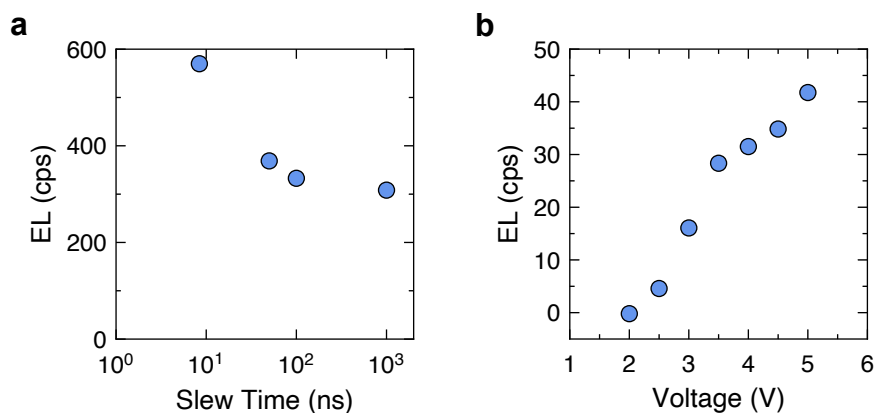


Figure 6.5: **Device characterization.** Electroluminescence intensity for varying (a) function generator slew time and (b) amplitude of square wave gate voltage from a custom pulsed voltage board. The data point at  $10^3$  ns slew time corresponds to sine wave excitation. Data were measured at 20 V in (a) and 100 kHz in (b).

Quantum dot electroluminescence can be obtained from these devices at temperatures ranging from room temperature down to cryogenic temperatures. At low temperature (near 4 K), we captured the spectrum of emission from a single blinking spot and found a fairly sharp electroluminescence spectrum with a narrowed linewidth typical of single quantum dot emission (Figure 6.6d) [177, 178]. The electroluminescence spectrum is consistent with measurements of single quantum dot photoluminescence spectra at cryogenic temperature (Figure 6.6c), and is also noticeably sharper than other single-dot electroluminescence spectra previously reported in the literature [161]. For comparison, in a device with an ensemble film of quantum dots, the electroluminescence spectrum remains broad from room temperature down to cryogenic temperatures due to inhomogeneous broadening from polydispersity in the colloidal synthesized solution of quantum dots (Figures 6.6a-b, 6.7). Finally, we performed AFM imaging on the devices to verify physically the presence of single quantum dots on carbon nanotubes which yield emission spots. To aid the location of specific emission points from electroluminescence imaging, the silicon dioxide/silicon substrate on which the devices are fabricated is pre-patterned with a grid of coordinate markers (Figure 6.1b). Figure 6.6e shows the electroluminescence image of a single emitting spot as well as the corresponding AFM image from that region. A quantum dot is found along the CNT from which electroluminescence is observed, thus confirming that EL can be obtained from single quantum dots using single CNT contacts.

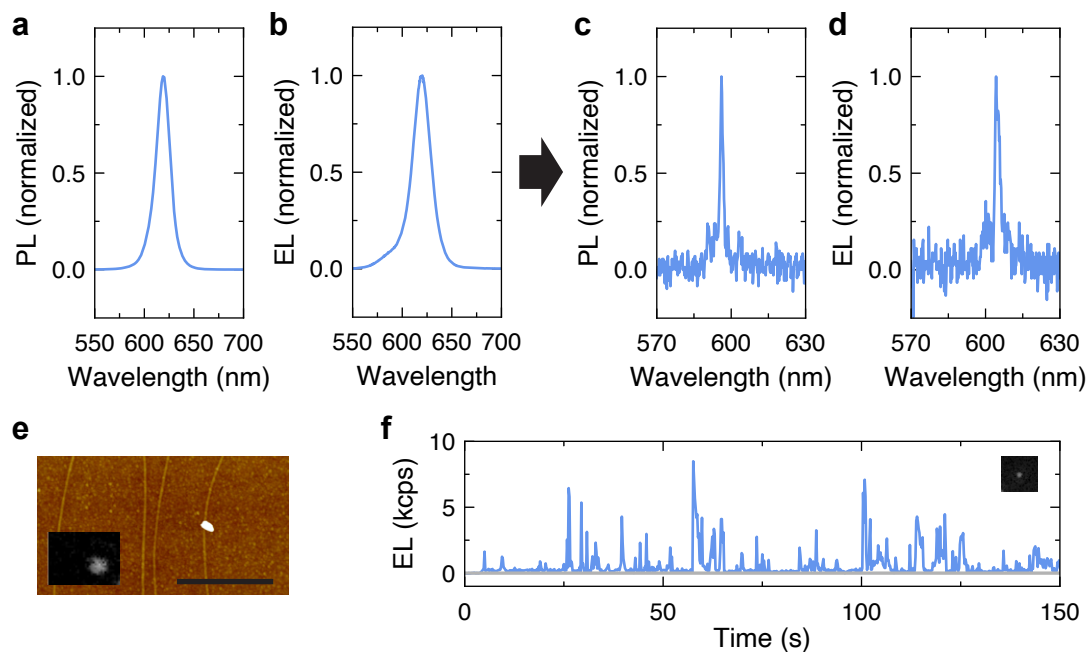


Figure 6.6: **Single quantum dot emission.** (a) Photoluminescence and (b) electroluminescence spectrum of a film of quantum dots at room temperature. (c) Photoluminescence and (d) electroluminescence spectrum of single quantum dots at cryogenic temperature. (e) AFM image of a single quantum dot on a carbon nanotube contact with no nearby quantum dots on the substrate (scale bar: 1  $\mu\text{m}$ ). Inset shows the electroluminescence image from the quantum dot in the AFM scan. (f) Fluctuation in electroluminescence intensity as a function of time for the emitting spot shown in the inset.

### 6.3 Conclusion

The device platform presented in this work presents a means by which electrically driven light emission can be achieved from nanoscale emitters down to single particles. While here we focus on large core-shell quantum dots, the device could be extended to study emission from other luminescent entities like single molecules for which molecular optoelectronic devices are difficult to construct or rely on highly specific chemistry or emission physics [179]. The ability to perform single-particle measurements may also reveal information useful to the design of micro- and macro-scale light-emitting devices with ensemble films. Although the performance of alternating current-driven light-emitting capacitors has been previously studied and high efficiencies obtained for organic emissive layers [53, 127], the performance of these devices with films of colloidal quantum dots could still be markedly improved towards applications in quantum dot-based displays and lighting. To this end, single-particle spectroscopic studies could provide insights on fundamental performance-limiting factors, including

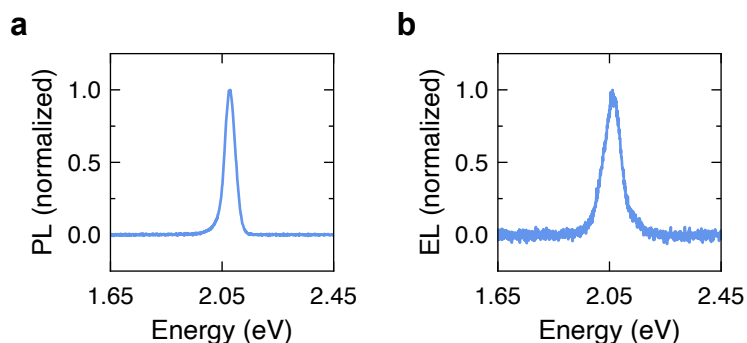


Figure 6.7: (a) Photoluminescence and (b) electroluminescence spectrum of a thin film of quantum dots at 4 K. The film was deposited by spin-casting the stock solution of quantum dots at 4000 rpm on the device substrate.

correlations between quantum yield, lifetime, and blinking in individual nanocrystals under the influence of high electric fields, heating, charging, and other effects [180–182]. Careful statistical characterization of heterogeneity in individual nanocrystal properties could guide routes of future material and device optimization [142, 183].

From an engineering perspective, such a platform opens up plentiful opportunities for design of integrated nanoscale light-emitting devices in the future. For instance, single quantum dots could be deterministically placed on single carbon nanotube contacts in order to achieve light emission from defined, localized spots in a scalable manner. With more precise fabrication, regular arrays of single quantum dots with desired spatial patterns could be envisaged, opening up avenues towards the fabrication of unusually designed optoelectronic devices at the nanoscale [184]. Since no processing steps are required after deposition of the luminescent material, single particle emitters could be patterned through a variety of top-down or bottom-up techniques [185–187]. A relatively simpler approach might consist of depositing a monolayer of quantum dots on top of an insulating masking layer patterned by e-beam lithography, in which the masking layer contains line openings of nanometer-scale width in which only single quantum dots can contact the underlying CNT. Because the device is patterned by conventional lithographic processes, the locations of carbon nanotube contacts can be defined beforehand, thereby pre-constraining the emission locations along a single lateral dimension and allowing the active area to be easily defined to individual nanotubes. As such, the device provides a viable route towards individually addressable, electrically pumped point emitters, unlike other approaches which use microscale or larger electrical contacts which cannot inject current into only a single quantum dot due to the inability to confine electrical current at the nanoscale [161, 162]. Finally, exploration of more nuanced properties of light emission (e.g. single-photon emission purity) from these devices could inform their potential functional use for quantum optic and other yet to be explored nanoscale optoelectronic applications [159, 188].

## 6.4 Methods

### Growth of aligned carbon nanotube arrays

Carbon nanotube samples were graciously provided by Qing Lin from H.-S. Philip Wong's group at Stanford University. The CNT arrays are grown by a previously reported chemical vapor deposition process [189]; for this work, growth is conducted on annealed quartz substrates starting with approximately 2.5 Å or 6.5 Å thick patterned Fe catalyst (producing a CNT density that is around 1 CNT/10 $\mu$ m or 2-5 CNT/ $\mu$ m with CNT length around 30-100  $\mu$ m or 30  $\mu$ m, respectively).

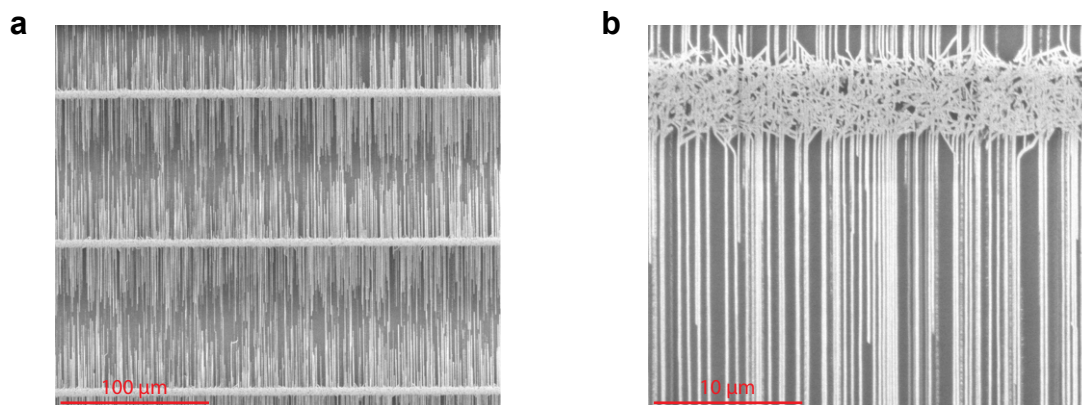


Figure 6.8: Representative SEM images of CVD-grown aligned carbon nanotube arrays with high density, at (a) low and (b) high magnification. The catalyst is patterned into 5  $\mu$ m wide strips with around 100  $\mu$ m spacing.

### Device fabrication

Aligned CNT arrays are transferred to a 50 nm silicon dioxide/p<sup>++</sup> silicon substrate (which is pre-patterned with metal alignment markers) using a PVA-based transfer process. In this transfer process, a 10 wt% solution of poly(vinyl alcohol) (PVA; MW 13,000-23,000, 87-89% hydrolyzed) is drop-cast on the quartz substrate with as-grown CNTs. After waiting 5 min, the substrate is heated at 60 °C for 10 min. Thermal release tape (Revalpha 3198MS) is pressed onto the quartz/PVA substrate and the tape with attached PVA is peeled off of the quartz substrate. The tape with PVA film is then pressed onto the target silicon substrate, which is then placed on a hot plate at 130 °C to release the tape. The PVA film is dissolved in deionized (DI) water at 60 °C for 10 min, leaving behind a transferred array of CNTs on the silicon substrate.



Metal contacts are patterned by photolithography using a direct-write tool (Heidelberg  $\mu$ PG 101) and deposited by e-beam evaporation of Ti (3 nm)/Au (30 nm), followed by liftoff in 60 °C acetone. The contacts are patterned such that the aligned carbon nanotube arrays are perpendicular to the metal line contacts. The active area of the device is defined by a second photolithography step and CNTs outside the active area are removed by O<sub>2</sub> plasma treatment. A tri-layer photolithographic process consisting of methyl methacrylate (MMA) EL9 (170 °C, 5 min bake)/LOR-5A (170 °C, 5 min bake)/S1818 (100 °C, 2 min bake) was used, in which the photoresist is developed in MF-26A followed by acetone to transfer the pattern to the MMA layer. An optional annealing step (300 °C for 1 h in air) reduces surface residue from the fabrication process. A solution of colloidal quantum dots (CdSe/CdZnSe (4.5 nm)/ZnSeS (4.5 nm), 85 mg mL<sup>-1</sup>) is diluted up to 50,000 times in octane ( $\geq 99\%$ ) and spin-coated on top of the substrate at 4000 rpm. Wire-bond connections are made to the metal contacts for application of electrical bias.

## Device measurement

Pulsed voltages are applied using a function generator (33522A, Agilent) and voltage amplifier (Model 2340, TEGAM) or a custom switching board (CoolGaN 600 V half-bridge evaluation board with GaN EiceDRIVER) as diagrammed in Figure 6.9. Optical measurements are performed using a custom-built micro-photoluminescence (PL) setup in which PL/EL is imaged by an electron-multiplying charge-coupled device (CCD) (Luca, Andor) or dispersed by a spectrograph (Shamrock 500i, Andor) with a 1501/mm grating and detected by a Si CCD (Newton 971, Andor). The dark background of the CCD is subtracted from the acquired signal for each measurement. Devices are operated under vacuum in a closed-cycle cryostat (Cryostation s200, Montana Instruments) at temperatures ranging from room temperature down to 4 K. Measurements are performed using a 50 $\times$  objective (NA=0.42). Hardware control and data acquisition are performed using custom Python software based on the open-source ScopeFoundry platform.



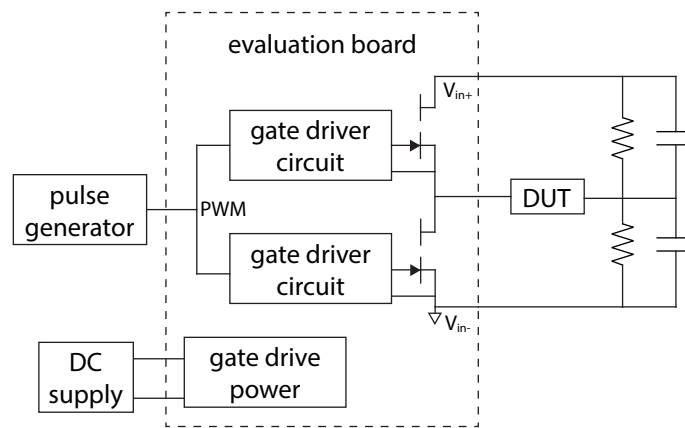


Figure 6.9: Diagram of a half-bridge circuit board (EVAL\_1EDF\_G1\_HB\_GAN, Infineon) used to output pulsed voltages to the electroluminescence device (DUT) at a frequency dictated by the pulse generator with peak-to-peak voltage determined by  $V_{in+} - V_{in-}$  as supplied by a DC power source. The offset voltage depends on the voltage reference set by the parallel resistor/capacitor voltage divider.

# Chapter 7

## Conclusion

Throughout the course of this thesis, we have investigated a singular light-emitting device structure based on a metal-oxide-semiconductor capacitor. Although seemingly simple in design, its operation is subtly complex and its tunable characteristics give way to varied avenues of exploration in other areas of optoelectronic engineering. Many questions still remain, particularly if practical use is to be obtained from such a device. At present, its efficiency compares to that of its direct-current light-emitting diode counterparts for several organic materials, suggesting that its performance is not necessarily out of practical scope. However, the performance metrics vary widely by choice of emissive material, and it remains to be seen whether its performance could be improved for key materials of emerging interest, such as colloidal quantum dots. To this end, finer-grained characterization would provide more insight – for instance, super-resolved or near-field scanning optical measurements would allow the emission distance from individual carbon nanotube contacts to be determined experimentally. Such a result might suggest yet another geometric reformulation of the metal-semiconductor contact, perhaps with three-dimensional structure across the emissive film, to enable brighter and more efficient emission.

As a light source, another critical factor is the stability of light emission, with regards to both spectrum and intensity. While not included in the scope of this thesis, we have found that the stability of light emission tends to worsen with increasing material energy gap, akin to the worse lifetimes of blue (organic) LEDs; as such, themes pertinent to the engineering of conventional devices may find relevance to the devices considered here. Emission from these devices can be sustained with a half life lasting half a day or so, depending on the material and driving conditions, but new strategies are necessary to establish better stability at biases required for bright emission. If accomplished, realistic applications of the platform can be more reasonably envisioned. For example, the manually pipetted multicolored arrays demonstrated in this work could be upgraded to hundreds of colors or miniaturized to even smaller footprints using automated microdispensing techniques or robotic pipetting systems with higher precision and accuracy.

While we focus mostly on the visible spectrum in this work due to its easily accessible nature, with only sparing mentions to the ultraviolet and infrared regime, the potential spectral

breadth of the device is perhaps one of its stronger suits due to its ability to inject charge in a dopant-free and contact-independent manner. To this end, it is worthy to consider the possibility of light emission at more extreme wavelengths in the ultraviolet and infrared regime which lie farther past the edges of the visible spectrum. Light-emitting devices in these regimes remain lesser developed and offer ripe opportunities in applications beyond visual displays and lighting. Wider spectral control would elevate the proof-of-concept examples in the later chapters by making truly broad spectrum compact spectral measurements possible, or by enabling fast, triggerable sources of light at wavelengths relevant for photonic applications. Besides light emission, the pulsed-driven nanoscale contacts shown here may find relevance to other physical phenomena requiring facile charge injection or high localized electric fields. While the fate of the devices discussed in this body of work remains uncertain, it is the hope that at the very least, some enjoyable scientific entertainment has been provided through the array of experiments presented here.

# Bibliography

1. Pattison, P. M., Tsao, J. Y., Brainard, G. C. & Bugbee, B. LEDs for photons, physiology and food. *Nature* **563**, 493–500 (2018).
2. Nakamura, S., Mukai, T. & Senoh, M. Candela-class high-brightness InGaN/AlGaN double-heterostructure blue-light-emitting diodes. *Appl. Phys. Lett.* **64**, 1687–1689 (1994).
3. Round, H. J. in *Semiconductor Devices: Pioneering Papers* 879–879 (WORLD SCIENTIFIC, 1991).
4. Pust, P., Schmidt, P. J. & Schnick, W. A revolution in lighting. *Nat. Mater.* **14**, 454–458 (2015).
5. Holonyak, N. & Bevacqua, S. F. Coherent Visible Light Emission from Ga(As<sub>1-x</sub>P<sub>x</sub>) Junctions. *Appl. Phys. Lett.* **1**, 82–83 (1962).
6. Tang, C. W. & VanSlyke, S. A. Organic electroluminescent diodes. *Appl. Phys. Lett.* **51**, 913–915 (1987).
7. Helfrich, W. & Schneider, W. G. Recombination Radiation in Anthracene Crystals. *Phys. Rev. Lett.* **14**, 229–231 (1965).
8. Forrest, S. R. *Organic Electronics: Foundations to Applications* (Oxford University Press, 2020).
9. Butler, K. H. Electroluminescence. *Science* **129**, 544–550 (1959).
10. Destriau, G. Recherches sur les scintillations des sulfures de zinc aux rayons  $\alpha$ . *Journal de Chimie Physique* **33**, 587–625 (1936).
11. Rack, P. D., Naman, A., Holloway, P. H., Sun, S.-S. & Tuenge, R. T. Materials Used in Electroluminescent Displays. *MRS Bull.* **21**, 49–58 (1996).
12. Lien, D.-H. *et al.* Large-area and bright pulsed electroluminescence in monolayer semiconductors. *Nat. Commun.* **9**, 1229 (2018).
13. Chao, T.-C. *et al.* Highly efficient UV organic light-emitting devices based on bi(9,9-diaryluorene)s. *Adv. Mater.* **17**, 992–996 (2005).
14. Kneissl, M., Seong, T.-Y., Han, J. & Amano, H. The emergence and prospects of deep-ultraviolet light-emitting diode technologies. *Nat. Photonics* **13**, 233–244 (2019).

15. Li, X. *et al.* Bright colloidal quantum dot light-emitting diodes enabled by efficient chlorination. *Nat. Photonics* **12**, 159–164 (2018).
16. Liu, Y., Li, C., Ren, Z., Yan, S. & Bryce, M. R. All-organic thermally activated delayed fluorescence materials for organic light-emitting diodes. *Nature Reviews Materials* **3**, 1–20 (2018).
17. Yao, Y., Hoffman, A. J. & Gmachl, C. F. Mid-infrared quantum cascade lasers. *Nat. Photonics* **6**, 432–439 (2012).
18. Pan, Y. *et al.* Recent Advances in Alternating Current-Driven Organic Light-Emitting Devices. *Adv. Mater.* **29** (2017).
19. Kong, S. H., Lee, J. I., Kim, S. & Kang, M. S. Light-Emitting Devices Based on Electrochemiluminescence: Comparison to Traditional Light-Emitting Electrochemical Cells. *ACS Photonics* **5**, 267–277 (2018).
20. Fresta, E. & Costa, R. D. Beyond traditional light-emitting electrochemical cells – a review of new device designs and emitters. *J. Mater. Chem.* **5**, 5643–5675 (2017).
21. Cho, S. H. *et al.* Extremely bright full color alternating current electroluminescence of solution-blended fluorescent polymers with self-assembled block copolymer micelles. *ACS Nano* **7**, 10809–10817 (2013).
22. Jayathilaka, W. A. D., Chinnappan, A., Tey, J. N., Wei, J. & Ramakrishna, S. Alternative current electroluminescence and flexible light emitting devices. *J. Mater. Chem.* **7**, 5553–5572 (2019).
23. Russ, M. J. & Kennedy, D. I. The Effects of Double Insulating Layers on the Electroluminescence of Evaporated ZnS : Mn Films. *J. Electrochem. Soc.* **114**, 1066 (1967).
24. Fischer, A. G. Electroluminescent Lines in ZnS Powder Particles: II . Models and Comparison with Experience. *J. Electrochem. Soc.* **110**, 733 (1963).
25. Perumal, A., Lüssem, B. & Leo, K. High brightness alternating current electroluminescence with organic light emitting material. *Appl. Phys. Lett.* **100**, 103307 (2012).
26. Chen, Y. *et al.* Solution-processable hole-generation layer and electron-transporting layer: Towards high-performance, alternating-current-driven, field-induced polymer electroluminescent devices. *Adv. Funct. Mater.* **24**, 2677–2688 (2014).
27. Wang, C. *et al.* Extremely bendable, high-performance integrated circuits using semi-conducting carbon nanotube networks for digital, analog, and radio-frequency applications. *Nano Lett.* **12**, 1527–1533 (2012).
28. Sung, J. *et al.* AC field-induced polymer electroluminescence with single wall carbon nanotubes. *Nano Lett.* **11**, 966–972 (2011).
29. Chen, Y. *et al.* Effect of multi-walled carbon nanotubes on electron injection and charge generation in AC field-induced polymer electroluminescence. *Org. Electron.* **14**, 8–18 (2013).

30. McCarthy, M. A. *et al.* Low-voltage, low-power, organic light-emitting transistors for active matrix displays. *Science* **332**, 570–573 (2011).
31. Nobeshima, T., Nakakomi, M., Nakamura, K. & Kobayashi, N. Alternating-current-driven, color-tunable electrochemiluminescent cells. *Adv. Opt. Mater.* **1**, 144–149 (2013).
32. Ahn, J. H., Wang, C., Perepichka, I. F., Bryce, M. R. & Petty, M. C. Blue organic light emitting devices with improved colour purity and efficiency through blending of poly(9,9-dioctyl-2,7-fluorene) with an electron transporting material. *J. Mater. Chem.* **17**, 2996–3001 (2007).
33. Rudmann, H. & Rubner, M. F. Single layer light-emitting devices with high efficiency and long lifetime based on tris(2,2' bipyridyl) ruthenium(II) hexafluorophosphate. *J. Appl. Phys.* **90**, 4338–4345 (2001).
34. Kang, G.-W., Ahn, Y.-J., Park, D. Y. & Lee, C. *Efficient blue electroluminescence from 9,10-diphenylanthracene* in *Organic Light-Emitting Materials and Devices VI* **4800** (SPIE, 2003), 208–215.
35. Snow, E. S., Novak, J. P., Campbell, P. M. & Park, D. Random networks of carbon nanotubes as an electronic material. *Appl. Phys. Lett.* **82**, 2145–2147 (2003).
36. Jin, Y., Yu, C., Denman, R. J. & Zhang, W. Recent advances in dynamic covalent chemistry. *Chem. Soc. Rev.* **42**, 6634–6654 (2013).
37. Nakamura, T., Sharma, D. K., Hirata, S. & Vacha, M. Intrachain Aggregates as the Origin of Green Emission in Polyfluorene Studied on Ensemble and Single-Chain Level. *J. Phys. Chem. C* **122**, 8137–8146 (2018).
38. Zhao, Y. *et al.* Synthesis of porphyrin-based two-dimensional metal–organic framework nanodisk with small size and few layers. *J. Mater. Chem. A* **6**, 2828–2833 (2018).
39. Amani, M. *et al.* Near-unity photoluminescence quantum yield in MoS<sub>2</sub>. *Science* **350**, 1065–1068 (2015).
40. Nakamura, S., Mukai, T. & Senoh, M. Candela-class high-brightness InGaN/AlGaN double-heterostructure blue-light-emitting diodes. *Appl. Phys. Lett.* **64**, 1687–1689 (1994).
41. Kuo, C. P. *et al.* High performance AlGaInP visible light-emitting diodes. *Appl. Phys. Lett.* **57**, 2937–2939 (1990).
42. Won, Y.-H. *et al.* Highly efficient and stable InP/ZnSe/ZnS quantum dot light-emitting diodes. *Nature* **575**, 634–638 (2019).
43. Dai, X. *et al.* Solution-processed, high-performance light-emitting diodes based on quantum dots. *Nature* **515**, 96–99 (2014).
44. Kaji, H. *et al.* Purely organic electroluminescent material realizing 100% conversion from electricity to light. *Nat. Commun.* **6**, 8476 (2015).

45. Tsutsui, T., Lee, S.-B. & Fujita, K. Charge recombination electroluminescence in organic thin-film devices without charge injection from external electrodes. *Appl. Phys. Lett.* **85**, 2382–2384 (2004).
46. Cho, S. H. *et al.* High performance AC electroluminescence from colloidal quantum dot hybrids. *Adv. Mater.* **24**, 4540–4546 (2012).
47. Cho, J. *et al.* Centimeter-scale and visible wavelength monolayer light-emitting devices. *Adv. Funct. Mater.* **30**, 1907941 (2020).
48. Liu, X. *et al.* A perovskite light-emitting device driven by low-frequency alternating current voltage. *Adv. Opt. Mater.* **6**, 1800206 (2018).
49. Maddalena, F., Chin, X. Y., Cortecchia, D., Bruno, A. & Soci, C. Brightness Enhancement in Pulsed-Operated Perovskite Light-Emitting Transistors. *ACS Appl. Mater. Interfaces* **10**, 37316–37325 (2018).
50. Yamao, T., Shimizu, Y., Terasaki, K. & Hotta, S. Organic light-emitting field-effect transistors operated by alternating-current gate voltages. *Adv. Mater.* **20**, 4109–4112 (2008).
51. Simon, J. & Andre, J.-J. *Molecular Semiconductors* (Springer Berlin Heidelberg, 1985).
52. Shirota, Y. & Kageyama, H. Charge carrier transporting molecular materials and their applications in devices. *Chem. Rev.* **107**, 953–1010 (2007).
53. Zhao, Y., Wang, V., Lien, D.-H. & Javey, A. A generic electroluminescent device for emission from infrared to ultraviolet wavelengths. *Nature Electronics* **3**, 612–621 (2020).
54. Pierret, R. F. *Semiconductor Device Fundamentals* (Pearson, Upper Saddle River, NJ, 1995).
55. Blades, C. D. J. & Walker, A. B. Simulation of organic light-emitting diodes. *Synth. Met.* **111-112**, 335–340 (2000).
56. Wood, V., Halpert, J. E., Panzer, M. J., Bawendi, M. G. & Bulović, V. Alternating current driven electroluminescence from ZnSe/ZnS:Mn/ZnS nanocrystals. *Nano Lett.* **9**, 2367–2371 (2009).
57. Wood, V. *et al.* Electroluminescence from nanoscale materials via field-driven ionization. *Nano Lett.* **11**, 2927–2932 (2011).
58. Robertson, J. High dielectric constant oxides. *Eur. Phys. J. - Appl. phys.* **28**, 265–291 (2004).
59. Crone, B. K., Davids, P. S., Campbell, I. H. & Smith, D. L. Device model investigation of single layer organic light emitting diodes. *J. Appl. Phys.* **84**, 833–842 (1998).
60. Shuttle, C. G., Hamilton, R., O'Regan, B. C., Nelson, J. & Durrant, J. R. Charge-density-based analysis of the current-voltage response of polythiophene/fullerene photovoltaic devices. *Proc. Natl. Acad. Sci. U. S. A.* **107**, 16448–16452 (2010).

61. Deng, Z., Lee, S. T., Webb, D. P., Chan, Y. C. & Gambling, W. A. Carrier transport in thin films of organic electroluminescent materials. *Synth. Met.* **107**, 107–109 (1999).
62. Liu, J. *et al.* High mobility emissive organic semiconductor. *Nat. Commun.* **6**, 10032 (2015).
63. Li, J. *et al.* Aromatic Extension at 2,6-Positions of Anthracene toward an Elegant Strategy for Organic Semiconductors with Efficient Charge Transport and Strong Solid State Emission. *J. Am. Chem. Soc.* **139**, 17261–17264 (2017).
64. Harkin, D. J. *et al.* Decoupling Charge Transport and Electroluminescence in a High Mobility Polymer Semiconductor. *Adv. Mater.* **28**, 6378–6385 (2016).
65. Malliaras, G. G. & Scott, J. C. The roles of injection and mobility in organic light emitting diodes. *J. Appl. Phys.* **83**, 5399–5403 (1998).
66. Matsushima, T. *et al.* High performance from extraordinarily thick organic light-emitting diodes. *Nature* **572**, 502–506 (2019).
67. Patel, N. K., Cina, S. & Burroughes, J. H. High-efficiency organic light-emitting diodes. *IEEE J. Sel. Top. Quantum Electron.* **8**, 346–361 (2002).
68. Bernhard, S. *et al.* Electroluminescence in ruthenium(II) complexes. *J. Am. Chem. Soc.* **124**, 13624–13628 (2002).
69. Elfring Jr, W. H. & Crosby, G. A. Excited states of mixed-ligand chelates of ruthenium(II). Quantum yield and decay time measurements. *J. Am. Chem. Soc.* **103**, 2683–2687 (1981).
70. Jabbour, G. E., Wang, J.-F. & Peyghambarian, N. High-efficiency organic electrophosphorescent devices through balance of charge injection. *Appl. Phys. Lett.* **80**, 2026–2028 (2002).
71. Yablonovitch, E. & Cody, G. D. Intensity enhancement in textured optical sheets for solar cells. *IEEE Trans. Electron Devices* **29**, 300–305 (1982).
72. Lien, D.-H. *et al.* Engineering light outcoupling in 2D materials. *Nano Lett.* **15**, 1356–1361 (2015).
73. Wang, Z. B. *et al.* Optical design of organic light emitting diodes. *J. Appl. Phys.* **109**, 053107 (2011).
74. Takahashi, T. *et al.* Carbon nanotube active-matrix backplanes for mechanically flexible visible light and X-ray imagers. *Nano Lett.* **13**, 5425–5430 (2013).
75. Stelzl, F. F. & Würfel, U. Modeling the influence of doping on the performance of bulk heterojunction organic solar cells: One-dimensional effective semiconductor versus two-dimensional donor/acceptor model. *Phys. Rev. B Condens. Matter* **86**, 075315 (2012).
76. Kaienburg, P., Rau, U. & Kirchartz, T. Extracting Information about the Electronic Quality of Organic Solar-Cell Absorbers from Fill Factor and Thickness. *Phys. Rev. Appl.* **6**, 024001 (2016).



77. Kirchartz, T., Nelson, J. & Rau, U. Reciprocity between Charge Injection and Extraction and Its Influence on the Interpretation of Electroluminescence Spectra in Organic Solar Cells. *Phys. Rev. Appl.* **5**, 054003 (2016).
78. Dupuis, R. D. & Krames, M. R. History, Development, and Applications of High-Brightness Visible Light-Emitting Diodes. *J. Lightwave Technol.* **26**, 1154–1171 (2008).
79. *EL Wire* <https://learn.adafruit.com/el-wire/>. Accessed: 2023-3-14. 2012.
80. Shi, X. *et al.* Large-area display textiles integrated with functional systems. *Nature* **591**, 240–245 (2021).
81. Hanton, O., Wessely, M., Mueller, S., Fraser, M. & Roudaut, A. *ProtoSpray: Combining 3D Printing and Spraying to Create Interactive Displays with Arbitrary Shapes* in *Proceedings of the 2020 CHI Conference on Human Factors in Computing Systems* (Association for Computing Machinery, Honolulu, HI, USA, 2020), 1–13.
82. Bernanose, A. Electroluminescence of organic compounds. *Br. J. Appl. Phys.* **6**, S54 (1955).
83. Adachi, C., Baldo, M. A., Thompson, M. E. & Forrest, S. R. Nearly 100% internal phosphorescence efficiency in an organic light-emitting device. *J. Appl. Phys.* **90**, 5048–5051 (2001).
84. Reineke, S. *et al.* White organic light-emitting diodes with fluorescent tube efficiency. *Nature* **459**, 234–238 (2009).
85. Gessmann, T. & Schubert, E. F. High-efficiency AlGaInP light-emitting diodes for solid-state lighting applications. *J. Appl. Phys.* **95**, 2203–2216 (2004).
86. Mitschke, U. & Bäuerle, P. The electroluminescence of organic materials. *J. Mater. Chem.* **10**, 1471–1507 (2000).
87. Kajiwara, K., Terasaki, K., Yamao, T. & Hotta, S. Light-emitting field-effect transistors consisting of bilayer-crystal organic semiconductors. *Adv. Funct. Mater.* **21**, 2854–2860 (2011).
88. Marconi, A., Anopchenko, A., Pucker, G. & Pavese, L. Power efficiency estimation of silicon nanocrystals based light emitting devices in alternating current regime. *Appl. Phys. Lett.* **98**, 201103 (2011).
89. Hecht, D. S., Hu, L. & Irvin, G. Emerging transparent electrodes based on thin films of carbon nanotubes, graphene, and metallic nanostructures. *Adv. Mater.* **23**, 1482–1513 (2011).
90. Topinka, M. A. *et al.* Charge transport in interpenetrating networks of semiconducting and metallic carbon nanotubes. *Nano Lett.* **9**, 1866–1871 (2009).
91. Bowick, C. *RF Circuit Design* (2008).
92. Slinker, J. D. *et al.* Efficient yellow electroluminescence from a single layer of a cyclometalated iridium complex. *J. Am. Chem. Soc.* **126**, 2763–2767 (2004).

93. Ràfols-Ribé, J. *et al.* High-performance organic light-emitting diodes comprising ultrastable glass layers. *Sci Adv* **4**, eaar8332 (2018).
94. Goushi, K., Yoshida, K., Sato, K. & Adachi, C. Organic light-emitting diodes employing efficient reverse intersystem crossing for triplet-to-singlet state conversion. *Nat. Photonics* **6**, 253–258 (2012).
95. Uoyama, H., Goushi, K., Shizu, K., Nomura, H. & Adachi, C. Highly efficient organic light-emitting diodes from delayed fluorescence. *Nature* **492**, 234–238 (2012).
96. Wu, T.-L. *et al.* Diboron compound-based organic light-emitting diodes with high efficiency and reduced efficiency roll-off. *Nat. Photonics* **12**, 235–240 (2018).
97. Kotadiya, N. B., Blom, P. W. M. & Wetzelaer, G.-J. A. H. Efficient and stable single-layer organic light-emitting diodes based on thermally activated delayed fluorescence. *Nat. Photonics* **13**, 765–769 (2019).
98. Wang, V., Zhao, Y. & Javey, A. Performance Limits of an Alternating Current Electroluminescent Device. *Adv. Mater.* **33**, e2005635 (2021).
99. Chen, Y., Xia, Y., Smith, G. M. & Carroll, D. L. Frequency-dependent, alternating current-driven, field-induced polymer electroluminescent devices with high power efficiency. *Adv. Mater.* **26**, 8133–8140 (2014).
100. Murawski, C., Leo, K. & Gather, M. C. Efficiency roll-off in organic light-emitting diodes. *Adv. Mater.* **25**, 6801–6827 (2013).
101. Wang, L., Xiao, L., Gu, H. & Sun, H. Advances in alternating current electroluminescent devices. *Adv. Opt. Mater.* **7**, 1801154 (2019).
102. Chen, Y. *et al.* Solution-processable hole-generation layer and electron-transporting layer: Towards high-performance, alternating-current-driven, field-induced polymer electroluminescent devices. *Adv. Funct. Mater.* **24**, 2677–2688 (2014).
103. Kim, A. Y. *et al.* Performance of high-power AlInGaN light emitting diodes. *Physica Status Solidi A Appl. Res.* **188**, 15–21 (2001).
104. Peter, M. *et al.* New developments in green LEDs. *Phys. Status Solidi* **206**, 1125–1129 (2009).
105. Seino, Y., Inomata, S., Sasabe, H., Pu, Y.-J. & Kido, J. High-Performance Green OLEDs Using Thermally Activated Delayed Fluorescence with a Power Efficiency of over 100 lm W<sup>(-1)</sup>. *Adv. Mater.* **28**, 2638–2643 (2016).
106. Xie, G. *et al.* Very low turn-on voltage and high brightness tris-(8-hydroxyquinoline) aluminum-based organic light-emitting diodes with a MoOx p-doping layer. *Appl. Phys. Lett.* **92**, 093305 (2008).
107. Fröbel, M. *et al.* Enhancing the efficiency of alternating current driven organic light-emitting devices by optimizing the operation frequency. *Org. Electron.* **14**, 809–813 (2013).

108. Wan, Y. *et al.* Efficient Organic Light-Emitting Transistors Based on High-Quality Ambipolar Single Crystals. *ACS Appl. Mater. Interfaces* **12**, 43976–43983 (2020).
109. Gwinner, M. C. *et al.* Highly efficient single-layer polymer ambipolar light-emitting field-effect transistors. *Adv. Mater.* **24**, 2728–2734 (2012).
110. Waldrip, K. E. *et al.* Improved electroluminescence of ZnS:Mn thin films by codoping with potassium chloride. *J. Appl. Phys.* **89**, 1664–1670 (2001).
111. Migita, M., Kanehisa, O., Shiiki, M. & Yamamoto, H. The preparation of ZnS:Mn electroluminescent layers by MOCVD using new manganese sources. *J. Cryst. Growth* **93**, 686–691 (1988).
112. Wang, C. *et al.* User-interactive electronic skin for instantaneous pressure visualization. *Nat. Mater.* **12**, 899–904 (2013).
113. Sanderson, S., Philippa, B., Vamvounis, G., Burn, P. L. & White, R. D. Understanding charge transport in Ir(ppy)<sub>3</sub>:CBP OLED films. *J. Chem. Phys.* **150**, 094110 (2019).
114. Wang, T. *et al.* An optical neural network using less than 1 photon per multiplication. *Nat. Commun.* **13**, 123 (2022).
115. Bacon, C. P., Mattley, Y. & DeFrece, R. Miniature spectroscopic instrumentation: Applications to biology and chemistry. *Rev. Sci. Instrum.* **75**, 1–16 (2004).
116. Müller, C. D. *et al.* Multi-colour organic light-emitting displays by solution processing. *Nature* **421**, 829–833 (2003).
117. Ning, C.-Z., Dou, L. & Yang, P. Bandgap engineering in semiconductor alloy nanomaterials with widely tunable compositions. *Nature Reviews Materials* **2**, 1–14 (2017).
118. Wang, X., Zhang, Y., Ma, X., Xu, T. & Arce, G. R. Compressive spectral imaging system based on liquid crystal tunable filter. *Opt. Express* **26**, 25226–25243 (2018).
119. Bao, J. & Bawendi, M. G. A colloidal quantum dot spectrometer. *Nature* **523**, 67–70 (2015).
120. Yang, Z. *et al.* Single-nanowire spectrometers. *Science* **365**, 1017–1020 (2019).
121. Yuan, S., Naveh, D., Watanabe, K., Taniguchi, T. & Xia, F. A wavelength-scale black phosphorus spectrometer. *Nat. Photonics* **15**, 601–607 (2021).
122. Yang, Z., Albrow-Owen, T., Cai, W. & Hasan, T. Miniaturization of optical spectrometers. *Science* **371** (2021).
123. Han, T.-H. *et al.* Ultrahigh-efficiency solution-processed simplified small-molecule organic light-emitting diodes using universal host materials. *Sci Adv* **2**, e1601428 (2016).
124. Zheng, H. *et al.* All-solution processed polymer light-emitting diode displays. *Nat. Commun.* **4**, 1971 (2013).
125. Costa, R. D. *et al.* Luminescent ionic transition-metal complexes for light-emitting electrochemical cells. *Angew. Chem. Int. Ed Engl.* **51**, 8178–8211 (2012).

126. Shirasaki, Y., Supran, G. J., Bawendi, M. G. & Bulović, V. Emergence of colloidal quantum-dot light-emitting technologies. *Nat. Photonics* **7**, 13–23 (2012).
127. Wang, V. & Javey, A. A Resonantly Driven, Electroluminescent Metal Oxide Semiconductor Capacitor with High Power Efficiency. *ACS Nano* **15**, 15210–15217 (2021).
128. Kulkarni, A. P., Kong, X. & Jenekhe, S. A. Fluorenone-Containing Polyfluorenes and Oligofluorenes: Photophysics, Origin of the Green Emission and Efficient Green Electroluminescence. *J. Phys. Chem. B* **108**, 8689–8701 (2004).
129. Rörich, I., Mikhnenko, O. V., Gehrig, D., Blom, P. W. M. & Crăciun, N. I. Influence of Energetic Disorder on Exciton Lifetime and Photoluminescence Efficiency in Conjugated Polymers. *J. Phys. Chem. B* **121**, 1405–1412 (2017).
130. Lane, P. A. *et al.* Origin of electrophosphorescence from a doped polymer light emitting diode. *Phys. Rev. B Condens. Matter* **63**, 235206 (2001).
131. Stears, R. L., Martinsky, T. & Schena, M. Trends in microarray analysis. *Nat. Med.* **9**, 140–145 (2003).
132. Zhang, F., Xu, H. & Wang, Z. Spectral design methods for multi-channel LED light sources based on differential evolution. *Appl. Opt.* **55**, 7771–7781 (2016).
133. Belušič, G., Ilić, M., Meglič, A. & Pirih, P. A fast multispectral light synthesiser based on LEDs and a diffraction grating. *Sci. Rep.* **6**, 32012 (2016).
134. Franke, K. *et al.* An arbitrary-spectrum spatial visual stimulator for vision research. *Elife* **8** (2019).
135. David, A., Young, N. G., Hurni, C. A. & Craven, M. D. Quantum Efficiency of III-Nitride Emitters: Evidence for Defect-Assisted Nonradiative Recombination and its Effect on the Green Gap. *Phys. Rev. Appl.* **11**, 031001 (2019).
136. Nguyen, R. M. H., Prasad, D. K. & Brown, M. S. *Training-Based Spectral Reconstruction from a Single RGB Image in Computer Vision – ECCV 2014* (Springer International Publishing, 2014), 186–201.
137. Kurokawa, U., Choi, B. I. & Chang, C.-C. Filter-Based Miniature Spectrometers: Spectrum Reconstruction Using Adaptive Regularization. *IEEE Sens. J.* **11**, 1556–1563 (2011).
138. Wang, Z. *et al.* Single-shot on-chip spectral sensors based on photonic crystal slabs. *Nat. Commun.* **10**, 1020 (2019).
139. Yako, M. *et al.* Video-rate hyperspectral camera based on a CMOS-compatible random array of Fabry–Pérot filters. *Nat. Photonics*, 1–6 (2023).
140. Zhang, W. *et al.* Deeply learned broadband encoding stochastic hyperspectral imaging. *Light Sci Appl* **10**, 108 (2021).
141. Yoon, H. H. *et al.* Miniaturized spectrometers with a tunable van der Waals junction. *Science* **378**, 296–299 (2022).

142. Deng, W. *et al.* Electrically tunable two-dimensional heterojunctions for miniaturized near-infrared spectrometers. *Nat. Commun.* **13**, 4627 (2022).
143. Park, J.-I., Lee, M.-H., Grossberg, M. D. & Nayar, S. K. *Multispectral Imaging Using Multiplexed Illumination* in *2007 IEEE 11th International Conference on Computer Vision* (2007), 1–8.
144. Goel, M. *et al.* *HyperCam: hyperspectral imaging for ubiquitous computing applications* in *Proceedings of the 2015 ACM International Joint Conference on Pervasive and Ubiquitous Computing* (Association for Computing Machinery, Osaka, Japan, 2015), 145–156.
145. Ma, X., Yuan, X., Fu, C. & Arce, G. R. LED-based compressive spectral-temporal imaging. *Opt. Express* **29**, 10698–10715 (2021).
146. Ma, X., Yuan, X., Fu, C. & Arce, G. R. *Active illumination compressive 4D spectral video imaging system* in *OSA Imaging and Applied Optics Congress 2021* (Washington, DC, 2021).
147. Wagadarikar, A., John, R., Willett, R. & Brady, D. Single disperser design for coded aperture snapshot spectral imaging. *Appl. Opt.* **47**, B44–51 (2008).
148. Arce, G. R., Brady, D. J., Carin, L., Arguello, H. & Kittle, D. S. Compressive Coded Aperture Spectral Imaging: An Introduction. *IEEE Signal Process. Mag.* **31**, 105–115 (2014).
149. Anikeeva, P. O., Halpert, J. E., Bawendi, M. G. & Bulović, V. Quantum dot light-emitting devices with electroluminescence tunable over the entire visible spectrum. *Nano Lett.* **9**, 2532–2536 (2009).
150. Moreels, I. *et al.* Size-tunable, bright, and stable PbS quantum dots: a surface chemistry study. *ACS Nano* **5**, 2004–2012 (2011).
151. Levchuk, I. *et al.* Brightly Luminescent and Color-Tunable Formamidinium Lead Halide Perovskite FAPbX<sub>3</sub> (X = Cl, Br, I) Colloidal Nanocrystals. *Nano Lett.* **17**, 2765–2770 (2017).
152. Danielson, E. *et al.* A combinatorial approach to the discovery and optimization of luminescent materials. *Nature* **389**, 944–948 (1997).
153. Huang, L., Luo, R., Liu, X. & Hao, X. Spectral imaging with deep learning. *Light Sci Appl* **11**, 61 (2022).
154. Fu, Y., Zou, Y., Zheng, Y. & Huang, H. Spectral reflectance recovery using optimal illuminations. *Opt. Express* **27**, 30502–30516 (2019).
155. Lee, C.-L., Lee, K. B. & Kim, J.-J. Polymer phosphorescent light-emitting devices doped with tris(2-phenylpyridine) iridium as a triplet emitter. *Appl. Phys. Lett.* **77**, 2280–2282 (2000).
156. Meng, T. *et al.* Ultrahigh-resolution quantum-dot light-emitting diodes. *Nat. Photonics* **16**, 297–303 (2022).

157. Joo, W.-J. *et al.* Metasurface-driven OLED displays beyond 10,000 pixels per inch. *Science* **370**, 459–463 (2020).
158. Fiore, A., Chen, J. X. & Ilegems, M. Scaling quantum-dot light-emitting diodes to submicrometer sizes. *Appl. Phys. Lett.* **81**, 1756–1758 (2002).
159. Aharonovich, I., Englund, D. & Toth, M. Solid-state single-photon emitters. *Nat. Photonics* **10**, 631–641 (2016).
160. Kagan, C. R., Bassett, L. C., Murray, C. B. & Thompson, S. M. Colloidal Quantum Dots as Platforms for Quantum Information Science. *Chem. Rev.* **121**, 3186–3233 (2021).
161. Lin, X. *et al.* Electrically-driven single-photon sources based on colloidal quantum dots with near-optimal antibunching at room temperature. *Nat. Commun.* **8**, 1132 (2017).
162. Nothaft, M. *et al.* Electrically driven photon antibunching from a single molecule at room temperature. *Nat. Commun.* **3**, 628 (2012).
163. Huang, H., Dorn, A., Bulovic, V. & Bawendi, M. G. Electrically driven light emission from single colloidal quantum dots at room temperature. *Appl. Phys. Lett.* **90**, 023110 (2007).
164. Dorn, A., Huang, H. & Bawendi, M. G. Electroluminescence from nanocrystals in an electromigrated gap composed of two different metals. *Nano Lett.* **8**, 1347–1351 (2008).
165. Gudiksen, M. S., Maher, K. N., Ouyang, L. & Park, H. Electroluminescence from a single-nanocrystal transistor. *Nano Lett.* **5**, 2257–2261 (2005).
166. Marquardt, C. W. *et al.* Electroluminescence from a single nanotube-molecule-nanotube junction. *Nat. Nanotechnol.* **5**, 863–867 (2010).
167. Yang, C. *et al.* A Tunable Single-Molecule Light-Emitting Diode with Single-Photon Precision. *Adv. Mater.*, e2209750 (2023).
168. Hettick, M. *et al.* Shape-controlled single-crystal growth of InP at low temperatures down to 220 °C. *Proc. Natl. Acad. Sci. U. S. A.* **117**, 902–906 (2020).
169. Rahman, I. K. M. R., Uddin, S. Z., Kim, H., Higashitarumizu, N. & Javey, A. Low voltage AC electroluminescence in silicon MOS capacitors. *Appl. Phys. Lett.* **121**, 193502 (2022).
170. Hu, L., Hecht, D. S. & Grüner, G. Percolation in Transparent and Conducting Carbon Nanotube Networks. *Nano Lett.* **4**, 2513–2517 (2004).
171. Arnold, M. S., Stupp, S. I. & Hersam, M. C. Enrichment of single-walled carbon nanotubes by diameter in density gradients. *Nano Lett.* **5**, 713–718 (2005).
172. Rosenberger, M. R. *et al.* Measuring individual carbon nanotubes and single graphene sheets using atomic force microscope infrared spectroscopy. *Nanotechnology* **28**, 355707 (2017).

173. Efros, A. L. & Nesbitt, D. J. Origin and control of blinking in quantum dots. *Nat. Nanotechnol.* **11**, 661–671 (2016).
174. Galland, C. *et al.* Two types of luminescence blinking revealed by spectroelectrochemistry of single quantum dots. *Nature* **479**, 203–207 (2011).
175. Lee, T.-H., Gonzalez, J. I. & Dickson, R. M. Strongly enhanced field-dependent single-molecule electroluminescence. *Proc. Natl. Acad. Sci. U. S. A.* **99**, 10272–10275 (2002).
176. Lee, T.-H. & Dickson, R. M. Single-Molecule LEDs from Nanoscale Electroluminescent Junctions. *J. Phys. Chem. B* **107**, 7387–7390 (2003).
177. Empedocles, S. A., Norris, D. J. & Bawendi, M. G. Photoluminescence Spectroscopy of Single CdSe Nanocrystallite Quantum Dots. *Phys. Rev. Lett.* **77**, 3873–3876 (1996).
178. S. A. Empedocles, R. Neuhauser, K. Shimizu, M. G. Bawendi. Photoluminescence from Single Semiconductor Nanostructures. *Adv. Mater.* **11** (1999).
179. Lee, T.-H., Gonzalez, J. I., Zheng, J. & Dickson, R. M. Single-molecule optoelectronics. *Acc. Chem. Res.* **38**, 534–541 (2005).
180. Zhou, J., Chizhik, A. I., Chu, S. & Jin, D. Single-particle spectroscopy for functional nanomaterials. *Nature* **579**, 41–50 (2020).
181. Honmou, Y. *et al.* Single-molecule electroluminescence and photoluminescence of polyfluorene unveils the photophysics behind the green emission band. *Nat. Commun.* **5**, 4666 (2014).
182. Sharma, D. K., Hirata, S. & Vacha, M. Single-particle electroluminescence of CsPbBr<sub>3</sub> perovskite nanocrystals reveals particle-selective recombination and blinking as key efficiency factors. *Nat. Commun.* **10**, 4499 (2019).
183. Ebenstein, Y., Mokari, T. & Banin, U. Fluorescence quantum yield of CdSe/ZnS nanocrystals investigated by correlated atomic-force and single-particle fluorescence microscopy. *Appl. Phys. Lett.* **80**, 4033–4035 (2002).
184. Gopinath, A. *et al.* Absolute and arbitrary orientation of single-molecule shapes. *Science* **371** (2021).
185. Xie, W. *et al.* Nanoscale and Single-Dot Patterning of Colloidal Quantum Dots. *Nano Lett.* **15**, 7481–7487 (2015).
186. Zhang, H., Kinnear, C. & Mulvaney, P. Fabrication of Single-Nanocrystal Arrays. *Adv. Mater.* **32**, e1904551 (2020).
187. Zhu, W., Satterthwaite, P. F., Jastrzebska-Perfect, P., Brenes, R. & Niroui, F. Nanoparticle contact printing with interfacial engineering for deterministic integration into functional structures. *Sci Adv* **8**, eabq4869 (2022).
188. Hoshino, K., Gopal, A., Glaz, M. S., Vanden Bout, D. A. & Zhang, X. Nanoscale fluorescence imaging with quantum dot near-field electroluminescence. *Appl. Phys. Lett.* **101**, 043118 (2012).

189. Patil, N. *et al.* Wafer-Scale Growth and Transfer of Aligned Single-Walled Carbon Nanotubes. *IEEE Trans. Nanotechnol.* **8**, 498–504 (2009).